Vol 10 • No. 1• April 2016

ISSN: 0976 - 1330

Journal of GEOMATICS

INDIAN SOCIETY OF GEOMATICS

Journal of Geomatics

(A publication of the Indian Society of Geomatics)

Indian Society of Geomatics
Executive Council 2014 – 2017

Secretary: (address for correspondence)
39, Basant Bahar-II, Bopal, Ahmedabad – 380058, India
Email : *nsmehta55@gmail.com* or *secretary@isgindia.org*

Journal of Geomatics
(A publication of the Indian Society of Geomatics)

Vol. 10 No. 1 April 2016

Research articles

Published biannually by the Secretary, Indian Society of Geomatics on behalf of the Society

ISG Website: www.isgindia.org

Journal of Geomatics

Vol 10 No. 1 April 2016

Flood hazard zoning using analytic hierarchy process: A case study for Pampa river basin, Kerala, India

N.A. Mayaja[1] and C.V. Srinivasa[2]

[1]Department of Civil Engineering, Atria Institute of Technology, Anand Nagar, Bangalore, 560098, India

[2]Department of Civil Engineering, Global Academy of Technology, Bangalore, 560024, India

Email: mayaja@hotmail.com, svasa@gat.ac.in

(Received: Jan 06, 2016; in final form: Mar 06, 2016)

Abstract: The river Pampa is the third largest river of Kerala with a catchment area of 2235 km^2. This river almost every year causes substantial damage to human life, properties and the cropland during monsoon. In this study an attempt is made to classify the regions in the river basin in order of risk and severity due to floods. The severity of flood hazard in these locations varies due to various geospatial factors. The hazard due to flood in any particular location and its impact can be assessed in relative terms by using an analytical approach as applied to a set of geospatial factors ranging from qualitative to quantitative type. This paper evolves appropriate risk indices for the entire Pampa river basin and classifies them according to the severity of flood risk using a popular Analytic Hierarchy Process (AHP). The study brought out that two regions in the river basin fall under very high flood risk category whereas four villages come under high risk category. It was revealed that highly populated and urbanized regions located in the downstream of this river basin are more vulnerable to flood hazard.

Key Words: Flood Hazard Index (FHI), Analytic Hierarchy Process (AHP), Pampa river basin, Kerala floods

1. Introduction

The holy river Pampa (also referred as Pamba) in Kerala state is the third largest river (about 176 km) with a catchment area of 2235 km^2. It originates on the Western Ghats and flows through Kuttanadu, the rice bowl of the state and drains into the Vembanadu lake. The severity of floods caused by this river and consequent disasters are increasing annually. Some studies have revealed that the recurring incidents of flood are mainly on account of the human interventions like deforestation, reclamation, sand mining beside indiscriminate developmental activities. It has thereby caused severe damages to the physical and biological environment of this river system. A GIS based study of flood-prone areas of Pampa river basin has been carried out using the ground parameters and satellite imagery (Mayaja and Srinivasa, 2012). In this paper, appropriate flood hazard indices for the river basin have been generated based on the severity due to floods. The study has made use of the well known Analytic Hierarchy Process (AHP) (Saaty and Alexander, 1989).

2. Study area and data used

This study focuses the basin of Pampa river (approximately 2235 km^2) which is shown in Figure 1. The river basin stretches over four districts of Kerala, viz., Idukki, Kottayam, Pathanamthitta and Alappuzha. The area extends over dense tropical monsoon forests, semi-urbanized settlements, one famous pilgrim center – Sabarimala and also a rich agricultural (rice) bowl of Kerala, called Kuttanad. The study area lies between $76^0$20’ to $76^0$59’ East in longitude and $9^0$19’ to $9^0$39’ North in latitude. With humid tropical monsoon climate (average annual rainfall 3000 mm with summer rains constituting about 10%), the basin experiences two distinct rainy seasons, South-West monsoon (June to September) contributing about 60% of the rainfall and North-East monsoon (October to December), providing about 30% of the rainfall. With a relative humidity of 70% to 90%, the study area experiences a temperature in the range of 21^0 to 36^0 C. The peak altitude of the basin is about 1677 m (at the origin of the river) and while flowing through a distance of about 176 km the river reaches the sea level and finally joins the Vembanad lake and Arabian sea.

Figure 1: Study area

The population density of the regions (number of persons per km^2) was obtained from the latest National census data. Rainfall data (in mm) was obtained from the India Meteorological Department and Department of Irrigation, Government of Kerala. Land use data and basin slope were availed from the National Remote Sensing Centre of Indian Space Research Organization. Data related to types of soil were taken from the official website of the Department of soil survey and soil conservation, Government of Kerala. The geomorphic data and the details of road networks were collected from the Kerala State Remote Sensing Centre, Thiruvananthapuram. The basin elevation was available in the Survey of India toposheets.

3. Methodology

3.1 Analytic Hierarchy Process (AHP)

The Analytic Hierarchy Process (AHP) is a multi-criteria decision making statistical technique, which provides a systematic approach for assessing and integrating the impacts of various factors, involving several levels of dependent and independent variables. It is a statistical tool popularly used in assessing the impact of various conflicting factors and computing risk indices. AHP attempts to resolve conflicts and analyze judgments through a process of determining the relative importance of a set of activities or criteria by 'pair-wise' comparison (Saaty and Alexander, 1989, Saaty 1994, Saaty and Vargas 2002). This technique has been effectively used to identify and rank the factors affecting flood in Kosi river basin (Venkata Bapalu and Sinha, 2014).

In order to perform AHP analysis, a complex problem is first divided into a number of simpler problems in the form of a decision hierarchy. Once the hierarchy is built, the decision makers systematically evaluate its various elements by comparing them to one another, two at a time, with respect to their impact on an element above it in the hierarchy. In making the comparisons, the decision makers can use concrete data on the elements, or they can use their judgments about the element's relative meaning and importance. It is the essence of the AHP that human judgments, and not just the underlying information, can be used in performing the evaluations.

In AHP computation, the decision vectors are constructed at each level of the hierarchy by pair-wise comparison of the elements (decision factors). The eigen vectors so formed are then normalised. The Relative Importance Weights (RIWs) of each decision factor is obtained as the sum of the values in the corresponding row of the normalised eigen vector. Similar computation of RIWs is performed at each level of the hierarchy. The RIWs thus computed are assigned to specific part of the study area. The final solution is evolved by aggregating the product of RIWs at each level. (Saaty and Alexander, 1989).

3.2 Primary decision factors

The first level of the analysis is the generation of the Flood Hazard Index (FHI). In level 2 analysis, this study considered eight primary decision factors viz. population density, rainfall, land use, soil type, basin slope, geomorphic factors, quality of roads and elevation. Once the level 2 decision factors are selected, they are further sub-divided into level 3 sub-factors of smaller class for finer evaluation (Table 1).

The factors considered at level 1, 2 and 3 are illustrated in Appendix 1. The values of the sub-classification at level 3 for level 2 factors is shown in Table 1.

Table 1: Level 3 sub-classifications of decision factors

Level-2 factor	**Level 3 sub-factors**			
Population density (number of persons / km^2)	<1000 (Low)	1000 to 2000 (medium)	2000 to 3000 (high)	>3000 (very high)
Annual average rainfall (mm)	2500 to 3000 (Less)	3000 to 3500 (medium)	3500 to 4000 (high)	>4000 (very high)
Land use-land cover	Agriculture	Forest	Built up	Waste land
Soil type	Hill soil	Clayey loam	Laterite soil	Sandy soil
Slope	3°- 5° (Gentle)	5°-15° (Moderate)	15° - 30° (Steep)	>30° (Very steep)
Geomorphic factors	Denudati-onal Hills	Lower Plateau	Coastal Plain	Alluvial Plain
Road quality	High	Medium	Low	Very low
Elevation (metres)	0 - 10 (Low)	10 to 30 (Medium)	30 to 150 (High)	>150 (very High)

Appendix 1 shows the hierarchy and the relative importance weight of level 2-decision factors (RIWi2) arrived at by pair-wise comparison of the decision factors. This was followed by pair wise comparison within each level 3-decision factor to get the corresponding relative importance weight (RIWi3).

4. Flood Hazard Index (FHI)

4.1 Algorithm

The FHI for each location was determined by aggregating RIWs of decision factors at each level of the hierarchy. FHI was calculated by multiplying the RIWs of level 3-decision factor by the associated RIWs of the level 2 factors at each level and summing the values of all grouped elements. As the problem is defined in three level hierarchies, the simplified generic equation used is as follows:

$$\mathrm{FHI} = \sum_{i=1}^{N2}[(\mathrm{RIW}_i{}^2) * (\mathrm{RIW}_{ij}{}^3)] \tag{1}$$

where, FHI = Flood Hazard Index; $N2$ = the number of level-2 decision factor; RIW_i^{2} = Relative importance weight of level2 decision factor i; RIW_{ij}^{3} = Relative Importance Weight of level 3 sub-factor j of level-2 decision factor i.

The level 2 normalised relative importance weight matrix computed for various decision factors are given in Table 2.

Table 2: Normalised relative importance weights of level 2

Sl.No	Decision factor	Level–2 Relative Importance Weight
1	Population density	0.35
2	Rainfall	0.091
3	Land Use Land cover	0.076
4	Soil	0.096
5	Slope	0.129
6	Geomorphic	0.04
7	Road quality	0.038
8	Elevation	0.18

The level 3 normalised RIW matrices computed for each of the sub-decision factor are given in Appendix 2. FHI and consistency ratios at levels 2 & 3 are given in appendix 3 and 4, respectively.

4.2 Region specific FHIs

The river basin consists of 52 regions (Panchayaths and Municipalities) as per the local administrative classification of Government of Kerala. All the 52 regions were considered for the purpose of analysis in this study. The FHI in respect of all these regions were computed as per the algorithm given under 4.1. The frequency distribution of FHI is shown in Fig. 2.

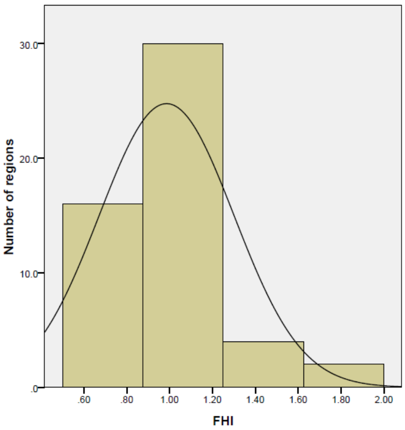

Figure 2: Histogram distribution of FHI

It can be seen that the 52 FHIs so computed are predominantly falling in four frequency bandwidths (Fig. 2). Based on the histogram distribution, the regions of Pampa river basin have been grouped into low, moderate, high and very high flood-risk category. The risk category of these regions along with their respective FHI values are shown in Table 3. A schematically classified risk map of the river basin is shown in Fig. 3.

Table 3: Flood prone regions in Pampa river basin

No.	Zone / region	FHI	Category
1	Thiruvanvandoor	1.87	VERY HIGH
2	Veeyapuram	1.87	VERY HIGH
3	Chengannur	1.32	HIGH
4	Pandanadu	1.32	HIGH
5	Niranam	1.32	HIGH
6	Kuttoor	1.31	HIGH
7	Chenneerkkara	1.20	MEDIUM
8	Omalloor	1.20	MEDIUM
9	Aranmula	1.19	MEDIUM
10	Mulakkuzha	1.19	MEDIUM
11	Mezhuveli	1.19	MEDIUM
12	Kulanada	1.19	MEDIUM
13	Mannar	1.19	MEDIUM
14	Kozhencherry	1.16	MEDIUM
15	Iraviperoor	1.15	MEDIUM
16	Naranganam	1.15	MEDIUM
17	Puliyoor	1.14	MEDIUM
18	Cherukole	1.11	MEDIUM
19	Koipram	1.11	MEDIUM
20	Mylappra	1.09	MEDIUM
21	Mallappuzhassery	1.09	MEDIUM
22	Ilanthoor	1.08	MEDIUM
23	Ala	1.06	MEDIUM
24	Ayiroor	1.05	MEDIUM
25	Ezhamattoor	1.05	MEDIUM
26	Thottapuzhassery	1.05	MEDIUM
27	Manimala	1.04	MEDIUM
28	Naranammoozhi	1.02	MEDIUM
29	Ranni-Perunnadu	1.02	MEDIUM
30	Malayalappuzha	1.02	MEDIUM
31	Kottanadu	1.01	MEDIUM
32	Kottangal	1.01	MEDIUM
33	Ranni-Angadi	1.01	MEDIUM
34	Vadaserikkara	1.00	MEDIUM
35	Ranni	0.99	MEDIUM
36	Ranni-Pazhavangadi	0.99	MEDIUM
37	Kadapra	0.67	LOW
38	Peruvanthanam	0.62	LOW
39	Vechuchira	0.61	LOW
40	Bhudhanoor	0.61	LOW
41	Chennithala-Thripperunth	0.61	LOW
42	Thannithode	0.61	LOW
43	Erumely	0.60	LOW
44	Seethathode	0.60	LOW
45	Elappara	0.59	LOW
46	Aurvappulam	0.59	LOW
47	Konni	0.58	LOW
48	Chittar	0.58	LOW
49	Vandiperiyar	0.57	LOW
50	Peerumade	0.56	LOW
51	Kumily	0.56	LOW
52	Mundakkayam	0.56	LOW

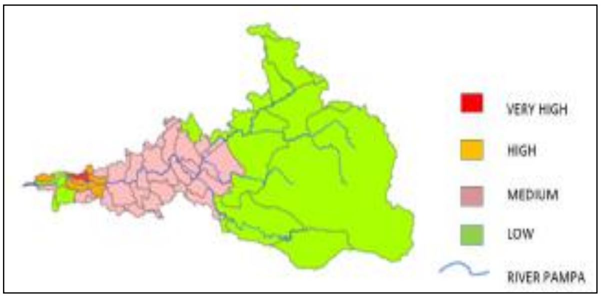

Figure 3: Flood risk map of Pampa river basin

5. Results and discussions

In this study, a set of composite flood hazard indices for the Pampa river basin has been worked out by adopting the AHP methodology. The indices have been derived from primary decision factors viz: population density, annual average rainfall, land use, type of soil, slope, geomorphic features, quality of roads and elevation. The Panchayaths/ municipalities of Pampa river basin have been accordingly classified into low, medium, high and very high risk categories based on histogram distribution of FHI.

The analysis revealed two regions - Thiruvanvandoor, and Veeyapuram - covering about 7.5 km^2 of the basin as areas prone to 'very high' levels of flood risk. Four regions, covering about 35 km^2 come under the 'high risk' category of flood where as another 30 regions (395 km^2) fall under the 'medium risk' category. Remaining portions of the basin are relatively under 'low risk'. It is observed that though the regions falling under very high and high level of flood hazard constitute only 0.3% and 2 % respectively of the basin area, these are densely populated and highly urbanised regions (with density of population more than 3000 persons / km^2), located at the downstream of the river. Further, the land use pattern of these regions reveals high level of built up area and they have good network of paved highways. Thus, it can be inferred that the prime reasons of flood hazard are high rate of urbanization and human interventions in this region. The extensive road networks recently developed in the river basin also testify this finding. Owing to the same reasons the flood occurrence at these regions causes more damages to both humans as well as infrastructure.

Amongst the eight primary decision factors influential in causing flood hazard, the most prominent anthropogenic factor identified is population density. This calls for urgent need of an effective urban planning in the basin and also implementing regulatory mechanisms to check uncontrolled and haphazard rate of urbanisation, which is detrimental to both humans as well as the river itself. The land use and land cover also is identified as an influencing factor. Hence proper environmental and ecological regulations and auditing can reduce the vulnerability of the region to flood. A flood mitigation policy based on the above suggestions can effectively help in reducing the flood risk.

6. Conclusions

Ranking the villages in the flood plain is of utmost importance in flood management planning. In this study, 52 villages in the Pampa river basin are classified according to their Flood Hazard using Analytic Hierarchy Process. The indices have been derived from a variety of parameters (factors) ranging from geospatial data to population density, rainfall, land use, type of soil, slope, geomorphic factors, quality of road and elevation. The flood prone areas of Pampa river basin have been classified into four categories viz. low, medium, high and very high. The analysis reveals that human activities, which result in increased population density, land use land cover changes etc. make the region more vulnerable to flood hazards. Hence a comprehensive basin planning, considering the above factors only will be effective in mitigating flood hazard

References

Mayaja, N.A. and C.V. Srinivasa (2012). A GIS based flood mapping study for Pampa river basin, Kerala. Research dissertation of Visweswaraya Technological University, Karnataka.

Saaty, T.L. and J. Alexander (1989). Conflict resolution: The analytic hierarchy process. Praeger, New York.

Saaty, T.L. (1994). Fundamentals of decision making and priority theory with the analytic hierarchy process. ISBN 0-9620317-6-3.

Saaty, T.L. and L.G. Vargas (2002). Models, methods, concepts & applications of the analytic hierarchy process. Book. ISBN 0-7923-7267-0, Kluwer Academic.

Venkata Bapalu, G. and R. Sinha (2014). GIS in flood hazard mapping: A case study of Kosi river basin,India. download from internet, http://GISdevelopment.net

Journal of Geomatics Vol 10 No. 1 April 2016

Appendix-1
(FHI computation: Decision Hierarchy at levels 1, 2 and 3)

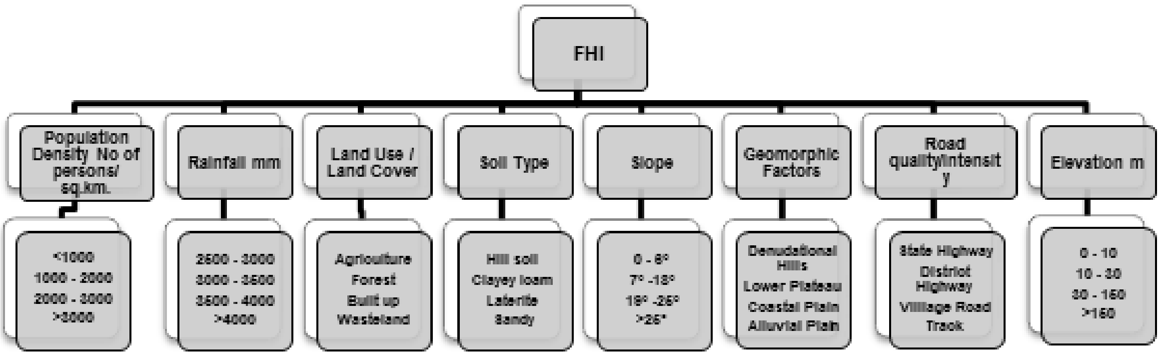

Appendix 2
(The comparison matrix for level- 2)

Factor	Population Density	Rainfall	LULC	Soil	Slope	Geomor-phic factors	Roads	Elevation
Population Density	**1**	3	4	5	5	7	4	5
Rain-fall	0.333	**1**	0.5	0.333	0.2	4	7	0.25
LULC	0.25	2	**1**	0.333	0.2	3	4	0.2
Soil	0.2	3	3	**1**	0.5	2	2	0.5
Slope	0.2	5	5	0.5	**1**	3	3	0.333
Geomorphic factors	0.143	0.25	0.333	0.5	0.333	**1**	2	0.25
Roads	0.25	0.148	0.25	0.5	0.333	0.5	**1**	0.333
Elevation	0.2	4	5	2	3	4	3	**1**

Appendix 3
(FHI computation)

The FHI for each location was determined by aggregating RIWs at each level of the hierarchy. FHI was calculated by multiplying the RIWs of level 3-decision factor by the associated RIWs of the level 2 factors at each level and summing the values of all grouped elements. The level 2 and level 3 Relative Importance Weight matrices computed are shown below:

Level 2	**Population Density**	RIW = 0.35	**Rainfall**	RIW = 0.091	**LULC**	RIW = 0.076	**Soil**	RIW = 0.096
Level 3	Low	0.048	Very High	0.466	Agriculture	0.238	Hill soil	0.145
	Medium	0.108	High	0.277	Forest	0.116	Clayey loam	0.462
	High	0.259	Medium	0.161	BuiltUp	0.584	Laterite	0.282
	very High	0.586	Less	0.096	WasteLand	0.062	Sandy	0.111

Level 2	**Slope**	RIW = 0.129	**Geomorphic factors**	RIW = 0.04	**Road quality**	RIW = 0.038	**Elevation**	RIW = 0.18
Level 3	Gentle	0.586	Denudational Hills	0.222	very Low	0.468	Low	0.554
	Moderate	0.259	Lower Plateau	0.237	Low	0.279	Medium	0.219
	Steep	0.108	Coastal Plain	0.122	Medium	0.149	High	0.133
	Very steep	0.048	Alluvial Plain	0.419	High	0.103	very High	0.094

Appendix 4

(The consistency ratios at levels 2 and 3)

Consistency Ratio CR	**Level 2**	**Level 3**								Overall CR
		Population Density	Rainfall	LULC	Soil	Slope	Geomorphic factors	Roads	Elevation	
	0.176	0.048	0.014	0.071	0.129	0.048	0.027	0.008	0.029	3.106

Journal of Geomatics Vol 10 No. 1 April 2016

Performance evaluation of dimensionality reduction techniques on CHRIS hyperspectral data for surface discrimination

Veeramallu Satya Sahithi and Iyyanki V Murali Krishna
Research Centre Imarat (RCI-DRDO), Vigyana Kancha, Hyderabad – 500069
Email: sahithi.geo@gmail.com, iyyanki@gmail.com

(Received: Jun 19, 2015; in final form: Dec 31, 2015)

Abstract: Dimensionality reduction (DR) techniques help in reducing the volume of the hyperspectral data with minimum loss of information. The three most commonly used DR techniques – PCA, MNF and ICA have their own advantages and limitations in transforming the redundant hyperspectral data to non-redundant data thus aiding in an improved feature extraction. In the present work, an attempt was made to analyze the performance of hybrid dimensionality reduction method which uses a combination of three non – linear DR techniques for extracting the concrete materials from the CHRIS hyperspectral data. SAM and SID classifiers were used for classifying six different surface materials (concrete, paved and unpaved) in the study area along with four different vegetation types. Analysis has shown that the hybrid method gave satisfactory results for classifying the surface materials in CHRIS data. The SAM classifier gave the best results with an accuracy improvement of 10% after adapting the hybrid method. The classification accuracies have increased from 79.54% to 85.14% for SAM classification and 80.24% to 84.90% for SID classification.

Keywords: Principle component analysis(PCA), Minimum noise function (MNF), Independent component analysis (ICA), Hybrid method, Classification

1. Introduction

Hyperspectral data contain high spectral information due to the continuous spectral bands and narrow band width. Such high voluminous data may lead to redundant information. To overcome the problem of redundancy and for flexible feature extraction from the voluminous hyperspectral datasets, certain dimensionality reduction (DR) techniques are used. The dimensionality reduction techniques transform the data into a new domain where the data in each band is made uncorrelated to the other band based on certain criteria. There are many kinds of DR techniques that are broadly classified as linear and non – linear DR techniques. The three well known feature extraction/dimensionality reduction techniques include the principal component analysis (PCA), minimum noise fraction (MNF) and independent component analysis (ICA) techniques. Each of these techniques works on a unique principle and has its own advantages and disadvantages. Besides, each technique extracts unique features that are totally different to that others extract. The PCA techniques works on the data variance, MNF sorts the information based on the SNR
and the ICA assumes each band to be a linear mixture of some independent hidden components and thus applies a linear unmixing procedure to extract the independent features. PCA and MNF measure the second order statistics of the data with a gaussian assumption, while ICA uses higher order statistics and gives statistically independent components with non – gaussian assumption (Wang et.al., 2014). The second order statistics used in PCA and MNF cannot uncover the subtle material substances that are uncovered by hyperspectral images (Wang et.al., 2014). Hence, to make the most out of each of these techniques and to overcome their disadvantages, Galal and Hasan, 2012, in his paper "Learning Flexible Hyperspectral Features" proposed an improved method of feature extraction, where a combination all the three unsupervised DR techniques is used to extract the features of interest. Initially an MNF transform was applied on AVIRIS hyperspectral data and the bands containing the highest signal to noise ratio (SNR) were considered for the next step. In the next step, the first 10 MNF bands containing high SNR were used as inputs for PCA and ICA and the outputs of these transformations were stacked together to form a new vector for each pixel in the image. Each of these vectors was then classified using a Support Vector Machine. The method proposed in Galal and Hasan (2012) improved the overall performance of the SVM classifier and gave good results statistically. In the present work, the performance of this method was tested on a hyperspectral CHRIS image for extracting various concrete structures. The objective of the present study is to extract different kinds of concrete materials from dimensionally reduced the CHRIS hyperspectral image.

1.1. Principal Component Analysis (PCA)

PCA, also called the Karhunen-Love transform (KLT) or the Hotelling transform, is a classical statistical technique used to reduce the dimensionality of the multi-dimensional data. PCA finds a new set of orthogonal axes that have their origin at the data mean and that are rotated to maximize the data variance. The covariance matrix which is used as a transformation matrix is defined as:

$$\sum cov = \sum_{i=1}^{n} (\bar{x}_i - \bar{m})\,(\bar{x}_i - \bar{m})^T \qquad (1)$$

where $\bar{x}_i$ is the i th spectral value, $\bar{m}$ is the mean spectral values, n is the number of pixels in the image. The eigen decomposition of the covariance matrix is performed in order to calculate the new orthogonal axes, which can be given as:

$$\sum \hat{a}_k = \lambda_k \hat{a}_k \qquad ; k= 1,2,\ldots\ldots N \qquad (2)$$

where λ_k is the kth eigen value, $\hat{a}_k$ is the corresponding eigenvector and N being the number of bands. The eigen vector forms the axes of PCA space while the eigen values are the measure of variance of the corresponding eigenvector. The information content of the band increases with the increasing value of variance (Panwar et al., 2014). The PCA bands are arranged based on the variance value – first band contains highest information with a largest eigen value, the second PC band contains the second largest amount of information and is orthogonal to the first PC, the third PC has the third largest variance value and is orthogonal to both first and second PC's and so on.

1.2. Minimum Noise Fraction (MNF)

MNF is one of the most commonly adopted unsupervised DR techniques for the hyperspectral data. The MNF transform is specifically designed as a linear transformation that maximizes the signal-to-noise ratio, thus ordering images in terms of decreasing image quality in lower order components. The foundations of the MNF transform were developed by Green *et al.* (1988) and Lee *et al.* (1990). The former explained it based on signal to noise ratio and demonstrated noise filtering via complex matrix inversion. Lee *et al.* (1990) simplified this as a two-cascaded PCA transform. The first phase of the MNF transform starts with image noise determination and noise covariance matrix calculation of the image which is subsequently followed by eigen value decomposition. The third step includes image mean correction, noise decorrelation and finally normalization of the linear noise in the data which is called as noise whitening (Mundt et al., 2007). This noise whitened data is decorrelated using a PCA transform which is the second step of MNF transform. The higher order images will have high SNR which gradually reduces towards the lower order images (which are noise dominated). Transformed MNF data are highly decorrelated and have zero mean and a unit noise variance. The covariance matrix of an MNF transformed dataset is a diagonal matrix with elements equal to the MNF eigen values.

1.3. Independent component Analysis (ICA)

ICA on multispectral or hyperspectral datasets transform a set of mixed random signals into components that are mutually independent. The major advantage of this ICA transform over PCA and MNF methods is that it is based on the non-Gaussian assumption of the independent sources which is a typical characteristic of hyperspectral datasets. It uses higher-order statistics to discover some interesting features in non-Gaussian hyperspectral datasets (Yusuf and He, 2011). IC transformation can distinguish features of interest even when they occupy only a small portion of the pixels in an image while in PCA these small features are buried in the noisy bands (ENVI 2010). Hence ICA analysis is very much helpful in spectral unmixing, anomaly and target detections.

ICA is a blind source separation technique. It assumes that each band is a linear mixture of independent hidden component and extracts the independent feature using a linear unmixing operation (Panwar et al., 2014).

Suppose we have N statistically independent signals, $s_i(t)$, i=1,…….,N. let X(t) denote the original source signal. ICA estimates X(t) by,

$$s(t)= U\,X(t) \qquad (3)$$

where U is an unknown matrix called the unmixing matrix. This is a blind source separation algorithm since we do not have any prior information about unmixing matrix or even on the source themselves.

2. Datasets and study area

The dataset used for the present study is the hyperspectral Compact High Resolution Imaging Spectrometer (CHRIS) on board the Proba mission of the European Space Agency. CHRIS is an experimental satellite which monitors the earth in five modes and in five different look angles - +55º, +36º, 0º,-36º and -55º (Sahithi and Agrawal, 2014). The image considered is a nadir (0º) looking image obtained in mode 5 (land use/land cover applications). It has a spatial resolution of 17m with 18 spectral bands in the range of 400 – 1500nm. The present study area is one of the test sites of CHRIS experimental sensor. The study area is a part of Suratgarh airbase station located in Sri Ganganagar district, Rajasthan. It falls within the latitude and longitude of $29^0$22'24"N to $29^0$24'49"N and $73^0$52'44"E to $73^0$55'54"E. It has a total area of the airbase and is mostly composed of different concrete materials and two to three kinds of vegetation. A location map of the study area is given in Fig 1.

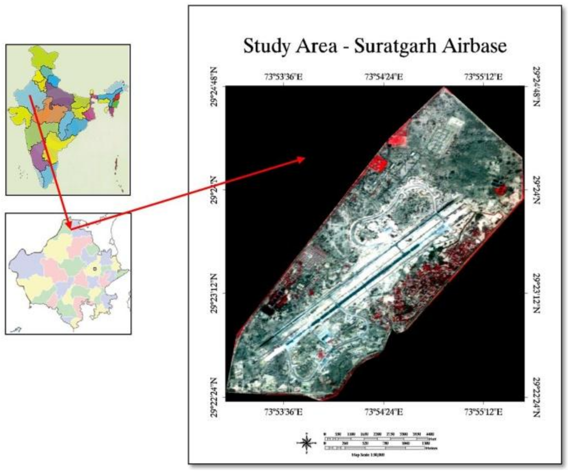

Figure 1: Study area used - LISS IV image of Suratgarh airbase, Rajasthan, India

3. Methodology

The radiometrically and atmospherically corrected CHRIS data is first reduced using the MNF transformation. The MNF components having high information are considered for further analysis. A principal component transformation and independent component analysis is performed over the selected MNF components which gave a set of components for each of these transformations. All these components are then stacked to form a new vector for each pixel in the image.

A simple SAM (Spectral Angle Mapper) classifier and Spectral Informed Divergence (SID) classifier are used over this stacked image to classify various surface materials in the study area. Total of 10 classes were considered - new concrete, old concrete, tar, white paint, sand, cemented area, croplands, shrubs, thorny trees, bushy trees. The average spectra of various materials considered for classification are shown in Fig 3. A constant SAM angle of 0.15 was used for classifying the final hybrid DR reduced image and the original CHRIS image.

Observations were made to trace some inherent features which are not observed in CHRIS original hyperspectral image. The extracted features after classification are validated using the temporal google earth images.

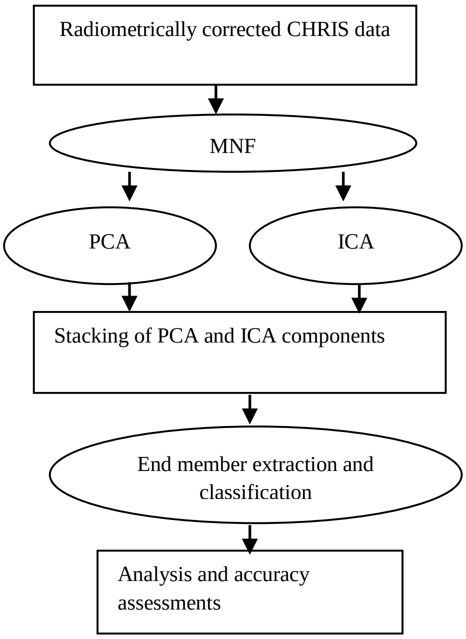

Figure 2: Methodology

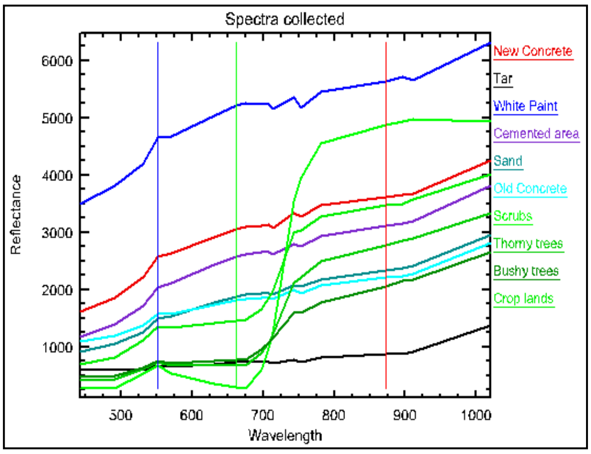

Figure 3: Average spectra of various materials collected for classification

4. Results and analysis

On performing the MNF transform over the CHRIS image, the first 8 bands are considered for further processing due to their high signal to noise ratio. The components were chosen based on their eigen value and visual information content. Apart from the MNF transform, a simple PCA and ICA are also applied over the hyperspectral image to test the performance of various dimensionality reduction techniques. The eigen values of PCA, MNF and ICA transformations of the hyperspectral image are shown in table 1. The components having the highest eigen values are considered as the informative bands and hence the first 8 bands are considered in this work. The huge difference in the eigen values of first and second PCA component shows the diversity in information content and non-correlation between the adjacent bands. Visual inspections have shown that independent component analysis had more noise. An observation was made on the eigen values of PCA, MNF and ICA transformations which showed that PCA and ICA had similar eigen values. This was due to the fact that ICA is a two step process which starts with an initial PCA transform of the image. PCA and ICA transforms performed on the MNF components produced better results than the direct PCA and ICA results.

Table 1: The eigen values of PCA, MNF and ICA transformations

Band number	PCA after MNF	ICA after MNF	MNF Eigen values
1	79.764	79.764	79.764
2	10.259	10.259	10.259
3	7.670	7.670	7.670
4	5.995	5.995	5.995
5	3.626	3.626	3.626
6	3.284	3.284	3.284
7	2.519	2.519	2.519
8	2.309	2.309	2.309

However, the eigen values of the PCA post MNF and ICA post MNF were same (Table 2) over the original CHRIS image.

Table 2: The eigen values of PCA after MNF, MNF and ICA after MNF transformations

Band number	PCA Eigen Values	MNF Eigen values	ICA Eigen Values
1	23439699.36	79.765	23439699.36
2	174555.788	10.260	174555.788
3	8415.922	7.671	8415.923
4	5898.305	5.995	5898.305
5	625.206	3.626	625.206
6	551.119	3.284	551.119
7	340.441	2.519	340.441
8	208.063	2.3094	208.063

The stacked image obtained by laying the PCA post MNF components over the ICA post MNF components was used for classification of various surface materials. Supervised SAM and SID classifications were used for surface material classification over the stacked image and the original atmospherically corrected CHRIS nadir image. A comparative study of classified stacked image and the classified original image for six different concrete (paved and unpaved) surfaces have shown that the considered method yielded better classification results than the original image. The DR techniques not only helped in reducing the size of the input image but also removed the unwanted and redundant noise from the image. This technique highlighted certain hidden man made concrete features like roads, houses etc.

The removal of unwanted noise from the bands improved the results of SAM classification. Thin structures like road path, smaller concrete structures etc which were poorly classified in the original hyperspectral image were well classified after using the stacked vector. The overall accuracies improved by 5 to 6% after using this methodology. Some of the positive visual observations noticed using the classification results are shown in the following figures. The classification of the stacked image extracted the roads in the airbase more distinctly than the classification of the original CHRIS image. Improvements in the extraction of road structures and curved paths are shown in Fig 6.

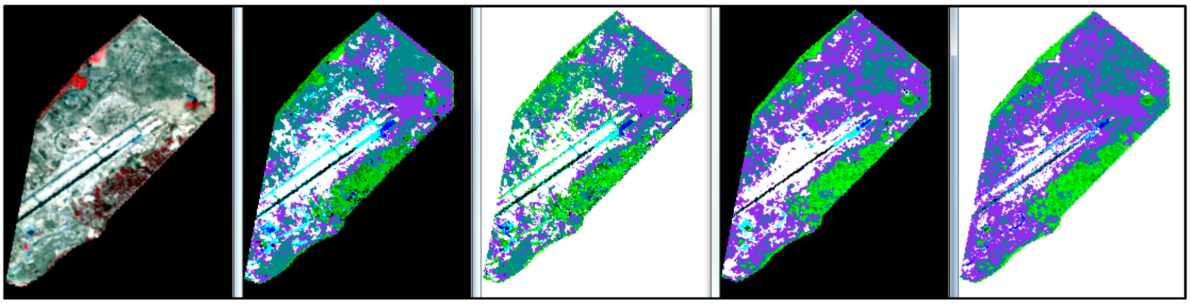

	New Concrete		Old Concrete
	Tar		Scrubs
	White Paint		Thorny trees
	Cemented area		Bushy trees
	Sandy surface		Croplands

Figure 4: Classification of Stacked image (PCA after MNF and ICA after MNF) and the CHRIS atmospherically corrected image using SAM and SID classifiers

Table 3: Classification accuracies of various surface materials considered in classification

	Spectral Angle Mapper		**Spectral Informed Divergence**	
Class name	**Original CHRIS**	**Stacked Vector**	**Original CHRIS**	**Stacked Vector**
New Concrete	78.56%	85.25%	79.56%	87.67%
Tar	85.45%	87.63%	84.68%	88.65%
White Paint	88.56%	91.58%	89.25%	91.44%
Cemented area	72.66%	85.86%	73.58%	80.25%
Sandy surface	74.56%	84.78%	81.21%	82.56%
Old Concrete	80.45%	87.45%	81.56%	87.24%
Scrubs	81.25%	83.15%	79.54%	81.45%
Thomy trees	75.45%	77.63%	74.68%	78.65%
Bushy trees	79.21%	83.47%	80.12%	84.65%
Croplands	79.25%	84.56%	78.21%	86.46%
Average accuracy	79.54%	85.14%	80.24%	84.90%

Accuracy assessment was performed over the four classified images - SAM classified original and transformed stacked images, SID classified original and transformed stacked images. The accuracies for each class in all the four classified maps are shown in table 3. Both SAM and SID classifiers had equal performance in classification. A SAM angle of 0.15 was used for classification of both the original and transformed images. The overall average accuracies (Fig. 5) have increased from 79.54% to 85.14% for SAM classification and 80.24% to 84.90% for SID classification.

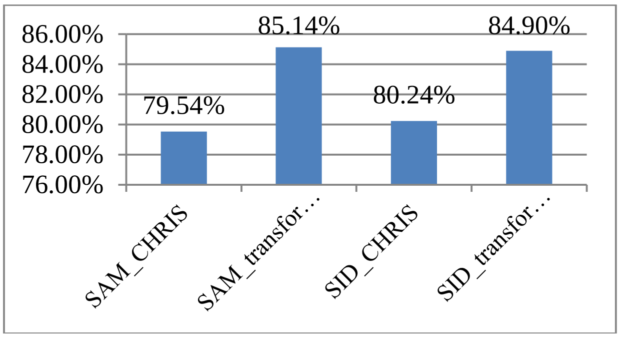

Figure 5: Overall classification accuracies

The spatial resolution of the hyperspectral image plays a major role in the image classification, apart from its high spectral resolution. In the present work, the spatial resolution of 17m of the CHRIS hyperspectral image is still coarse to misclassify the pixel into a different class (mixed pixel effect).

Also it is accepted that the transformed image could not completely restore the spectral resolution of the original CHRIS image after using the DR techniques. Hence, a compromise in the overall accuracy rate of the classifiers is accepted.

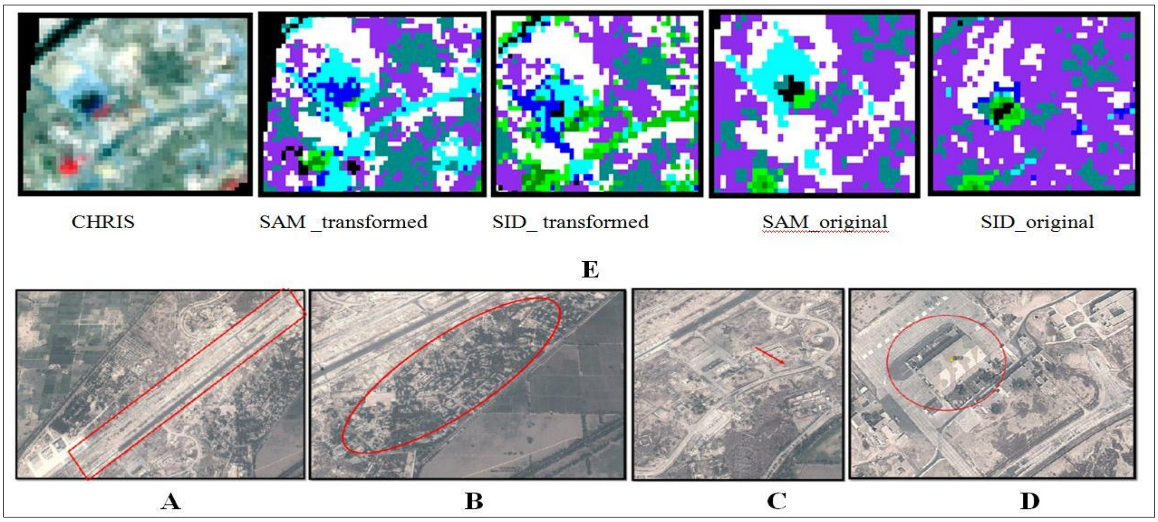

Figure 6: A - Improvements in the extraction of road paths up on classification; B - Improvements in the extraction of urban and concrete buildings in a township; C- Extraction of curved path; D - Extraction of building roof coated with artificial paints; E - Google Earth images of figures – A, B, C, D respectively

5. Conclusions

In this paper, an existing methodology was tested in extracting the features from dimensionally reduced CHRIS hyperspectral data. The MNF technique helped in extracting the data with high signal to noise ratio and in removing the noisy bands from the voluminous hyperspectral data. PCA and ICA transformation of the transformed MNF components helped in bringing out some features which could not be directly observed in the atmospherically corrected untransformed hyperspectral data. ICA technique disclosed the spectral differences in a patch of mixed urban and vegetation. The PCA technique de-correlated the MNF transformed data and some features like roads and other structures hidden within the various bands of the CHRIS image were revealed after this transform. On the whole a combined method of MNF, PCA and ICA techniques seemed to be of great use in detecting the smallest information present in the hyperspectral data. The performance of SAM classifier ameliorated on using the transformed non-redundant and decorrelated data showing a significant improvement in the classification accuracies.

Acknowledgement

The authors are thankful to Dr Sateesh Reddy, the outstanding scientist and Director, Dr BV Rao, Technology Director, Dr Arindan Biswas, Scientist from IIRS and Rama Sarma, DOMS, RCI, DRDO for their interest and for providing the necessary infrastructure and extending all support whenever required.

References

Galal, A. and H. Hasan (2012). Learning Flexible Hyperspectral Features. International Journal of Remote Sensing Applications. IJRSA Vol.2 Iss. 2, 44-48

Green, A.A., M. Berman, P. Switzer and M.D. Craig (1988). A transformation for ordering multispectral data in terms of image quality with implications for noise removal. Transactions on Geoscience and Remote Sensing, 26(1), 65-74.

Lee, J.B., S. Woodyatt and M. Berman (1990). Enhancement of high spectral resolution remote sensing data by a noise-adjusted principal components transform. IEEE Transactions on Geoscience and Remote Sensing, 28(3), 295-304.

Mundt, J.T., D.R. Streutker and F.G. Nancy (2007). Partial unmixing of hyperspectral imagery: Theory and methods. Proceedings of the American Society of Photogrammetry and Remote Sensing.

Panwar, A., A. Singh and H.S Bhaduria (2014). International Journal of Emerging Technology and Advanced Engineering. ISSN 2250-2459, ISO 9001:2008 Certified Journal, Volume 4, Issue 5, 701 - 705.

Sahithi, V.S. and S. Agrawal (2014). Sub pixel location identification using super resolved multilooking CHRIS data. ISPRS-International Archives of the Photogrammetry, Remote Sensing and Spatial Information Sciences, 1, 463-468.

Tutorial, E.Z. (2010). ENVI user guide. Colorado Springs, CO: ITT.

Wang, Y., G. Wu and L. Ding (2014). Plant Species Identification Based on Independent Component Analysis for Hyperspectral Data. Journal of Software 9.6: 1532-1537.

Yusuf, B.L. and Y. He (2011). Application of hyperspectral imaging sensor to differentiate between the moisture and reflectance of healthy and infected tobacco leaves. African Journal of Agricultural Research, 6(29), 6267-6280.

Journal of Geomatics Vol 10 No. 1 April 2016

Accuracy evaluation for online Precise Point Positioning services

Ashraf Farah
College of Engineering, Aswan University, Aswan, Egypt
Email: ashraf_farah@aswu.edu.eg

(Received: Aug 11, 2015; in final form: Jan 01, 2016)

Abstract: Precise Point Positioning (PPP) has been proved by many researchers in the last decade as a cost-effective alternative for Differential GPS (DGPS) with an estimated precision sufficient for many applications. PPP implementation needs state-of-art software to correct GNSS observations from different types of errors. Several online PPP services have been developed recently by government agencies, universities, industries and individuals. The PPP software centre managed by University of New Brunswick (UNB), Canada is offering the user four online PPP services (CSRS-PPP, GAPS, APPS and magicGNSS) (UNB-PPP, 2015). This research presents an accuracy assessment evaluation study for those services by processing 3h 52min. dual frequency-static GPS observations which were divided into 10 sessions with different observation duration (10min, 20min, 30min, 45min., 1 hr, 1.5 hr, 2 hr, 2.5 hr, 3 hr and 3hr 52min.)

Keywords: GPS, Static, Precise point positioning (PPP), Observation duration

1. Introduction

Precise point positioning (PPP) is an enhanced single point positioning technique for code or phase measurements using precise orbits and clocks instead of broadcast data. PPP became viable with the existence of the extremely precise ephemerides and clock corrections, offered by different organizations.To compensate for ionospheric effects (the largest source of error for GPS observations), dual frequency measurements are used for an ionosphere free combination (Rizos et al., 2012).

PPP can provide positioning accuracy of centimeters or millimeters using un-differenced carrier phase observations where ambiguities are usually estimated as float values. PPP precision varies based on observation type (single or dual frequency) and the duration of observations among other factors (Farah, 2013).

The PPP software centre managed by University of New Brunswick (UNB), Canada is offering the user four online PPP services (CSRS-PPP, GAPS, APPS and magicGNSS) (UNB-PPP, 2015) which allows for:

- An easy comparison of PPP solutions provided by different online PPP services
- An increased reliability for the user by giving access to independent PPP solutions
- An insight at the performance of different implementation strategies
- A means of validation for potential PPP software developers

2. Precise Point Positioning (PPP) Approach

The basic observable for PPP is the ionosphere-delay-free (up to first order effects) pseudo-range and carrier-phase observations. The simplified observation equations are given as:

$$P_{if} = \rho + c\,(dT - dt) + T, \qquad (1)$$

and

$$\Phi_{if} = \rho + c\,(dT - dt) + T + \lambda_{if} N_{if}, \qquad (2)$$

where P_{if} is the ionosphere-delay-free pseudorange observation, Φ_{if} is the ionosphere-delay-free carrier-phase observation, in units of meters, ρ is the geometric distance between the satellite and the receiver antenna phase centers, *c* is the vacuum speed of light, *dT* and *dt* are the receiver and satellite clock errors, *T* is the tropospheric slant delay, λ_{if} is the ionosphere-delay-free wavelength and N_{if} is the carrierphase ambiguity. In the standard PPP model, N_{if} is not an integer as it is contaminated by instrumental delays. It is possible to solve this problem by estimating separate pseudorange and carrier-phase clock offsets. However, for this approach, both the pseudorange and carrier phase require a satellite-specific clock bias parameter which must be provided externally, in a similar manner to the clock and orbit products which are already used in PPP, to prevent the normal matrix from being singular (Collins, 2008).

The tropospheric slant delay is normally separated into the zenith delayand a mapping function which is required to make the zenith delay parameter common over all satellites. Table 1 presents the PPP biases and errors that have to be considered (Rizos et al., 2012).

Table 1: The PPP biases and errors that have to be considered (Rizos et al., 2012)

Satellite specific errors
Precise satellite clock corrections
Satellite antenna phase centre offset
Satellite antenna phase centre variations
Precise satellite orbits
Satellite antenna phase wind-up error
Receiver specific errors
Receiver antenna phase centre offset
Receiver antenna phase centre variations
Receiver antenna phase wind-up error
Atmospheric modelling
Troposphere delay
Ionosphere delay (L1 only)
Geophysical models
Solid earth tide displacements
Ocean loading
Polar tides
Plate tectonic motion

3. UNB-PPP Software Centre

PPP implementation needs state-of-art software to correct GNSS observations for different types of errors. Several online PPP services have been developed recently by government agencies, universities, industries and individuals. The University of New Brunswick (UNB), Canada has ongoing effort to promote PPP technique. The PPP software centre managed by UNB, Canada is providing the user four online PPP services CSRS-PPP, GAPS, APPS and magicGNSS (UNB-PPP, 2015). Each service is implemented and managed by an independent organization, however submitting Rinex observation file through UNB-PPP centre will recover solutions from the four PPP services. A simple presentation for the four PPP services is followed. Table 2 presents processing parameters for the used four PPP online services.

3.1 CSRS-PPP Service

The Canadian Spatial Reference System (CSRS) PPP service provides post-processed position estimates over the internet from GPS observation files submitted by the user. Precise position estimates are referred to the CSRS standard North American Datum of 1983 (NAD83) as well as the International Terrestrial Reference Frame (ITRF). Single station position estimates are computed for users operating in static or kinematic modes using precise GPS orbits and clocks (IGS, 2015; Kouba, 2001). The online PPP positioning service is designed to minimize user interaction while providing the best possible solution for a given observation availability. Currently, users need only to specify the mode of processing (static or kinematic) and the reference frame for position output (NAD83 (CSRS) or ITRF). CSRS-PPP service is processing both single and dual frequency observations from GPS and GLONASS (Farah, 2014; CSRS-PPP, 2015).

3.2 GAPS-PPP Service

The GPS Analysis and Positioning Software (GAPS) is a GPS PPP application developed at the UNB (Leandro et al., 2007). GAPS exists in two forms: a web-based positioning service, to which users can upload GPS observations to be processed, and a command-line executable version, which can be used to process large amounts of GPS data in a fast and convenient manner.The algorithms and code structure used in GAPS follows standard GPS PPP approaches but with some important and unique differences.

The ionospheric delay estimation uses a spherical ionospheric shell model, in which the vertical delays are described by means of a zenith delay at the station position and two horizontal gradients. This estimation makes use of carrier-phase measurements only.

The code multipath estimation is based on the assumption that the several effects present in code measurements are dealt with within PPP, but strongly based on carrier-phase measurements. Based on this, these effects can be removed from pseudorange measurements, and the leftover effect is essentially the code multipath plus receiver noise. Another effect which afflicts pseudorange measurements is the code bias. The code biases are important because satellite clock data products are computed using a certain arbitrary convention of observation type, such as P1 code measurements (from semicodeless P(Y) tracking) rather than the C1 code (from C/A-code tracking). If the user´s receiver uses a different observation type than the one which was used to generate the satellite clock error corrections, one has to apply an offset to the correction, equivalent to the bias between the observations, to be able to use these clock products. One of GAPS' analysis tools produces values of the satellite code biases, based on a positioning observation model, as opposed to being based on a satellite clock estimation observation model as is usually the case when bias values are provided to users. Regarding satellite clock error estimates, GAPS was enhanced in order to provide estimates of satellite clock offsets. This tool was created aiming at a suitable approach for real-time carrier-phase based satellite clock estimation (Leandro et al., 2007).

3.3 APPS-PPP Service

The Automatic Precise Positioning (APPS) service of the Global DGPS System is an online service from the JPL (California Institute of Technology, CA, USA). The APPS online service is currently based on JPL's GIPSY-OASIS software, v6.3. It provides a PPP solution for the uploaded RINEX files in static or kinematic techniques. Currently, it deals only with dual frequency data (Table 2). The result is shown on the webpage interface in static technique and in case of kinematic technique, the result is sent to the user's email address. Moreover, the elevation angle and the solution output interval can be controlled by the user (JPL, 2015).

Journal of Geomatics Vol 10 No. 1 April 2016

3.4 magicGNSS-PPP Service

The magicGNSS, v2.5, operated by GMV Aerospace and Defence, Spain, is based on software developed for GALILEO orbit determination and time synchronization. A batch least-squares algorithm is used to minimize measurement residuals and to determine orbits, satellite and station clock offsets, phase ambiguities, tropospheric zenith delays, and station coordinates. The magicGNSS software is processing only dual-frequency observations and does not accept single-frequency observations. (Piriz et al., 2009).

Table 2: Processing parameters for PPP online services

PPP Service	CSRS-PPP	GAPS-PPP	APPS-PPP	magicGNSS-PPP
Reference system	ITRF2008			
Coordinate format	LLH/XYZ			
Satellite orbit and clock ephemeris	IGS	IGS	JPL	IGS
Satellite phase centre offsets	IGS ANTEX			
Receiver phase centre offsets	IGS ANTEX			
Tropospheric model				
Dry model	Davis (GPT)	UNB-VMF1 (CMC)	Standard formula	A batch least squares algorithm that minimizes measurement residuals solving for orbits, satellite and station clock offsets, phase ambiguities and station tropospheric zenith delays.
Wet model	Hopfield model (GPT)	Gradient Chen and Herring model	Standard(0.10m) Gradient model	
Mapping function	GMF	VMF1	GMF	-
Ionospheric model	Second-order linear ionospheric combination	Linear ionospheric free combination	Second-order linear ionospheric combination	Linear ionospheric free combination
Min. Elevation angle	10º	10º	7.5º	10º
GNSS System	GPS/GLONASS	GPS	GPS	GPS/GLONASS/Galileo
Software	CSRS-PPP	GAPS v5.2.0	GIPSY-OASIS v6.3	magicGNSS v5.3
Observation Data	Single/dual frequency Static/kinematic	dual frequency Static/kinematic	dual frequency Static/kinematic	dual frequency Static/kinematic
Ocean tide loading	FES 2004	FES 2004	Desai	Onsala Space Observatory parameters

APPS: Automatic Precise Point Service; CSRS: Canadian Spatial Reference System; GAPS: GPS Analysis and Positioning Software; PPP: precise point positioning; IGS: International GNSS Service; JPL: Jet Propulsion Laboratory; GPT: global pressure and temperature data; GMF: global mapping function; FES: Finite Element Solution; (CMC):Canadian Meteorological Centre ;(GPS)Global Positioning System

Journal of Geomatics Vol 10 No. 1 April 2016

Table 3: The estimated coordinates from the four PPP-services for the 10 observation batches

10 min. observation batch			
Coordinate	Latitude	longitude	Height (m)
Reference	24º 43′ 25.8626″	46º 37′ 02.7899″	645.290
CSRS-PPP	24º 43′ 25.8640″	46º 37′ 02.7916″	645.361
GAPS	24º 43′ 25.8636″	46º 37′ 02.7906″	645.721
magicGNSS	No data	No data	No data
APPS	No data	No data	No data
20 min. observation batch			
Reference	24º 43’ 25.8626’’	46º 37′ 02.7899″	645.290
CSRS-PPP	24º 43′ 25.8637″	46º 37′ 02.7868″	645.035
GAPS	24º 43′ 25.8642″	46º 37′ 02.7866″	645.321
magicGNSS	24º 43′ 25.8748″	46º 37′ 2.8024″	645.944
APPS	24º 43′ 25.8655″	46º 37′ 2.7807″	645.169
30 min. observation batch			
Reference	24º 43′ 25.8626″	46º 37′ 02.7899″	645.290
CSRS-PPP	24º 43′ 25.8627″	46º 37′ 02.7876″	645.146
GAPS	24º 43′ 25.8641″	46º 37′ 02.7869″	645.291
magicGNSS	24º 43′ 25.8685″	46º 37′ 2.7941″	646.882
APPS	24º 43′ 25.8651″	46º 37′ 2.7822″	645.324
45 min. observation batch			
Reference	24º 43′ 25.8626″	46º 37′ 02.7899″	645.290
CSRS-PPP	24º 43′ 25.8625″	46º 37′ 02.7895″	645.292
GAPS	24º 43′ 25.8632″	46º 37′ 02.78946″	645.443
magicGNSS	24º 43′ 25.8662″	46º 37′ 2.7935″	647.217
APPS	24º 43′ 25.8638″	46º 37′ 2.7871″	645.331
1 hr. observation batch			
Reference	24º 43′ 25.8626″	46º 37′ 02.7899″	645.290
CSRS-PPP	24º 43′ 25.8626″	46º 37′ 02.7907″	645.318
GAPS	24º 43′ 25.8631″	46º 37′ 02.7906″	645.501
magicGNSS	24º 43′ 25.8621″	46º 37′ 02.7927″	647.557
APPS	24º 43′ 25.8628″	46º 37′ 02.7913″	645.454
1.5 hr. observation batch			
Reference	24º 43′ 25.8626″	46º 37′ 02.7899″	645.290
CSRS-PPP	24º 43′ 25.8629″	46º 37′ 02.7899″	645.282
GAPS	No data	No data	No data
magicGNSS	24º 43′ 25.8639″	46º 37′ 2.7887″	647.169
APPS	24º 43′ 25.8626″	46º 37′ 2.7896″	645.542
2 hr. observation batch			
Reference	24º 43′ 25.8626″	46º 37′ 02.7899″	645.290
CSRS-PPP	24º 43′ 25.8630″	46º 37′ 02.7898″	645.281
GAPS	24º 43′ 25.8634″	46º 37/ 02.7896″	645.517
magicGNSS	24º 43′ 25.8634″	46º 37′ 02.7895″	647.320
APPS	24º 43′25.8626″	46º 37′ 02.7895″	645.541
2.5 hr. observation batch			
Reference	24º 43′ 25.8626″	46º 37′ 02.7899″	645.290
CSRS-PPP	24º 43′ 25.8628″	46º 37′ 02.7898″	645.303
GAPS	none	none	none
magicGNSS	24º 43′ 25.8625″	46º 37′ 02.7891″	647.371
APPS	24º 43′ 25.8628″	46º 37′ 02.7895″	645.558
3 hr. observation batch			
Reference	24º 43′ 25.8626″	46º 37′ 02.7899″	645.290
CSRS-PPP	24º 43′ 25.8627″	46º 37′ 02.7899″	645.301
GAPS	24º 43′ 25.8631″	46 37′ 02.7896″	645.554
magicGNSS	24º 43′ 25.8629″	46º 37′ 02.7898″	647.372
APPS	24º 43′ 25.8627″	46º 37′ 02.7895″	645.535
3 hr. 52min observation batch			
Reference	24º 43′ 25.8626″	46º 37′ 02.7899″	645.290
CSRS-PPP	24º 43′ 25.8626″	46º 37′ 02.7899″	645.290
GAPS	No data	No data	No data
magicGNSS	24º 43′ 25.8629″	46º 37′ 02.7896″	647.328
APPS	24º 43′ 25.8627″	46º 37′ 02.7897″	645.519

Journal of Geomatics Vol 10 No. 1 April 2016

Table 4: The (estimated coordinates – reference coordinates) from the four PPP-services for the 10 observation batches

10 min. observation batch			
Estimated coordinate – Reference coordinate	Latitude (m)	Longitude (m)	Height (m)
CSRS-PPP	0.042	0.051	0.071
GAPS	0.029	0.021	0.431
magicGNSS	No data	No data	No data
APPS	No data	No data	No data
20 min. observation batch			
CSRS-PPP	0.033	-0.093	-0.255
GAPS	0.049	-0.099	0.031
magicGNSS	0.366	0.375	0.654
APPS	0.087	-0.275	-0.121
30 min. observation batch			
CSRS-PPP	0.003	-0.069	-0.144
GAPS	0.044	-0.090	0.001
magicGNSS	0.177	0.126	1.592
APPS	0.075	-0.232	0.034
45 min. observation batch			
CSRS-PPP	-0.003	-0.012	0.002
GAPS	0.017	-0.013	0.153
magicGNSS	0.108	0.108	1.927
APPS	0.037	-0.085	0.041
1 hr. observation batch			
CSRS-PPP	0	0.024	0.028
GAPS	0.014	0.021	0.211
magicGNSS	-0.015	0.084	2.267
APPS	0.007	0.042	0.164
1.5 hr. observation batch			
CSRS-PPP	0.009	0	0.008
GAPS	No data	No data	No data
magicGNSS	0.039	-0.036	1.879
APPS	0.001	-0.008	0.252
2 hr. observation batch			
CSRS-PPP	0.012	-0.003	-0.009
GAPS	0.023	-0.010	0.227
magicGNSS	0.024	-0.012	2.030
APPS	0.001	-0.011	0.251
2.5 hr. observation batch			
CSRS-PPP	0.006	-0.003	0.013
GAPS	No data	No data	No data
magicGNSS	-0.003	-0.024	2.081
APPS	0.006	-0.011	0.268
3 hr. observation batch			
CSRS-PPP	0.003	0	0.011
GAPS	0.014	-0.008	0.264
magicGNSS	0.009	-0.003	2.082
APPS	0.004	-0.012	0.245
3 hr. 52min observation batch			
CSRS-PPP	0	0	0
GAPS	No data	No data	No data
magicGNSS	0.009	-0.009	2.038
APPS	0.004	-0.006	0.229

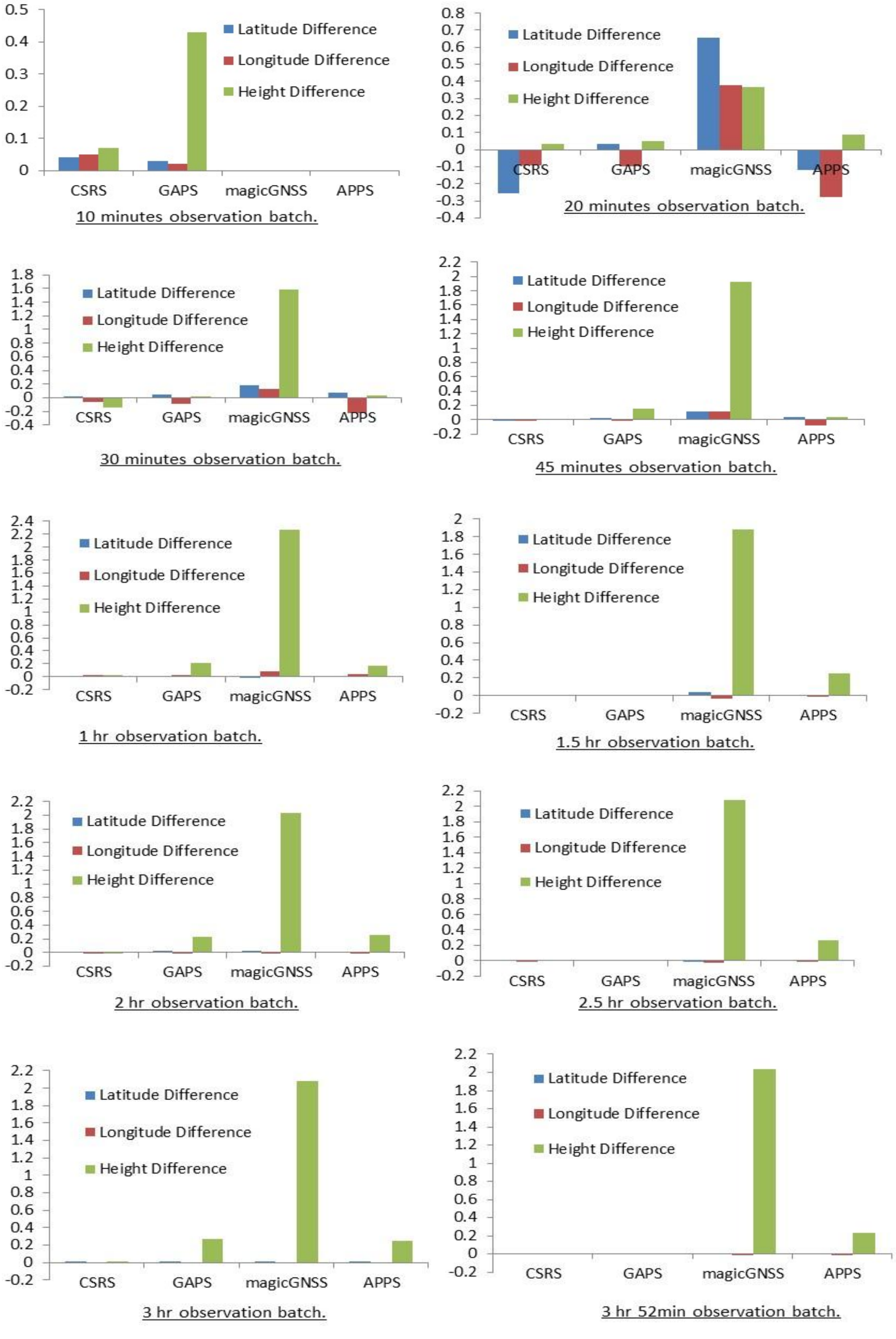

Figure 1: The (estimated coordinates – reference coordinates) in meters from the four PPP-services for the 10 observation batches

4. Test Study

To compare the accuracy of these four online PPP services, an observation set of 3h 52 min. dual frequency-static GPS observations was collected (GPS day 17191) with Topcon GR-3 dual frequency receiver (Topcon GR-3, 2013) using 15 sec observation interval and 10^{o} cut-off elevation angle.

The quality of observation data was checked using UNAVCO's translation, editing, and quality check utility (TEQC) software (TEQC, 2012). This set of observations was divided using TEQC software into 10 batches with different observation duration (10min, 20min, 30min, 45min., 1 hr, 1.5 hr, 2 hr, 2.5 hr, 3 hr and 3hr 52min.). The PPP coordinates for each session were estimated using the four PPP services and compared with the reference coordinates for the tested station. The reference coordinates is obtained from processing the (3 hr 52 min.) batch using CSRS-PPP service.

5. Results and discussion

Table 3 presents the estimated coordinates from the four PPP-services for the 10 observation batches (10min, 20min, 30min, 45min., 1 hr, 1.5 hr, 2 hr, 2.5 hr, 3 hr and 3hr 52min.).Table 4 and Figure 1 present the difference between the estimated coordinates and the reference coordinates for the tested station for the tested batches. It can be seen from these tables that each PPP-service provide different coordinate estimates comparing with the other services. GAPS service provides no estimates for some observation batches such as (1.5 hr, 2.5 hr and 3hr 52 min.). APPS service did not process 10 min. batch for low number of observations where observation interval was 15 seconds, so the 10min. Rinex file has 40 epochs.

CSRS-PPP service provides the most accurate coordinate estimates for the (10min. up to 1hr) observation batches with centimeter accuracy for latitude, longitude and height coordinates. CSRS provides millimeter accuracy for latitude, longitude and height coordinates from 1.5hr observation batch and up to 3hr 52min. batch.

APPS-service provides the second best accuracy for coordinate estimates after the CSRS service with slightly worse values for the height coordinate. GAPS service provides similar accuracy for APPS service when it returns solutions. magicGNSS service did not provide a solution for 10min. observation batch. magicGNSS service provides the worst coordinate estimates for the total tested 10 batches comparing with other services. magicGNSS provides better results with long observation batches such as 1 hr and more for the latitude and longitude coordinates, However, the height coordinate has the worst accuracy ever with an average error of 2 m.

6. Conclusions

It can be concluded from this research that different PPP services provide different solutions according to processing strategy. The user should compare his solutions from number of services and not depend on one service. The difference between PPP estimates from different services could reach 2 meters for height coordinate and at a decimeter level for latitude and longitude coordinates. The study recommends the CSRS and APPS services to be used by PPP-users.

References

Collins, P. (2008). Isolating and estimating undifferenced GPS integer ambiguities. In: Proceedings of ION NTM 2008, San Diego, 28–30 January 2008, pp 720–732

CSRS-PPP (2015). Canadian Spatial Reference System (CSRS) Precise Point Positioning (PPP) service. http://webapp.geod.nrcan.gc.ca/geod/tools-outils/. (Accessed 8/8/2015).

Farah, A. (2013). Effect analysis of GPS observation type and duration on convergence behavior of static PPP. Journal of Geomatics, vol.7, no.2, October 2013.

Farah, A. (2014). Assessment study of static-PPP convergence behavior using GPS, GLONASS and mixed GPS/GLONASS observations. Artificial Satellites, Vol. 49, No. 1 – 2014 DOI: 10.2478/arsa-2014-0005

IGS (2015). International GNSS service. https://igscb.jpl.nasa.gov/components/prods_cb.html (Accessed 8/8/ 2015).

JPL (2015). Website for JPL products, Available at: https://gipsyoasis. jpl.nasa.gov/index.php (Accessed 8/8/2015).

Kouba, J. and P. He´roux (2001). Precise point positioning using IGS orbit and clock products. GPS Solutions. 5 (2), 12–28, 2001

Leandro, R.F., M.C.Santos and R.B. Langley (2007). GAPS: The GPS analysis and positioning software – a brief overview. In: Proceedings of the 20th international technical meeting of the satellite division of the institute of navigation — ION GNSS 2007. The Institute of Navigation, Fort Worth, 25–28 September, pp 1807–1811.

Pı´riz, R., D. Calle, A. Mozo, P. Navarro, D. Rodrı´guez and G. Tobı´as (2009). Orbits and clocks for GLONASS precise-point-positioning. In: Proc. ION GNSS 2009. Savannah, Georgia, pp. 2415–2424, September 22– 25, 2009.

Rizos, C., V. Janssen, C. Roberts and T. Grinter (2012). Precise point positioning: is the era of differential GNSS positioning drawing to an end?. FIG Working Week 2012. Rome, Italy, 6–10 May 2012.

TEQC (2015). TEQC-UNAVCO tutorial. http://facility.unavco.org/software/teqc/doc/UNAVCO_Teqc_ Tutorial.pdf. (Accessed 8/8/2015).

Topcon GR-3 (2015). Topcon Positioning Systems (GR-3). http://www.topcon.co.jp/en/positioning/products/pdf/gr-3_e.pdf.(Accessed 8/8/2015).

UNB-PPP (2015). The precise point positioning service. University of New Brunswick (UNB) http://www2.unb.ca/gge/Resources/PPP/. (Accessed 8/8/2015.

Journal of Geomatics Vol 10 No. 1 April 2016

REIS: A spatial decision system for land valuation

Himanshu Deshmukh[1], Rupali Khare[2], Kamal Pandey[1] and Dheeraj Kumar[2]
[1]Indian Institute of Remote Sensing, Dehradun
[2]Indian School of Mines, Dhanbad
Email: himanshu.deshmukh@pilliwar.com, rupalikhare91@gmail.com, kamal@iirs.gov.in, dheeraj@dkumar.org

(Received: Mar 01, 2016; in final form: April 13, 2016)

Abstract: Land is a vital asset for any federal government. Valuation of land is a very important activity as it has high impact on revenue generation for any country. Present valuation technique is time consuming and cannot quantify the spatial importance of the land for decision making related to real estate. GIS provides a technical platform for management of geographic data and inherent location information to support application of spatial statistical and location econometric tools. Spatial database helps to take decisions for their projects and act as a base data for further functions like tax calculation, land purchase etc. The main objective of this study is to develop a Real Estate Information System (REIS) for the valuation purpose especially for the buying, selling and taxation of land properties. This computerized standalone application, as a repository of land value data is capable to providing easy access to the user/customer about the land information. The technology used for development is open source and hence offers easy modification and customization at user end also. The current version is developed for windows environment and can be used and installed in any windows based system with very less effort. The system can be utilized by the users interested in real estate market for the land procurement process. The system can also assist government agency for taxation purpose.

Keywords: Geographical information system (GIS), Real Estate Information System (REIS), Open source, Land valuation

1. Introduction

Development activity in India is increasing at a high rate and is only expected to increase further in the future. Rising urbanization offers opportunities for the development of real estate market. The growth in real estate industry is visible in every city. Land plays a crucial role in the life of people. Difference in position, fertility or natural resources make some locations and land parcels more desirable and valuable than the others. System of valuation provides control of real estate market. Property valuation is a process of identifying and assigning those factors that affect the value (Horsley, 1992). For the purpose of valuation, the valuation methods are classified as comparative methods, cost methods and interactive analysis method (Dale, et. al 1999; Rangawala et al., 2011). But for this study, valuation purpose is mainly for buying and selling the real properties. The valuation is done on the basis of parameters and rules set by the local governing body i.e. in the case of present study area District Collector, Bhopal & District Valuation Association. These parameters are used for the valuation of land properties for payment of registration charge of ownership. These parameters are per unit area called *circle rate*. Thisis defined for the different locations. These circle rates are taken as bench mark rates for this study. These rates are revised yearly by the District Collector in India.

GIS provides a technical platform on which market analysis as well as spatial representation of property information can be shown in the form of maps (Waytt, 1997). Maps improve the decision making capabilities of human being. Capabilities of GIS facilitate the management of geographic data, as well as it enables to take full advantage of location information contained in these databases to support the application of spatial statistical and spatial econometric tools

The main objective of the study is to develop a GIS based system which facilitates decision making related to land valuation information. The sub objectives of the study are as follows:

- To create a spatial database of unit rate for real estate properties.
- To generate parameter based valuation of properties using GIS functionalities.
- To develop interactive application which enables prospective user in decision making related to land or real estate properties.

2. Study area and data used

2.1 Study area

The study area is a part of Bhopal city, the capital of Madhya Pradesh, which is situated in Central India.The total population of Madhya Pradesh is about 7.26 crores. According to census of India, population of Bhopal has increased from 10,62,771 in 1991 to 14, 37,351 in year 2001 at 35.24% increase and up to 17,98,218 in 2011 at a 25.10% increment. Population wise, it is the second largest city of Madhya Pradesh. Study area is north-east part of city having coordinates 77°26´12´´E, 23°16´10´´N at an average altitude of 427m from mean sea level. The study area includes Raisen road, Vidisha road and Ring road. The study is carried out along these roads for various land parcels for valuation purpose.

2.2 Data used

The study is based on data that are collected from various sources including internet. The primary requirement is the detail about land records in spatial format, which is to be valued. A land use map of the study area is also required for classifying the properties as residential, commercial, etc. The development plan of the study area viz. Bhopal city is also a crucial requirement which contains the data provided by the Town and Country Planning Department, Bhopal. For valuation purpose unit rates and rules of valuation of properties are required. For each year circle rates and guidelines for valuation of immovable properties under Bhopal district are announced by District collector, Bhopal, taken from website of Collector office Bhopal (www.mp.nic.in). The circle rates are taken as benchmark in the place of market rates and the guidelines are helpful in making parameters for the valuation purpose. But the rates vary from place to place in different wards, so a ward map is also needed because neither development plan nor land records are based on wards. The complete dataset used in the study is listed in Table 1.

3. Tools and technologies

The tools and technologies used in the development of the software solution are listed in Table 2.

4. Methodology

The overall methodology adopted for the study is given in Figure 1.

Table 1: Data sets used for the study

S. No.	Data	Type	Source
1	Khasra Boundry	Vector	Wardmap
2	Commercial area	Vector	Landuse map
3	Industrial area	Vector	Landuse map
4	PSP area	Vector	Town and Country Planning Bhopal
5	Existing PUF area	Vector	Town and Country Planning Bhopal
6	Recreational area	Vector	Town and Country Planning Bhopal
7	Residential area	Vector	Landuse map
8	Existing Transport	Vector	Landuse map
9	Wardmap	Vector	Wardmap
10	Circle rate of Bhopal City	Text file	Wardmap
11	Satellite image	Raster	http://earthexplorer.usgs.gov/ (ORBVIEW-3)

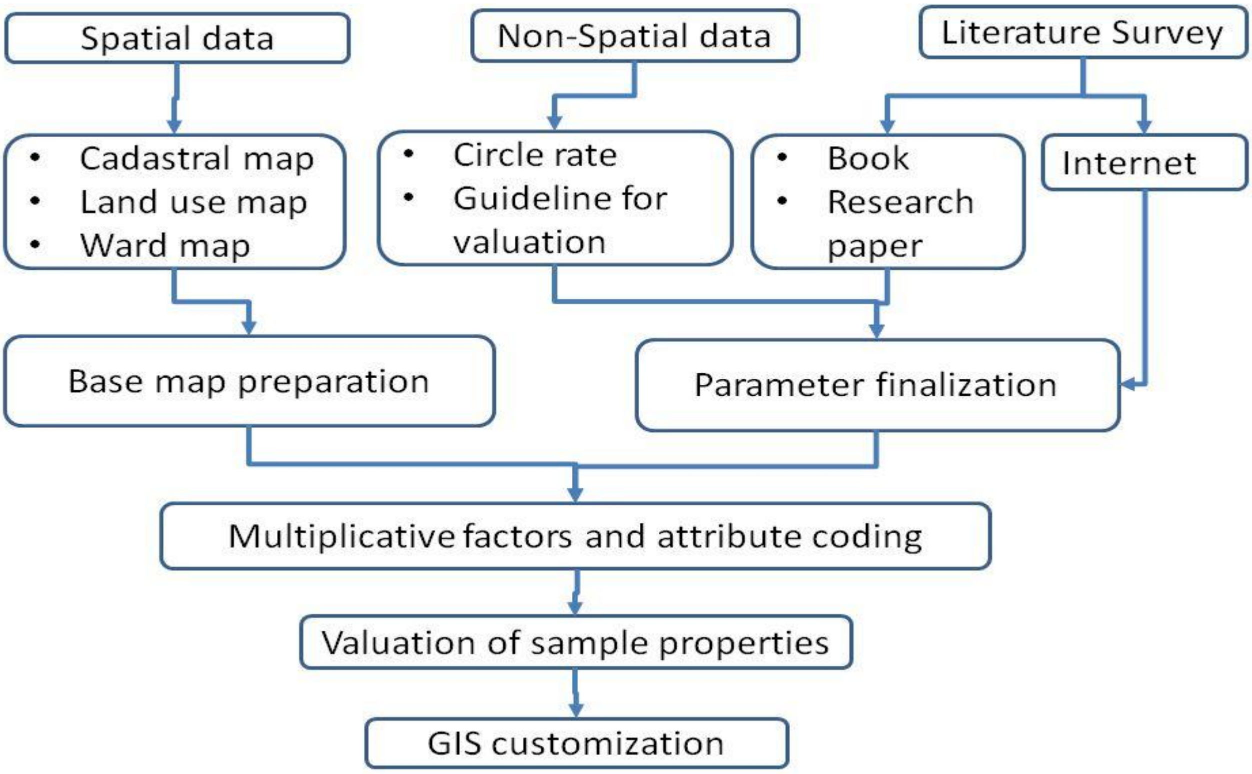

Figure-1: Methodology of the study

Table-2: Tools and Technologies used in the study

S. No.	Component	Specification
1	Operating system	Windows (32 Bit &64 Bit)
2	GIS package	Map window
3	Programming language	VB.net
4	Database	File based(.shp)
5	Libraries	Map window active control(.ocx)

The data available for ward boundaries and road network was available in image form. These data are converted in .shp files by digitization. After base map, attribute coding was done which includes ward name, ward no., area for wards and road width, road length, road name for roads. This work was done in open source GIS and final base map was prepared. The available data was cadastral map which contains Khasra no. area, P. H. No. and village name. This map was further improvised by adding unit circle land rates applicable for various areas as per the guidelines for circle rates issued by administration of that area. Multiplicative factors are worked out for each of the parameter which affect the land unit rate and hence added to the base map file. The parameters and multiplicative factors as listed below:

- **Landuse**

Land use	**Commercial**	**Industrial**	**Agricultural**	**Residential**
MF	**1.50**	**1.50**	**1.00**	**1.00**

- **Depth from road**

Depth from road	**Less than 20 Meter**	**More than 20 meter**
MF	**1.00**	**0.75**

- **Type of road**

Road type	**National Highway**	**State Highway**	**Other Roads**
MF	**2.00**	**1.50**	**1.20**

5. Results and discussion

The development of Real Estate Information System i.e. REIS using geospatial techniques has been carried out in the following stages-

- Creation of geospatial database
- Valuation of properties
- Development of software solution.

5.1 Creation of geospatial database

A variety of database has been utilized in the study. First of all the wardmap was obtained from municipal corporation Bhopal. The map was scanned and geo-referenced with the help of ground control points. The geo-referenced wardmap was converted to vector layer by manual digitizing. The vector ward map layer was attribute coded with ward name and population collected from census of India 2011.

Figure 2 shows the ward map and road map with the help of the scanned and georeferenced wardmap. After digitization, an attribute table was prepared for the wardmap layer with the attributes ward_no, shape_length, shape_area and ward_name.

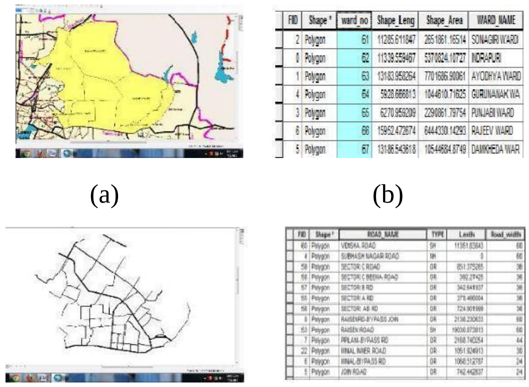

(a) (b) (c) (d)

Figure 2: (a) **Digitized ward map;** (b) **attribute table of ward map;** (c) **digitized roads map; and** (d) **attribute table of road map**

5.2 Preparation of ward wise land value map

Ward map so prepared is used to assign the individual cadastral units to different ward the land values as per the Govt. guidelines and other attributes are coded in the attribute table with the help of Field Calculator tool. Field names in the value map attribute table are Khasra_no, type, ward_name, area, land_value and PH_HALKA.

5.3 Finalizing parameters for valuation and valuation of sample properties

The parameters affecting the value of any property are taken from the "Valuation Guidelines of Immovable Properties" issued by the District Collector, Bhopal. These guidelines describe various parameters such as depth from road, roadtype, land use etc, which are inputs for working out valuation. Every parameter has been given a weight and these weights are filled across the polygons in the attribute table of cadastral maps.

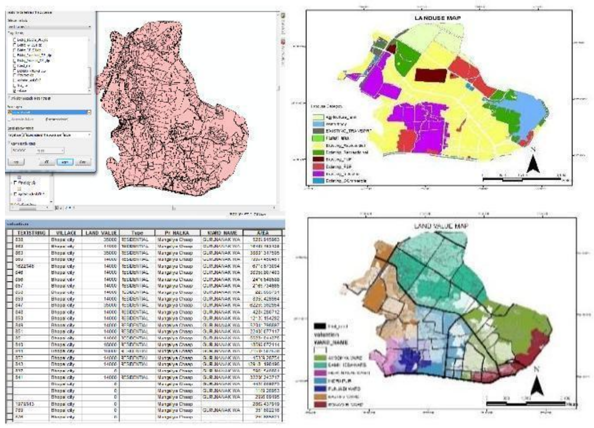

Figure 3: Ward wise value map

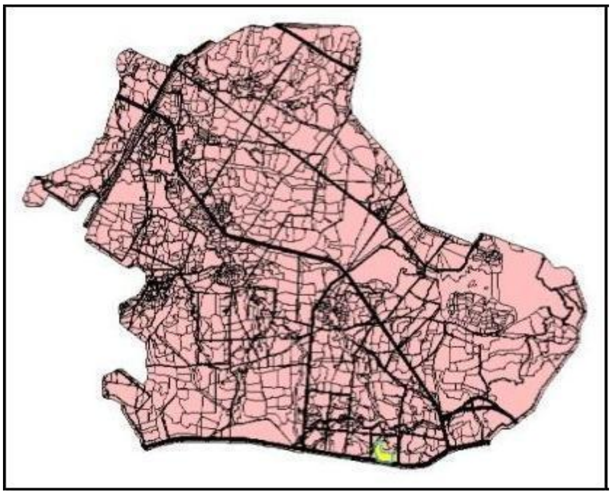

Figure 4: A sample land value map

Case 1	
Khasra Number	172
Patwari halka	M.P. Nagar 1
Land use	Industrial
Ward name	Indrapuri
Circle Land Rate (Rs./ Sqm)	33000
Land area (Sqm)	25772.14
Multiplicative Factors	
For Land use	1.5
For Depth from road	1
For Road type	1.2
For Area	1
Value= Land area x Circle Land Rate x Land use MF x Depth from road MF x Road type MF x Area MF	1530865116

Figure 5: Valuation of properties

5.4 GUI designing and coding of basic structure of REIS

To fulfil the third objective, a software application has been developed using open source technology that facilitates prospective users to search a property according to their needs. In the present study a simple graphical user interface (GUI) is created wherein dynamic map are displayed and it allows to perform basic GIS operation and user-based queries (Figure 6). The GUI have been developed using visual basic programming language.

The query window is the main part of the application which has been customized to meet the needs of the user. The query window is linked with the database to fetch the requested results and to display it on the map window. The user interface contains basic display components like zoom-in, zoom-out, pan etc. It also provides the facility of spatial query and it provides the attribute data of any land parcel where the user has clicked. On click by the user on any part of the map, a new window pops up and the attribute information is displayed in that window.

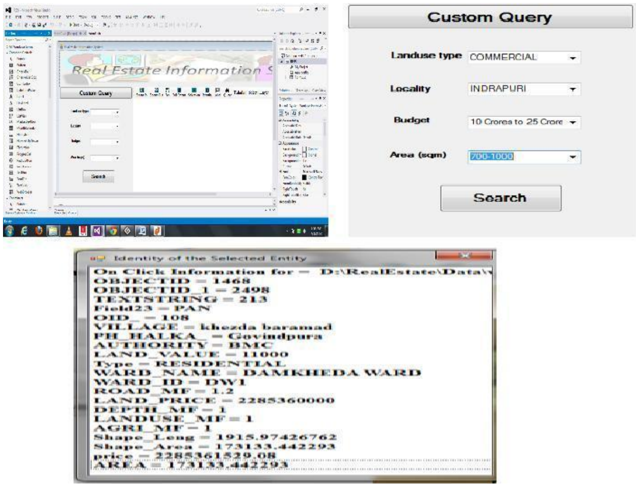

Figure 6: Graphical User Interface (GUI) of REIS

5.5 Sample use case of REIS application

CASE 1: land type=commercial, Locality = Indrapuri, Budget (Rs.) = Above 50 Crores, Area (m^2) = Above 50,000 m^2, Result: One area selected.

5.6. Discussion

The application (REIS) is developed for realizing an analytical system to study the real estate market by the user. It provides results based on the input and also can be used for finding costliest or cheapest properties in any particular area or in the city. Any kind of analysis can be done like comparison of values in same area or comparison of same extent of land in different wards. This study has provided the GIS based system to work out the valuation of open land parcels but further parameters and multiplication factors can be added for built up parcels owned by individuals so that entire valuation will become more scientific and customised. Creation of spatial database is very useful for valuation purpose and it can be recommended to prepare spatial databases for the government departments related to the land. It can help them to take decisions for their projects and can act as a base data for the further functions like Tax calculation, etc. by adding appropriate attributes. System integration or a development of centralized system for all the departments related to the land records is important so that benefit could be obtained from business as well as technical point of view. REIS can also be linked to other databases of different departments so that user can access the other types of data. This would save the resources, time and effort and can help in the fast decision making. This system can be improved by adding the market rate, which can help user a better understanding of the real estate market.

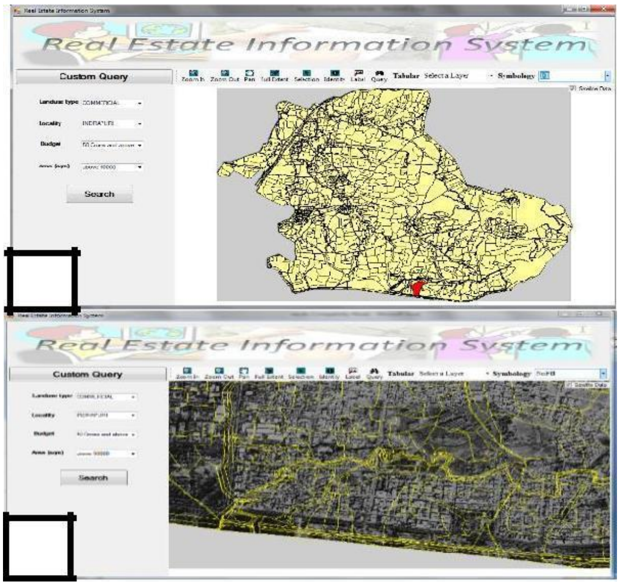

Figure 7: Result of the sample use case query (a) overlaid on ward map; and (b) overlaid on satellite image

6. Conclusion

A Real Estate Information System (REIS), which is useful for the valuation purpose, has been developed for standalone windows platform using open GIS. This can also be linked to other databases of different departments so that user can access the other types of data. This system can be improved by adding the market rate, which can help user a better understanding of the real estate market.

References

Dale, P. and J. McLaughlin (1999). Land Administration. Oxford University Press, New York.

Directorate of Town & Country Planning, (2001). Development plan Bhopal 2031.

Goodall, B. (1972). The Economics of Urban Areas. Oxford: Pergamon Press, New York.

Horsley, G.J. (1992). Market value: The sacred cow. Journal of Property Valuation and Investment, 10, 694-700.

http://www.mapwindow.org/. Accessed on 22.06.2013

http://www.microsoft.com/visualstudio/ Accessed on 22.06.2013

http://msdn.microsoft.com/en-us/library/hh127540. Accessed on 22.06.2013

Rangawala,S.C., K.S. Rangawala and P.S. Rangawala (2011). Valuation of Real Properties. Charotar Publishing House pvt. Ltd., Surat.

Tomić, H., H. Matijević, S. Mastelić Ivić and A. Rončević (2006): Development of Land Valuation System, FIG XXIII Congress, Munich 8-13 October 2006.

Wyatt, P,J. (1997). The development of a GIS-based property information system for real estate valuation. International Journal of Geographical Information Science, 11, 435-450.

Wofford, L.E. and Thrall Grant (1997). Real estate problem solving and geographic information systems: A stage model of reasoning. Journal of Real Estate Literature, 5,177-201.

www.mp.nic.in Accessed on 28.06.2013

www.99acres.com Accessed on 18.05.2013

www.olx.in/real-estate-cat-16 Accessed on 18.05.2013

Yomralioglu, T. and R. Nisanci (2004). Nominal asset land valuation technique by GIS. TS27.4, FIG Working Week May 22-27, Athens, Greece.

Journal of Geomatics Vol 10 No. 1 April 2016

Unfolding the time relationship of structural events through Landsat data: A case study from Khandia formation, Champaner group, Gujarat

M.A. Limaye
Department of Geology, Faculty of Science
The Maharaja Sayajirao University of Baroda, Vadodara 390002
Email: manoj_geol@rediffmail.com

(Received: Feb 23, 2016; in final form: Apr 13, 2016)

Abstract: Imprints of multistructural events recorded within the rocks are visualised through satellite data. The events of superposed folding and shearing at Koba-Rustampura area belonging to Khandia Formation of Champaner group has been studied. Classification of such multiple events becomes simple with the help of their respective trends. These structural events have been delineated by using visual image interpretation techniques to study the spatial pattern and textures on the Landsat image. By deciphering axial traces and directions of displacement, one can build the chronology of the structural events revealing the deformational history.

Keywords: Remote sensing, Time relationship, Koba, Rustampura, Champaner group

1. Introduction

Applications of remote sensing in geosciences are well established and widely accepted for identifying and correlating structures, regionally. Identification of structures on regional scale have been a necessity to understand overall deformational pattern of any terrain. Such attempts includes mapping of large scale features, extracting lineament patterns, identifying regional fold trends, quantifying the fault directions, etc and its correlation up to plate dynamics (Nama, 2004; Kenea, 1997; Heddi et al., 1999; Semere and Ghebread, 2006; Marghany et al., 2009; Maged and Mazlan, 2010; Stefouli and Osmaston, 1986; Shuichi, 2002; Stamouslis and Rogers, 2003; Yamaguchi and Naito, 2003; Rowan and Mars, 2003; Gomez et al., 2005; Harding and Berghoff, 2000; Misra et al., 2014; Joshi et al., 2014).

In order to establish the correlation, in terms of regional structures, it is prerequisite to appreciate the continuity from meso to micro scale. The present work reports a study on the time relation of structural events in Koba-Rustampura area which is situated 24 Km east of Vadodara district, Gujarat (falls under latitude and longitude 22o16’38.61” – 22o21’21.18” N and 73o28’25.63” – 73o38’51.38” E respectively). The study area belongs to Khandia formation of Champaner group, Aravalli Supergroup having meso-proterozoic age. The region has experienced polyphase deformational history and are characterised by lithological entities such as phyllite, quartzite, meta-conglomerate. Based on the Landsat image of 2016, acquired from the google earth portal, characterisation of rocks holding different structural trends have been attempted. The same have been delineated in a chronological order and supplemented by field as well as micro-structural studies.

2. Data used and methodology

The true colour composite of Landsat image of 2016 with 30m spatial resolution has been used to identify different structural events present within the study area. Deformational events from later to former have been interpreted by studying the spatial pattern on the image through visual image interpretation techniques. The information collected during ground truth carried out in 2016, have been used to build the time relationship and to understand overall deformational history pertaining to the Koba-Rustampura area.

3. Regional geological setup

The Koba-Rustampura area belongs to a part of Champaner group, which is well known for its low-grade meta-sedimentary sequence. The group consists of lithological entities such as quartzite, phyllite, meta-conglomerate, schist, impure dolomitic limestone and intermixed variety of granites and gneisses (Gupta et al., 1992, 1995; Joshi et al., 2014). Geographically Champaner group is surrounded on three sides (i.e. north, east and south) by younger plutonic intrusive (Godhra granite) and one side (i.e. west) by Deccan trap rocks. Geologically the Champaner group represent an example of inlier due to the presence of younger rocks neighbouring from all sides (Gupta et al., 1997).

Structurally, rocks of Champaner group display two significant trends of axial traces. D1 phase of deformation has resulted F_1 folds of E-W trend where as D_2 phase of deformation has resulted F_2 folds of N-S trend. The proximity of F_2 folds decreases from eastern end to western end of Champaner group (Jambusariya and Merh, 1967; Gopinath et al., 1977; Merh, 1995; Shah et al., 1984).

Interpretation of satellite imagery reveals that the Koba-Rustampura area manifests two major tonal and textural variations with a distinct elevation difference between them on the image (Fig. 1). The high land region consisting of quartzite and meta-conglomerate display light green tone with medium to rough texture, whereas the low lying areas consist softer rocks such as phyllites representing light brown tone and medium texture. The south-western part of the study area represents crescent shaped outcrop pattern whereas there has been development of broad sinuous curve over the linear ridge in the northern part. Furthermore, evidences of top to NW, top to NE and down to SE displacement can be appreciated, between the linear and crescent shaped ridge and within the 'C' shape outcrop pattern respectively.

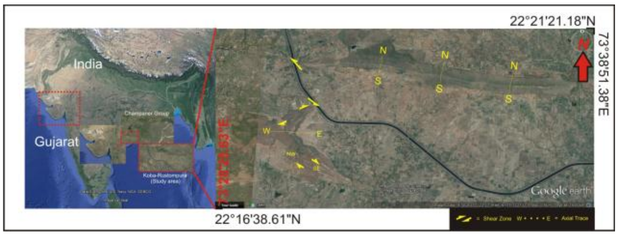

Figure 1: Location map and Landsat data of the study area

In order to appreciate the overall deformational pattern of the study area, chronologically, restoration of deformational events needs to be applied by unfolding the terrain sequentially. With the help of image interpretation, it can be seen that the latest event, which has occurred in the study area is shearing. Such idea can be profound due to its cross-cutting relationship embracing on later deformational patterns (i.e) folding.

The former structural event occurred in the study area is folding, which is represented in the form of 'C' shaped outcrop and broad sinuous curve over the linear ridge. The major fold event occurred in the study area has E-W trend whereas minor one suggest N-S trend of axial trace. Moreover, the N-S trending folds are developed on Km long limb of E-W trending fold.

4. Ground truth verification and inferences

The Koba-Rustampura area represents the part of Khandia Formation and located in the south-western part of Champaner group. The main rock type includes meta-conglomerates, quartzites, phyllite and breccia. The study area constitutes a mega scopic westerly plunging anticlinal fold. The northern limb is long in comparison to the southern limb and strikes E-W, having dip direction due north and due south respectively. Based on the attributes through stereographic projection the fold has its axial trace E-W with a plunge of 15^{o} in the direction of N 270^{o}. The axial plane is vertical, which strikes along the direction of fold axes (i.e. N270^{o}). Apart from that there has been generation of open folds on the northern limb having direction of axial plane N-S. Based on the overall structural pattern suggested by folding it can be said that there are two sets of folds superposed on one another. The first phase (F_1) having E-W axial trace has found to be superimposed by (F_2) having N-S axial trace (Fig. 2).

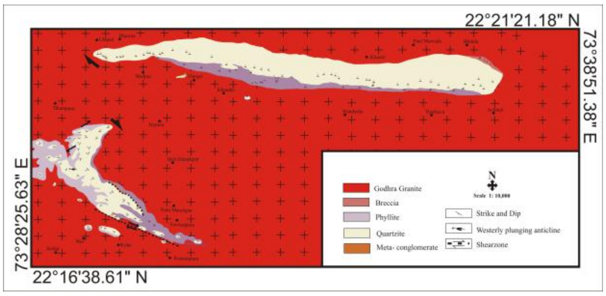

Figure 2: Geological map of the study area

With the same connection there are good evidences of shear present throughout the study area. The northern limb, which shows the displacement with the major fold present in the south-western part, shows the shear (i.e.) top to NW. Also, within the major fold morphology there has been generation of several shears resulting into intrafolial fold at the southernmost margin of the study area. The direction of these shear include top to NE shear and down to SE shear. The main litho-units affected by shears are meta-conglomerate and quartzite. The signatures include brittle fracturing and crushing of quartzite, elongation of clasts in meta-conglomerate, formation of breccia and dragging of quartzite ridge parallel to the shear plane. In addition to that microstructural analysis suggest dominant S-C fabric of oriented mica grains, quartz fish, group 2 mica fish and 'V' pull apart mechanism with domino like microstructure in quartz clast of meta-conglomerate. In quartzite evidences of shearing are supported by oriented mica flakes having inclusions of quartz aliened in the direction of shearing. Furthermore, breccia consists of medium to coarse grain angular clasts of quartz cemented by fine grained quartz and Fe rich matrix. Sweeping undulose extinction is observed within the coarser angular quartz clasts (fig. 3).

5. Discussion and conclusion

On the basis of satellite data interpretation and field observation/ ground truth, similarity exists between the fold morphology and shearing events. As per satellite image and field evidences the superimposed pattern of one fold event over the other has been confirmed. The N-S trending open folds are found to be superimposed over E-W trending gentle fold. Considering regional structural setup, it can be observed that the two significant fold events, F_1 and F_2 are occurred throughout the group. Furthermore, the proximity of F_2 folds in the Champaner group increases from W-E. Hence, in order to establish a time relationship between fold events, E-W represent the first fold event, whereas second fold event is characterised by N-S axial trace.

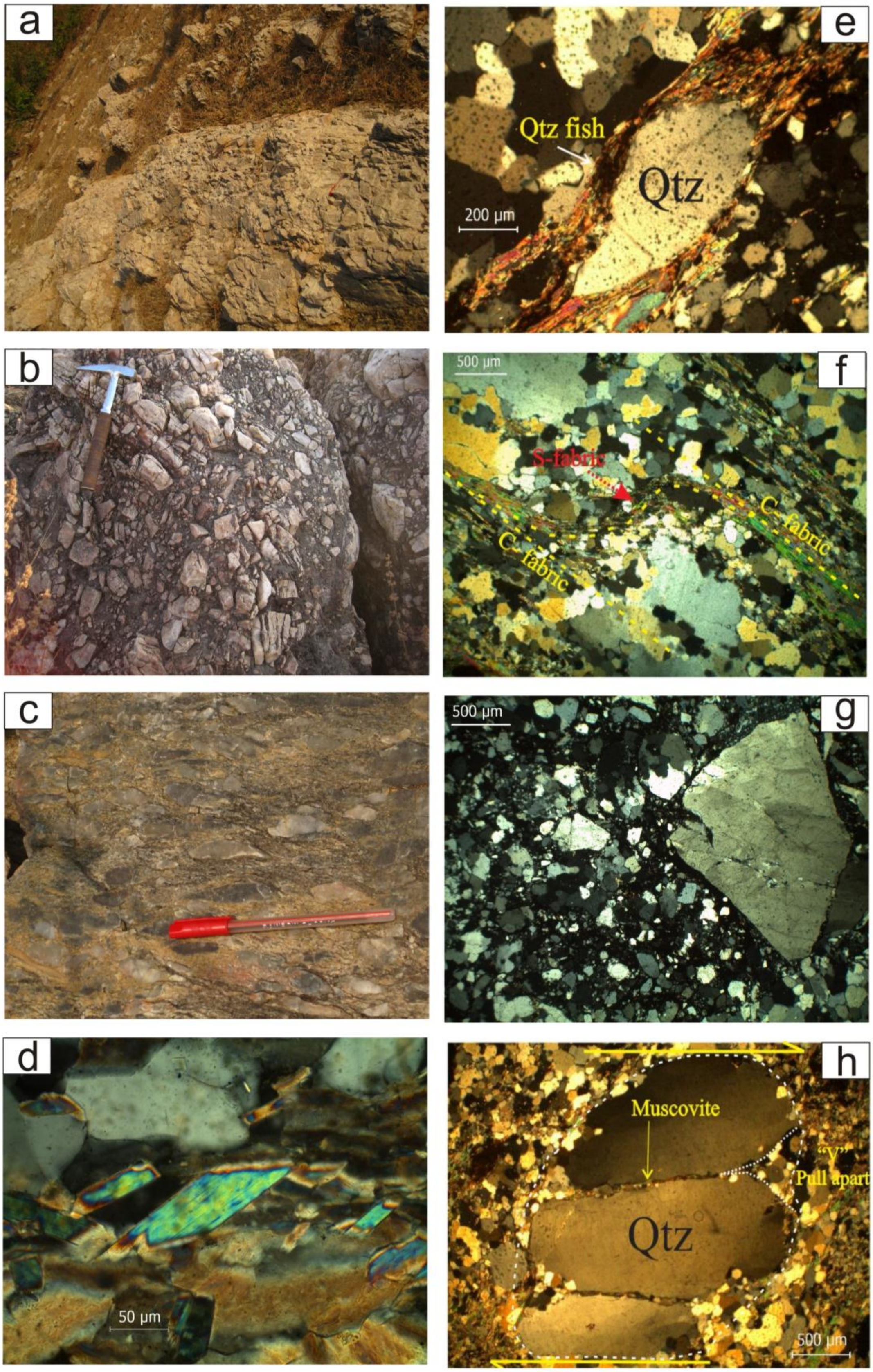

Figure 3: Field Photograph showing: (a) Closely spaced factures in quartzites. Loc. Koba village; (b) Breccia containing angular fragments of quartz embedded in ferruginous matrix. Loc. Rustampura village; (c) Elongated clasts of quatz in meta-conglomerate, ball pen signifies the stretching direction. Loc. Koba village; (d) Group II mica fish in meta-conglomerate (10XCN); (e) Quartz fish in meta-conglomerate (10XCN); (f) Development of S-C fabric of mica grains in meta-conglomerate (4XCN); (g) Breccia containing medium to coarse grained angular quartz clasts in ferruginous matrix (4XCN); (h) 'V' pull apart microstructure with domino like arrangement of quartz clasts, arrows indicated shear direction (4XCN)

These fold events have undergone post deformational shearing along the weak planes. Directions of these shears includes top to NW, top to NE and down to SE displacement. Field evidences, such as brittle fracturing in quartzites and elongation of clasts in meta-conglomerate, gives sustainable sense of shear. In addition to field evidences, supportive microstructural evidences are also envisaged. These include dominant S-C fabric of oriented mica grains, quartz fish, group 2 mica fish and 'V' pull apart mechanism with 'domino' like microstructure.

Based on the above facts the time relationship of deformational events is established. Chronologically it can be represented from older to younger as: 1. E-W trending folds; 2. N-S trending open folds on limbs of earlier folds; 3. Shearing.

Acknowledgement

The author is thankful to Prof. L.S. Chamyal, Head, Dept of Geology, M.S. University, Baroda for providing necessary facilities. The author is sincerely thankful to Mr. Aditya Joshi for academic discussion. Author is also grateful to the Forest Department of Vadodara and Panchmahal District, Gujarat for granting the permission to carry out fieldwork in the Sanctuary area. Author will never forget the help rendered by Mr. H.J. Bhatt during the fieldwork.

References

Gomez, C., C. Delacourt, P Allemand, P Ledru and R Wackerle (2005). Using ASTER remote sensing data set for geological mapping, in Namibia. Physics and Chemistry of the Earth, 30, pp. 97–108.

Gopinath,K., A.D. Prasad Rao, Y.G.K. Murty and K.K. Krishnaunni (1977). Precambrian of Baroda and Panchmahals, Gujarat. Elucidation of stratigraphy and structure. Rec. Geol. Surv. India.108, pp. 60-68**.**

Gupta, S.N., R.K. Mathur and Y.K. Arora (1992). Lithostratigraphy of Proterozoic rocks of Rajasthan and Gujarat - A review: Records of Geological Survey of India, 115, pp. 367-379.

Gupta, S.N., Y.K. Arora, R.K. Mathur, B.P. Iqbaluddin, T.N. Sahai and S.B. Sharma (1995). Geological map of the Precambrian of the Aravalli region, Southern Rajasthan and northeastern Gujarat, India. Geological Survey of India Publication, Hyderabad.

Gupta, S.N., Y.K. Arora, R.K. Mathur, B.P. Iqbaluddin, T.N. Sahai and S.B. Sharma (1997). The Precambrian geology of the Aravalli region, Southern Rajasthan and NE Gujarat, India. Mem. Geological Survey of India 123, pp. 262.

Harding, D.J. and G.S. Berghoff (2000). Fault scarp detection beneath dense vegetation cover: airborne Lidar mapping of the Seattle fault zone, Bainbridge island, Washington state. Proceedings of the American Society of Photogrammetry and Remote Sensing, Annual Conference, Washington, DC, 9 pp.

Heddi, M., D.J. Eastaff and J Petch (1999). Relationships between tectonic and geomorphological linear features in the Guadix-Basa basin, Southern Spain. Earth Surface Process and Land-forms, 24, pp.931-942.

Jambusaria, B.B. and S.S. Merh (1967). Deformed greywacke conglomerates of Jaban near Sivrajpur, Panchmahals district, Gujarat. Ind. Minerals. 8, pp. 6-10**.**

Joshi, Aditya and M.A. Limaye (2014). Evidence of syn-deformational granitoid emplacement within champaner group, Gujarat. Journal of, The Maharaja Sayajirao University of Baroda, 49(1), pp. 45-54.

Joshi, Aditya, M.A. Limaye and B.S. Deota (2014). Structural footprints extraction from rocks of Lunavada region,Gujarat through IRS LISS III. Journal of, Geomatica, 8(2), pp. 170-173.

Kenea, N.H. (1997). Improved geological mapping using Landsat TM data, Southern Red Sea Hills, Sudan: PC and his decorrelation stretching. International Journal of Remote Sensing, 18, pp. 1233-1244.

Maged, M. and H. Mazlan (2010). Lineament mapping using multispectral remote sensing satellite data. Research Journal of Applied Sciences, 5(2), pp. 126-130.

Marghany, M., M. Hashim and S. Mansor (2009). Geologic mapping of United Arab Emirates using multispectral remotely sensed data. American Journal of Engineering and Applied Sciences, 2(2), pp. 476-480.

Merh, S. (1995). Geology of Gujarat. Geol. Soc. India, Publ. Bangalore, p.244.

Misra, A.A., G. Bhattacharya, S. Mukherjee and N. Bose (2014). Near N-S Paleo-Extension in the western Deccan region, India: Does it link strike-slip tectonics with India-Seychelles rifting?, 103,pp. 1645-1680.

Nama, E.E. (2004). Lineament detection on Mount Cameroon during the 1999 volcanic eruptions using Landsat ETM. International Journal of Remote Sensing, 25, pp. 501-510.

Rowan, L.C. and J.C. Mars (2003). Lithologic mapping in the Mountain Pass, California, area using Advanced Spaceborne Emission and Reflection Radiometer (ASTER) data. Remote Sensing of Environment, 82, pp.350-366.

Semere, S. and W. Ghebread (2006). Lineament characterization and their tectonic significance using Landsat TM data and field studies in the central highlands of Eritrea. Journal of African Earth Sciences, 46, pp. 371-378.

Shah, A.M., R.V. Karanth and S.A. Barot (1984). Geology of the area around Khandia with special reference to the lead mineralization, Dist., Baroda, Gujarat, Proc. Ind. Geol. Congress., pp. 127-134.

Shuichi, M. (2002). Regional lineament analysis and alteration mineral mapping for intrusive-related copper exploration in the Myanmar central volcanic belt. Asian Conference on Remote Sensing 2002 (Kathmandu, Nepal)

Stamoulis, V. and P. Rogers (2003). Geological mapping for mineral exploration using ASTER data. MESA Journal, 30, pp. 16-19.

Stefouli, M. and H. Osmaston (1986). The analysis of linear geologic features on Landsat images of Crete. Journal of the British Interplanetary Society, 39, pp. 546-551.

Yamaguchi, Y. and C. Naito (2003). Spectral indices for lithologic discrimination and mapping by using the ASTER SWIR bands. International Journal of Remote Sensing, 24(22), pp. 4311-4323.

Journal of Geomatics Vol 10 No. 1 April 2016

Runoff estimation from a tributary of lower Tapi basin using SCS-CN method integrated with remote sensing and GIS data

Sudhakar B. Sharma[1], Anupam K. Singh[2] and Ajay S. Rajawat[3]
[1]Institute of Science, Nirma University, Ahmedabad
[2]Institute of Engineering & Technology, J.K. Lakshmipat University, Jaipur
[3]Geoscience Division, Space Applications Centre (SAC/ISRO), Ahmedabad
Email: sudhakar_rsgis@yahoo.co.in, anupam.singh@gmx.net, asrajawat@sac.isro.gov.in

(Received: Sep 28, 2015; in final form: Jan 27, 2016)

Abstract: The purpose of this research paper is to identify watersheds with high flood potential based on their characteristics for formation of surface runoff. The SCS-CN method relies on remote sensing and GIS data for obtaining watershed characteristics. A 30m raster grid size digital elevation model (DEM) has been generated from field survey using Global Positioning System (GPS) of 3m accuracy integrating with Survey of India topographical maps of 1:50,000 scale having 10m contour interval. The undisturbed soil samples from field have been collected and laboratory analysis was carried out using modified proctor compaction test as per ASTM D1557 and sieve analysis as per ASTM C136. This has helped in establishing hydrological soil map while land use map has been prepared using Landsat 7 ETM+ image band 2, 3, 4 (30m) merged with PAN band 8 (15m) for classification. The supervised maximum likelihood classification approach has been employed for preparation of land use map for Varekhadi catchment having 442 km^2 of geographical coverage. The major land use categories classified on 10 Nov 2001 Landsat 7 ETM+ image were agriculture (32%), forest (29%), wasteland (20%), fallow land (14%), built-up (4%) and water bodies (2%). The hydrological soil groups generated in GIS environment have identified two soil groups viz. group B and group C that exist under study area. The Varekhadi catchment has been delineated into five watersheds viz. Amli, Zankhwaw, Visdaliya, Godsambha and Wareli delineated using DEM and stream network. The SCS-CN model was applied for estimating of daily run-off for each sub-watershed. The results obtained on the flood potential analysis shows that Wareli watershed has highest flood potential while the Amli watershed lowest. It should be noted that highest value of flood potential belongs to lowest part of watershed, where high population density is found. This analysis reflects an increased vulnerability and risks to floods and inundations for Wareli watershed. Stream gauge data has been used for result validation with a common event of 2010 and it shows good agreement with the model. The flood potential analysis within the lower Tapi basin tributary suggests that the SCS-CN method with hydrological parameters derived using remote sensing and GIS data can be applied to predict run-off in poorly gauged watersheds.

Keywords: SCS-CN method, Remote sensing, GIS, Landsat 7 ETM+, Runoff, Ungauged catchment

1. Introduction

Surface runoff generation is dependent on climatic, geo-morphological, topographical and landuse characteristics of a catchment or watershed. Of above, the topographical characteristics and soil types with land use as hydrological soil group have been of immense importance. A combination of characteristics favourable for runoff generation and runoff concentration increases the flood potential in a watershed. Most of the watersheds in India have been poorly gauged or un-gauged, as they do not have adequate records of runoff generation for a rainfall event to understand the hydrological response. In the flood prone catchments, it is required to calculate peak flood discharge or flood potential from each watershed. A number of discharge estimation methods available in the literature namely Rational method, Soil Conservation Service- Curve Number (SCS-CN) method, Cook's method and Unit hydrograph method. However, the SCS-CN method for predicting direct run-off or discharge from rainfall excess of ungauged watershed is extremely important. Balvanshi and Tiwari (2014) have reviewed SCS CN method for runoff estimation and recommended that. It is being used in a wide range of design situations by the practicing engineers and hydrologists. Sindhu et al. (2013) have carried out estimation of surface runoff in Nallur Amanikere Watershed using SCS-CN method. They found the variation in runoff potential with different land use/land cover and with different soil conditions.

This method allows the identification and zoning of watersheds with a high risk of generating floods and of those exposed to runoff generation processes. Soil and landuse parameters, which control surface runoff, can be evaluated and mapped through remote sensing satellite images. Sharma and Singh (1992) in their research work for Luni river catchment have successfully used Landsat TM and SCS-CN model to estimate runoff potential. Katimon et al. (2003) estimated flood potential of two small watersheds of Salengor and Pontian in Malaysia using SCS-CN method and GIS based empirical approach to predict daily event storm runoff. They have pointed out that SCS-CN and GIS have limitations in flood estimation in absence of accurate hydrologic soil group data. They have noted large variations in the surface runoff if hydrological soil group changes. Later, Behzad et al. (2012) used SCS-CN method for estimating flood potential for different return periods. They emphasised on geomorphologic characteristics of Tarik flood basin in Iran. Several other methods on peak flood discharge and associated parameters estimation have been suggested in the literature for ungauged basins. Zhang and Haung (2004) have developed Arc-CN tool integrated with ArcGIS and applied SCS-CN method for estimating run-off and preparing CN and run-off maps. However, the parameter reliability between various methods varies to a large extent and none is found to be suitable universally. In spite of few limitations, SCS-CN along with hydrological soil group and land use remain to be a popular method for estimation of flood potential under poorly gauged or ungauged catchments due to its performance and reliability.

SCS-CN has been applied in the present study for the estimation of run-off from five watersheds of Varekhadi catchment- a tributary of lower Tapi basin. This SCS-CN requires information on catchment characteristics related to DEM, land use and hydrologic soil group for estimation of catchment runoff. The purpose of this method is to determine the curve number (CN) of the catchment accurately that assesses the estimated runoff potential. Hydrologic soil group, land use type, vegetation cover are important physical characteristics of a watershed used for the calculation of CN. Thus, the most important step in estimation of surface runoff or flood discharge is to calculate watershed characteristics accurately. Remote sensing and GIS data together with field surveys and field measurements are input for classification of watershed characteristics. Landsat 7 ETM+ image band 2, 3, 4 (30m resolution) have been merged with PAN (15m resolution) data for supervised classification of land use classes using Gaussian maximum likelihood classifier. Hence, the runoff CN for different watersheds were determined using land use and hydrological soil group map within the study area.

2. Study area

Tapi river basin covers three states viz. Madhya Pradesh (9804 km^2), Maharashtra (51504 km^2) and Gujarat (3837 km^2) having a geographical area of 65145 km^2 and is the India’s second largest inter-state westward draining river in Arabian sea. The Tapi river basin can be classified in three zones, viz. upper Tapi basin, middle Tapi basin, and lower Tapi basin (LTB). The area between Ukaidam to Arabian sea has been considered as LTB, mainly occupying Surat and Hazira twin city along with tens of small towns and villages along the river course. LTB has a geographical area of 2920km^2 which has been experiencing periodic floods in urban settlements of Surat and Hazira. The Surat and Hazira are about 106km and 122km downstream of Ukai dam, respectively. Both these cities have been affected by recurrent floods during last 5-decades and flood frequency in the basin has been estimated to be occurring once in 6-years. One among the major causes of flood in LTB is attributed to formation of peak discharge early from various tributaries such as Varekhadi, Anjanakhadi, Serulkhadi, Mau khadi and Gal khadi. The flood during August 2006 in LTB caused huge damage to personal and property resulting into 300 people being killed and US$ 4.5 billion value property damage (Singh et al., 2009).

Varekhadi catchment is a tributary of LTB having a river length 50 km covering a geographical area is 442km^2 (figure 1) which confluences near Mandvi town. The Varekhadi catchment has been divided into 5-watersheds consisting of lone urban centre Zankhwaw along with almost 150 rural settlements. It has 2 major surface water reservoirs viz. Issar and Amli dams which are located in the study area. The dam storage is mainly used for flood control during monsoon season and for irrigation during the post-monsoon through gravity canal system. The right bank canal from Kakrapar weir located 30km upstream of Varekhadi confluence passes through watershed and is being predominantly used for irrigation purpose.

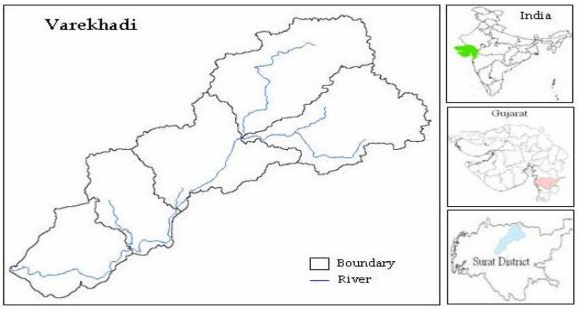

Figure 1: Study area

The geographic coordinates of the study area are 21^{0}14'N 73^{0}07'E to 21^{0}30'N 73^{0}30'E as lower left and upper right corners. The study area receives an average yearly rainfall of 1376mm. The temperature in the catchment is variable which has a range of 22°C and 40°C as minimum and maximum temperature. Major land use categories are built-up area as settlements, agriculture, forest, fallow land, water bodies and other uses. Considering the definition of land use CN and soil types, the hydrological soil groups available in Varekhadi catchment are B and C. Major problem in study area is flood in low laying areas near Wareli village at the confluence of Varekhadi catchment with main Tapi river.

3. Methodology

The proposed research methodology can be considered to have two parts. The part one is the modelling of the spatial variability of topographical parameters using remote sensing and GIS while the part two involves analysis of the digital data base to derive hydrological model parameters. The research methodology used for estimation of surface run-off vis.a.vis flood potential using SCS-CN method consist of five steps viz. Sub-watershed delineation, land use map and hydrological soil group map generation, CN calculation and run-off estimation. The flow chart of methodology is given in figure 2.

Journal of Geomatics Vol 10 No. 1 April 2016

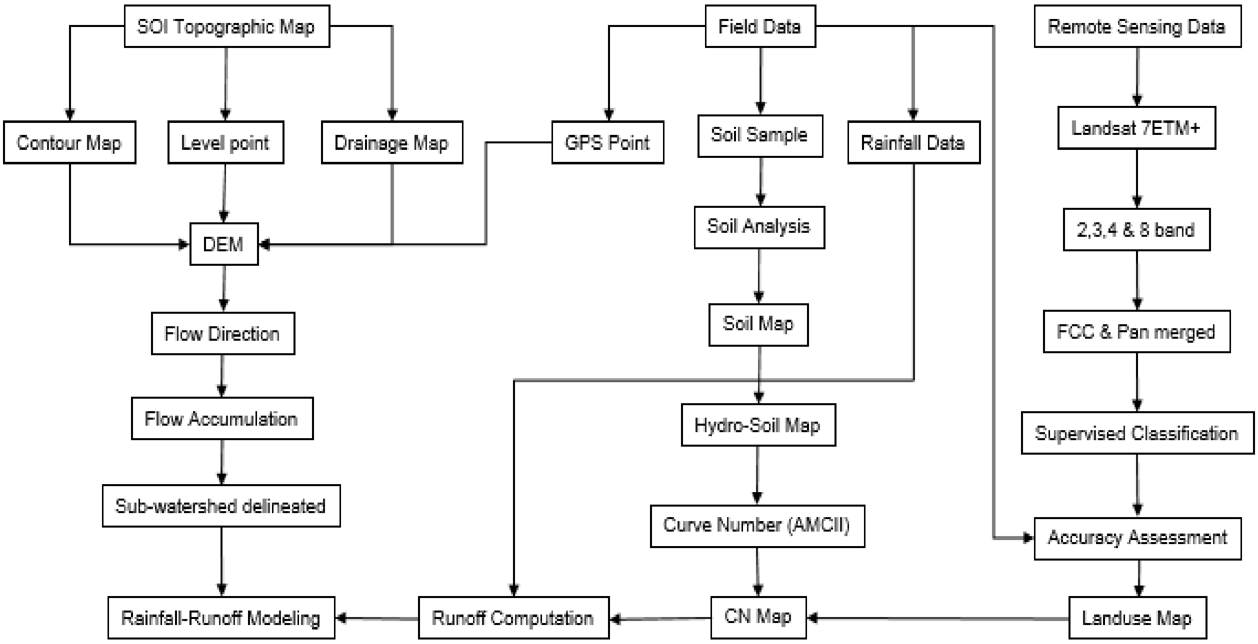

Figure 2: Flow chart of methodology

In this paper, hydrological data related to runoff estimation such as DEM, Landsat 7 ETM+ satellite imagery, global positioning system (GPS) for level points, soil map for grain size and soil moisture, land use for CN, hydrological soil group as AMC (antecedent moisture condition) and rainfall have been used. A DEM of 30m raster grid size has been generated from field survey using GPS of 3m accuracy integrating with Survey of India topographical maps of 1:50,000 scale having 10m contour interval.

3.1 Watershed delineation

A DEM of 30m raster cell size and 0.5m vertical accuracy has been used to delineate 5-watersheds for Varekhadi river basin using BASIN hydrological model. The steps followed in a given sequence are (i) creating a depressionless DEM; (ii) calculating flow direction based on 3x3 cell neighbourhood algorithm; (iii) calculating flow accumulation and identify cell having given area; (iv) delineation of watershed outlet points leading to delineation of watersheds for a given threshold area. Five such watersheds have been delineated named as Amli, Zankhwaw, Visdaliya, Godsambha and Wareli. Watershed parameters such as flow length, river length, watershed outlet point, watershed area, river length and river slope were obtained from DEM (Figure 3). The validation of DEM has been done using 24 ground control level points using GPS.

3.2 Generating landuse map

The land use map of Varekhadi watershed has been generated by image analysis of satellite data. The image of Landsat 7 ETM+ (10 Nov 2001) bands 2, 3, 4 with (30m) spatial resolution and PAN with (15m) ground resolution were analysed.

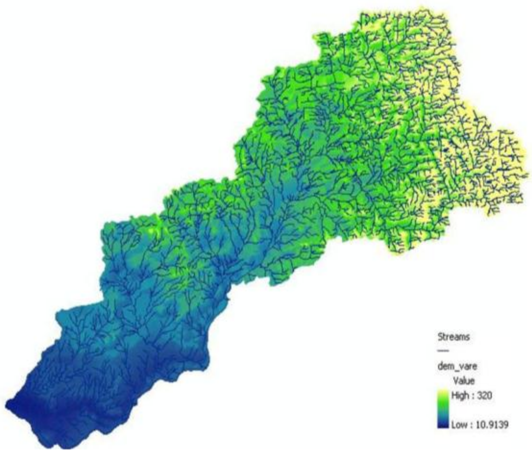

Figure 3: Digital Elevation Model (DEM)

Image geometric correction has been done and land use map were derived using Gaussian maximum likelihood algorithm of supervised classification with field sample. Land use categories considered in the study area are built-up land, agriculture, forest, fallow land, water bodies and other as shown in figure 4 and their statistics are given in table 1. SCS-CN method related land use description as an input for runoff generation process. The CN can be empirically determined based on SCS (1985) land use description, hydrological soil group and AMC conditions

3.3 Generating hydrological soil group map

To create hydrological soil group map, soil survey of study area was conducted. Thirty points were selected for soil sample in study area and soil samples have been analysed in the laboratory. Soil properties have been identified and a GIS map of hydrological soil group was prepared. There are two type of soil in study area group B and C as shown in figure 5.

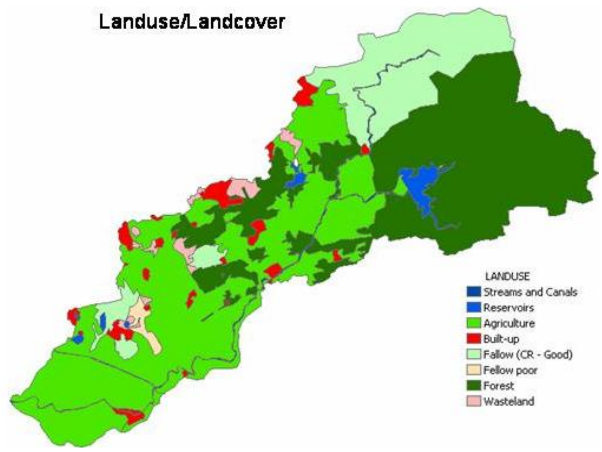

Figure 3: Land use / land cover map

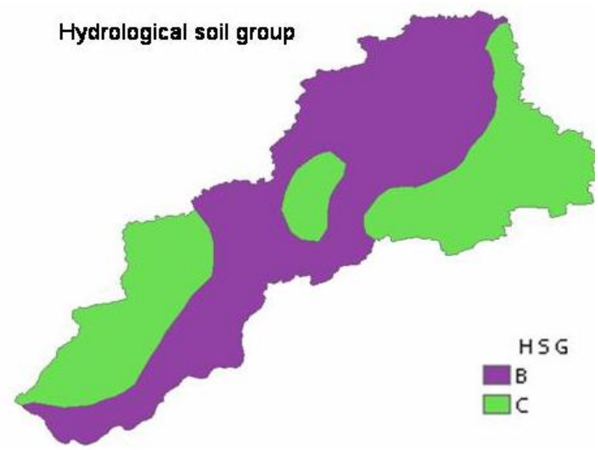

Figure 4: Hydrological soil map

3.4 Generating CN map

The CN value has been used to estimate potential maximum soil retention. The value of CN is 100 for impervious surfaces and between $0<CN\leq100$ for other surfaces. The maximum potential storage which relates to CN depends on land use, hydrological soil group, hydrological condition and AMC (Ponce and Hawkins, 1996). Arc CN extension of ArcGIS software has been used to generate the CN map of Varekhadi watershed. The hydrologic soil group field from the soil map and the land use field from the land use map were selected for intersection under vector environment in GIS. After intersection, a map with new polygons representing the merged soil hydrologic group and land use (land-soil map) was generated.

CN map directly effect on surface runoff, all the surface water bodies gives the CN value zero and resulted run off is also zero. Average CN also have been calculated and the details are given in table 2. In shows that Wareli watershed has highest CN value 86.07 and Zankhwaw has lowest CN value 68.95.

3.5 Run-off estimation

The SCS-CN method assumes that surface runoff will be generated once initial losses are satisfied. The SCS-CN method explaining the water balance can be given by equation 1. The main hypothesis in this method is that the ratio of direct runoff to the rainfall depth minus initial losses (P- Ia) is equal to the cumulative infiltration as given in equation 2 (Mishra and Singh, 2003).

$$P = Q + F + I_a \quad \ldots\ldots\ldots\ldots\ldots\ldots\ldots.. \quad (1)$$

$$Q \;/ (P\text{-}Ia) = F / S \ldots\ldots\ldots\ldots\ldots.. \quad (2)$$

where the terms P is total precipitation (mm); Ia is the initial abstraction (mm); F is cumulative infiltration (mm); Q is direct runoff (mm); S is the potential maximum retention or storage capacity of soil (mm). As per USDA-SCS (1985) guidelines the initial abstraction (mm) is assumed to be abstraction fraction (usually λ= 0.2) of the potential maximum retention as shown in equation 3.

$$Ia = \lambda.S \quad \ldots\ldots\ldots\ldots\ldots\ldots\ldots\ldots\ldots\ldots\ldots\ldots.. (3)$$

The direct storm runoff Q (mm)can be related to the effective rainfall and actual retention through the water balance equation 4 (Yu, 1998). Equation 4 is valid only

When $P \geq \lambda S$ and generally $I_a = 0.2S$, hence equation 4 can be written as;

$$Q_p = (P\text{-}I_a)^2/(P\text{-}I_a+S)$$

$$= (P\text{-}0.2S)^2/(P+0.8S) \ldots\ldots\ldots. (4)$$

If effective rainfall $P \leq \lambda S$, then direct storm runoff Q (mm) is taken as zero

In practice, the potential maximum retention S (mm) of the soil is determined using the CN given in equation 5.

$$S = (254400/CN) – 254 \ldots\ldots\ldots\ldots.. (5)$$

The term CN is determined from a table based on land use, hydrological soil group and AMC. The hydrological soil group has four classes A, B, C and D based on landuse, hydrological soil group and AMC. The hydrological soil group has four classes A, B, C and D based on infiltration rate of soil. AMC has three classes I, II and III according to rainfall limits for sowing and growing season.

3.6 Stream gauge installation

Varekhadi has no discharge measurement gauging station and is classified as un-gauged watershed. This being a remote location, it has been proposed to install automatic sensors with data logger capabilities. WL-16U stream gauge sensors of 25m cable from Global Water USA were procured and installed in field during June 2010. The sensor has 0.1mm measurement accuracy and can record 10 reading per second. Three discharge sites viz. Amli, Visdalia and Godsamba have been selected for installation of stream gauge. The output data has been used for result validation for deferent sub watershed.

4. Results and discussion

The direct storm runoff depends on land use, soil type and hydrological soil group and CN. Landsat 7 ETM+ data of 10 Nov 2001 has been used for supervised classification of 5-land use classes. A merge product of Landsat 7 ETM+ band 2, 3, 4 of 30m cell size with PAN band of 15m spatial resolution was used for classification. The land use distribution within Varekhadi catchment shows that it is primarily an agriculture catchment as 32% of study area is under agriculture, 46% of area under agriculture and current fallow; 66% of area under wasteland, fallow land and agriculture (Table 1).

Table 1: Landuse Classification

Land use	Area km^2	% of total area
Agriculture	142	32
Fallow Land	60	14
Wasteland	87	20
Built-up land	17	4
Water bodies	7	2
Total	442	100

The value of volume and surface runoff were calculated for extracting percentage flood contribution for each sub-watershed which is shown in table 2.

Table 2: Estimation of runoff for each watershed (1999-2008)

Location	Zankhwaw	Amli	Godsamba	Vishdalia	Wareli
Area (km^2)	100.52	91.85	78.85	71.05	99.73
Retention S (mm)	83.40	114.12	100.6	75.95	41.11
Weighted CN (-)	75.28	68.95	71.63	76.98	86.07
Rainfall (mm)	277.0	267.5	251.0	251	252
Runoff (mm)	197.15	166.68	160.81	178.77	201.73

It can be seen that sub-watershed Wareli has high flooding potential and Amli has low flooding potential. Flooding potential depends on CN and CN depends on land use and soil properties of watershed which is clearly reflected in results.

It is required to estimate a coefficient that reduces the total rainfall to runoff potential after losses in terms of evaporation, absorption, transpiration and surface storage. It can be stated that the higher the CN value leads the higher runoff generation. Wareli watershed has 86.07 weighted CN so that Wareli is a high flooding potential watershed and Amli has 68.95 weighted CN sothat it gives low run-off. Geospatial distribution of CN value in figure 6

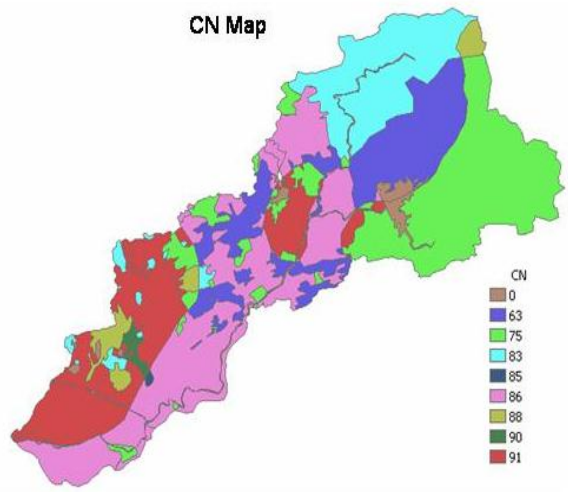

Figure 5: Curve number (CN) map

Runoff depth value calculated for each grids from the equation. Figure 7 depicts the distribution of runoff depth upon 262mm rainfall. Figure 8 (a), (b), (c), (d), (e) depict the graphs of runoff vs. rainfall data will conform to a simple linear relationship with a good fit polynomial trend line. The 10 years rainfall data from 1998-2008 run-off has been used to calculate runoff for each sub-watersheds and graphs was drawn. The correlation coefficient R^2values are similar for all 5 sub-watershed 86.07 weighted CN so that Wareli is a high flooding potential watershed and Amli has 68.95 weighted CN so that it gives low run-off. The details run-off depth map is given in figure 7.

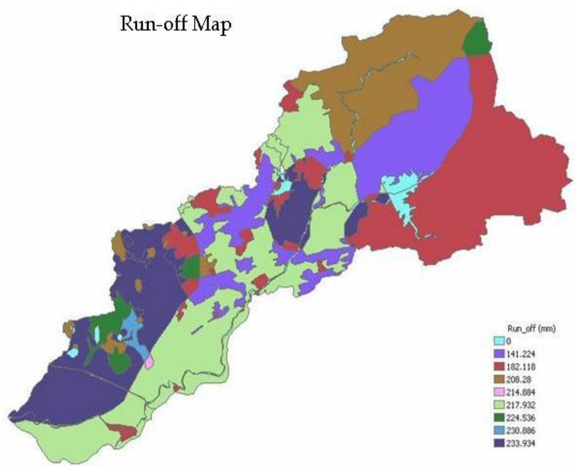

Figure 6: Runoff distribution

Regression analysis has been carried out for each sub-watershed. This can be used for calibration purpose as given in table 3.

Stream gauge data were used for result validation (figure 9) for a common event of 2010. It is found that model can give a good and accurate result for ungauged catchment.

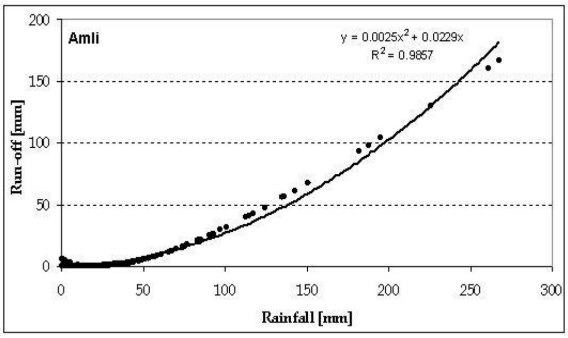

(a)

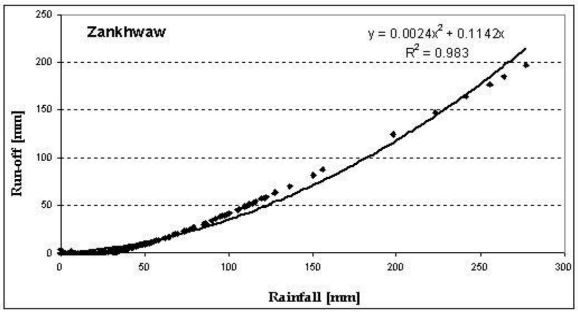

(b)

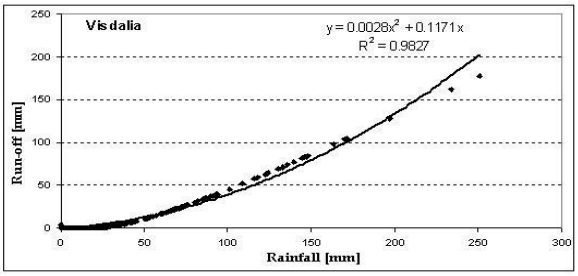

(c)

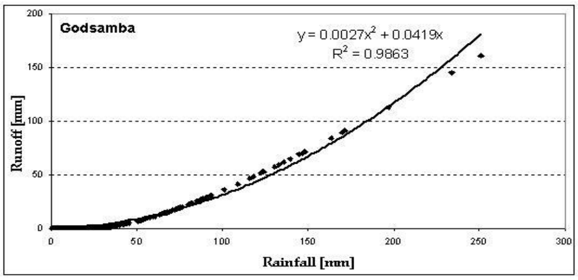

(d)

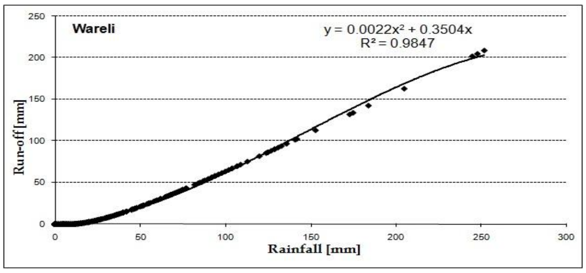

(e)

Figure 8: Results of rainfall runoff relationship for sub-watersheds (a) Amli; (b) Zamkhwaw; (c) Visdalia; (d) Godsamba; and € Wareli

Table 3: Regression relationship between rainfall and runoff for the sub watershed

Sub-watershed	Second order polynomial relationship between rainfall [X] and runoff [Y]; Y=AX^2+Bx		
	A	B	R^2
Zankhwaw	0.0024	0.1142	0.9830
Amli	0.0025	0.0229	0.9857
Visdalia	0.0028	0.1171	0.9827
Godsamba	0.0027	0.01419	0.9863
Wareli	0.0022	0.3504	0.9847

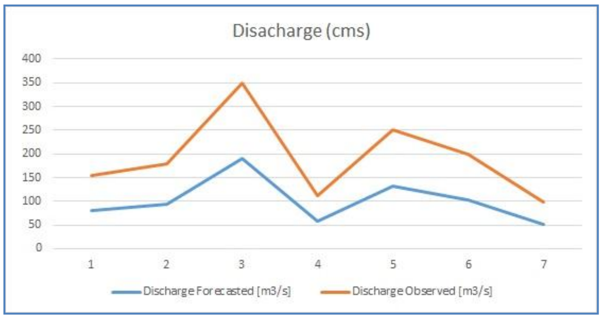

Figure 9: Results of validation of predicted or calculated with stream gauge data

5. Conclusion

Remote sensing and GIS data are of great use for surface runoff estimation when conventional methods of runoff estimation are inadequate. Both the techniques have been used for generating model input for determination of physical characteristics of watershed such as land use, hydrology soil group and CN number. Gaussian maximum likelihood classifier has been used for classification of land use and shows good field acceptability. It has been integrated with SCS-CN method for identification of watershed, estimation of flood potential for a part of lower Tapi basin.

This analysis provides satisfactory results for rainfall-runoff modelling. It will be useful for flood forecasting, flood contribution of each watershed and flood discharge measurements. The method may be good tool for runoff estimation for lower Tapi basin and un-gauged catchment like Varekhadi catchment. It can also state that higher the CN value of catchment leads to more runoff and gives highest contribution for flood.

Acknowledgement

The authors express their sincere thanks to State Water Data Centre officers Mr MG Golawala, Superintending Engineer and Mr SG Shah, Deputy Executive Engineer for supplying daily rainfall data of 8-stations in and around study area. We acknowledge assistance rendered by graduate students of Department of Civil Engineering, Nirma University for carrying out field surveys and soil analysis in laboratory.

Reference

Balvanshi, A. and H.L. Tiwari (2014). A comprehensive review of runoff estimation by the curve number method. International Journal of Innovative Research in Science, Engineering and Technology, Vol.3 (11), pp17480-17485.

Behzad, A., R.S. Mohsmmsd and E. Moghimi (2012). Estimating flood potential emphasizing on geomorphologic characteristics in Tarikn basin using the SCS method. European Journal of Experimental Biology, Vol. 2 (5), pp 1928-1935.

Katimon, A., M. Zulkifli and M. Yunos (2003). Flood potential estimation of two small vegetated watershed. Journal Kejuruteraan Awam, vol 15 (1), pp 1-15.

Mishra, S.K. and V.P. Singh (2003). Soil conservation service curve number methodology. Volume 43. Kluwer Academic Publishers, Dordrecht, The Netherlands.

Ponce, V.M. and R.H. Hawkins (1996). Runoff curve number: Has it reached maturity? Journal of Hydrologic Engineering, 1(1): 11-19.

SCS (1985). National engineering handbook, Section 4: Hydrology, Soil Conservation Service, USDA, Washington, DC.

Sharma, K.D. and S. Singh (1992). Runoff estimation using Landsat Thematic Mapper data and the SCS model. Hydrological Sciences 37 (1/2): 39-52.

Sindhu D, B.L. Shivakumar, A.S. Ravikumar (2013). Estimation of surface runoff in Nallur Amanikere watershed using SCS-CN method. International Journal of Research in Engineering and Technology (2) pp 404-409

Singh, A.K. and A.K. Sharma (2009). GIS and a remote sensing based approach for urban flood-plain mapping for the Tapi catchment, India. In IAHS Publ. 331, 389-394.

Yu, B. (1998). Theoretical justification of SCS method for runoff estimation. ASCE Journal of Irrigation and Drainage Engineering, 124: 306-310.

Zhan, X. and M.L. Huang (2004). ArcCN-Runoff: An ArcGIS tool for generation curve number and runoff maps. Environmental Modelling and Software 19: 875-879.

Journal of Geomatics Vol 10 No. 1 April 2016

Change detection on the Volta river due to the construction of the Kpong dam using remote sensing techniques

E.M. Osei Jnr[1], A.S. Amoah[2], B.E.K. Prah[1], F.K. Anyah[3] and K.A. Addo-Gyan[3]
[1]Department of Geomatic Engineering, Kwame Nkrumah University of Science and Technology, Ghana
[2]Department of Civil Engineering, Kumasi Polytechnic, Ghana
[3]Survey and Mapping Division, Ghana Lands Commission, Ghana
Email: Chief_osei@yahoo.com

(Received: July 08, 2015; in final form: Oct 09, 2015)

Abstract: Construction of dams brings about changes and this is the situation on the Volta River with the construction of the Kpong dam. The aim of this study is to detect these changes and the trend of change after some years of construction of the dam. Topographic map of the lake (1974), Landsat Thematic Mapper (TM) image (1990), Landsat Enhanced Thematic image (2000) and Landsat (UTM) image (2010) were used. The images were georeferenced and classified into six (6) classes namely, closed forest vegetation, open forest vegetation, dense shrub, grass/herbaceous cover, built up/bare surfaces and water body for the purpose of our study, using supervised classification. Maps were produced to show the changes in the land cover features. Careful observations of the produced maps showed that the most dominant change happened after the construction of the dam. wherebythe river overflew its boundary submerging some islands and communities along the river.This caused the Islands to reduce from 340.607ha in 1974 to 319.959ha in 1990 whilst the lake increased from 2266.398ha in 1974 to 4007.07ha in 1990. After that the water increase has been gradual and all other changes have been as a result of anthropogenic activities.

Keywords: Volta river, Kpong dam, Supervised classification, Land cover changes, Landsat images

1. Introduction

Construction of hydro electric dam comes as a joy to all Ghanaians since it will increase the power generation capacity and connect rural communities also to the national grid which helps in the development of a nation. Although having far reaching benefits, they also exert a number of adverse impacts as a result of potential negative impacts from the construction of infrastructures (Tortajada, 2001; Ledec and Quintero, 2003) on their immediate environment.
The Kpong dam was constructed to purposely generate electricity for the industrial and domestic uses to supplement that of Akosombo. The completion of the Kpong dam with a capacity of 160MW in 1981 has raised the power generation capacity of the hydro electric power projects on the Volta river to 1,072MW (Amankwaa, 2002).

Even though the main aim for the construction was attained, Girmay (2006) asserts that at the time of the construction Environmental Impact Assessment (EIA) was not a planning and management tool available in Ghana and in view of that, several issues of environmental impacts, have not been considered under mitigation measures as should have been done.
In most instances, changes along water bodies result in environmental, social and economic impacts of greater damage (i.e. flooding) than benefit to the area (Moshen, 1999). Also coastal zones are most vulnerable for land use changes in this rapid industrialization and urbanization epoch. It is necessary to evaluate land use – land cover changes to develop efficient management strategies (Prabaharan et al., 2010). It is therefore important to look at some of effects of the Kpong dam on the Volta river, islands on it and communities along it.

Remote sensing provides synoptic view of the terrestrial landscape and is used for inventorying, monitoring, and change detection analysis of environmental and natural resources (Narumalani et al., 1997). Although remotely sensed images seldom replace the usual sources of information concerning water resources, they can provide valuable supplements to field data by revealing broad scale patterns not recognizable at the surface, recording changes over time, and providing data for inaccessible regions (Campbell, 1996).

Change detection analysis, which is the process of identifying differences in the state of an object or phenomenon by observing it at different times (Singh, 1989), is employed with multi temporal data sets to discriminate areas of land cover change between dates of imaging of the Kpong dam and its environs from 1974 to 1990 and 1990 to 2010.

The main aim of the work is to apply remote sensing techniques to detect the extent of land cover changes that have occurred as a result of the construction of the Kpong dam and the trend of change.

2. Materials and methodology

2.1 Study area

The Kpong dam is located in the Lower ManyaKrobo district in the Eastern region of Ghana. Its coordinates are 6°4'60" N and 0°12'0" E. The administrative capital of the district is Odumase. The district covers an area of

1,476 km^2, constituting about 8.1% of the total land area within the region (18,310 km^2).

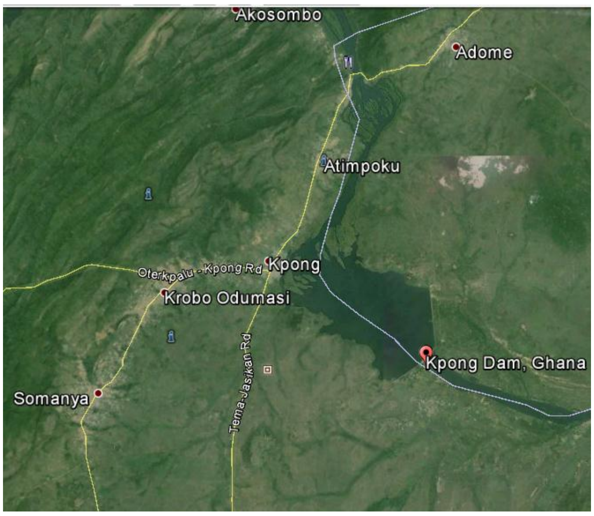

Figure 1: Google earth image showing the study area

The major towns in the district include Odumase township (which incorporates Atua, Agormanya and Nuaso), Akuse and Kpong in the Lower Manya area The district shares boundaries with Upper ManyaKrobo district to the north, to the south with DangmeWest and YiloKrobo respectively, to the west with YiloKrobo municipal and to the east with Asuogyaman district.

2.2 Methodology

Landsat Thematic Mapper (TM) image of 1990, Landsat Enhanced Thematic Mapper (ETM) 2000 and Landsat Thematic Mapper (UTM) 2010 of the study area on the Volta tiver were obtained. These images were dry season images captured in the months of March and April. The images underwent radiometric and geometric corrections.

The topographic map of 1974 and the 1990 image were used to produce another map showing the boundaries of the lake for the two different years. The Landsat images were classified into six (6) different land covers namely closed forest, Open forest, dense shrub, grass, built up/bare lands and water body using maximum likelihood method of supervised classification. Classifications for the various images were guided by observations on the ground, local residents and other techniques such as PCA and NDVI. Statistics were generated for these classes on each image to know the area covered by each land cover. Each classified image was superimposed with the data of the boundary of the river.

3. Results and analysis

A composite map of the river was produced from the map of 1974 and Landsat image of 1990 which showed the difference in size of the river before and after the construction of the dam. From figure 1, two shades of blue are used. A deep blue shows the river as at 1974 before the Kpong dam was constructed and light blue shows the size as at 1990 after the construction of the dam.

Obviously there has been an increase in the river size after the Kpong dam was constructed.

This increase occurs especially at the upstream of the river which caused the displacement of some communities. The Islands decreased from 340.61 ha to 319.96 ha whilst the lake increased from 2266.40 ha to 4007.07 ha. The change can be clearly seen in figure 2. According to the Volta river authority eight villages were fully submerged and these include Vivokope, Fremankope, Lomen, Nobotsukope, Fodzoku, Ageteklekyi, Pokyenu and Gabrunya and the villages that are partly submerged are four namely Glornu, Kasa, Alabonu, Klamadaboe. The classified maps depict the land cover/ use of the area for the three different years at an interval of ten years, i.e. in 1990, 2000 and 2010. Amount of change in area and percentages were generated to quantify the changes.

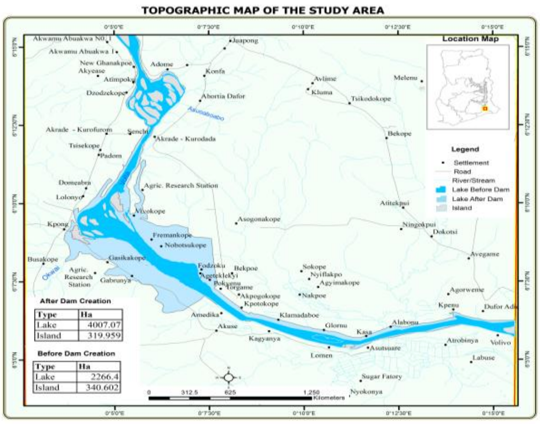

Figure 2: Map showing the boundaries of the river at 1974 and 1990 after construction of the dam

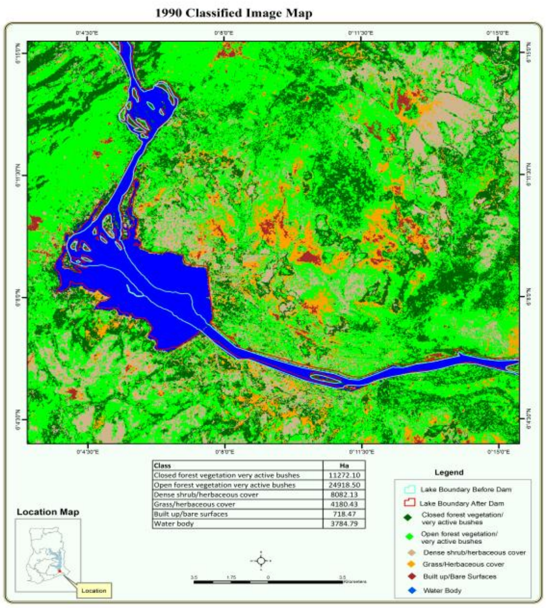

Figure 3: Land cover/use map of 1990

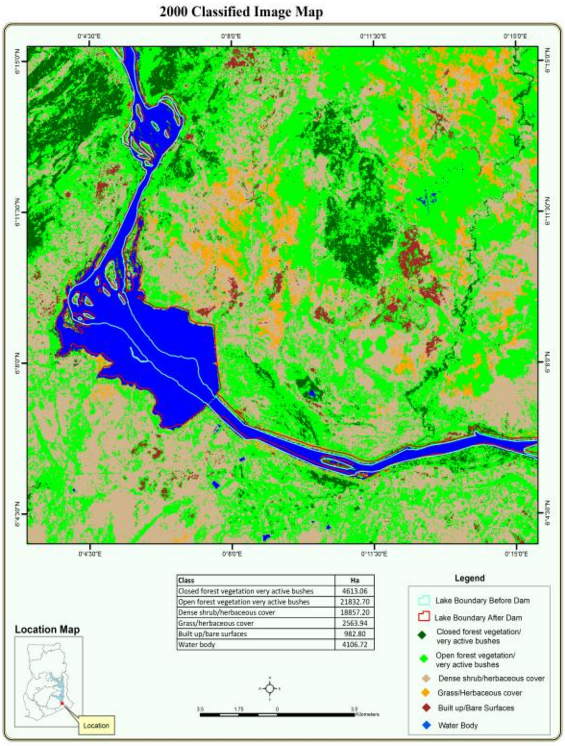

Figure 4: Land cover/use map the year 2000

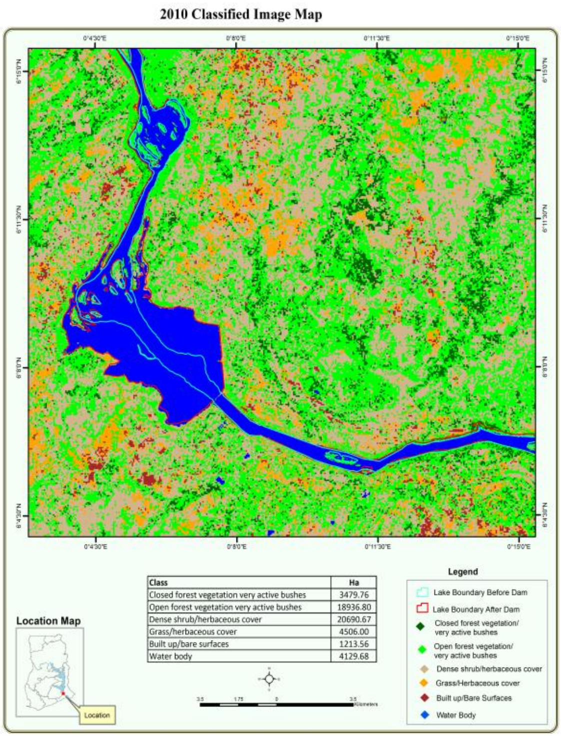

Figure 5: land cover/use for the year 2010

4. Conclusion

All the results of this study have revealed the extent of change in the Lake after the dam construction and changes in land cover from 1990 to 2010. It is obvious from the resultant thematic map that the size of the lake has almost doubled and this happened between the years 1974 and 1990. Land cover has also encountered changes due to anthropogenic activities.

Table 1: Total acreages of the individual islands and average area of the water body before and after the construction

Distribution of Land cover/use classes for the years 1990, 2000 and 2010						
Class	**1990**		**2000**		**2010**	
	Area (Ha)	%	Area (Ha)	%	Area (Ha)	**%**
Closed forest	11049.8	20.9	4613.1	8.71	3479.8	6.57
Open forest	24918.5	47.1	21833	41.2	18937	35.8
Dense shrub/herbaceous	8082.13	15.3	18857	35.6	20691	39.1
Grass/herbaceous	4180.43	7.89	2563.9	4.84	4506	8.51
Built up/bare surfaces	718.47	1.36	982.8	1.86	1213.6	2.29
Water Body	4007.07	7.57	4106.7	7.75	4129.6	7.8
Total	52956.4	100	52956	100	52956	100

Table 2 shows the rate of change of the different classes and this has been interpreted in chart 1. All the land covers that reduced in area have their bars along the negative axis whilst those that gained are on the positive axis. Closed and open forest vegetation always decreased. Changes in the built–up/bare and water body are not that significant even though they have increased along the years. Dense shrub has also increased along the years. Grass/ herbaceous however has no consistent change, from 1990-2000 there was a decrease then from 2000-2010 there was an increase in change. All these changes are due to human activities.

Table 2: Percentage and area rate change of each land cover

Land Cover	**1990-2000**		**2000-2010**	
	Area	%	Area	%
Closed forest	-6436.8	-12.2	-1133.3	-2.1
Open forest	-3.85.8	-5.82	-2895.9	-5.5
Dense Shrub/herbaceous	10775.1	20.35	1833.47	3.46
Grass/herbaceous	-1616.5	-3.05	1942.06	3.67
Built up/bare surfaces	264.33	0.5	230.76	0.43
Water Body	99.65	0.18	22.91	0.05

According to Agbenyo, (2009) hydropower-projects which include the Kpong dam on the Volta river have brought untold hardship onto the lives of the people, influencing human-induced environmental degradation in the area. Activities like farming, firewood and charcoal burning and out-migration among a number of coping measures have been adopted by people in the area to make livelihood comfortable.

The accuracy of the 1990 and 2000 images were not verified but that of 2010, 100 points were picked with the GPS and used to validate the classification. This gave an overall accuracy of 84% and a Kappa of 80.25%.

Acknowledgement

Sincere thanks to the Survey department of the Centre for Remote Sensing and Geographic Information System (CERSGIS) and Environmental department of the Volta River Authority.

References

Agbenyo, P.K. (2009). Effects of the Akosombo and Kpong power schemes on six selected mafi-communities in the Volta region. MSc Thesis: The Institute for Development Studies, Universsity of Cape coast, Ghana

Amankwaa, O.P.J. (2002). Ghana: A human geography for secondary schools. Takoradi, Ghana: St. Francis Press Ltd.

Campbell, J.B. (1996). Introduction to remote sensing. Second edition, The Guilford Press, USA.

Girmay, Y. (2006). Assessing the environmental impacts of a hydropower project: The case of Akosombo/Kpong dams in Ghana; MSc Thesis: Department of Land and Water Resources Engineering, Royal Institute of Technology, Stockholm, Sweden.

Ledec, G. and J.D. Quintero (2003). Good dams and bad dams: Environmental criteria for site selection of hydroelectric projects. Sustainable Development Working Paper16, November 2003

Moshen, A. (1999). Environmental land use change detection and assessment using with multi – temporal satellite imagery. Zanjan University.

Narumalani, S., Y. Zhou and J.R. Jensen (1997). Application of remote sensing and geographic information systems to the delineation and analysis of riparian buffer zones. Aquatic Botany 58: 393-409.

Prabaharan, S., K. Srinivase Raju, C. Lakshumanan and M. Ramalingam (2010). Remote sensing and GIS applications on change detection study in coastal zone using multi temporal satellite data. International Journal of Geomatic and Geosciences, Volume 1, No. 2, 2010.

Singh, A. (1989). Digital change detection techniques using remotely sensed data. International Journal of Remote Sensing. Vol. 10, No. 6, p. 989-1003.

Tortajada, C. (2001). Environmental sustainability of water projects. Doctoral thesis: Division of Hydraulic Engineering, Department of Civil and Environmental Engineering, Royal Institute of Technology, Stockholm.

Journal of Geomatics Vol 10 No. 1 April 2016

An objective method for detecting night time fog using MODIS data over northern India

Sasmita Chaurasia and B.S. Gohil
Space Applications Centre, ISRO
Ahmedabad- 380015 (INDIA)
Email: sasmita@sac.isro.gov.in, bsgohil@sac.isro.gov.in

(Received: Feb 22, 2016; in final form: Mar 29, 2016)

Abstract: An objective method for detecting night time fog based on bi-spectral difference of 3.9µm and 11µm channel brightness temperature has been developed. The thresholds used in this are dynamically derived, based on the data and have been tested with MODIS AQUA/TERRA data for December 2012-January 2013 and December 2013-January 2014 winter season over northern India. The generated fog maps for December 2012-January 2013 have been validated qualitatively with the fog map generated by IMD (India Meteorological Department) using MODIS data. Quantitative validation has been carried out for January 2014, against visibility data at five locations of Northern India. Fog was detected with 70% success rate using this objective method over this region for the validation period.

Keywords: Fog, MODIS, Bi-spectral, Brightness Temperature Difference (BTD), Indo Gangetic Plains (IGP)

1. Introduction

Fog is a meteorological weather phenomenon in which the cloud has its base very close to ground and the visibility reduces to 1000m or less. Apart from its impact on the transportation system as an important socio-economic factor, it has great impact in the field of meteorology, climate studies as well as on human health and crops. Therefore, an improved understanding, monitoring, forecasting and nowcasting of fog will benefit the society as a whole (Gultepe et al., 2009).

Over northern India, fog occurs for a considerable period particularly during winter season (Singh et al., 2004; Dutta et al., 2004; Tiwari et al., 2011). The Indo-Gangetic (IG) plains along the Himalayan region form a trough region, where cold air drainage flowing from the higher plateau gets collected leading to the enhancement of relative humidity. Under clear sky condition, fog forms basically due to radiative cooling of the earth's surface during winter season. In this period a series of low and high pressure zones moves from NW to NE along the Himalayas. During a low pressure zone, it may rain to add more moisture to the atmosphere. This moisture content immediately after the high pressure zone gets condensed due to radiative cooling of the surface, which may lead to the formation of dense fog over a wide region (Singh et al., 2004). Apart from the meteorological condition the local levels of surface as well as atmospheric conditions also leads to the intensification of fog. Once fog layer is formed it persists for the whole duration of the passage of the high pressure zone and typically may extend from Punjab to the Bay of Bengal region along the trough. In the IG plains, it is also observed that during winter season i.e. from November to February the wheat fields are irrigated which adds to the relative humidity over this region. The pollution over the metro city Delhi and surrounding is also responsible for fog formation due to availability of sufficiently large condensation nuclei (Ram Kripa et al., 2012). Emissions from agricultural waste and biomass burning dominate during winter time among other major source of aerosols.

Even though the effect of winter fog in the north Indian region is very high it has not been studied extensively. Specifically, its formation, spatial extent and evolution are required to be studied in detail. It is difficult to monitor the spatial and temporal extent of fog over large-scale areas such as the IG plains using a limited conventional and ground based observational network, so satellite based fog monitoring becomes popular due to its enhanced spatial, spectral and temporal resolution and offers new opportunities for near real-time fog detection and monitoring.

The night time fog detection is very important because fog at night causes difficulties in aviation, land and marine transport. Numbers of surface observations are also limited during night because many of the stations do not operate during this time. Because of the low density of surface observation at night, and to get information about the complete coverage of fog, remote sensing technology provides better opportunity. Many approaches have been developed to detect fog at night (Eyre et al., 1984; Turner et al., 1986; Bendix, 2002). Detection of fog at night using satellite observation relies on the thermal emission of the surface. As it is not contaminated with solar radiation, the false alarm in night time fog detection is less. Most of these methods are based on the particular emissive properties of fog at 3.9µm and 10.8µm wavelengths (Bendix and Bachmann, 1991). The small droplets found in fog are less emissive at 3.9µm than at ~11µm, whereas for larger drops both emissivities are roughly same (Hunt, 1973). Thus the difference between brightness temperatures at these wavelengths are useful and tested for detecting fog against other clouds and land features. The method has been successfully implemented on Geostationary Operational Environmental satellite which provides the required spectral bands (Ellord, 1995; Wetzel et al., 2004; Lee et al., 1997; Greenwarld and Christopher 2000; Underwood et al., 2004). Recently Cermak and Bendix (2007, 2008) have applied the same algorithm to data of Spinning Enhanced Visible and Infrared Imager (SEVIRI) on board Meteosat Second Generation (MSG). As an extension to earlier work (Chaurasia et al., 2011), in this study an objective approach has been developed for the detection of fog during night time over the IG plains.Asthe brightness temperaturedifference depends on the optical depth, particle size, type of fog etc. (Chaurasia et al., 2011) a fix threshold leads to false detection or there is a probability of miss. In order to minimize this a dynamic thresholding approach has been developed and the thresholds are dynamically set for each image under consideration.

2. Data used

Night time fog detection has been carried out using data from MODIS AQUA/TERRA. The MODIS sensor on board the EOS TERRA and AQUA platforms shows the best spectral resolution from operational Low Earth Observation (LEO) systems with 36 spectral bands from visible to thermal infrared portion of the electromagnetic spectrum (Schueler and Barnes, 1998; Levy et al., 2007) (29 spectral bands with 1km, 5 spectral bands with 500m and 2 spectral bands with 250m nadir pixel dimensions). The MODIS Terra/Aqua Level 1B data for night time over north India were obtained from http://ladsweb.nascom.nasa.gov for the period December 2012 to January, 2013 and December 2013 to January 2014. The data of MODIS AQUA having passes over India around 2000UTC is more appropriate for night time fog analysis, because the formation of fog gets initiated at night and is more intense towards early morning. However, the MODIS Terra data at an earlier over pass time from 1600UTC to 1900UTC is also used, because it covers more area of the IG plains of India.

3. Methodology

The flowchart for the objective dynamical thresholding method as has been developed for the present study is shown in figure 1. Besides using the thresholding scheme in the brightness temperature difference image, an attempt has also been made to eliminate the false alarm due to other cloud types and snow by using behavior of cloud and snow in individual channel.

The Level 1B emissive channels were geo-referenced and the data corresponding to 3.9µm and 10.8µm (Band 22 and 31 of MODIS channels) of MODIS were extracted. The radiance values of both channels were converted to brightness temperature through Planck's function. As mentioned in previous paragraph for gross cloud check the long wave infrared or thermal infrared (TIR) channel centered around 10.8 µm has been used. In the long wave infrared (10.8 µm) channel the radiation from land and fog/cloud is the main radiation source. The higher the temperature greater will be the radiation from surface and fog will have higher temperature compared to medium and high level clouds. Thus brightness temperature of fog will also be higher than that of medium and high clouds. However, in case of fog there is always temperature inversion, so that the temperature of fog is similar or even higher than that of surface. Therefore, long wave IR channel can be used to eliminate medium and high clouds whereas it is very difficult to differentiate between fog and the under lying surface using thermal channel alone. The brightness temperature of the medium/ high cloud is the lowest and almost below 270° K (Yang et al., 2008). In order to determine this threshold dynamically, the histogram of 10.8µm channel brightness temperature are examined. It is smoothed to reduce spikes. The histogram of the images corresponding to both the channels show two maxima around one minimum (shown in figure 2a, 2b). The first maxima correspond to low brightness temperature values, which corresponds to pixels with high clouds and snow. Using the BT corresponding to the minima in TIR channel, high clouds and snow are eliminated. If more than one minimum is found then a threshold of 270°K for the TIR channel can be used to eliminate the high clouds and snow pixels considerably. The new image now contains only low clouds, fog as well as pixels corresponding to land. For bi-spectral differencing brightness temperature difference image ($BTD=BT_{10.8\mu m} - BT_{3.9\mu m}$) is generated.

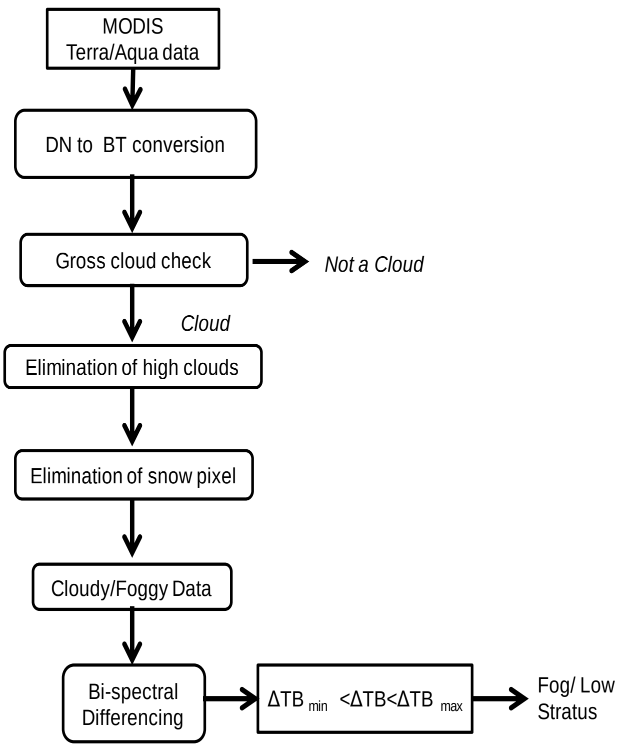

Figure 1: Flow chart for night time detection of fog using MODIS data

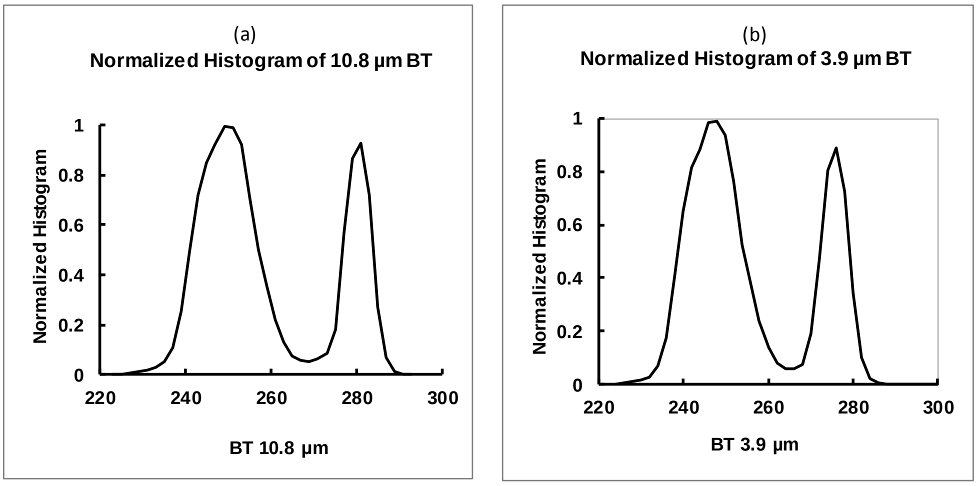

Figure 2: Histogram of brightness temperature in two channels (a) 10.8 µm and (b) 3.9 µm

In order to separate out the fog pixels only, the scatter plot between TIR brightness temperature and BTD values of the image is studied. Figure 3 shows the scatter plot between TIR BT and BTD for a typical case having fog, clear pixels, snow and cloud. From the scatter plot it is seen that for brightness temperature less than 270° K, the brightness temperature difference values are mostly negative or takes a very small positive value. This corresponds to the high level clouds and snow.

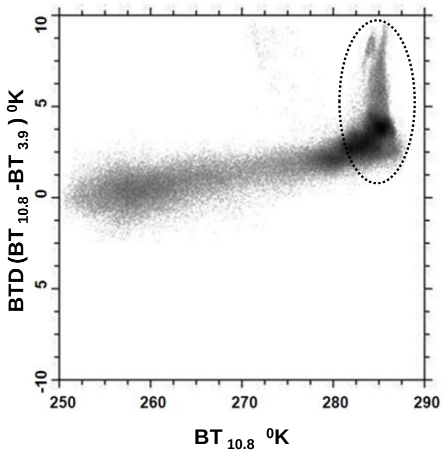

Figure 3: Scatter plot of brightness temperature of 10.8µm and brightness temperature difference (The cluster marked within the ellipse indicates the presence of pixels with fog)

However, for land, low clouds and fog regions where the brightness temperature is more than 280°K, the brightness temperature difference is positive. Due to temperature inversion the brightness temperature of fog is either similar or greater than that of the underlying land. Thus the pixels with TIR brightness temperature greater than 280 and less than 290° K, will correspond to land pixels over laid by fog or low cloud pixels during night (as observed from the figure 3). From the figure it is also observed that for these values of BT the BTD is having large positive value and appear as a separate cluster. It is a remarkable feature (Marked as ellipse in figure 3) which separates out the foggy pixels from the underlying land pixels. The information in this cluster is used to find out the minimum threshold value for BTD and the pixels having BTD value more than the minimum threshold value is classified as fog. The ΔTB_{min} is determined automatically from the histogram, of the BTD image. In a typical fog image, the histogram of BTD image shows one primary maximum, a secondary maximum and a minimum in between (figure 4a). In such a condition, BTD corresponding to the minima value can be considered as the ΔTB_{min} and pixels havingΔTB more than $\Delta TB_{min}$is classified as fog. For such type of scenes, the detection of fog is completely objective as well as dynamic.

However, the MODIS data which has been used for this analysis is in tile form and for each acquisition the frame of the image changes and thus the proportion of different features in the image also changes. Therefore, for some cases in the histogram of BTD image of MODIS data, only single maximum is obtained (figure 4b). In such cases the threshold for BTD (ΔTB_{min}) is set to a point where the slope of the clear sky pixel drops considerably and ΔTB more than $\Delta TB_{min}$is classified as fog. By applying this methodology fog region has been identified with MODIS nighttime data from 01 December 2012 to 31 January 2013 as well as for 01 December 2013 to 31 January 2014 and compared with MODIS fog image of IMD (India Meteorological Department, www.imd.gov.in), whenever available as well as with the early morning MODIS RGB data of next day. However, a quantitative validation of fog map generated for January 2014 has been carried out with visibility data at five different locations i.e. Delhi, Lucknow, Jaipur, Amritsar and Varanasi situated in northern India.

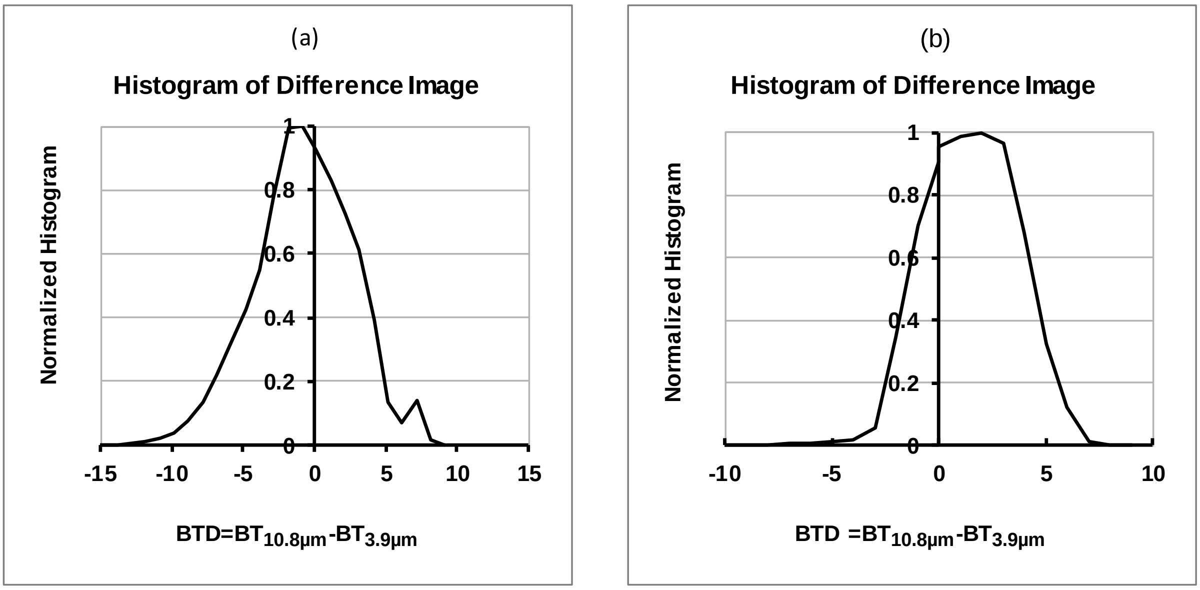

Figure 4: Histogram of brightness temperature difference image (a) BTD image showing double peak (b) BTD image showing single peak

4. Results and discussion

The evolution of fog over Indo-Gangetic plain in December 2012 and January 2013, using MODIS Terra/AQUA data (Different colour shows the BTD values) is shown in figure 5. In order to show the evolution of fog to the maximum extend over the IG plains, both the fog map generated using MODIS AQUA/TERRA has been shown in this figure. Care has been taken to incorporate maximum fog period to show the evolution. Therefore, few days with in December 2012 and January 2013 is missing in the figure 5. As observed from the fog map generated by the above method, the 2012-2013 fog periods started around early December. On December 09, 2012, fog was initiated in the eastern states like Bihar and gradually it extended spatially and covered Bihar and part of Uttar Pradesh by December 15, 2012. The spatial extent continued to increase both from east to west as well as in the southern direction starting from the foot hill of Himalaya. During December 22-25, 2012 it covered the entire Indo-Gangetic plain starting from Bihar at the east to Punjab at the west. This is the time when the wheat cultivation in the four major wheat growing states Bihar, UP, Haryana and Punjab are in full swing and the fields are irrigated, which adds to the local moisture availability apart from the prevailing meteorological condition and temperature inversion in this region which is conducive for fog formation. Similar situation continued till January 07, 2013.

On January 10, 2013 part of north-western region of Uttar Pradesh was covered with fog which extended in width till January 14, 2013. On January 19, 2013 there was heavy fog condition over Punjab and parts of Haryana. On January 21, 2013 again Uttar Pradesh region was engulfed with fog which continued till February 2013 (results shown till end of January). The gradient in the fog map shows the category of fog i.e. shallow, dense and very dense depending on the change in brightness temperature difference. The minimum difference in brightness temperature ΔTB_{min} which is obtained to detect fog varies from 3° to 8° K for the period of analysis. For each image the threshold is found to be different. This change in threshold is attributed to the change in fog optical depth and droplet size (Chaurasia et al., 2011). BTD value of 3° K corresponds to very thin fog. However, for BTD values between 4 to 5° K corresponds to moderately dense fog. BTD value of 6 and >6 °K represents very thick fog. This gradation is empirically made based on our earlier study (Chaurasia et al., 2011) as well as from the visibility data.

The generated fog map has also been compared with the next day morning RGB image and fog map generated by IMD using MODIS data. The qualitative inter-comparison of the two maps is shown in figures 6 and 7 indicating good agreement with each other. Bi-spectral differencing technique has also been used in the generation of fog map by IMD using MODIS data, and a pixel is classified as fog/low stratus when the BTD is greater than 2.5^0 K (Product catalog, www.imd.gov.in). This threshold is fixed for all images. In order to make the two maps comparable instead of showing the variation of BTD over fog, only fog and no- fog regions are generated. The blue colour in both the images shows fog. It is observed from the figure 7 that, for December 25, 2012, there is a systematic data loss in IMD fog map. It is also observed that it has also picked up some of the high cloud part in the southern part of the image, which is filtered by new developed dynamical thresholding algorithm. Similarly, the cloud captured by IMD fog map on January 10, 2013 is also not captured by our algorithm.

A quantitative validation of the generated fog map has been carried against the in-situ visibility data over five different locations on north India i.e. Delhi, Jaipur, Varanasi, Lucknow and Amritsar. Table 1 shows the error statistics of validation. It shows that the percent of detection is 70%, the percent of false detection was 15% and percent of miss was 12.8%. The false detection is because of the presence of low cloud. For which the horizontal visibility at surface level was high but spectral behavior is similar.The brightness temperature difference for low clouds is also very high like fog. The algorithm is not able to detect fog when it is over laid by high clouds due to advection. As this algorithm first eliminates the high cloud region, the fog beneath remains undetected.

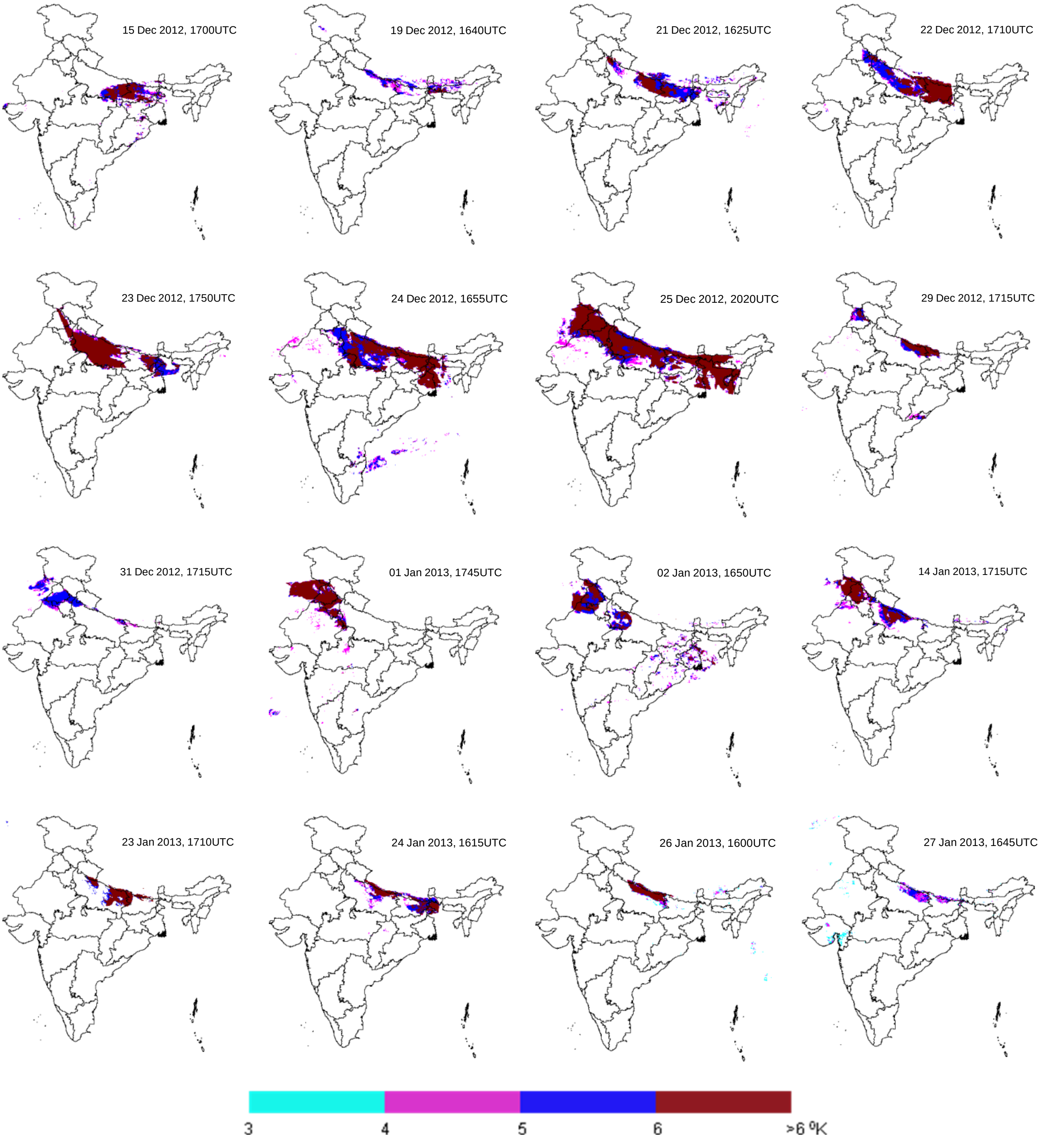

Figure 5: Evolution of fog over Indo-Gangetic plain in December 2012 and January 2013, using MODIS Terra/AQUA data (Different colour shows the BTD values)

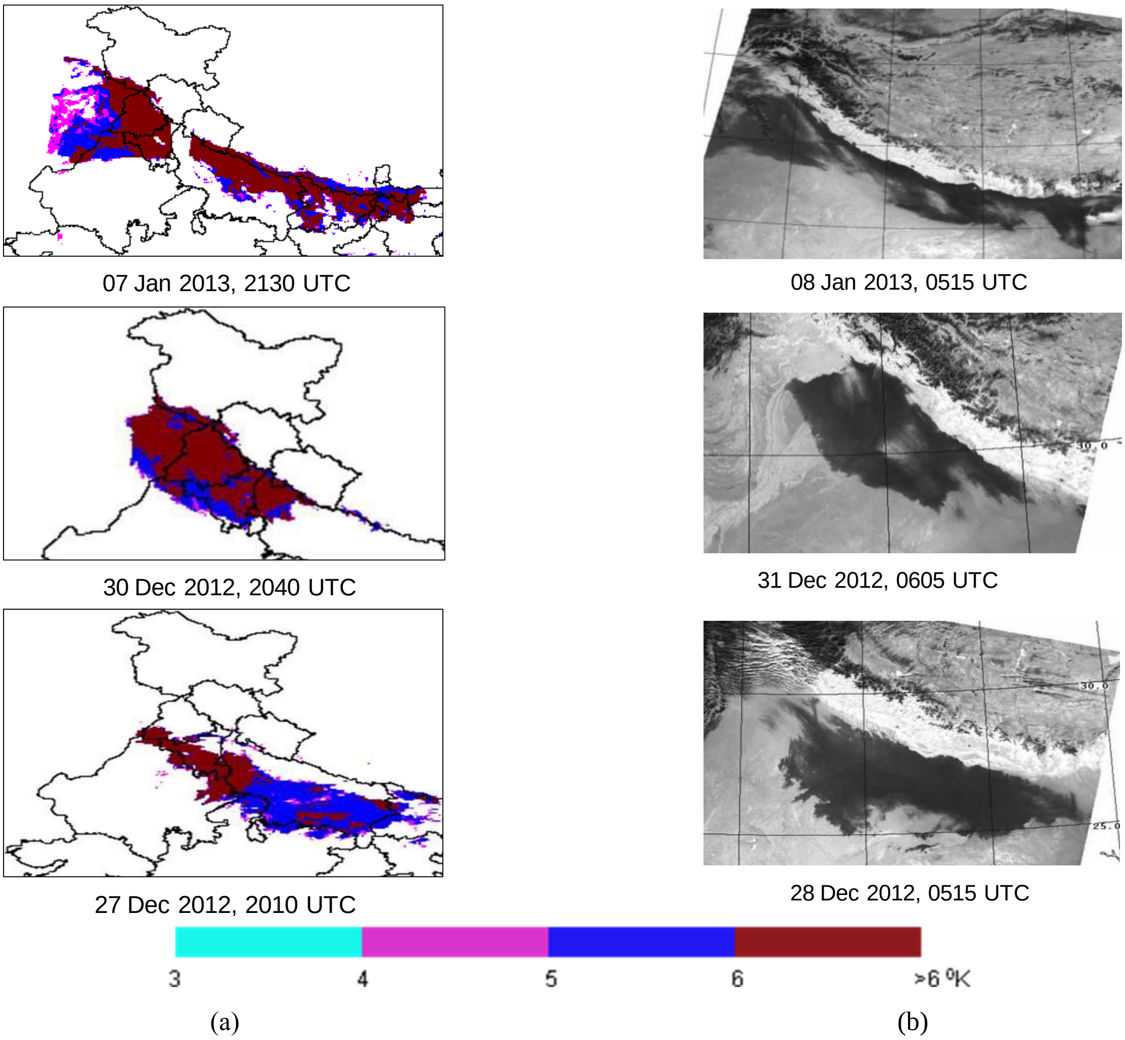

Figure 6: Inter-comparison of (a) generated fog map using MODIS Terra/AQUA of night time (Different colour shows the BTDvalue) with (b) next day morning MODIS RGB image (recoloured)

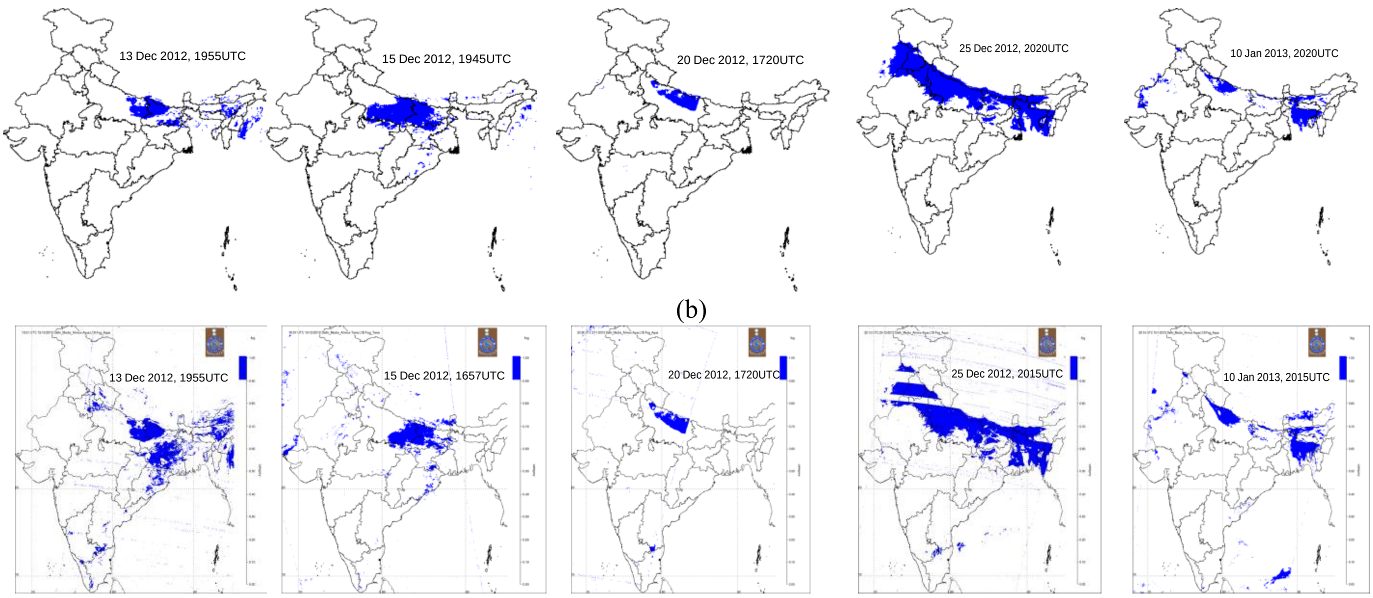

Figure 7: Inter-comparison of generated fog map using (a) MODIS AQUA data with that of (b) IMD fog map using MODIS data (recoloured)

Table 1: Statistics of night time fog detection at five locations (Delhi, Jaipur, Amritsar, Varanasi and Lucknow) in the IG plains from January 01-31, 2014

Total no. of Observations	140
No. of non-concurrent data	25
Number of Hits	81
Number of Miss	16
Number of false detection	18
Percent of Detection (POD)	70%
Percent of False Detection	15%
Percent of Miss	12.8%

5. Conclusions

This technique yields a very good probability of night time fog detection with acceptable false alarm conditions. It has been observed that with the proposed dynamical thresholding, for 70% of the cases the generated fog map successfully detects fog using satellite IR imagery during night time. In future, it may be required to develop algorithm to minimize mis-classification between low clouds and fog.

Acknowledgements

The authors wish to thank the Director, Space Applications Centre, for his keen interest in this work. We are also thankful to www.ladsweb.nascom.nasa.gov for MODIS data and India Meteorological Department for providing the visibility data.

References

Bendix, J. (2002). A satellite-based climatology of fog and low-level stratus in Germany and adjacent areas. Atmospheric Research, 64, 3-18.

Bendix, J. and M. Bachmann (1991). A method for detection of fog using AVHRR-imagery of NOAA satellites suitable for operational purposes. MeteorologischeRundschau, 43, 178 (in German), 1991.

Cermak, J. and J. Bendix (2007). Dynamical nighttime fog/low stratus detection based on Meteosat SEVIRI data – a feasibility study. Pure and Applied Geophysics, 64, 1179-1192.

Cermak, J. and J. Bendix (2008). A novel approach to fog/low stratus detection using Meteosat 8 data. Atmospheric research, 87, 279-292.

Chaurasia, S., V. Sathiyamoorthy, B. Paul Shukla, B. Simon, P.C. Joshi and P.K. Pal (2011). Night time fog detection using MODIS data over Northern India. Meteorological Applications, 8(4), 483–494.

Dutta, H.N., B. Singh and A. Kaushik (2004). Role of western disturbances in the development of fog over Northern India. Presented in XIII National Space Science Symposium (NSSS), Koteyam.

Ellord, G.P. (1995). Advances in the detection and analysis of fog at night using GOES multi spectral infrared imagery. Weather Forecasting,10, 606-619.

Eyre, J.R., J.L. Brownscombe and R.J. Allam (1984). Detection of fog at night using Advanced Very High Resolution Radiometer. Meteorological Magazine, 113, 266–271.

Greenwarld, T.J. and S.A. Christopher (2000). The GOES I-M imagers: New tools for studying microphysical properties of boundary layer stratiform clouds. Bulletin of American Meteorological Society, 81(11), 2607-2619.

Gultepe, I., S.G. Cober, G. Pearson, J. A. Milbrandt, B. Hansen, G.A. Isaac, S. Platnick, P. Taylor, M.Gordon and J.P., Oakley (2009). The Fog Remote Sensing and Modelling (FRAM) field project and preliminary report. Bulletins of American Meteorological Society, 90(3), 341-359.

Hunt, G.E. (1973). Radiative properties of terrestrial clouds at visible and infra-red thermal window wavelengths. Quarterly Journal of Royal Meteorological Society, 99, 346-369.

Lee, T.F., F.J. Turk and K. Richardson (1997). Stratus and fog products using GOES-8-9 3.9µm data. Weather Forecasting, 2, 664-677.

Levy, W.F., L.A. Remer, S. Mattoo, E. Vermote and Y.J. Kaufman (2007). Second-generation operational algorithm: Retrieval of aerosol properties over land from inversion of moderate resolution imaging specroradiometer spectral reflectance. Journal of Geophysical research, 112: D13211, DOI:10.1029/2006JD007811.

Ram Kirpa, M., M. Sarin, A. K.Sudheer and R. Rangaranjan (2012). Carbonaceous and secondary inorganic aerosols during wintertime fog and haze over urban cities in Indo-Gangetic plain. Aerosol and Air Quality Research, 12, 359-370.

Schueler, C.F. and W.F. Barnes (1998). Next generation MODIS for polar operational environmental satellites. Journal of Atmospheric and Ocean Technology, 5, 430-439.

Singh, B., H.N. Dutta and A. Kaushik (2004). Ecological restoration by fog water. Presented in XIII National Space Science Symposium (NSSS) Koteyam.

Tiwari, S., S. Payra M. Mohan, S. Verma and D.S. Bhisht (2011). Visibility degradation during foggy period due to anthropogenic urban aerosol at Delhi, India. Atmospheric Pollution Research, 2, 116-120.

Turner, J., R.J. Allam and D.R. Maine (1986). A case study of the detection of fog at night using channel 3 and 4 on the Advanced Very High Resolution Radiometer (AVHRR). Meteorological Magazine, 115, 285–290.

Underwood, S.J., G.P. Ellord and A.L. Kuhnert (2004). A multiple-case analysis of noctural radiation-fog development off California utilizing GOES nighttime fog product. Journal of Applied Meteorology, 43, 297-311.

Wetzel, M. A., R.D. Bory and L.E. Xu (2004). Satellite microphysical retrievals for land based fog with validation by balloon profiling. Journal of Applied Meteorology, 35, 810-829.

Yang, L., Y. Xu and M. Wei (2008). Fog detection using MODIS data in the Yangtze river delta. Fifth International Conference on Fuzzy Systems and Knowledge Discovery, IEEE Computer Society, 457-572, DOI:10.1109/FSKD.2008.302.

Journal of Geomatics Vol 10 No. 1 April 2016

Morphometric changes of the Varuna river basin, Varanasi district, Uttar Pradesh

K. Prakash, S. Singh and U.K. Shukla
Centre of Advanced Study, Department of Geology
Banaras Hindu University, Varanasi-221005
Email: kuldeep_prakash@yahoo.com, geosaurabh@gmail.com, shukla_umakant@yahoo.com

(Received: Jan 10, 2015; in final form: Dec 02, 2015)

Abstract: The Varuna is one of the important interfluves rivers joining the Ganga river near Varanasi city. The morphometric analysis of the Varuna river basin has been carried out. It covers an area of about 3622 km^2 of the Ganga plain. The dendritic drainage pattern diagnosed in the area exhibits homogeneous permeable substratum and gentle gradient. Spatio temporal changes (Land Use and Land Cover i.e. LULC) of the Varuna river basin, in Varanasi district, using Landsat multispectral imageries spanning 38 years (1972, 1988, 2002 and 2010) are also studied. The LULC patterns illustrate that in early 80's the basin is largely covered by the salt affected waste land. Later on the salt affected waste land area is reduced and area of agricultural land and built-up area has increased. The study underlines the necessity of a scientific approach for the sustainable river basin management, with the help of the hydrological conditions, recent climatic anomalies and geological control of the basin.

Keywords: Gangetic plain, Interfluves, Varuna river, Morphometric analysis, Confluence-shift

1. Introduction

The interfluves (doab) surfaces of the Gangetic plain, forming a part of Indo-Gangetic fore land basin system (Singh et al., 1996), are the most important, tens to hundreds of kilometer wide geomorphic surfaces and witness the oldest living civilization of the world. These plains are drained by numerous snow fed and alluvium fed rivers. Interfluve river basins undergo morphometric changes and transformation of channel patterns and their degradation and aggradations in response to varying set of climate and tectonics influencing the base level of the rivers through time (Denizman, 2003). According to Mesa (2006) geomorphic parameters are important and necessary to explore the basinal dynamics and basin architecture. The present study is targeting on quantitative approach of watershed and landscape development of the Varuna river, a tributary of Ganga river, with the help of remote sensing and GIS data. The river is flowing deeply incised in to the interfluve surface having a rather narrow valley (Shukla, 2013). Interfluve surface making the base level of the rivers is made up of silt, sand and clay horizons. Varuna river basin is a part of the central alluvial plain of the Ganga basin (Singh, 1996; Shukla and Raju, 2008) bounded by the Vindhyan rocks in the south forming the peripheral bulge. For watershed management practices and geotectonic control over the drainage basin through morphometric analysis has been attempted by several workers in the recent past (Sreedevi et al., 2004; Pati et al., 2006; Pati et al. 2008; Thomas et al., 2010; Sarmah et al., 2012). Channel characteristics of the interfluves alluvial river replicate the stability of bank material and erosive power of the stream and any small changes in geomorphology (or spatio temporal shift) in the river basin signify a consequence of variation in sediment load, sediment-water ratio and slope of the basin as a result of prevailing climate and neotectonics (Schumm et al., 2000; Raj, 2007). There are many small and large rivers such as Ganga, Yamuna, Brahmputra, Kosi, Gomati rivers and several others have shown changes in their channel courses through Quaternary-Holocene times in response to changing set of climate and tectonic conditions (Wells and Don, 1987; Srivastava and Singh, 1999; Kotoky et al.,2005; Roy and Sinha, 2005; Shukla et al., 2012, Shukla, 2013).

The focus of the study, the Varuna river emanates at 25°27′ N & 82°18′E near Mau Aima (Pratapgarh district, Uttar Pradesh) flows east-to-southeast for about 183km, and makes confluence with the western bank of the Ganga river at the 83°2'40.088"E 25°19'46.387"N near Raj Ghat bridge, just downstream of the Ganga in Varanasi city (Fig.1). The Varanasi city is one of the oldest living civilizations in the world and important pilgrim city of India with a population of about 1.5 million. The name Varanasi itself is believed to have been derived after the name of the rivers Varuna and Assi. Varuna river is one of the foremost controlling drainage system of Varanasi city (Khan et al., 1988). Assi river has deteriorated to become a drain, carrying domestic waste and sewerage of Varanasi city, and calls for immediate attention for its reclamation (Shukla, 2013). The study also analyses spatio-temporal changes in Land Use Land Cover (LULC) of the Varuna river basin based on available Landsat imageries. Moreover, the current environmental status of a region and ongoing modifications in terms of urban growth could be better appreciated by analysis of spatial and temporal change in land use planning (Turner et al., 1993).

Journal of Geomatics Vol 10 No. 1 April 2016

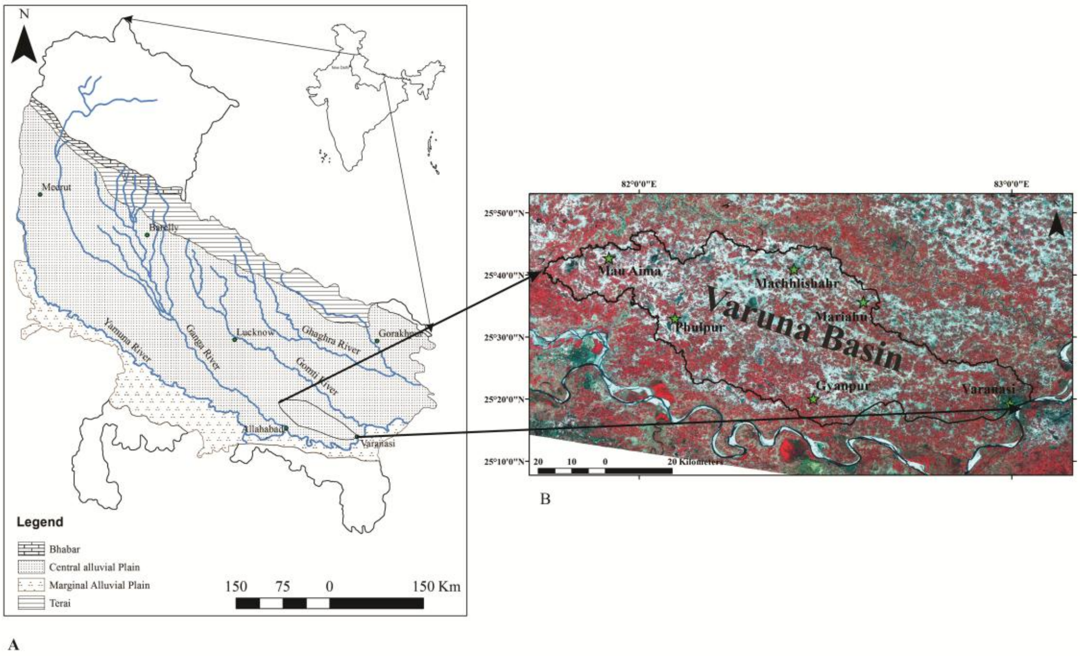

Figure 1: Location map of the Varuna basin (a) Map showing subdivision of Ganga plain in Uttar Pradesh (modified after Singh, 1996); (b) Landsat imagery (MSS Path 153 and Row 42 of 1972) representing Varuna river basin

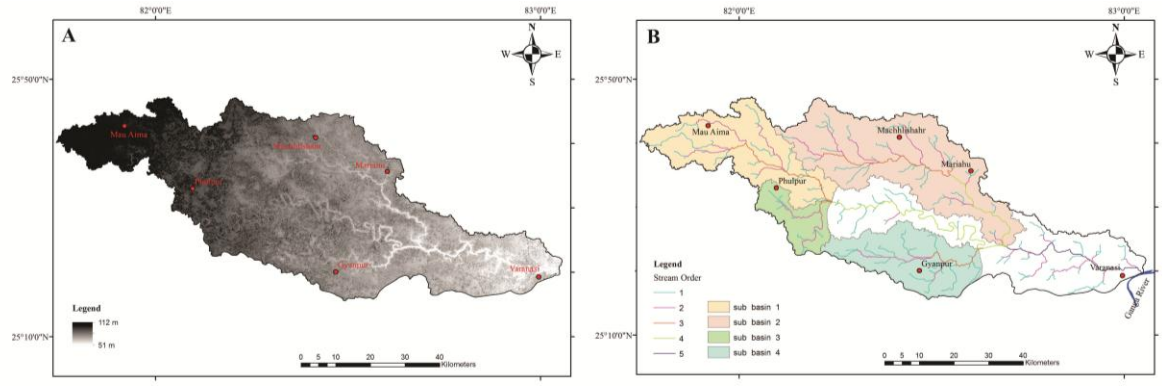

Figure 2: Varuna river basin (a) DEM (digital elevation model) from SRTM data; (b) Drainage pattern and 4 sub basins

2. Methodology

Shuttel Radar Topogrpaphy Mission (SRTM) data (Fig.2a) (of Sep 30, 2000) and SOI (Survey of India) topographic maps (1:50000) are used for extraction of the drainage network and sub water shed in the study area. Landsat Multispectral Scanning (MSS) data (of Sep 30, 1978) is used for delineation of old valley of the Varuna river and further identified and traced out by handheld 12-channel GPS (make Garmin E-Trax Vista). The paleo channels are identified here on the basis of higher moister content in soils, textural characters on the image and the vegetation pattern in the former river valley. The satellite data were obtained from the Global Land Cover Facility (http://www.landcover.org). Horton's (1945) and Strahler (1965) methods were adopted in the present study for characterization of watershed and drainage network. The morphometric parameters such as linear, areal and relief aspects were extracted using ARC GIS-10.0. Measurements pertaining to the confluence shifting of the Varuna river in time and space have been carried out using the available published data, SOI toposheets, Landsat MSS data and GPS readings.

3. Results

3.1. Morphometry

Morphometric analysis done in the present study incorporates quantitative study of the Varuna river valley, altitude, volume, slope, profiles of the land and drainage basin characteristics of the area concerned (Kondolf and Hervè, 2003).The stream network and the catchment area of the Varuna river with four 4th order sub-watersheds with as are shown in figure 2b.

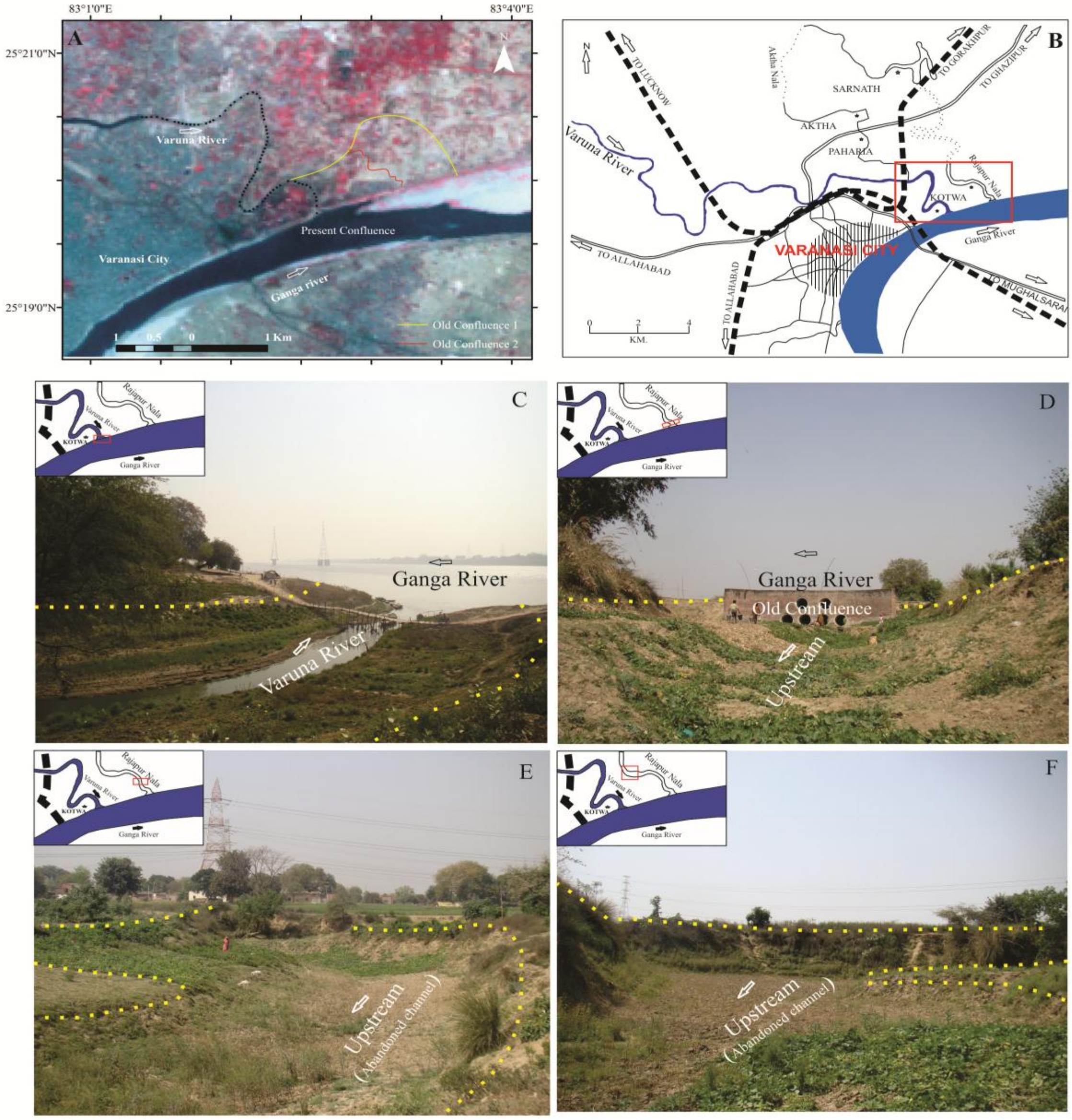

Figure 3: (A) Two discreet southward shifting of the confluence of the Varuna river near Varanasi, traced out in the field with hand GPS; (B) Traces (in doted lines) of the old Varuna River near Sarnath (after Jayaswal et al.); (C) Present confluence of the Varuna river; (D) Old confluence of the Varuna River; (E) Abandoned channel of the Varuna River; and (F)Low lying area showing abandoned channel of the Varuna river

Dendritic drainage pattern is the most common and widespread pattern found in the study area (Fig.2b). The dendritic patterns evolved in the area closely resemble to the area having homogeneous bed materials (mainly Gangetic alluvial) with a very gentle regional slope. The perimeter of the Varuna watershed is 482.07 km (Table 1). The values of the bifurcation ratio (Rb) generally set in between 2.0 and 5.0 for the drainage network. Such network generally develops in consistent lithologies and also signifies the minimum structural control over it. When the values are higher than 10.0, it indicates that structural control has played a dominant role on drainage network development (Mekel, 1970). Low Rb values indicate elongated shape of the basin (Morisawa, 1985). The Varuna river belongs to this category.

The variations among the stream length ratio (Rl) values are directly related to the geomorphology including topography and lithology and hence it governs the erosional stage of the watershed and discharge (Sreedevi et al., 2004). The Rl values in case of Varuna river basin varies between 0.66 and 0.75 (Table 1) and that implies accomplishment of geomorphic maturity. The Rho coefficient is used for determining the storage capacity of drainage network (Horton, 1945). The values of Rho coefficient of the Varuna river and its sub-watersheds vary from 0.14 to 0.26 (Table 1). The higher values of Rho coefficient of SW2 and SW3 (Fig.2b) are indicators of higher hydrologic storage during floods and decreased effects of erosion during elevated discharge.

Drainage density (Dd) is one of the significant indicators of the landform development and presents a numerical measurement of landscape dissection and hence the runoff potential (Smith, 1950). The study area has very low drainage density varying from 0.19- 0.31, and a very coarse drainage texture (Table 1), which implies permeable subsurface conditions (since the basin has chiefly clay and sandy clay subsurface material) and dense vegetation.

Form factor (Ff) is significant factors to envisage the shape of the drainage basin and the flow intensity of watershed with direct relationship to peak discharge (Horton 1945, Gregory and Walling 1973). The value of Ff (Table1) varies from 0.19 to 0.33. Low Ff values (<0.4) are characterized by shorter flow peaks of longer duration which in case of Varuna river seems to be its alluvium fed character and irregular rainfall in the area.

Length of overland flow (Lg) is an important morphometric parameter complementing both hydrologic and physiographic advancement of the watershed (Horton, 1945). The Varuna watershed accounts an Lg value of 1.19, whereas the SW1, SW2, SW3 and SW4 (Fig.2b) are having the Lg values between 1.61 and 2.63 (Table 1). The higher value of Lg of SW2 indicates geomorphic maturity while other sub-watersheds are charecterized by early mature or late youth stage of geomorphic advancement.

The Rc (Circulatory ratio) value of Varuna Watershed (VW) is 0.19, whereas it ranges between 0.15 and 0.23 in other sub-watersheds (Table 1). The low Rc values (<0.6) of the sub- watersheds are probably related to attenuated flood- discharge periods. The stage of evolution of the watersheds can also be explained by the numerical values of Rc of sub- watersheds. The low Rc values of the sub- watersheds, imply youth stages of watershed development.

The numerical value of Re (elongation ratio) for VW is 0.5, signifying an elongated nature of the basin. Re of 4 sub-watersheds varies from 0.56 and 0.65(Table 1). The elongated shapes of sub- watersheds, with the larger basin area, are insisting the role of head-ward erosion in development of lengthy channels.

Table 1: Mathematical formula adopted for the quantitative measurement and estimated values of the morphometric parameter

Parameters/ Sub-Watershed		SW1	SW2	SW3	SW4	VW
Linear parameters	Unit					
Area	km^2	694.25	1124.3	222.23	523.81	3622.5
Perimeter	Km	237.54	302.46	109.41	149.93	482.07
Basin length (Lb)	Km	52.27	66.51	25.67	42.53	135.57
Linear Aspect						
Bifurcation ratio (Rb) = Nu/N(u+1) Where Nu is number of any given order and N(u+1) is number in the next higher order	Dimensionless	4.03	3.2	2.81	5.33	3.84
Stream length ratio (Rl) = Lu/L(u-1) Where Lu is stream length order u and L(u-1) is stream segment of the next lower order	Dimensionless	0.66	0.67	0.74	0.75	0.68
Rho coefficient (ρ) = Rl/Rb	Dimensionless	0.16	0.2	0.26	0.14	0.17
Areal Aspect						
Drainage density (Dd) = Lt/A Where Lt is the total length of all ordered streams	km^{-1}	0.29	0.19	0.28	0.31	0.26
Stream frequency (Fs) = Nt/A Where Nt is the total number of all ordered streams	km^{-2}	0.05	0.08	0.1	0.05	0.06
Drainage Texture (T) = Dd×FS	km^{-3}	0.014	0.015	0.028	0.015	0.015
Length of overland flow (Lg) = 1/2Dd	km	1.72	2.63	1.78	1.61	1.92
Form factor (Ff) = A/Lb^2	Dimensionless	0.25	0.25	0.33	0.28	0.19
Circulatory ratio (Rc) = $4\pi A/P^2$	Dimensionless	0.15	0.15	0.23	0.29	0.19
Elongation ratio (Re) =	Dimensionless	0.56	0.56	0.65	0.61	0.5

(SW- sub-watershed, VW- Varuna watershed)

3.2. Confluence shift

The confluence shift of the Varuna river is ascertained by analysing the satellite imageries, toposheets (Survey of India) and supported by extensive field effort (Fig. 3). The shifting of the confluence points of the Varuna river is traced out by hand held 12 channels Garmin E-Trax Vista GPS with ± 3 meter accuracy in the field (fig. 3a). The confluence point of the Varuna river has shifted progressively southwards in detached steps by leaving behind older valley signatures like depression with meandering morphology, ponds and meander cut-offs away from the main river channel (Fig. 3b). Two discreet channel shifts have been noticed in the field. First shift is 1.64 km and the second shift is 0.96 km located north from the present day confluence of Varuna with the Ganga river (Fig.3a). The remnant valley of the Varuna river is identified on the basis of width of the abandoned channel/ valley in the field (Fig.3e-f).

It is to be noted that all the tributaries near the Varanasi city along with the Ganga River are deeply incised and at present do not have liberty to leave their valleys and shift (Shukla et al., 2012). Therefore, there are mainly three possibilities for shift of the tributary confluences. The causes are (i) when they were not incised and were freely shifting their channels (ii) in the recent past due to channel piracy by the Ganga river and (iii) periodic and linear change in rainfall.

However, the shift in confluence points of the Varuna river is well comprehended by the dynamic of the main Ganga River channel. Ganga river acts as the base level control for the Varuna river and any change in the dynamics of the former directly affects the later. Before the Last Glacial Maxima most likely in the late Quaternary, rivers were not incised and freely migrating within their broad valleys, shifting laterally for many kilometres (Shukla et al., 2012). The meanders of the present-day Ganga river in the study area around Varanasi appear deformed and elongated, with straight and highly-convoluted reaches, indicating tectonic control over the present-day river channel. Around Varanasi, where presently due to incision (Swamee et al., 2003; Shukla, 2013) the Ganga River is confined within a 1–2 km wide narrow valley, it previously had a much wider valley which was 10–15 km wide. With time it migrated eastward, leaving behind a large abandoned meander belt. The location of Varanasi represents the old flood plain of the Ganga River, characterized by numerous ponds formed due to the abandonment of the channels (Srivastava et al., 2003; Shukla et al., 2012). The incision of the Ganga River seems related to tectonics along a fault line passing in a NE–SW direction, controlling the course of the river and dynamics of tributary confluence (Shukla and Raju, 2008; Shukla et al., 2012; Singh, 2015).

3.3. Land use pattern

The Landsat data has been classified into six major classes (agriculture, river, water bodies, salt affected wasteland, wetland and urban- rural build-up area) and in view of that the land use changes in the Varuna river basin were investigated during four time spans of 1972, 1988, 2002 and 2010 (Fig. 4).

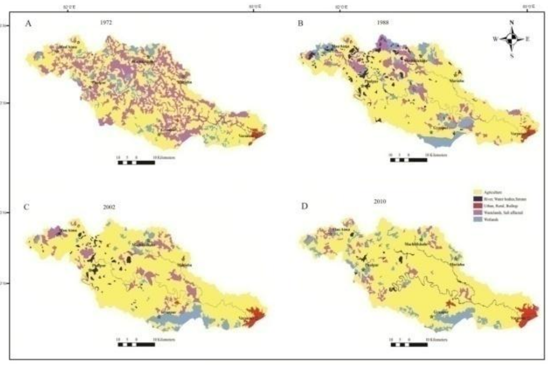

Figure 4: Land use and Land cover (LULC) map of the Varuna basin during four time spans of (A) 1972; (B) 1988; (C) 2002; and (D) 2010

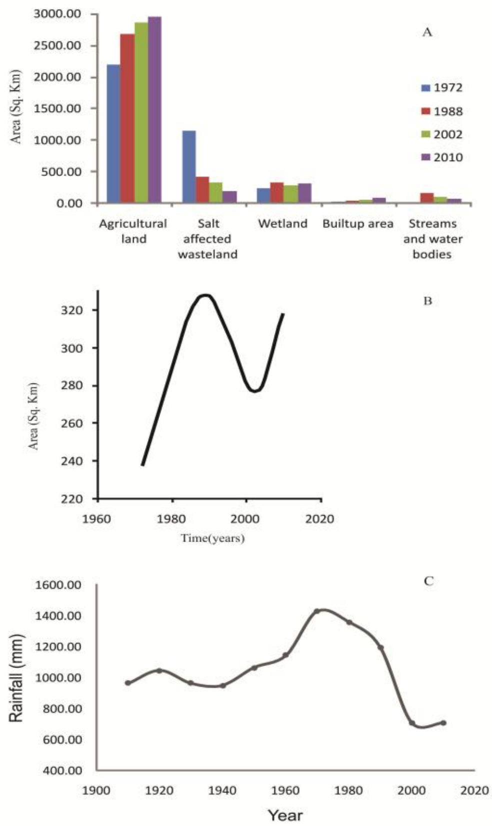

Figure 5:(A) Bar digram showing area and Landuse land cover changes in Varuna basin from 1972-2010; (B) Scatter diagram with smooth line showing change in wetland area with time; (C) Rainfall demonstrating anamolous rain fall in early 80's

In 1972, LULC of the Varuna river basin reveals that, 32% area is identified as salt affected waste land and about 60% area is used in agricultural practices (Fig.5a). The salt affected waste land area is reduced by 22% in 1988 from 1972 and the large proportion of the reclaimed land (from salt affected to useful land) is occupied by agricultural practices and some proportion is consumed in built-up areas (Fig.5a). The LULC scenario has drastically changed from 1988 to 2010 (Fig.4). In these years percentage of built up areas have increased exponentially, leaving behind the area of agricultural land and surface water bodies. The area of wetland is somehow constant with modest variation while streams and water bodies show large variation in studied time span, due to anomalous rain fall in early 80's (Fig. 5c).

Table 2: Land use land cover status in Varuna basin during 1972-2010

Area (km^2)	1972	1988	2002	2010
Agricultural land	2192.15	2688.05	2869.40	2961.74
Salt affected wasteland	1155.46	413.36	325.89	195.64
Wetland	237.15	327.44	276.62	317.90
Built-up area	28.04	32.59	57.11	78.84
Streams and water bodies	9.04	160.16	92.57	67.46
Total area	3621.83	3621.60	3621.58	3621.58

Rainfall data (Fig. 5c) from the India Meteorological Department (IMD) support the change in the surface water pattern in early 1980. The present study is confirming the important physiographic modification occurring in the Varuna River basin during the last four decades. The morphometric analysis, confluence shifting and change in land use with/ land cover pattern of the river basin highlight the necessity for sustainable development and management of ecological setup for the Varuna river basin.

4. Conclusion

The GIS techniques have been efficiently utilized for the assessment of the drainage characteristics of the Varuna river watershed and to comprehend the significance of morphometric studies and shifting of the confluence. The low bifurcation ratio and elongation ratio of the Varuna river signify the elongated shape of the basin. The elongated shapes of sub- watersheds, with the larger basin area, are due to head-ward erosion leading to expansion of channels. The study area is demonstrating very low drainage density because of permeable subsurface and dense vegetation. The low drainage density in the study area leads to very coarse drainage texture. The low values of circulatory ratio are characterized by attenuated flood- discharge periods and youth stages of watershed development. Thus the incorporation of morphometric analysis together with predictable watershed assessment methods would have a better understanding the status of land form, drainage management and evolution of groundwater potential for watershed planning and their management.

Near Varanasi, the Ganga river is flowing along a NE–SW tectonic lineament. The confluence of the Varuna river is shifted towards south from 1 to more than 1.5 km from north from its present confluence with the Ganga river. The study suggests that the morphodynamic change and confluence shift in the interfluves river (Varuna river), was controlled largely by monsoonal variability as well as directed by tectonic activity in trunk river. LULC has revealed that because of population growth build up area has drastically increased at the cost of agricultural land.

Acknowledgement

Authors are thankful to the Head of the CAS, Department of Geology, Banaras Hindu University for making available the functioning conveniences. S. Singh is grateful to the UGC, New Delhi for a fellowship in the form of BSR-SRF.

References

Denizman, C. (2003). Morphometric and spatial distribution parameter of karstic depressions, lower Suwannee river basin, Florida. Journal of Cave and Karst Studies 65(1), pp. 29-35.

Gregory, K.J. and D.E. Walling (1973). Drainage basin form and process - a geomorphological approach. London: Edward Arnold.

Horton, R.E. (1945). Erosional development of streams and their drainage basins hydrophysical approach to quantitative morphology. Geological Society of America Bulletine 56 (3), pp. 275-370.

Jayaswal, V., U.K. Shukla and M. Sharma (2015). Varanasi and Ganga (Report of Geo-morphological & Archaeological Investigations, at Ramanagar). Aryan Books International, New Delhi.

Khan, A.A., P.C. Nawani and M.C. Srivastava (1988). Geomorphological evalution of the area around Varanasi, Uttar Pradesh, with aid of aerial photography and Landsat imageries. Geological Survey of India, Rec. 113(8), pp. 31-39.

Kondolf, G.M. and P. Hervè (2003). Tools in fluvial geomorphology. John Wiley & Sons Ltd., England.

Kotoky, P., D. Bezbaruah, J. Baruah and J.N. Sarma (2005). Nature of bank erosion along the Brahmaputra river channel, Assam, India. Current Science 88 (4), pp. 634-640.

Mekel, J.F.M. (1970). The use of aerial photographs in geological mapping. ITC text book of photo-interpretations 8, pp. 1-169.

Mesa, L.M. (2006). Morphometric analysis of a subtropical Andean basin (Tucuman, Argentina). Environmental Geology 50, pp. 1235-1242.

Morisawa, M. (1985). Geomorphology text books: Rivers, form and processes, chapter 5 "Structural and lithological control".

Pati, J.K., V.P. Malviya and K. Prakash (2006). Basement re-acvtivation and its relation to Neotectonic activity in and around Allahabad, Ganga Plain. Journal of Indian Society of Remote Sensing 34, pp. 47-56.

Pati, J.K., J. Lal, K. Prakash and R. Bhusan (2008). Spatio- temporal shift of Western bank of the Ganga river, Allahabad city and its implications. Journal of Indian Society of Remote Sensing 36, pp. 289-297.

Raj, R. (2007). Strike slip faulting inferred from offsetting of drainages: lower Narmada basin, western India. Journal of Earth System Sciences 116, pp. 413–421.

Roy, N.G. and R. Sinha (2005). Alluvial geomorphology and confluences dynamics in the Gangetic plains, Farrukhabad–Kannauj area, Uttar Pradesh, India. Current Science v. 88, pp. 2000–2006.

Sarmah, K., L.K. Jha and B.K. Tiwari (2012). Morphomertic analysis of a highland microwatershed in East Khasi Hills District of Meghalaya, India: Using remote sensing and geographic information system (GIS) techniques. Journal of Geology and Regional Planning 5(5), pp. 142-150.

Schumm, S.A., J.F. Dumont and J.M. Holbrook (2000). Active tectonics and alluvial rivers. Cambridge University Press, Cambridge.

Shukla, U.K., I.B. Singh, M. Sharma and S. Sharma (2001). A model of alluvial megafan sedimentation: Ganga Megafan. Sedimentary Geology 144, pp. 243–262.

Shukla, U.K. and N.J. Raju (2008). Migration of the Ganga river and its implications on hydrogeological potential of Varanasi area, U.P. India. Journal of Earth System Science 117, pp. 489–498.

Shukla, U.K., P. Srivastava and I.B. Singh (2012). Migration of the Ganga river and development of cliffs in the Varanasi region, India during the late Quaternary: Role of active tectonics. Geomorphology 171–172, pp. 101–113.

Shukla, U.K. (2013). Varanasi and the Ganga river: A Geological Perspective. In: V. Jayaswal (Eds) Varanasi: Myths and Scientific Studies. Aryan Book International, New Delhi, pp. 100-113.

Singh, I.B. (1996). Geological evolution of Ganga plain - An overview. Journal of Palaeontological Society of India 41, pp. 99–137.

Singh, C.K. (2015). Middle Ganga Plain; May be on the Verge of Seismic Shock. Journal Geological Society of India 85, pp. 511-513.

Smith, K.G. (1950). Standards for grading texture of erosional topography. American journal of Science 248, pp.655-668.

Sreedevi, P.D., K. Subrahmanyam and S. Ahmed (2004). The significance of morphometric analysis for obtaining groundwater potential zones in a structurally controlled terrain. Environmental Geology 47, pp. 412-420.

Srivastava, P., I.B. Singh, S. Sharma, U.K. Shukla and A.K. Singhvi (2003). Late Pleistocene–Holocene hydraulic changes in the interfluve areas of the central Ganga Plain, India. Geomorphology 54, pp. 279–292.

Srivastava, A. and R.P. Singh (1999). Surface manifestation over a subsurface ridge. International Journal of Remote Sensing 20, pp. 3461– 3466.

Strahler, A.N. (1964). Quantitative geomorphology of basin and channel networks. Hand book of Applied Hydrology (Ed. Ven Te Chow). McgrowHill book company, New York, section 4-11.

Swamee, P.K., B. Parkash, J.V. Thomas and S. Singh (2003). Changes in channel pattern of river Ganga between Mustafabad and Rajmahal, Gangetic plains since 18th century. International Journal of Sediment Research 18(3), pp. 219-231.

Thomas, J., S. Joseph and K.P. Thrivikramaji (2010). Morphometric aspects of a small tropical mountain river system, the southern Western Ghats, India. International Journal of Digital Earth 3(2), pp. 135-156.

Turner, M.G., W.H. Romme, R.H. Gardner, R.V.O' Neill and T.K. Kratz (1993). A revised concept of landscape equilibrium: Disturbance and stability on scaled landscapes. Land Ecology 8(3), pp. 213- 227.

Wells, N.A. and J.A. Don (1987). A reconnaissance of sedimentation on Kosi alluvial fan of India. Special publication of SEPM, Tulsa 39, pp. 51-61.

Journal of Geomatics Vol 10 No. 1 April 2016

Malaria-risk assessment using geographical information system and remote sensing in Mecha district, West Gojjam, Ethiopia

Emebet Dessalegne[1], K.V. Suryabhagavan[1] and M. Balakrishnan[2]
[1]School of Earth Sciences, Addis Ababa University, P.O. Box 1176, Addis Ababa, Ethiopia
[2]Department of Zoological Sciences, Addis Ababa University, P.O. Box 1176, Addis Ababa, Ethiopia
Email: drsuryabhagavan@gmail.com

(Received: Dec 25, 2015; in final form: Feb 24, 2016)

Abstract: Malaria is a major global health problem. About 3.5 billion people are at risk of infection of malaria worldwide, with environmental factors contributing for about 70–90% of the disease-risk. Over one million cases of malaria are reported each year, out of which more than 80% is from the sub-Saharan Africa. Ethiopia is a predominantly malaria-prone country as about 75% of the landscape of the country is favorable for breeding of the malaria vector. Geographical Information System has emerged as a spatial technology, which integrates a wide range of datasets available from different sources including remote sensing and Global Positioning System. During the present study, a malaria-risk map of Mecha district of Ethiopia was prepared by establishing the relationship of various climatic and non-climatic factors related to the disease using regression analysis. Weighted overlay technique of multi-criteria evaluation was used to develop the malaria-risk map. Temperature, rainfall, altitude, distance from streams, distance from swamps and ponds, population density, health facilities and land-use/land-cover patterns were used to prepare malaria-risk areas. Malaria hazard, elements of risk and vulnerability layer were overlaid, and further verified by ground truth and village-wise reports of malaria cases to produce the final malaria-risk map. Four categories of malaria-risk ranging from very high to low were derived. Most of the study area (99.01%) was found to belong to high and moderate malaria-risk. It is suggested that effective identification and mapping of malaria-risk levels can be made using geospatial tools, to contribute for the prevention and control of this disease.

Keywords: GIS, Landsat, Malaria, Remote sensing, Regression analysis, Weighted overlay

1. Introduction

Malaria is a major health problem as it affects all age groups of the people in most parts of the world even for about 70–90% of the disease risk (Bautista et al., 2006; Erin et al., 2014). Around 300−500 million cases and more than two million deaths of malaria are reported each year, with more than 80% of these from the sub-Saharan Africa (Abdulhakim, 2013). Malaria is essentially an environmental disease, as the vectors require specific habitats with surface water for reproduction and humidity for adult mosquitoes to survive. The development rate of both the vector and the malaria parasite are influenced by temperature (Ashenafi, 2003). Approximately 4–5 million cases of malaria are reported annually in Ethiopia and malaria is prevalent in 75% of the extent of the country, putting over 50 million people at risk (Abdulhakim, 2013).

Integrated use of remote sensing (RS) and Geographical Information System **(**GIS) has been successfully demonstrated in many studies related to mapping of malaria-risk in different parts of Africa (Hay et al., 2000; Kleinschmidt et al., 2001; Sithiprasasna et al., 2005; Dongus et al., 2007). The severity of malaria is a function of the interactions between *Plasmodium*, the parasite; the *Anopheles* mosquito, the vector; the human host and the environment. Vector abundance combined with the probability of the vector feeding of susceptible human-host determines the risk of malaria infection, which is more prevalent in the tropics. It is a serious vector-borne disease. About 3.5 billion people are at risk of infection of malaria worldwide with environmental factors contributing for the disease transmission, and its seasonal patterns.

There are several factors associated with this disease and its control, such as water bodies, rainfall, temperature, population, land-use/land-cover and health facilities (Palaniyandi, 2012). Understanding the causal factors is a prerequisite to design and implement appropriate malaria-risk management. So as to mitigate the effect of this risk, effective malaria-risk management methods are required. Spatial information on malaria distribution helps to prioritize control measures.

2. The study area and methods

Mecha district lies within 11^o 8'−11^{o}39' N latitude and 36^{o}59' 51"−37^o 20' E longitude covering a total area of 149,119 km^2 (Figure 1), located in the West Gojjam Zone in the Amhara region, about 35 km from Bahir Dar, the capital town of Amhara Regional State of Ethiopia. There are 44 villages including three town administrative villages in the study area. Mecha district is situated at an altitude range of 1720 m−2800 m above sea level. The area is characterized by flat lying topography with some hilly terrain. This district has different climatic variables in different seasons. The annual rainfall pattern of the study area varies from 1000 to 2000 mm. The temperature varies from 23^{o}C to 27^{o}C. June, July and August are high rainfall months and December, January and February are low rainfall months. High temperature is recorded in March, April and May and low temperature is recorded in November, December and January.

2.1 Methodology

To develop the malaria-risk map of the study area, identification and selection of the major factors contributing for malaria breeding such as land-use/land-cover, water bodies, population, elevation, temperature, rainfall, ponds and swamps, slope and health station facilities were done. Regression analysis was applied to identify the statistical correlations between malaria cases and the above parameters. The mathematical formula applied to the explanatory variables in order to best predict the dependent variable was the following:

$$Y = \beta 0 + \beta 1 x1 + \beta 2 x2 \ldots . + \beta n x n + \varepsilon \qquad (1)$$

where, yis dependent variable, x1, x2, …, xn are independent variables, β0, β1, β2… βn are coefficients and ε is error term (residual).

In this study, global weighted regression (GWR) and ordinary least squares regression (OLS) were carried out to assess the spatial relationship between the parameters and malaria cases and to validate the model performance. To assess spatial model performance, values of R-squared, adjusted R-squared, Jarque-Bera p-value (JB), Akaike Information Criterion (AIC) and Variance Inflation Factor (VIF) were computed (Ehlkes et al., 2014). Independent variables greater than 7.5 VIF (strong multi-collinearity) were cut off to overlay. The dependent variable was malaria cases and the independent variables were temperature, rainfall, LU/LC, population density, slope, elevation, distance from swamps and ponds and distance from streams. Elevation variable (8.7) and slope variable (10.7) in the regression model are associated with large VIF values. To show the spatial clustering of the values associated with the geographic features in the study area, Moran's I. was also computed.

2.1.1 Moran's I: This is a tool to measure spatial autocorrelation based on both feature locations and feature values simultaneously. It evaluates whether the pattern expressed is clustered, dispersed or random (Oliveira et al., 2013). The Moran's index statistic for spatial autocorrelation is given as:

$$I = \frac{n}{So} \frac{\sum_{i=1}^{n} \sum_{j=1}^{n} w_{ij} Z_i Z_j}{\sum_{i=1}^{n} Z_i^2} \qquad (2)$$

where, Z_i = the deviation of an attribute for feature i from its mean

W_{ij}= the spatial weight between i and j,

n= total number of features and

So= the aggregates of all the spatial weights.

2.1.2 Image processing: To produce land-use/land-cover map of the study area, Landsat TM image of path 170 and row 052 of January 2015 was acquired.

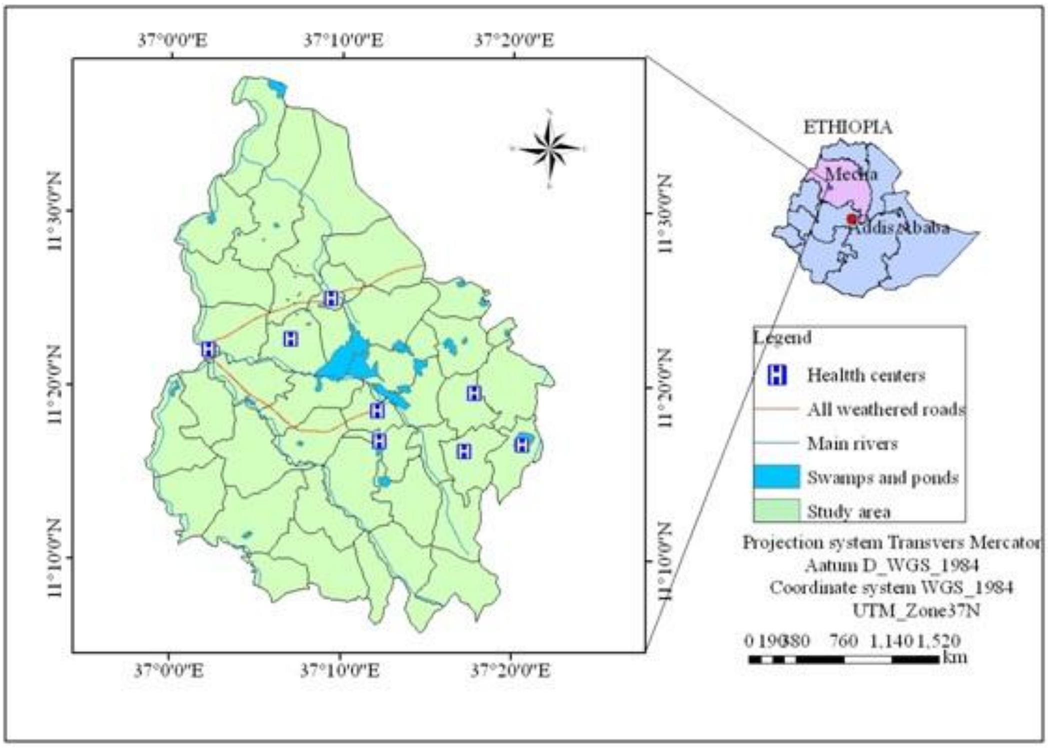

Figure 1: Location map of the study area Mecha District, Ethiopia

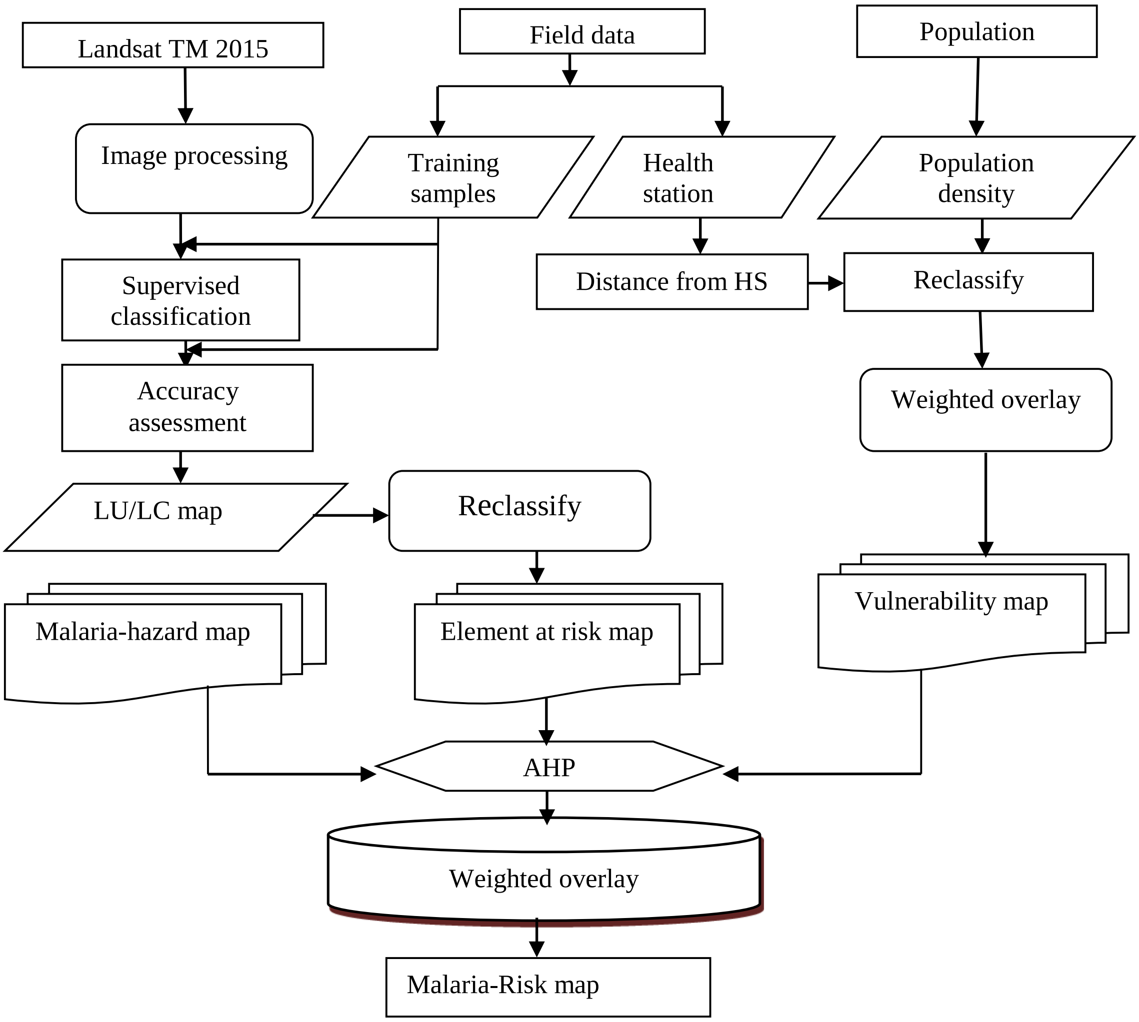

Figure 2: Malaria-risk flowchart

Image processing starting from image pre-processing (geometric and radiometric correction), layer stacking (band 2–7), image enhancement and image classification to the final accuracy assessment were done in ERDAS Imagine software. To correct the satellite image radiometrically, Operational Land Imager (OLI) band data were converted to top of atmosphere (TOA) to a planetary reflectance using reflectance rescaling coefficients provided in the product metadata file. The following equation was used to convert DN values to TOA reflectance:

$$\rho\lambda' = M\rho Qcal + A\rho \qquad (3)$$

The ρλ' does not contain the sun angle correction and hence the image was again converted to TOA reflectance with a correction for the sun angle as follows:

$$\rho\lambda = \frac{\rho\lambda\prime}{cos(\theta sz)} = \frac{\rho\lambda\prime}{sin(\theta SE)} \qquad (4)$$

After preparing the factors and validating the model and image processing, three malaria-risk layers were generated using their factors. The malaria-risk map was developed by combining the suitability of environmental conditions for malaria transmission based on climatic and non-climatic factors. All factor parameters compatible to hazard analysis were generated before weighted overlay. Hazard map was produced by computing and reclassifying the five parameters *viz.* meteorological (rainfall and temperature) data, distance from ponds and swamps, altitude and distance from streams layers. Each of the hazard parameters was ranked according to the importance for mosquito breeding and transmission. The process of weighting each factor was performed in IDRISI software. After assigning weight, the hazard map was computed by overlaying the five selected factors.

Vulnerability map was generated from distance from health facility map and population density map. The two layers were overlaid with 54% weight to population density map and 46% to health facility map. The weight was given by consulting health experts, who have advanced knowledge about malaria based on the regression result coefficients and available information. The element at the risk-map was computed by reclassifying the land-use/land-cover pattern of the study area. The land-use/land-cover types were ranked based on the importance from the most important to least important, and vulnerability map was developed by reclassifying land-use/land-cover types of the study area. In this study, malaria-risk was expressed as the product of malaria hazard map, vulnerability map and element at risk-map using Shook model. To produce the malaria-risk map, the influence factors were assigned for the three components of malaria-risk layers (malaria hazard, element at risk and vulnerability layer) and overlaid.

$$R=V\times H\times E \tag{5}$$

where; R=Malaria risk map; H= malaria hazard map; V= vulnerability map; E= malaria element risk map.

The methodological flowchart is presented in Figure 2.

3. Results

3.1 Malaria *vs* rainfall

Figure 3 shows the average rainfall and average malaria cases recorded in the study area during 2002–2012. Rainfall was the main climatic factor for the prevalence of malaria in the study area with 44% influence (Tables 1 and 2). The average rainfall of the study area varies from the lowest 2.056 mm to the highest 418.97 mm per month. Maximum rainfall was recorded during June−August and the minimum during December−February. A higher number of malaria cases was recorded during May−June and October−November, and lower in the months of August, March and April. There was a positive relationship between malaria cases and rainfall in the months December to February and May to July, but the relationship was negative in the months of August to November.

3.2 Malaria *vs* temperature

The present study has revealed that temperature also has influence in prevailing malaria. There was a negative relationship during the months of December−April, when the study area had lower number of recorded malaria cases, and in August when higher number of cases were registered. Although temperature favours *Plasmodium* development, lack of water prevents breeding and development of the vector. Figure 4 shows the relationship between monthly malaria incidence recorded during 2002−2012 with the data on monthly temperature variations in the study area.

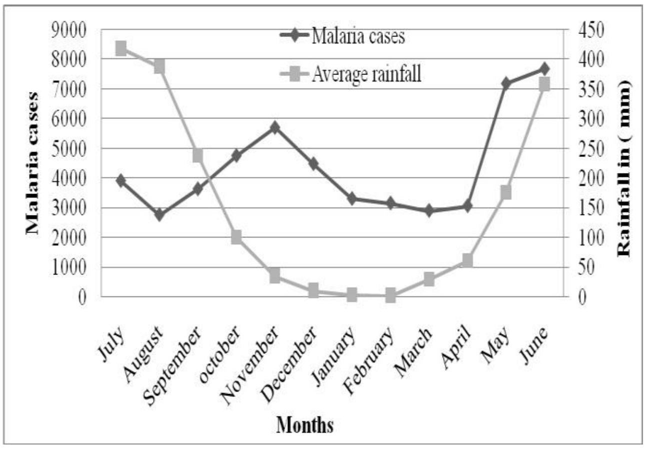

Figure 3: Malaria *vs* rainfall relationship in the study area during 2002−2012

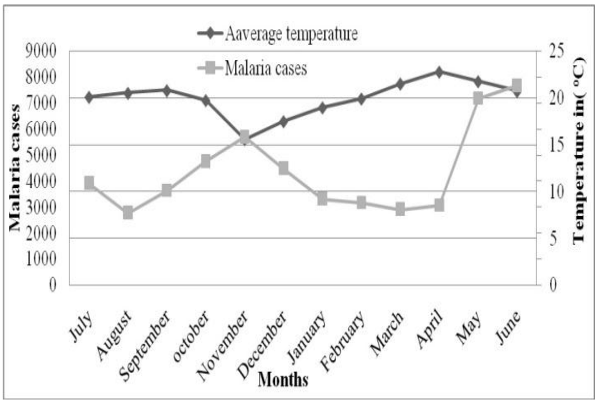

Figure 4: Malaria *vs* temperature relationship in the study area (2002−2012)

Table 1: Malaria cases and rainfall and temperature in Mecha district (2002–2012)

Months	July	Aug.	Sep.	Oct.	Nov.	Dec.	Jan.	Feb.	Mar.	Apr.	May	June
Malaria case	39164	2770	3638	4760	5705	4487	3313	3162	2909	3070	7188	7683
Rainfall	418.9	388.3	238.2	100.3	35.4	10.4	2.9	2.06	29.7	60.9	175.6	358.5
Temperature	20.07	20.5	20.78	19.72	15.52	17.45	18.94	19.89	22.5	23.78	22.76	20.69

3.3 Regression analysis for model validation

As shown in Table 2, rainfall, temperature and population density have strong positive relationship and altitude and slope have strong negative relationship with malaria incidence. These are the main factors for malaria prevalence in the study area relative to other factors analysed (Tables 2 and 3). The AIC, multiple R^2 and adjusted R^2 for this model were 657.72329, 0.8052 and 0.7566, respectively. Multiple R-squared and adjusted R-squared were both statistics derived from the regression equation to quantify model performance. In this model, R^2 was 80.5299%. Hence, 80.53% variation in the dependent variable (malaria cases) could be explained by the model.

Journal of Geomatics Vol 10 No. 1 April 2016

Table 2: Result of regression analysis

Variable	Coefficient	T-stat	Probability	Robust-t	Robust-p	R^2 (%)	VIF
Intercept	-75035357	-4.74	0.000041*	-7.994938	0.000000*		
Pop. density	+69.1356	4.037	0.000319*	6.851215	0.000000*	85.54	2.0
Health station Distance	-0.031	-4.051	0.007826*	-1.130710	0.000000*	19.6	1.7
Slope	-11.04497	-0.12	0.897635	-0.191535	0.849318	16.68	10.7
Temperature	+115.4472	0.52	0.526501	0.615132	0.542817	51.04	2.4
Rainfall	+752.86	4.76	0.000039*	7.638637	0.000000*	64.02	1.9
Elevation	-114.44	-2.06	0.488905	-0.848799	0.402299	17.04	8.7
Distance from swamps	-0.04183	-4.85	0.009351*	-0.746534	0.000014*	59.00	2.2
Distance from streams	-0.08	-0.58	0.56	-0.77	0.44	12.71	1.4

* indicates a statistically significant p-value ($p < 0.01$).

Coefficients are values that represent the strength and type of relationship the explanatory variable has to the dependent variable. When the relationship is positive, the sign for the associated coefficient is also positive (+) and negative relationships have negative (−) signs. When the relationship is strong, the coefficient is large such as rainfall, temperature, altitude, elevation and population density. Weak relationships are associated with coefficients near (zero) such as distance from swamps and ponds and distance from streams. Regression analysis computed a p-value for the coefficients associated with each independent variable. P-value was used to reject the null hypothesis for statistical test that states for all purposes, the coefficient is zero and the associated explanatory variable is not useful for the model.

The regression analysis revealed small p-values. Hence, the explanatory variables were important to the model with a value different from zero (the coefficient was not zero). Table 3 shows that some of the variables are both negative and positive. The explanatory variable that showed negative and positive significance were slope, distance from streams, distance from swamps and temperature. This indicates that these variables were not statistically significant (P>0.01). However, population density, distance from health stations, rainfall and distance from swamps and ponds were significant (P<0.01).

Table 3: Results of explanatory regression analysis

Variables	Variable significance (%)	
	Negative	Positive
Population density	0.00	100
Slope	75.44	24.56
Altitude	85.44	14.56
Distance health stations	100	0.00
Distance from streams	60.18	39.82
Distance from swamps & ponds	100	0.00
Rainfall	0.00	100
Temperature	21.58	78.42

In the present model, p-value was small (0.000015), and hence the null hypothesis was rejected. There was spatial autocorrelation between the values associated with the geographic features in the study area. Moran's index value was 0.357501, and hence spatial features and their associated data values tended to be clustered (positive spatial autocorrelation) as it was greater than 0. The tool returns a Z score of 3.429816, which indicated that standard deviations were away from the mean.

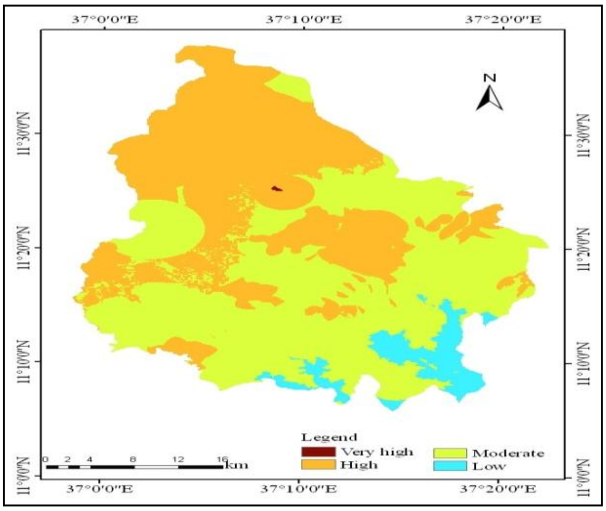

Figure 5: Malaria hazard map of the study area

3.4 Areas of malaria hazard

Rainfall, altitude, streams, temperature, swamps and ponds were the predictors of presence of malaria with percentage influence of 44%, 38%, 4%, 7% and 7%, respectively. Rainfall and altitude were the dominant factors for the existence of malaria as a hazard as compared with other selected factors, and streams showed the least percentage influence (Principal Eigenvector) for malaria prevalence. The consistency ratio for the Eigenvector of weights was within an acceptable range with the value 0.02. Table 4 shows the weight, rank and degree of vulnerability of the selected parameters of malaria hazard in the study area. Figure 5 shows the malaria hazard-risk map of the study area, which shows the level of malaria vulnerability in an extent of 46.77 km (0.31%) as very high, 64504.51 km^2 (43.25%) high, 76446.74 km^2 (51.26%) moderate and 8122.58 km^2 (5.44%) low. Thus, most of the study area is subjected to high and moderate malaria hazard-risk.

3.5 Malaria vulnerability

Figure 6 shows that in an extent of 1878.04 km^2 (1.26%) was moderately vulnerable for malaria 39794.21 km^2

(26.68%) was vulnerable for malaria at low level and 107446.73 km^2 (72%) was vulnerable for malaria at very low level. Thus, the majority of the study area is under very low malaria-risk.

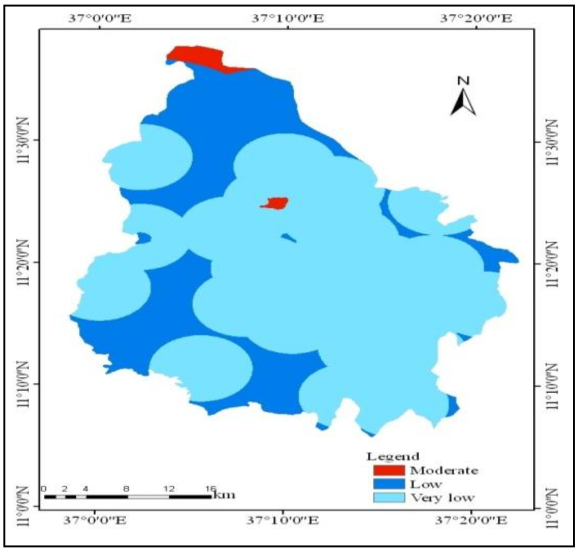

Figure 6: Malaria vulnerability

3.6 Element at risk map of malaria

The results of NDVI values ranged between -0.266708–0.569553. The lowest (negative) NDVI values indicate the water bodies. The highest NDVI values indicate plantation and bush lands. Table 5 shows the results of NDVI value for each of the LU/LC types of the area. Figure 7 illustrates that 48523.66 km^2 (32.54%) had very high, 21365.29 km^2 (14.32%) had high, 75556.48 km^2 (50.66%) had moderate and 3673.56 km^2 (2.46%) had low level of malaria vulnerability.

3.7 Identifying malaria-risk areas

As shown in Table 6, element at risk and malaria vulnerability had 63%, 31% and 6% of weight influence of hazard element at risk and vulnerability for the existence of malaria in the study area. Malaria hazard layer was the dominant factor for the final malaria-risk map. There was no area, which was free from malaria-risk. In the study district, 33.59 km^2 (0.23%) area was of very high, 69305.82 km^2 (46.47%) was high, 76830.96 km^2 (51.52%) was moderate and 2948.61 km^2 (1.97%) was of low malaria-risk. The majority of the study area was subject to high and moderate risk of malaria. The final malaria-risk model map has revealed that all parameters, analysed during the study had different weight influence for the prevalence of malaria in the Mecha district of Ethiopia. However, rainfall was the most dominant factor for the prevalence of malaria in the present study area, where as altitude had limiting effect for the prevalence of the disease as altitude has negative correlation with temperature. The total area and degree of vulnerability for malaria prevalence in the final malaria-risk map and its layers (malaria hazard map, element at risk map and vulnerability map) are presented in Table 7.

Table 4: Characteristic of factors in relation to malaria hazard area identification

Factors	Weight	Class	Rank	Degree of vulnerability
Rainfall	44	98–100 mm	5	Very low
		100–103 mm	4	Low
		103–105 mm	3	Moderate
		105–108 mm	2	High
		>108 mm	1	Very high
Altitude	38	<2000 m	1	Very high
		2000–2200 m	2	High
		2200–2400 m	3	Moderate
		2400–2600 m	4	Low
		>2600 m	5	Very low
Distance from Swamps and ponds	7	0–500 m	1	Very high
		500–2000 m	2	High
		2000–3500 m	3	Moderate
		3500–5000 m	4	Low
		>5000 m	5	Very low
Distance from Streams	4	0–500 m	1	Very high
		500–2000 m	2	High
		2000–3500 m	3	Moderate
		3500–5000 m	4	Low
		>5000 m	5	Very low
Temperature	7	<15°C	5	Very low
		15–17°C	4	Low
		17–19°C	3	Moderate
		19–21°C	2	High
		>21°C	1	Very high

Table 5: NDVI values for each land-use/land-cover types

Land-use/land-cover types	NDVI values
Irrigation	0.143
Water bodies	-0.075
Farmland	0.144
Plantation	0.245
Grassland	0.178
Bareland	0.148
Wetlands	0.103
Settlement	0.114
Bush and shrublands	0.188

3.8 Malaria risk levels of villages in Mecha district

All villages in the study area fall within the risk of malaria prevalence. One of the villages (Merawi town) fall in the very high malaria-risk area and the other villages are in the high to low levels of malaria-risk. Figure 8 shows the villages in the study area showing the levels of malaria-risk.

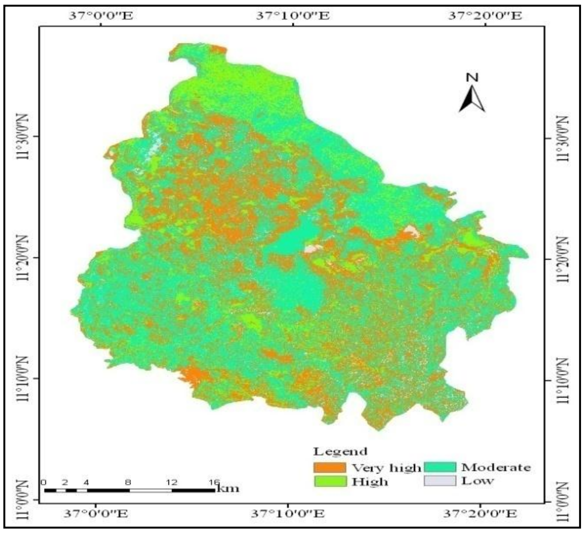

Figure 7: Element at risk map of malaria

Table 6: Characteristic of factors in relation to malaria risk area identification

Factors	**Weight**	**Rank**	**Degree of Vulnerability**
Hazard map	63	1 2 3 4	Very high High Moderate Low
Element at risk map	31	1 2 2 4	Very high High Moderate Low
Vulnerability map	6	2 3 4	Moderate Low Very low

Table 7: Summary of the results for malaria-risk and its layers

Type of area	**Area (km^2)**	**Area (%)**	**Degree of Vulnerability**
Malaria hazard map	46.77	0.31	Very high
	64504.51	43.25	High
	76446.74	51.26	Moderate
	8122.58	5.44	Low
Vulnerability map	1878.04	1.26	Moderate
	39794.21	26.68	Low
	107446.73	72	very Low
Element at risk map	48523.66	32.54	Very high
	21365.29	14.32	High
	75556.48	50.66	Moderate
	3673.56	2.46	Low
Final Malaria risk map	33.59	0.225	Very high
	69305.82	46.47	High
	76830.96	51.52	Moderate
	2948.61	1.97	Low

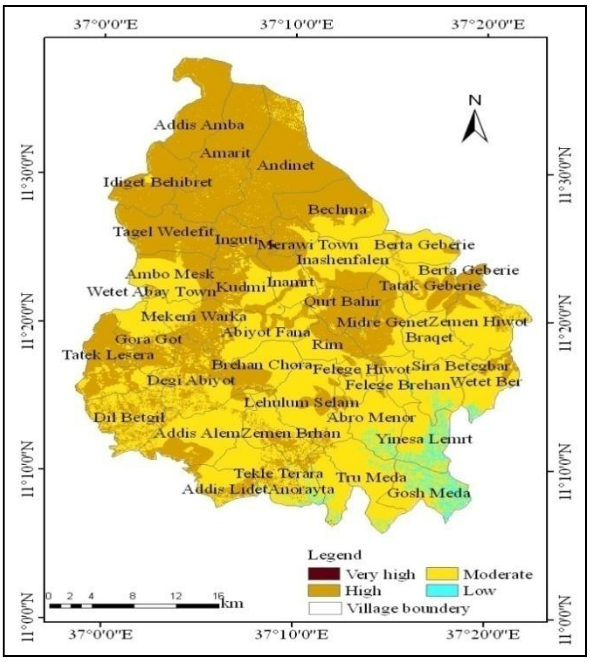

Figure 8: Malaria-risk map showing the status of villages in the study area

4. Discussion

The importance of GIS techniques is recognized in areas of disease prevalence and treatment (Carlos et al., 2010). The GIS-based malaria incidence mapping has been used for risk assessment at national, regional, and local levels in the context of resource allocation, management and to combat the disease (Saxena et al., 2009). Probability of the transmission of malaria to the present study area was determined by climatic, non-climatic and biological factors.

Areas near water bodies showed a low prevalence of malaria. There is no stagnation of water in the river. When there is heavy rain fall, mosquitoes cannot develop when the river flows fast in the absence of stagnant water bodies. However, in some areas, ponds are created close to the streams and rivers in order to store water for the dry season. Such ponds act as resourceful areas for mosquitoes to develop and contribute to increase malaria prevalence (Bautista et al., 2006). A negative association between distance from swampy areas and malaria-risk exists in the study area. It is already revealed that a strong positive association exists between malaria incidence and water bodies (Yihenew, 2007; Aster, 2010; Abdulhakim, 2013).

Higher elevation in general has long been recognized to be negatively associated with malaria due to its association with cooler temperatures that slows the development of anopheline vectors and the *Plasmodium* parasites they transmit (Patz et al., 2003). Malaria prevalence decreases with increase in altitude, particularly above 2000 m (Patz et al., 2003; Bautista et al., 2006). The present study shows higher negative correlation between monthly incidence of malaria and altitude (Yihenew, 2007; Yazoume et al., 2008).

Rainfall results in an increase in the prevalence of malaria as rains provide good breeding sites for the mosquito vectors (Stephen, 2006; Omukunda et al., 2013). The correlation coefficient for the association between monthly rainfall and monthly incidence of malaria was found greater than that for the association between other variables assessed. A rise in temperature enhances the survival chances of *Anopheles* mosquitoes and the *Plasmodium* and thus accelerates the transmission dynamics of malaria. There was a negative relationship between malaria and temperature during the months January to April and in August, when the study area had the minimum and maximum temperatures, respectively. Hence, an increase in temperatures does not mean an increase in the malaria transmission risk if this is accompanied by a decrease in rainfall. Although temperature favors *Plasmodium* to develop, lack of water prevents development of the vector.

The habitats of mosquitoes differ according to the vegetation and the nature of local environment. Land-use/land-cover types with plantation and bush lands have strong association with malaria indicating that this LU/LC may be a proxy for predictors of elevated malaria-risk (Richard and Poccard, 1998; Yasuoka and Levins, 2007; Ehlkes et al., 2014). The relationship of NDVI to Entomological Inoculation Rate (EIR) is highly correlated. The lower the NDVI value indicates the lower the vegetation level and the area is thought to be dry (Ceccato et al., 2005). The present results show high correlation between the incidence of malaria and vegetation due to the prevalence of high NDVI value as reported earlier (Oliveira et al., 2013; Ehlkes et al., 2014; Solomon et al., 2015).

In areas with low slopes, water tends to be logged, and such conditions accelerate chances for water stagnation. Absence of proper water drainage may lead to the creation of stagnant water pools, which in turn, encourages breeding and survival of mosquitoes (Thomson et al., 1999). The present study shows that slope gradient has negative influence on malaria incidence. This relationship could be attributed to the different slope types found on different geographic locations across the studied landscapes. The bottom areas characterized by flat or gentle slopes are mostly under swamps and water bodies. As slope increases from lower parts to middle and upper slopes, mosquito populations cannot sustain.

Presence of health institutions in a particular area is very important for treatment of patients, awareness creation and to implement preventive measures (Meron, 2010). These in turn influence the prevalence of disease in the locality. Absence and distant health institutions result in difficulties in accessibility and enhanced cost of treatment. Therefore, people who are near to health institutions are safer relative to those who are away from such centers. Identification of potential malaria-risk localities helps the health authorities to minimize expenditure. The present study shows negative correlation between monthly incidence of malaria and distance from health facilities. The relationship of distance from health stations and malaria incidence was statistically significant.

The high human population density has caused over-cultivation, and severe environmental manipulations leading to extensive drought and recurrent famine in many areas. This leads to more movement of people from one area to another resulting in transmission of malaria (Wakgari et al., 2006; Wiseman et al., 2006). Malaria-risk may increase in certain regions due to population movement by labor related to agriculture, mining, conflict and refugees (Martens and Hall, 2000). Work opportunities and resettlement programs in malaria endemic areas can easily attract a large number of people, making them vulnerable to the disease (Meron, 2010). Major environmental transformations like deforestation and new construction take place during resettlement, enhancing the proliferation of mosquito breeding sites, and result in malaria outbreaks (Martens et al., 1995; Kathleen, 2002; Aster, 2010). The present study shows strong positive correlation between monthly incidence of malaria and human population density.

Findings of the present study show that, a model-based malaria-risk map can be developed by establishing the relationship of various parameters using remote sensing and geographic information system. It also reveals that remote sensing and GIS techniques can be effectively used in mosquito larval habitat identification and risk area mapping. The risk area identification map indicates affected areas. The final malaria-risk map of the study area shows that the entire study area has malaria-risk factors. The study area falls under very high, high, moderate and low risk areas. The malaria-risk map developed can support decision makers to take precautions in space and time so as to control and manage malaria incidence.

Acknowledgements

The authors are grateful to the School of Earth Sciences, College of Natural and Computational Sciences, Addis Ababa University, Addis Ababa, for providing financial support to carry out this study.

References

Abdulhakim, A. (2013). GIS and remote sensing integrated for malaria risk mapping, Kersa, Ethiopia, MSc. Thesis. Teri University, New Delhi.

Ashenafi, M. (2003). Design and water management of irrigation systems to control breeding of anopheles mosquitoes. Case study: Hara irrigation project, Arba Minch, Ethiopia, MSc. Thesis, Wageningen University, Wageningen.

Aster, T. (2010). GIS and RS based assessment of malaria risk mapping for Boricha Woreda, Ethiopia, MSc. Thesis, Addis Ababa University, Addis Ababa.

Bautista, C.T., A.S. Chan, J.R. Ryan, C. Calampa, M.H. Ropers, A.W. Hightower and A.J. Magill (2006). Epidemiology and spatial analysis of malaria in the Northern Peruvian Amazon. American Journal of Tropical Medicine and Hygiene 75:1216−22.

Carlos, A.V., A.F. Julián, M.C. Zulma, R. Patricia, C.L. Myriam and D. Sofia (2010). Correlation between malaria incidence and prevalence of soil-transmitted helminthes in Colombia: An ecologic evaluation. Biomédica 30:501–508.

Ceccato, P., S. Connor and M.C. Thomson (2005). Application of geographical information systems and remote sensing technologies for assessing and monitoring malaria risk. Parassitologia 47: 81−96.

Dongus, S., D. Nyika, K. Kannady, D. Mtasiwa, H. Mshinda and U. Fillinger (2007). Participatory mapping of target areas to enable operational larval source management to suppress malaria vector mosquitoes in Dar es Salaam, Tanzania. International Journal of Health Geographics 6:37. doi:10.1186/1476-072X-6-37.

Ehlkes, L., C. Anne, B. Kreuels, R. Krumkamp and O. Adjei (2014). Geographically weighted regression of land cover determinants of *Plasmodium falciparum* transmission in the Ashanti Region of Ghana, International Journal of Health Geographics 13:13−35.

Erin, M., S. Jennifer, G. Katya, Y. Amrish, B. Teun, O. Wycliffe, K. Simon, D. Chris, A. Thomas, J.C. Smith and C. Nakul (2014). The cost effectiveness of malaria control interventions in the highlands of Western Kenya. PLoS One.; 9: e107700.

Hay, S.I., J.A. Omumbo, M.H. Craig and R.W. Snow (2000). Earth observation, geographic information system and Plasmodium falciparum malaria in sub-Saharan Africa. Advances in Parasitology 47:173–215.

Kathleen, W. (2002). A review of control methods for African malaria vectors. Environmental Health Project, Activity Report 108, U.S. Agency for International Development, Washington.

Kleinschmidt, I., B.L. Sharp, G.P.Y. Clarke, B. Curtis and C. Fraser (2001). Use of generalised linear mixed models in the spatial analysis of small area malaria incidence rates in KwaZulu Natal, South Africa. American Journal of Epidemiology 153:1213−21.

Kleinschmidt, I., J. Omumbo, O. Briët, N. Van de Giesen, N. Sogoba and N.K. Mensah (2001). An empirical malaria distribution map for West Africa. Trop Med Int Health 6:779–86.

Martens, P. and L. Hall (2000). Malaria on the move: Human population movement and malaria transmission. Emerging Infectious Diseases 6:103−109.

Martens, W.J., L.W. Niessen, J. Rotmans, T.H.Jetten and A.J. McMichael (1995). Potential impact of global climate change on malaria risk. Environmental Health Perspective 103:458−64.

Meron, M. (2010). Web GIS in decision support to control malaria: Case study in TiroAfetaWoreda, Oromia Region, Ethiopia, MSc. Thesis, Addis Ababa University, Addis Ababa.

Oliveira, E.C., E.S. Santos, P. Zeilhofer, R. Souza-Santos and M. Atanaka-Santos (2013). Geographic information systems and logistic regression for high-resolution malaria risk mapping in a rural settlement of the southern Brazilian Amazon. Malaria Journal, doi:10.1186/1475-2875-12-420.

Omukunda, E., A. Githeko, M.F. Ndong, E. Mushinzimana and G. Yanr (2013). Effect of swamp cultivation on distribution of anopheline larval habitats in Western Kenya. Journal of Vector Borne Disease 49: 61–71.

Palaniyandi, M. (2012). The role of remote sensing and GIS for spatial prediction of vector-borne diseases transmission. Journal of Vector Borne Disease 49: 197–204.

Patz, J.A., A.K. Githeko, J.P. McCarty, S. Hussein, U. Confalonieri and N. Wet (2003). Climate change and infectious diseases. Climate Change and Human Health: Risks and Responses103–137.

Richard, Y. and I. Poccard (1998). A statistical study of NDVI sensitivity to seasonal and inter- annual rainfall variations in Southern Africa. International Journal of Remote Sensing 19:2907–2920.

Saxena, R., B.N. Nagpal, A. Srivastava, S.K. Gupta and A.P. Dash (2009). Application of spatial technology in malaria research & control: Some new insights. Indian Journal of Medical Research 130:125−132.

Sithiprasasna, R., W.J. Lee, D.M. Ugsang and K.J. Linthicum (2005). Identification and characterization of larval and adult anopheline mosquito habitats in the Republic of Korea: Potential use of remotely sensed data to estimate mosquito distributions. International Journal of Health Geographics 4:1−11.

Solomon, N., K.V. Suryabhagavan and E. Gadisa (2015). Visceral Leishmaniasis (Kala-Azar) risk mapping using geo-spatial tools: A case study in Kafta Humera district, North Western Ethiopia, International Journal of Geoinformatics 11:21−26.

Stephen, M. (2006). Landscape determinants and remote sensing of mosquito larval habitats in the high land of Kenya. American Journal of Tropical Medicine and Hygiene 74:69−75.

Thomson, MC., S.J. Connor, U. D'Alessandro, B. Rowlingson, P. Diggle, M. Cresswell, C. Dark and G. Brian (1999). Predicting malaria infection in Gambian children from satellite data and bed net use surveys: The importance of spatial correlation in the interpretation of results. American Journal of Tropical Medicine and Hygiene 61:2–8.

Wakgari, D., A. Ahmed and B. Yemane (2006). The interplay between population dynamics and malaria transmission in Ethiopia. Ethiopian Journal of Health Development 20:137−144.

Wiseman, V.B., L. McElroy and W. Conteh (2006). Malaria prevention in the Gambia: Patterns of expenditure and determinants of demand at the household level. Tropical Medicine and International Health 11:419–431.

Yasuoka, J. and R. Levins (2007). Impact of deforestation and agricultural development on Anopheline ecology and malaria epidemiology. America Journal of Tropical Medicine and Hygiene **7**6:450–460.

Yazoume, Y., S. Osman, K. Bocar and S. Rainer (2008). Environmental factors and malaria transmission risk: Modelling the risk in a holoendemic area of Burkina Faso. Ashgate Publishing Ltd., Surrey.

Yihenew, A. (2007). Irrigation and socio-economic factors related to malaria transmission in Ziway. M.Sc Thesis, Addis Ababa University, Addis Ababa.

Journal of Geomatics Vol 10 No. 1 April 2016

Object based classification techniques for citrus orchards

Kadapala Bharath Kumar Reddy[1], J. Mohammed Ahamed[2], R. Hebbar[a], Uday Raj[2] and Rama Rao[1]
[1]Indian Institute of Space Science and Technology, Thiruvananthapuram, Kerala, India
[2]RRSC – South, National Remote Sensing Centre, Bengaluru, Karnataka, India
Email: bharathkadapala@gmail.com, (mohammedahamed_j, hebbar_kr, uday_raj)@nrsc.gov.in

(Received: Mar 02, 2016; in final form: Apr 13, 2016)

Abstract: Cultivation of citrus orchards is characterized by small field size, sparse distribution with different age groups and coexisting spectrally similar crops. Thus, classification of citrus crop using satellite data is quite challenging. The present study was carried out to evaluate object based classification techniques for mapping citrus orchards located at Indi hobli of Bijapur district, Karnataka state. Two date LISS-IV and single date Cartosat-1 data were used for classification. Spectral signature of young orchards less than 5 to 6 years and poorly managed orchards were mixed with pomegranate, sugarcane and grape orchards. Two approaches of segmentation techniques namely, threshold & clump and lambda schedule, were tested. The results revealed that the single date satellite data showed classification accuracy (around 75%) using both threshold and clump and lambda schedule segmentation approach. Inclusion of second date data along with vegetation indices significantly improved the mapping accuracy (around 85%) by eliminating short duration crops from evergreen citrus orchards. The study explored the potential use of high resolution data for inventory of citrus orchards and the methodology could be refined for operational application using textural and contextual information.

Keywords: Object based image analysis, Full lambda schedule Segmentation, Threshold and clumping, Citrus, Brovey transform

1. Introduction

Image classification is perhaps the most important part of digital image analysis. It is very nice to have a "pretty picture" or an image, showing a magnitude of colors illustrating various features of the underlying terrain, but it is quite useless unless it is known what the colors mean (Korgaonkar, 2012). The data obtained through remote sensing satellites has huge applications in the fields of agriculture, urban modeling, disaster management etc. For all these applications a well classified data is required i.e., image classification has to be carried out in order to group all the pixels into several land cover classes and this further can be used according to user needs.

1.1 Classification methods

Classification methods can be mainly categorized into two types namely:

1. Pixel based classification
2. Object based classification

1.1.1 Pixel based classification: The pixel based methods use the digital number associated with the pixel in order to assign it to a specific class *i.e.*, the spectral information of the pixel is used for the classification. There are mainly two methods in pixel based classification methods, Supervised and Unsupervised classification.

1.1.2 Object based classification: The object based image analysis (OBIA) or specifically Geographic Object Based Image Analysis (GEOBIA) when it comes to satellite images delineate readily usable objects from imagery while at the same time combining image processing and GIS functionalities in order to utilize spectral, texture and contextual information in an integrative way(Blaschke, 2010). Dissatisfaction of using pixels solely in the classification has been mentioned long back (Cracknell, 1998). Spectrally similar but compositionally different land cover may be misclassified. Similarly, the spectral heterogeneity of the land cover can lead to rogue pixels appearing within classes creating a 'salt and pepper' effect. In addition to this, the increased application of higher resolution imagery is problematic as it is difficult to classify accurately using traditional pixel-based methods. The increased amount of spatial information often leads to an inconsistent classification of pixels(Whiteside, 2005). In GEOBIA the spatial information in the neighborhood is also considered which allows increasing the dimensionality of the feature space of a pixel when compared to the traditional pixel based methods where, only spectral values of the pixel are used in the feature space and hence giving us the more reliable results than those methods. Hence, in this study the object based classification methods were evaluated to identify the best object based method in mapping citrus orchards.

2. Data used

Multi-spectral images of LISS IV camera and CARTOSAT data were used. Indi taluk of Bijapur District, Karnataka was identified for the study. This taluk is located with the following boundaries of coordinates: Upper bound ULX: 75° 43'36.13", ULY: 17° 0' 20.49" and Lower bound LRX: 76° 03'3.16" LRY: 16° 56'17.04". The dominant crop is Citrus with small amount of grapes, sugarcane and other crops grown in the region.

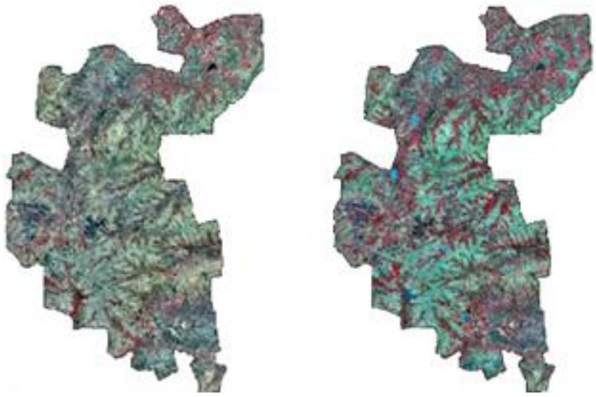

Figure: 1a) LISS IV May Figure: 1b) LISS IV November

Classification was done classification for the data obtained in the month of May (figure 1a) and also using the stacked data of May and November. Summer crops get harvested in the month of May and monsoon crops get harvested in the month of November (figure 1b). Therefore, these two months data was used to exclude seasonal crops as much as possible in the images.

LISS IV sensors have three bands with a spatial resolution of 5.8 m. CARTOSAT-1 panchromatic has one broad band with very good spatial resolution—2.5 m. Combining these two images to yield a three band data set with 2.5 m resolution provides the best characteristics of both sensors (NRSC, 2004).

Brovey Transform was used to merge the two data sets. The Brovey Transform was developed to visually increase contrast in the low and high ends of an image's histogram (*i.e.*, to provide contrast in shadows, water and high reflectance areas such as urban features). Consequently, the Brovey Transform should not be used if preserving the original scene radiometry is important. However, it is good for producing RGB images with a higher degree of contrast at the tails of the image histogram.

Our objective was to perform a binary class classification for the identification of Citrus orchards in the given area. Object based analysis of the image was carried out to identify the citrus orchards and mark all the other regions as the background.

3. Methodology and work flow

In ERDAS imagine, Objective Workstation was used. The first step was pixel level binary classification of the image and assigns probability for each and every pixel depending on how close it is to Citrus class. For this step sixtyfour training samples were given from both Citrus and Non Citrus equally covering all the variations. The next step *i.e.*, objects formation step which is an important step in the analysis. Two different methods were followed to create objects in this step. One was segmentation using full lambda schedule and the second was threshold and Clump.

3.1 Segmentation using full lambda schedule

This method iteratively merges adjacent segments based on a combination of spectral and spatial information. Merging occurs when the algorithm finds a pair of adjacent regions, *i* and *j*, such that the merging cost $t_{i,j}$ is less than a defined threshold lambda value:

$$t_{i,j} = \frac{\frac{|O_i|.|O_j|}{|O_i| + |O_j|}.\left\|u_i - u_j\right\|^2}{length(\partial(O_i, O_j))} \quad 1$$

where,

O_i is the area of region *i*.

Oj is the area of region *j*.

u_i is the average value in region *i*.

u_j is the average value in region *j*.

$\left\|u_i\text{-}u_j\right\|$ is the Euclidean distance between the spectral values of regions *i* and *j*.

length($\partial(O_i,O_j)$) is the length of the common boundary of O_i and *Oj* (Robinson, 2002).

While not necessarily derived from the Pixel Probability Layer, the raster object segments will have the zonal mean pixel probabilities as attributes. Output from the Probability Pixels to Raster Objects Operator contains pixels that are grouped as raster objects which have associated probability attributes (Erdas, 2013).

3.2 Threshold and clumping

This operator performs a threshold operation on a pixel probability layer which keeps only pixels with a probability greater than or equal to the threshold value specified. It converts the pixels to binary values (0's and 1's), then performs a contiguity operation (clump) on the binary values of 1(Imagine Objective, 2010).

Now the objects formed were edited from the above two methods by applying filters over the objects to refine the results. Focal filter was used in the beginning to make the object edges sharp and remove very narrow strips from the objects formed. This filter replaces the most repeating value in the window of specific size around the pixel. The optimum value for this was found to be 3. The next filter used was probability filter which removes the objects of lower probability and gives us more reliable objects after filtering. Later size filter was used to filter out very small objects. Finally, re-clump filter was used on objects to form bigger objects. Raster to vector conversion was made using polygon tracing and later two more filter are applied on the vector objects. The smoothening filter which eliminates the sharp edges of objects and the island filter takes out island like gaps in the formed objects were used in post processing operation. The work flow is pictorially represented in a flowchart in the Appendix-1.

4. Results and discussions

The main aim of the entire process was to classify the mature citrus orchards. It can be seen how different parameter sets (Table 1) had performed in citrus dominant and non-citrus dominant regions from images shown (Figure 2a, 2b).

Journal of Geomatics Vol 10 No. 1 April 2016

It was also observed that few parameter sets had classified the citrus very well in its dominant region but there was a lot of misclassification in the non-citrus dominant region. Two different assessment methods were used to calculate accuracy. The first method is from area estimation based on the actual data obtained from the government statistics. This method might not give precise idea about which method had the best performance because if some non- citrus dominant regions are classified as citrus and vice-versa, it may match the reported area even though spatially the classification was incorrect. The area accuracy results of this method are mentioned in table 1. To overcome the above mentioned problem the second method, i.e., Point based assessment was carried out. Here, random points were generated with 30samples per class. Later analysis was carried out to identify correctly classified samples using ground based GPS locations. The results of this assessment method are described in the form of confusion matrix (Table 2). It can be seen that highest accuracy of 85.07 per cent was observed for the set 11 in which NDVI was a stacked along with multi-data data using lambda schedule segmentation.

Table 1: Object creation methods, parameters used and respective area statistics and accuracy obtained in identifying citrus orchards

Single Date/ Multi Date	Object Creation Method	No.	Spectral	Texture	Size	Shape	Probability Threshold	Estimated area (ha)	Mapping Accuracy (%)
Single Date	Segmentation- Lambda Schedule	Set1	0.8	1	0.1	0.05	NA	2490	61.81
		Set2	0.6	1	0.15	0.05	NA	1146	63.59
		Set3	0.6	1	0.15	0.05	NA	1140	63.27
	Threshold/ Clump	Set4	NA	NA	NA	NA	0.95	1888	95.24
		Set5	NA	NA	NA	NA	0.9	1152	63.91
		Set6	NA	NA	NA	NA	0.95	1557	86.40
Multi Date	Segmentation- Lambda Schedule	Set7	0.5	1	0.02	0.02	NA	843	46.79
		Set8	0.6	1	0.15	0.05	NA	1402	77.79
		Set9	0.8	1	0.15	0.05	NA	1411	78.30
	Threshold/ Clump	Set10	NA	NA	NA	NA	0.9	1460	81.03
Multi Date + NDVI	Segmentation- Lambda Schedule	Set11	0.7	1	0.15	0.05	NA	1440	79.90

4.1 Lambda schedule segmentation (single date)

In raster object operation (ROO) process the probability filter values were tested iteratively from 0.45 to 0.8. The optimized value for probability filter was found to be 0.6 for lambda schedule and 0.7 for the Threshold and Clump process. For Lambda Schedule it was observed that by giving 0.7 as probability filter value area under citrus drastically changed resulting in under classification and decreasing it to 0.5, resulted in misclassifying non-citrus regions. Hence the optimum value for this parameter was found to be 0.6. In threshold and clump method the value was increased to 0.7 because in this step, only high probable pixels were taken into account in the raster object creation (ROC) step itself which precedes ROO step in segmentation. Hence, higher values were needed to be kept as cut-off for probability filter.

The set 1 estimated the area as 2490 hectares and overall accuracy was 73.13 per cent. But it was observed that a lot of non-citrus regions were classified as citrus orchards. Hence, changes were made in probability filter in ROO step and spectral value in ROC step by increasing the probability filter value to 0.6 and reducing the spectral value to 0.6, which gave very less area estimate 1146 hectares as compared with 1800 hectares of reported area. However, misclassification of non-citrus regions was reduced.

4.2 Threshold and clump segmentation (single date)

In threshold and clump the threshold probability in ROC was initially set to be 0.95 (table 2) and probability value of 0.6 in ROO, which resulted in smaller object size and misclassification of non-citrus segments. Even though the area estimated looked very precise (95.24 per cent) spatially there was significant misclassification. Hence, the probability filter value in ROO step was increased to 0.8 which reduced the misclassification. It also had smaller segments of objects existing adjacently which could join to form a bigger object if threshold in the object formation step is reduced. To achieve this, there was a need to decrease probability value in ROC. Hence, two changes were made i.e., the threshold probability was set to 0.9 and probability filter in ROO was set to 0.7.

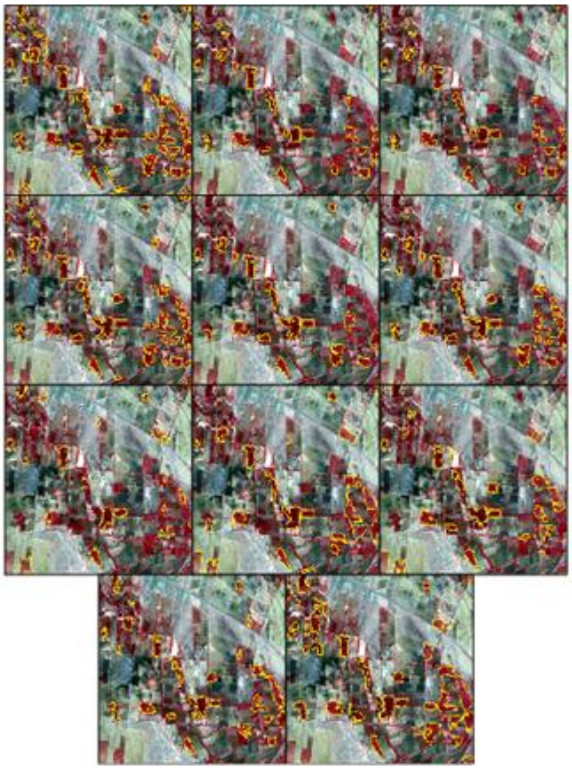

Figure 2a

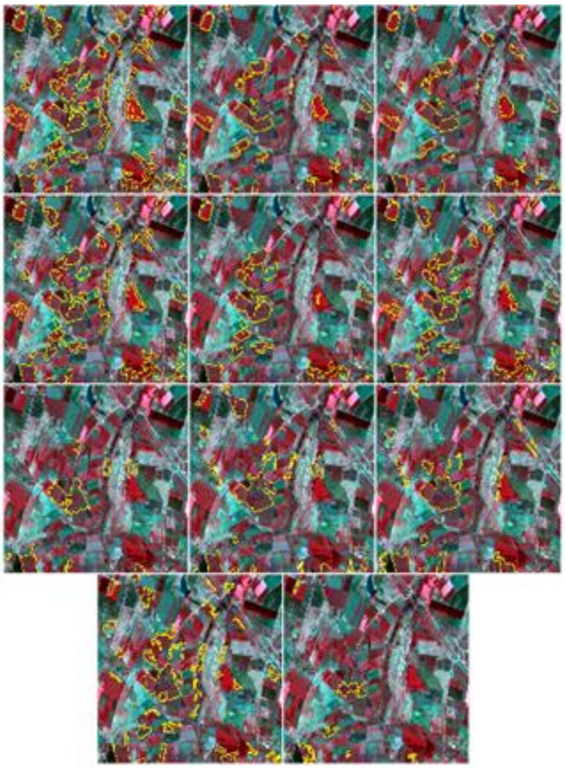

Figure 2b

Figure 2: From top left to bottom right in each of the figures show the classification results for 11 parameter sets from (a) citrus dominant region; and (b) non-citrus dominant region

Table 2: Table of confusion matrices for selected sets using point based assessment method

Lambda Schedule (Set 1)				Threshold and Clump(Set 5)			
	Citrus	Non citrus	Total Classified		Citrus	Non citrus	Total classified
Citrus	31	15	46	Citrus	27	11	38
Non citrus	3	18	21	Non Citrus	7	22	29
Total samples taken	34	33		Total samples taken	34	33	
Accuracy	91.17 %	54.55%	**73.13%**	Accuracy	79.41 %	66.67%	**73.13%**
Lambda Schedule (Set 2)				Lambda Schedule (Set 9)			
	Citrus	Non citrus	Total classified		Citrus	Non citrus	Total classified
Citrus	28	10	38	Citrus	29	9	38
Non citrus	6	23	29	Non Citrus	5	24	29
Total samples taken	34	33		Total samples taken	34	33	
Accuracy	82.35 %	69.70%	**76.12%**	Accuracy	85.29 %	72.72%	**79.10%**
Threshold and Clump (Set 10)				Lambda Schedule (Set 11)			
	Citrus	Non citrus	Total classified		Citrus	Non citrus	Total classified
Citrus	30	12	42	Citrus	31	6	37
Non citrus	4	21	25	Non Citrus	4	26	30
Total samples taken	34	33		Total samples taken	34	33	
Accuracy	88.23 %	63.63%	**76.12%**	Accuracy	91.14 %	78.90%	**85.07%**

The best methods in the two types of algorithms using single date data had accuracies around 76.12 per cent for lambda schedule segmentation (set 2 of table 2) and 73.13 per cent (set 5 of table 2) for threshold and clump method of segmentation. Hence there is a need to increase the feature space to capture the seasonal variability of crops and improve the classification. The data for the month of November was added which gave us better results (set 9 and 10 of table 2) compared to above mentioned single date classification methods.

4.3 Multi-date and multi-date with thematic layer included

Classification carried out using multi-date data, set 9 and set 10 (table 2) reduced the misclassification. Overall accuracy was 79.1 and 76.12 per cent respectively. The results of both the methods were observed and found that threshold clump method of segmentation had more misclassification occurring in non-citrus regions. This was observed clearly in the second accuracy assessment (Table 2). Also it was observed that threshold and clump method had unusual shaped objects. However, lambda schedule segmentation method reduced the misclassification significantly and the boundary shape of the objects created matched the field boundaries. Therefore, by considering the above factors into account lambda schedule segmentation method was used to include one more additional layer (Set 11 of table 1) of Normalized difference vegetation index (NDVI) to further attempt in improving the classification accuracy.

Since NDVI layer describes additional spectral information, iteratively a value of 0.7 was selected as spectral weightage instead of 0.8 which performed better by reducing misclassification with multi-date data. A lot of misclassification were removed which is desired. It was observed that temporal data with additional NDVI as a layer included in classification using lambda schedule segmentation significantly reduced the misclassification and also increased the mapping accuracy 79.9 per cent (table 1).

5. Conclusion and limitations

From the above results it was observed that lambda schedule segmentation algorithm worked well as a raster object creation method with multi-date data and when the data was combined with NDVI which adds the additional spectral information the results were enhanced. Although through the first assessment method where only total area is taken into consideration threshold and clumping method shows an accuracy of over 95.24% for set 4, however when checked with ground based GPS points, misclassification was clearly observed (table 2). Similar reason can also be concluded for other methods using different parameter sets. Even in the set 11 where NDVI was used along with multi-date data, it was observed that trees along the road side and clusters of trees were classified as citrus.

This method is applicable only to the mature Citrus orchards at this resolution limits. A similar attempt was made on young citrus plants too but unconvincing results were observed because of the resolution of this data as young citrus plants get mixed-up with other orchards. The young plants were not identifiable in the data; they looked similar to other fallow lands which made the method specific for mature orchards at this level of resolution.

Further this work can be validated by using this technique in dominant citrus growing regions in India. Use of higher resolution data products may enhance the classification accuracy. Reported statistics from state departments include both mature and young citrus orchards. Since, the classification technique targeted on mature citrus orchards, area estimated by this technique might be on par with the reported data.

References

Blaschke, T. (2010). Object based image analysis for remote sensing. ISPRS Journal of Photogrammetry and Remote Sensing, 1-6.

Blaschke T. and J. Stroble (2001). What's wrong with pixels? Some recent developments interfacing remote sensing and GIS, *GIS-Zeitschrift für Geoinformationsysteme* 6:12-17.

Cracknell, A. (1998). Synergy in remote sensing — what's in a pixel? International Journal of Remote Sensing, 2025–2047.

Crisp, D.J. P. Perry and N.J. Redding (2002). Fast segmentation of large images. Edenberg, South Australia: Defence Research and Surveillance & Reconnaisanse Division,*DSTO Electronics and Surveillance Research Laboratory.*

Erdas (2010). IMAGINE Objective. Norcross, USA: ERDAS Inc.

Erdas (2013). Erdas Field Guide.

Korgaonkar, G.S., R.R.Sedamkar and K. Bhandari (2012). Hyperspectral image classification on decision level fusion. International Journal of Computer Applications (IJCA), 1-2.

NRSC (2004). IRS-P6 data user's Manual. Hyderabad.

Robinson, D. J. (2002). Implementation of a fast algorithm for segmenting SAR imagery. Edinburgh, South Australia, Australia: DSTO Electronics and Surveillance Research Laboratory.

Whiteside, T. and W. Ahamad (2005). A comparison of object-oriented and pixel-based methods in northern

Australia. Proceedings of SSC2005 Spatial intelligence, innovation and praxis: The national biennial Conference of the Spatial Sciences Institute, September 2005. Melbourne: Spatial Sciences Institute.

APPENDIX – 1

(Flowchart describing the methodology adopted in identification of citrus orchards)

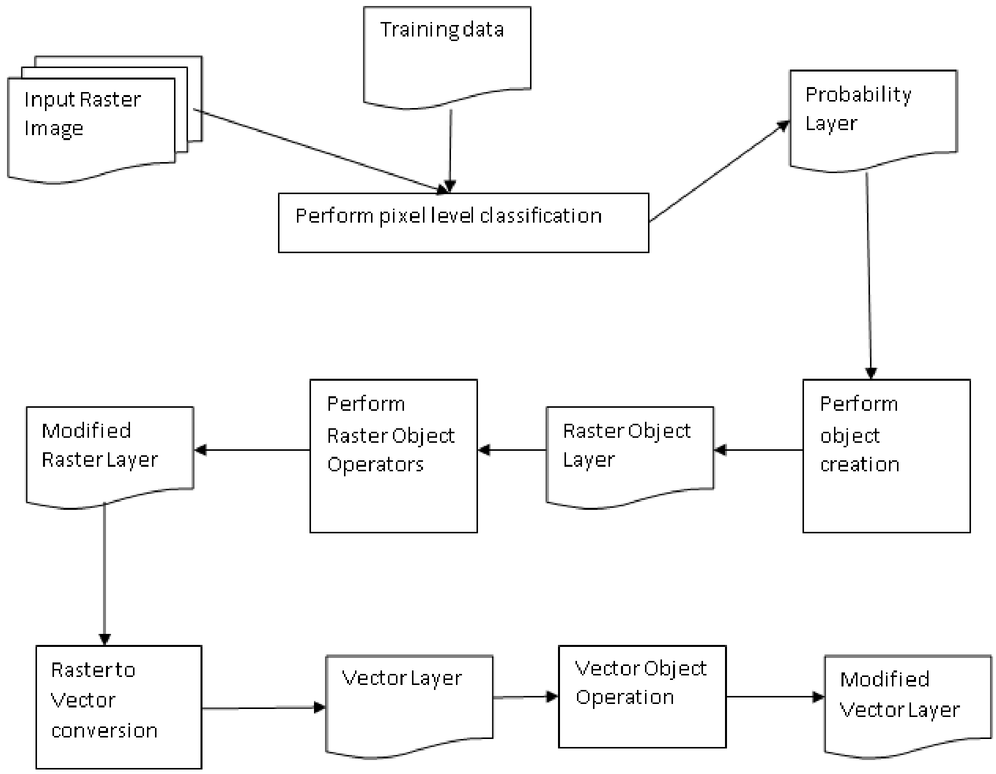

Journal of Geomatics Vol 10 No. 1 April 2016

Evaluation of predictive ability of support vector machines and naive Bayes trees methods for spatial prediction of landslides in Uttarakhand state (India) using GIS

Binh Thai Pham[1,2], DieuTien Bui[3], Indra Prakash[4] and M.B. Dholakia[1]

[1]Department of Civil Engineering, Gujarat Technological University, Ahmedabad - 382424, India
[2]Department of Geotechnical Engineering, University of Transport Technology, Hanoi, Vietnam
[3]Geographic Information System Group, Department of Business Administration and Computer Science, Telemark University College, HallvardEikasPlass 1, N-3800 BøiTelemark, Norway
[4]Bhaskarcharya Institute for Space Applications and Geo-Informatics (BISAG), Gandhinagar, India
Email: phambinhgtvt@gmail.com or binhpt@utt.edu.vn

(Received: Feb 11, 2016; in final form: Mar 29, 2016)

Abstract: The main objective of this study is to apply and evaluate the predictive capability of the Support Vector Machines (SVM) and Naïve Bayes Trees (NBT) methods for spatial prediction of landslides in a part of Uttarakhand state (India). SVM is one of the most efficient machine learning methods that has been applied widely in landslide prediction whereas NBT has not been applied for landslide problems. In these models, a total of 430 historical landslide locations have been first identified to construct landslide inventory map. Landslide locations have been split randomly into two parts to generate training dataset (70% landslide locations) and testing dataset (30% landslide locations). Secondly, landslide affecting factors such as slope angle, slope aspect, elevation, plan curvature, lithology, soil, land cover, distance to roads, distance to rivers, distance to lineaments, and rainfall have been selected to assess the spatial relationship with landslide occurrences. The predictive capability of these factors has been evaluated using the Gain Ratio method. Using training dataset, the SVM and NBT models have been constructed to assess the susceptibility of landslide occurrences. Finally, the performance of the SVM and NBT models have been validated and compared using receiver operating characteristic curve technique and statistical index-based evaluations. The results show that both the SVM and NBT models perform well for spatial prediction of landslides. Out of these, the SVM model (AUC = 0.881) outperforms the NBT model (AUC = 0.832). Overall, SVM and NBT indicate promising methods which could be used for spatial prediction of landslides in landslide prone areas. Moreover, the results obtained from this study could be helpful for planning and decision making in landslide hazard management.

Keywords: Landslides, GIS, Support vector machines, Naïve Bayes trees

1. Introduction

Landslide is one of the most devastating natural disasters causing loss of human life and properties all over the world. India is known as one of the most affected countries by landslides in Asia (Guha-Sapir et al., 2014). Approximately 300 people die and 46 USD millions in properties loss every year in India (GSI, 2009). Most of landslides (about 80%) have occurred in Himalayan area (Onagh et al., 2012). Landslide studies have been turning into urgent tasks not only in India but also all over the world in order to reduce their harmful impaction to human life.

Spatial prediction of landslides is the probability of potential instability of slopes related to a set of casual factors (Guzzetti et al., 2005). It can be carried out by analyzing the spatial relationship between past landslide events and a set of geo-environmental factors. It is based on an assumption that future landslides will occur under same conditions with previous landslides (Ermini et al., 2005). Landslide susceptibility map is a final outcome of spatial prediction of landslides. It helps in land use planning and decision making for landslide hazard management (Pham et al., 2015a; Wang et al., 2009). To produce this map, Geographic Information System (GIS) is known as standard tool for integration of different types of data collected from various sources.

Many methods have been applied for spatial prediction of landslides using GIS in recent decades. These methods are based on main approaches (i) expert opinion-based approach and (ii) data mining based approach (Song et al., 2012). Expert opinion-based approach is subjective because it is based on the perspective of experts in selecting variables and assigning weights to variables. On the other hand, data mining based approach is objective as it uses machine learning algorithms to determine factors leading to landslide occurrences and calculate weights of the factors during learning of models. Out of these approaches, data mining based approach is more commonly utilized for spatial prediction of landslides. Common machine learning methods are logistic regression (Devkota et al., 2013; Lucà et al., 2011), decision tree (Pradhan, 2013; Yeon et al., 2010), artificial neural network (Choi et al., 2010; Zare et al., 2013) and support vector machines (Kavzoglu et al., 2014; Pradhan, 2013). In addition, Naïve Bayes Trees (NBT) is also an efficient machine learning technique that has been applied successfully in other fields but landslide problems.

In the present study, Support Vector Machines (SVM) and NBT methods have been applied and compared for spatial prediction of landslides. A small portion of Uttarakhand state, India had been selected as the study area. Receiver Operating Characteristic (ROC) curve method and statistic index-based evaluations have been used to validate and compare these landslide models. The analysis process has been done by using GIS application and Weka 3.7.12 software.

2. Description of study area

The study area lies between TehriGarhwal district and PauriGarhwal district of Uttarakhand state in India (longitudes 78º29'01'E to 78º37'06''E and latitudes 29º56'38''N to 30º09'37''N) covering an area of about 323.815 km² (Fig. 1). The study area is situated in subtropical monsoon region. The highest temperature is about 45°C in summer season whereas the lowest temperature is around 1.3°C in winter season. The humidity varies from 25% to 85%. Heavy rainfall often occurs in monsoon season (June to September) with annual average rainfall ranging from 770mm to 1684mm.

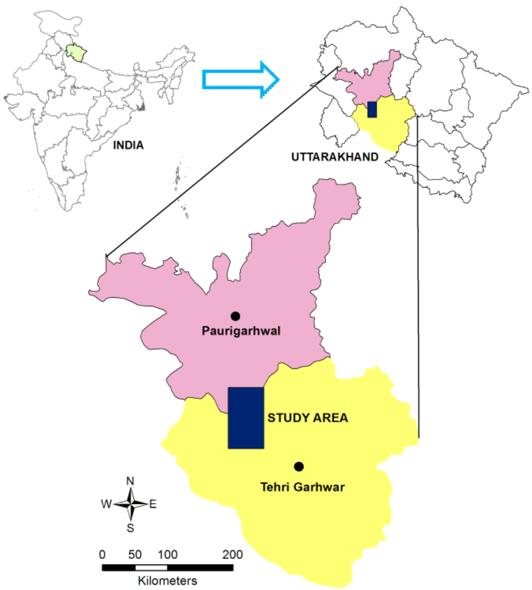

Figure 1: Location of the study area

Topographically, the study area is occupied by high mountains and intervening deep valleys (Pham et al., 2015b). Elevation ranges from 380m to 2180m (above mean sea level) with average elevation of 1081m. Slope angles are relatively steep up to 70 degrees. Slope angles of 15 to 45 degrees occupy the largest area (85.45%).Geologically, six lithological groups have presented in this study area namely Amri group (quartzite, phyllite),Blaini and Krol group (boulder bed and limestone), Bijni group (quartzite, phyllite), Jaunsar group (phyllite and quartzite), Manikot shell limestone (limestone), Tal group (sandstone, shale, quartzite, phyllite, and limestone) (Pham et al., 2015b). Baliana and Krol group and Bijni group are dominant with 30.1% and 28.1% of the study area, respectively. There are two types of soils in this study area viz., silty and loamy. Loamy soil occupies 73.73% of area.

Land cover in this study includes four categories such as dense forest, open-forest, non-forest, and scrub land. Non-forest is the dominant land cover (39.02%).

3. Methodology

Methodology of this study includes four main steps (i) constructing database for spatial prediction of landslides, (ii) evaluating predictive capability of landslide affecting factors, (ii) constructing landslide models (SVM, NBT) to assess landslide susceptibility, (iii) evaluating landslide models, (iv) constructing landslide susceptibility maps using Geo-informatics technology.

3.1. Data collection and interpretation

3.1.1. Landslide inventory map: Landslide inventory map is a compilation of landslide locations that have been occurred in the past and present. It is one of the most important data for spatial prediction of landslides. In the study area, many landslides occur every year (Onagh et al., 2012). By interpretation of Google Earth images using Google Earth pro 7.0, a total of 430 landslide location has been identified based on morphology and texture of past landslides to construct landslide inventory map (Fig. 2). These landslide locations have been evaluated in comparison with historical landslide reports, newspaper records and extensive field investigation. Subsequently, 70% landslide inventory (301 locations) has been used to construct training dataset for building landslide models whereas 30% remaining landslide inventory (129 locations) has been utilized to build testing dataset for validating landslide models.

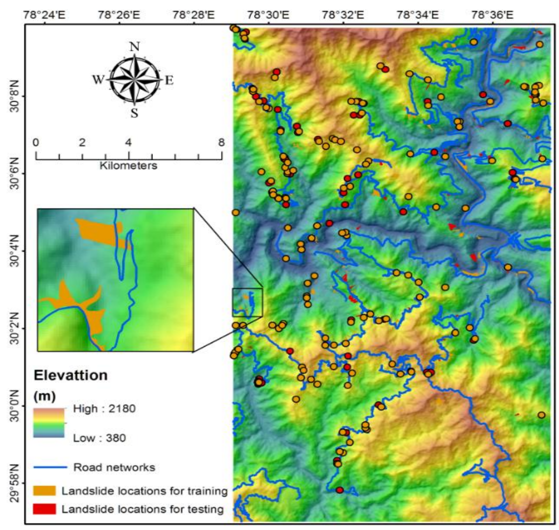

Figure 2: Landslide locations and elevation map of the study area

3.1.2. Landslide affecting factors: Landslides in the study area usually occur under various conditions such as geological activities, rainfall, geomorphological characteristics, vegetation, human activities (Sarkar et al., 1995; Sengupta et al., 2010). Based on the mechanism of landslide occurrences and geo-environmental characteristics of the study area, eleven landslide affecting factors (slope angle, slope aspect, elevation, plan curvature, lithology, soil, land cover, distance to roads, distance to rivers, distance to lineaments, and rainfall) have been selected to assess the spatial relationship between them and landslide occurrences for spatial prediction of landslides.

Maps of these landslide affecting factors have been generated using GIS application. Specifically, slope angle map (Fig. 3a), slope aspect map, curvature map, and elevation map have been extracted from DEM with 20 m resolution generated from ASTER Global DEM collected from United States Geological Survey (http://earthexplorer.usgs.gov). Lithological map (Fig. 3b) has been extracted from state geological map on a scale of 1:1000000. Land cover map (Fig. 4a) has been extracted from state land cover map at a scale of 1:1000000 (http://www.ahec.org.in/wfw/maps.htm). Soil map (Fig. 4b) has been generated from state soil map at a scale of 1:1000000. Rainfall map has been constructed using meteorological data for 30 years from 1984 to 2014 (NCEP, 2014). Distance to roads map has been constructed by buffering road networks on the high slopes (larger than 15 degrees) in the study area. Distance to rivers map has been generated by buffering river networks on the high slopes (larger than 15 degrees) in the study area. Distance to lineaments map has been constructed by buffering lineament network generated from Landsat-8 sattelite image in the study area. Eleven landslide affecting factors and their classes is shown in Table 1.

3.2. Methods for spatial prediction of landslides

3.2.1. Support vector machines (SVM): SVM was first proposed by Vapnik (1995) that is one of the most effective machine learning techniques for classification (Kavzoglu et al., 2014). It is based on the statistical learning theory in order to find an optimal hyper-plane in separating two classes for classification (Tien Bui et al., 2015). SVM can be trained in two main steps (i) the original input space is first mapped into a high-dimensional feature space, (ii) the optimal hyper-plane in the feature space is determined by maximizing the margins between classes (Abe, 2005).

The performance of the SVM method depends significantly on the choice of the kernel function (Dixon and Candade, 2008). According to Tien Bui et al. (2012), Radial Basis Function (RBF) is one of the most widely used in landslide models among kernel functions. Therefore, RBF has been selected in this study in training SVM. In addition, two calculating parameter of radial basis function kernel have been optimized to obtain the best performance of the SVM model such as regularization parameter (C = 0.1) and kernel width (γ = 1).

Table 1: Landslide affecting factors and their class utilized in this study

No.	Landslide causal factors	Classes
1	Slope angle (degree)	(1) 0-8; (2); (3) 8-15; (4) 15-25; (5) 25-35; (6) 35-45; (7)> 45
2	Slope aspect	(1) flat[-1]; (2) north [0-22.5 and 337.5-360]; (3) northeast [22.5-67.5]; (4) east [67.5-112.5]; (5) southeast [112.5-157.5]; (6) south [157.5-202.5]; (7) southwest [202.5-247.5]; (8) west [247.5-292.5]; (9) northwest [292.5-337.5]
3	Elevation (m)	(1) 0-600; (2) 600-750; (3) 750-900; (4) 900-1050; (5) 1050-1200; (6) 1200-1350; (7) 1350-1500; (8) 1500-1650; (9) 1650-1800; (10) > 1,800
4	Curvature	(1) concave (<-0.05); (2) flat (-0.05-0.05); (3) and convex (> 0.05)
5	Lithology	(1) Amri group [quartzite, phyllite], (2) Blaini and Krol group [boulder bed and limestone], (3) Bijni group [quartzite, phyllite]; (4) Jaunsar group [phyllite and quartzite]; (5) Manikot shell limestone [limestone]; (6) Tal group [sandstone, shale, quartzite, phyllite, and limestone].
6	Soil	(1) coarse-loamy; (2) skeletal-loamy; (3) fine-loamy; (4) mixed-loamy; (5) fine-silt
7	Land cover	(1) non-forest; (2) dense-forest; (3) open-forest; (4) scrub-land;
8	Rainfall (mm)	(1) 0-900; (2) 900-1000; (3) 1000-1100; (4) 1100-1200; (5) 1200-1300; (6) 1300-1400; (7) 1400-1500; (8) > 1,500
9	Distance to lineaments (m)	(1) 0-50; (2) 50-100; (3) 100-150; (4) 150-200; (5) 200-250; (6) 250-300; (7) 300-350; (8) 350-400; (9) 400-450; (10) 450-500; (11) > 500
10	Distance to roads (m)	(1) 0-40; (2) 40-80;(3) 80-120; (4) 120-160; (5) 160-200; (6) > 200
11	Distance to rivers (m)	(1) 0-40; (2) 40-80;(3) 80-120; (4) 120-160; (5) 160-200; (6) > 200

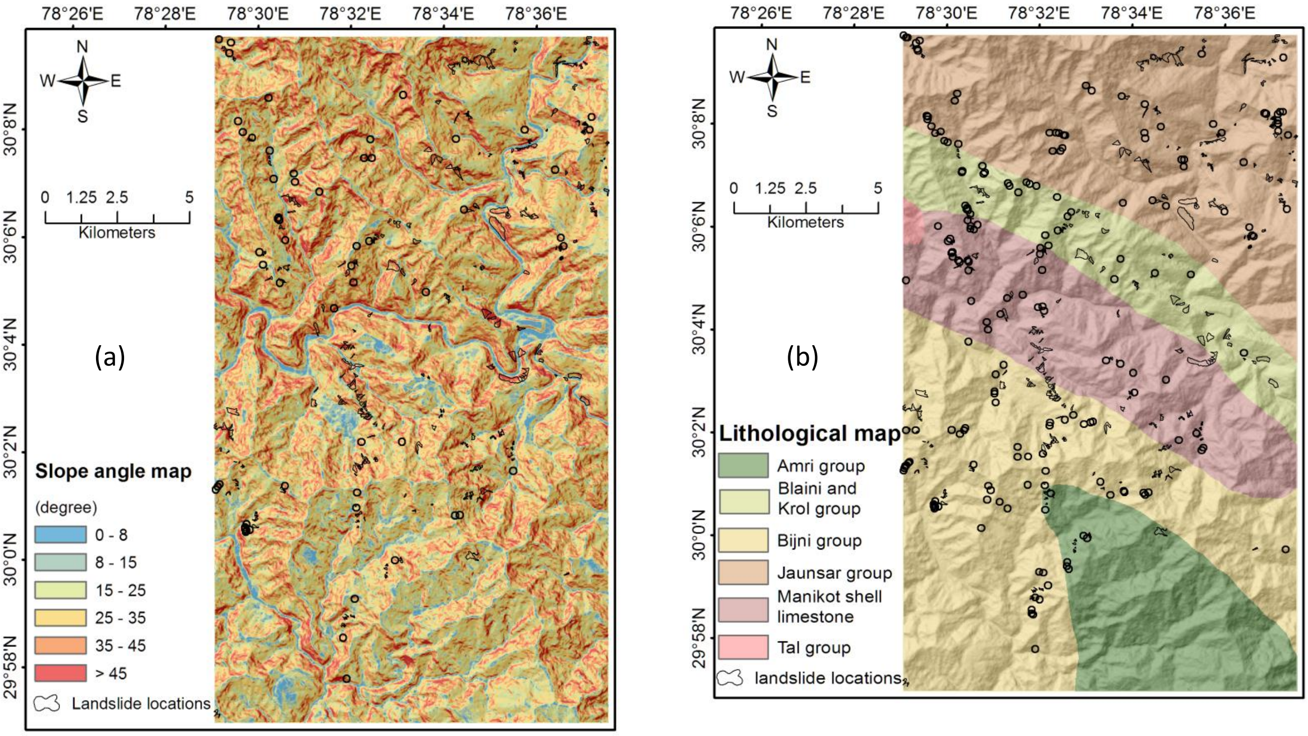

Figure 3: (a) Slope map and (b) Lithological map

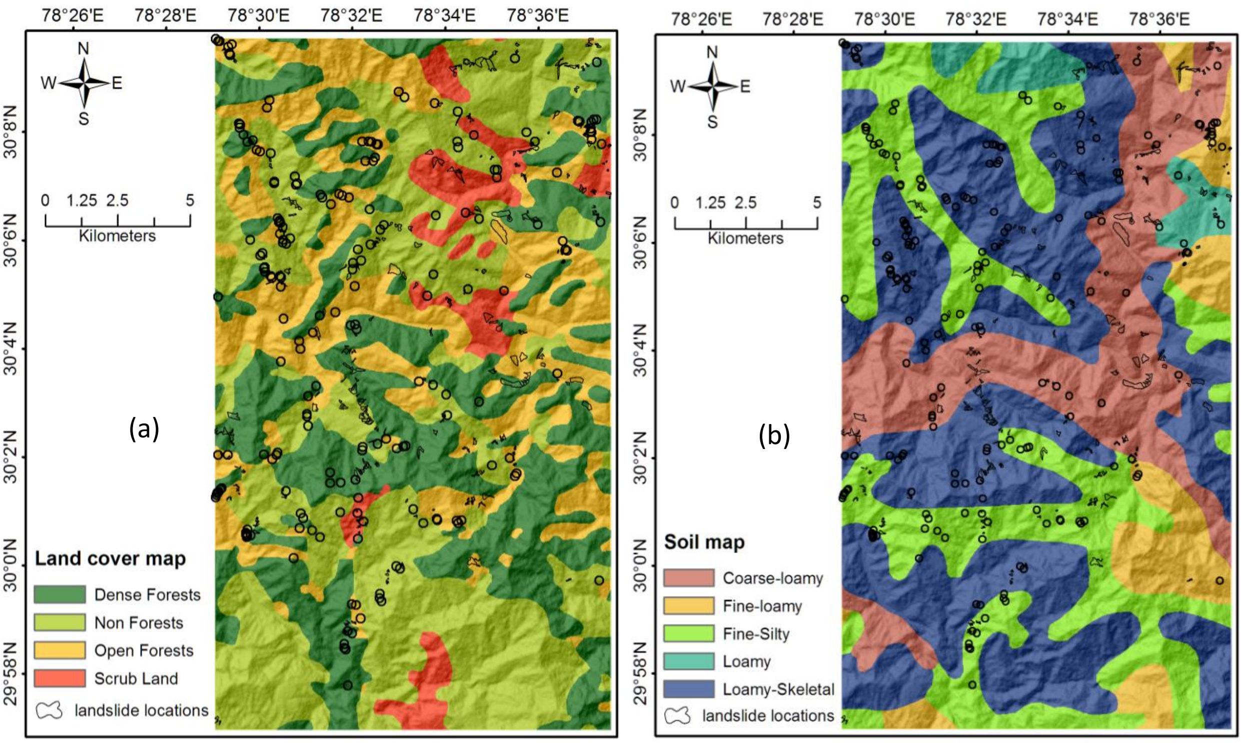

Figure 4: (a) Land cover map and (b) Soil map

3.2.2. Naïve Bayes Tree (NBT): NBT was first introduced by Kohavi (1996) which is a hybrid approach of Naïve Bayes and decision tree classifiers. Decision tree is one of the most commonly used in machine learning techniques that is based on a tree-like hierarchy for classification (Zhao and Zhang, 2008). Naïve Bayes is based on Bayes' theorem that considers all attributes are independent to maximize the posterior probability in determination the classified classes (Pham et al., 2015b; Soni et al., 2011). NBT is also a classification tree based method; however, it contains both nodes and leaves. The nodes consist of univariate splits as normal decision tree. The leaves include Naïve Bayes classifier (Kohavi, 1996). NBT is trained in two main steps (i) decision tree classifier is utilized to segment the data (ii) naïve Bayes classifier uses each segment of the data to create leaves for classifying variables. The performance of NBT is considered better than naïve Bayes and decision tree (Kohavi, 1996).

In this study, NBT has been applied at the first time for spatial prediction of landslides. Its performance has been compared with the performance of the SVM method.

4. Results

4. 1. Predictive capability of landslide affecting factors: Evaluation of predictive capability of landslide affecting factors to landslide models in the study area has been carried out using Gain Ratio (GR) technique. It is known as an efficient feature selection method in evaluation the importance of input data to models (Quinlan, 1986). Factors with higher GR values have better predictive capability than those with lower GR values. Factors with zero GR value have no contribution to landslide models, thus it must be removed in analyzing process.

Predictive capability of eleven landslide affecting factors to landslide models in this study is shown in Fig. 5. It can be observed that distance to roads has the highest predictive capability to landslide models (GR = 0.149), followed by rainfall (GR = 0.058), curvature (GR = 0.042), elevation and slope angle (GR = 0.037), soil types (GR = 0.025), lithology (GR = 0.021), land cover (GR = 0.01), slope aspect (GR = 0.008), distance to rivers (GR = 0.006), and distance to lineaments (GR = 0.003), respectively. In general, all eleven landslide affecting factors are having contribution to landslide models in the study area (GR > 0). Therefore, they all have been selected for landslide analysis in the present study.

4. 2. Landslide susceptibility map

Landslide models such as SVM and NBT have been constructed using training dataset. Thereafter, landslide susceptibility mapsusing these landslide models have been constructed. Firstly, landslide susceptibility indices(LSIs) have been generated for all pixels in whole study area. These susceptible indices have been then reclassified into five intervals using geometrical interval method (Frye, 2007). Five landslide susceptibility classes have been named corresponding to five susceptible index intervals such as very low, low, moderate, high, and very high (Table 2 and Fig. 6).

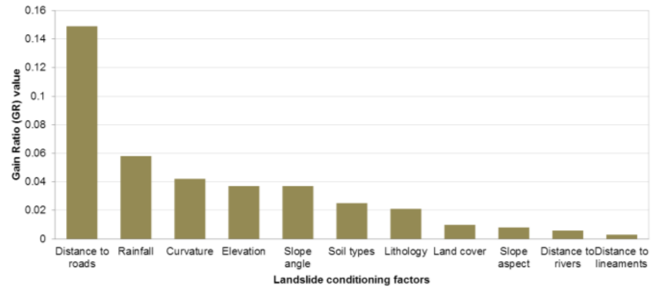

Fig 5: The Gain Ratio (GR) values of landslide affecting factors using

The performance of landslide susceptibility maps has been validated by overlaying them with landslide inventory map to calculate landslide density for each susceptible class. Landslide density is a ratio of the percentage of landslide pixels and the percentage of all pixels on each susceptible class. It can be observed from Table 2 that both landslide susceptibility maps perform well due to the fact that most of landslides have occurred on high and very high classes.

4. 3. Evaluation and comparison of landslide models

The performance of landslide models (SVM, NBT) has been validated using statistical index-based evaluations and ROC technique. Statistical indices such as sensitivity and specificity have been taken into account to evaluate the performance of landslide models. Sensitivity is the probability of the landslide pixels that have been classified correctly as “landslide” class (Pham et al. 2016a). It indicates how good landslide models for classification of landslide pixels. On the other hand, specificity is the probability of the non-landslide pixels that have been classified correctly as “non-landslide” class (Pham et al. 2016a). It shows how good landslide models for classification of non-landslide pixels.

ROC curve is a standard method to evaluate general performance of landslide models. It is constructed by plotting pairs of values (“sensitivity” and “100-specificity”). Area under ROC curve (AUC) is used to evaluate quantitatively the performance of landslide models. If the AUC value is larger than 0.8, the performance of landslide models is good and acceptable (Kantardzic, 2011).

The performance of landslide models is shown in Fig. 7 and Fig. 8. It can be observed that both landslide models perform well for spatial prediction of landslides in this study (AUC > 0.8). Out of these, the SVM model (AUC = 0.881) outperforms the NBT model (AUC = 0.832). More specifically, the SVM model (sensitivity = 84.4%, specificity = 81.6%) performs better than the NBT model (sensitivity = 82.5%, specificity = 76.6%) for classification of both landslide and non-landslide pixels. For both the SVM model

Journal of Geomatics Vol 10 No. 1 April 2016

and the NBT model, the classification of landslide pixels is significantly better than those of non-landslide pixels.

Table 2: Landslide density on landslide susceptibility maps

Class	LSIs		% Pixels		% Landslides		Landside Density	
	SVM	NBT	SVM	NBT	SVM	NBT	SVM	NBT
Very low	0-0.01	0-0.001	0.176	0.164	0.005	0.011	0.026	0.064
Low	0.01-0.039	0.001-0.009	0.248	0.205	0.012	0.004	0.047	0.021
Moderate	0.039 - 0.121	0.0089-0.043	0.260	0.257	0.035	0.016	0.134	0.063
High	0.121-0.352	0.043-0.207	0.130	0.203	0.061	0.078	0.472	0.384
Very high	0.352-1	0.207-1	0.186	0.171	0.887	0.891	4.772	5.205

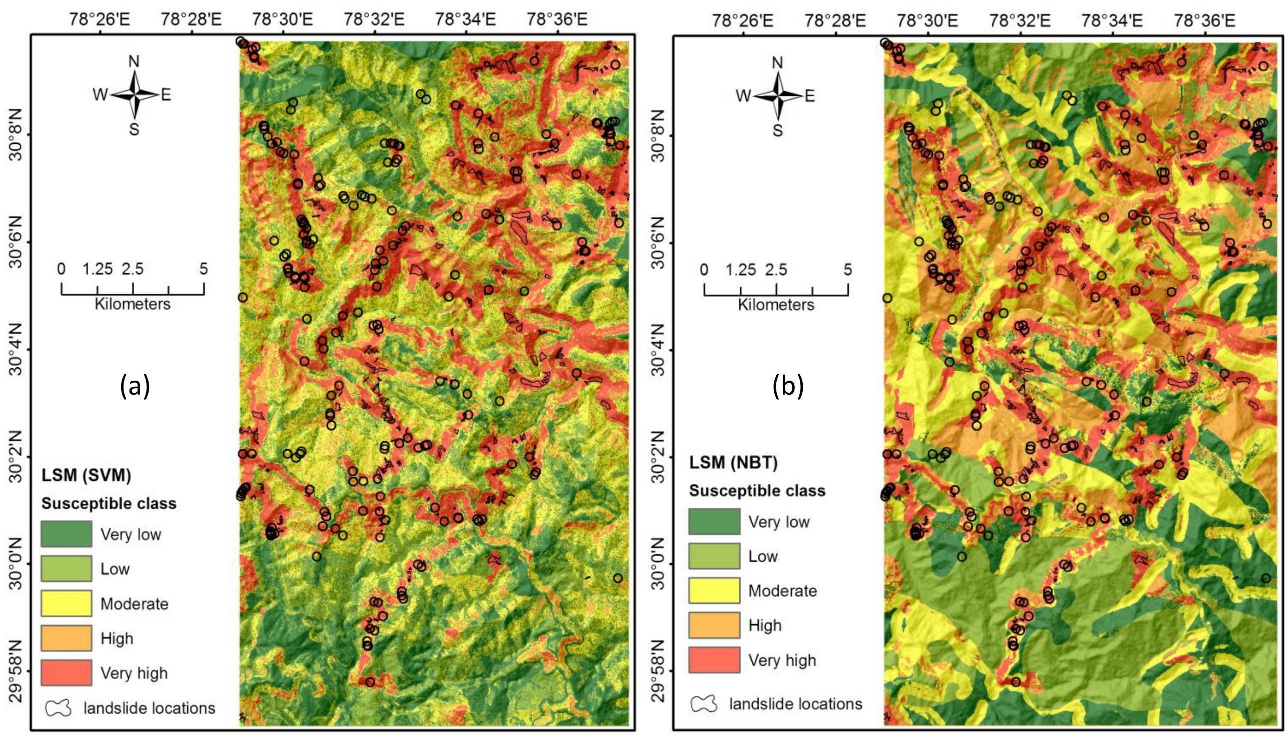

Figure 6: Landslide Susceptibility Maps (LSM) using (a) the SVM model and (b) the NBT model

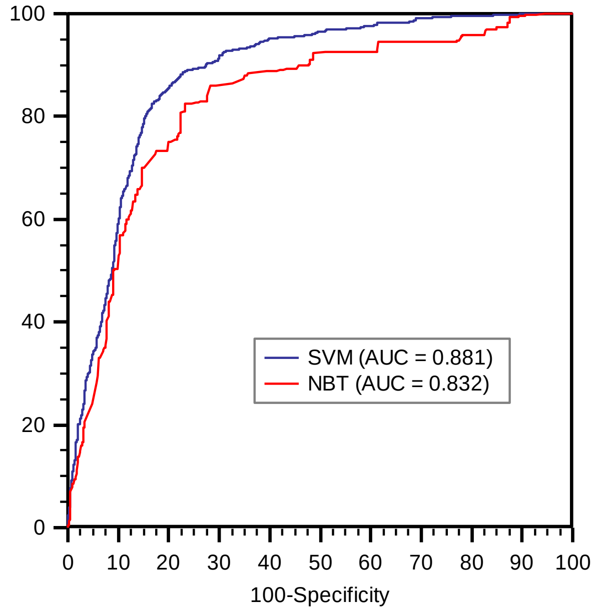

Figure 7: The performance of landslide models using ROC curve

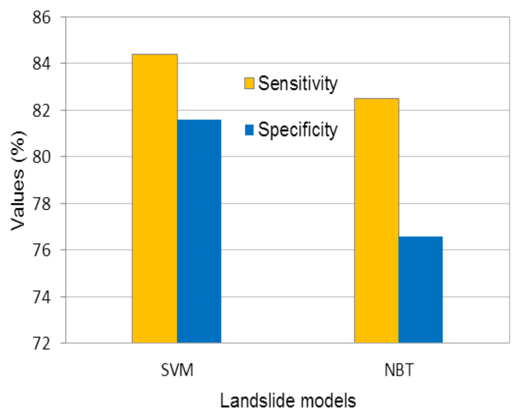

Figure 8: The performance of landslide models using statistical index-based evaluations

4.4 Discussions

The results show that both landslide models perform well for spatial prediction of landslides. Out of these, the SVM model outperforms the NBT model. This corroborates the fact of early study that the SVM model is one of the most efficient methods compared to conventional methods (Hassanien et al., 2015; Salama et al., 2013; Tien Bui et al., 2012). It might be due to the reason that NBT uses an assumption that all parameters are independent which is not really true in landslide problems (Tien Bui et al., 2015).

In addition, it is also necessary to evaluate the predictive capability of landslide affecting factors to landslide models in order to select suitable parameters to construct dataset for model learning process (Pham et al. 2016b). It is because the performance of landslide models depends significantly on the quality of input data that is constructed from landslide affecting factors (Pradhan, 2013). In the present study, the predictive capability of eleven landslide affecting factors has been evaluated using the GR method which is one of the most widely used feature selection techniques (Karegowda et al., 2010). The results show that in this area, distance to roads is important factor that has the highest predictive capability for landslide models. It is reasonable because most of identified landslides are on or adjacent to roads or highways. In addition, rainfall is also having high contribution to landslide models; this observation confirms the landslides occurrences during long-term heavy rain (Sengupta et al., 2010). Other factors are also having contribution to landslide models. Therefore, all eleven landslide affecting factors are appropriate for spatial prediction of landslides in the present study.

Conclusions

Overall, SVM and NBT indicate promising methods for spatial prediction of landslides which could be also used in other landslide prone areas. Out of these, the SVM model is having better predictive capability than NBT model. The present study would be helpful for land use planning, decision making and management of landslide hazard prone areas.

Acknowledgement

Authors are thankful to the Director, Bhaskarcharya Institute for Space Applications and Geo-Informatics (BISAG), Department of Science & Technology, Government of Gujarat, Gandhinagar, Gujarat, India for providing facilities to carry out this research work.

References

Abe, S. (2005). Support vector machines for pattern classification, 2. Springer.

Choi, J., H.J. Oh, J.S. Won and S. Lee (2010). Validation of an artificial neural network model for landslide susceptibility mapping. Environmental Earth Sciences, 60(3), pp 473-483.

Devkota, K.C., A.D. Regmi, H.R. Pourghasemi, K. Yoshida, B. Pradhan, I.C. Ryu, M.R. Dhital and O.F. Althuwaynee (2013). Landslide susceptibility mapping using certainty factor, index of entropy and logistic regression models in GIS and their comparison at Mugling–Narayanghat road section in Nepal Himalaya. Natural Hazards, 65(1), pp 135-165.

Dixon, B. and N. Candade (2008). Multispectral landuse classification using neural networks and support vector machines: One or the other, or both? International Journal of Remote Sensing, 29(4), pp 1185-1206.

Ermini, L., F. Catani and N. Casagli (2005). Artificial neural networks applied to landslide susceptibility assessment. Geomorphology, 66(1), pp 327-343.

Frye, C. (2007). About the geometrical interval classification method. https://blogs.esri.com/esri/arcgis/2007/10/18/about-the-geometrical-interval-classification-method/.

GSI (2009). Geological Survey of India. www.portal.gsi.gov.in.

Guha-Sapir, D., P. Hoyois and R. Below (2014). Annual disaster statistical review 2013: The numbers and trends. Brussels: CRED.

Guzzetti, F., P. Reichenbach, M. Cardinali, M. Galli and F. Ardizzone (2005). Probabilistic landslide hazard assessment at the basin scale. Geomorphology, 72(1–4), pp 272-299.

Hassanien, A.E., M.A. Salama, J. Platos and V. Snasel (2015). Rough local transfer function for cardiac disorders detection using heart sounds. Logic Journal of IGP.

Kantardzic, M. (2011). Data mining: Concepts, models, methods and algorithms. John Wiley & Sons.

Karegowda, A.G., A. Manjunath and M. Jayaram (2010). Comparative study of attribute selection using gain ratio and correlation based feature selection. International Journal of Information Technology and Knowledge Management, 2(2), pp 271-277.

Kavzoglu, T., E.K. Sahin and I. Colkesen (2014). Landslide susceptibility mapping using GIS-based multi-criteria decision analysis, support vector machines and logistic regression. Landslides, 11(3), pp 425-439.

Kohavi, R., 1996. Scaling Up the Accuracy of Naive-Bayes Classifiers: A Decision-Tree Hybrid, KDD. Citeseer, pp. 202-207.

Lucà, F., M. Conforti and G. Robustelli (2011). Comparison of GIS-based gullying susceptibility mapping using bivariate and multivariate statistics. Northern Calabria, South Italy, Geomorphology, 134(3–4), pp 297-308.

NCEP (2014). Global weather data for SWAT. http://globalweather.tamu.edu/home.

Onagh, M., V. Kumra and P.K. Rai (2012). Landslide susceptibility mapping in a part of Uttarkashi district (India) by multiple linear regression method. International Journal of Geology, Earth and Environmental Sciences.

Pham, B.T., D. Tien Bui, P. Indra and M.B. Dholakia (2015a). Landslide susceptibility assessment at a part of Uttarakhand Himalaya, India using GIS – based statistical approach of frequency ratio method. International Journal of Engineering Research & Technology 4(11), pp 338-344.

Pham, B.T., D. Tien Bui, H.R. Pourghasemi, P. Indra and M.B. Dholakia (2015b). Landslide susceptibility assesssment in the Uttarakhand area (India) using GIS: A comparison study of prediction capability of naïve bayes, multilayer perceptron neural networks and functional trees methods. Theor Appl Climatol, pp 1-19.

Pham, B.T., D. Tien Bui, MB. Dholakia, I. Prakash and H.V. Pham (2016a). A comparative study of least square support vector machines and multiclass alternating decision trees for spatial prediction of rainfall-induced landslides in a tropical cyclones area. Geotechnical and Geological Engineering 34:1-18.

Pham, B.T., D. Tien Bui, I. Prakash and M.B. Dholakia (2016b). Rotation forest fuzzy rule-based classifier ensemble for spatial prediction of landslides using GIS. Natural Hazards:1-31.

Pradhan, B. (2013). A comparative study on the predictive ability of the decision tree, support vector machine and neuro-fuzzy models in landslide susceptibility mapping using GIS. Computers & Geosciences, 51, pp 350-365.

Quinlan, J.R. (1986). Induction of decision trees. Machine Learning, 1(1), 81-106.

Salama, M.A., O.S. Soliman, I. Maglogiannis, A.E. Hassanien and A.A. Fahmy (2013). Rough set-based identification of heart valve diseases using heart sounds. Rough Sets and Intelligent Systems-Professor Zdzisław Pawlak in Memoriam. Springer, pp 475-491.

Sarkar, S., D.P. Kanungo and G.S. Mehrotra (1995). Landslide hazard zonation: A case study in Garhwal Himalaya, India. Mountain Research and Development, 15(4), pp 301-309.

Sengupta, A., S. Gupta and K. Anbarasu (2010). Rainfall thresholds for the initiation of landslide at Lanta Khola in north Sikkim, India. Natural hazards, 52(1), pp 31-42.

Song, Y., J. Gong, S. Gao, D. Wang, T. Cui, Y. Li and B. Wei (2012). Susceptibility assessment of earthquake-induced landslides using Bayesian network: A case study in Beichuan, China. Computers & Geosciences, 42(0), pp 189-199.

Soni, J., U. Ansari, D. Sharma and S. Soni (2011). Predictive data mining for medical diagnosis: An overview of heart disease prediction. International Journal of Computer Applications, 17(8), pp 43-48.

Tien Bui, D., B. Pradhan, O. Lofman and I. Revhaug (2012). Landslide susceptibility assessment in Vietnam using support vector machines, decision tree and naive Bayes models. Mathematical Problems in Engineering.

Tien Bui, D., T.A. Tuan, H. Klempe, B. Pradhan and I. Revhaug (2015). Spatial prediction models for shallow landslide hazards: A comparative assessment of the efficacy of support vector machines, artificial neural networks, kernel logistic regression and logistic model tree. Landslides, pp 1-18.

Vapnik, V.N. (1995). The nature of statistical learning theory. Springer Verlag, New York.

Wang, W.D., C.M. Xie and X.G. Du (2009). Landslides susceptibility mapping based on geographical information system, GuiZhou, south-west China. Environmental geology, 58(1), pp 33-43.

Yeon, Y.-K., J.-G. Han and K.H. Ryu (2010). Landslide susceptibility mapping in Injae, Korea, using a decision tree. Engineering Geology, 116(3), pp 274-283.

Zare, M., H.R. Pourghasemi, M. Vafakhah and B. Pradhan (2013). Landslide susceptibility mapping at Vaz Watershed (Iran) using an artificial neural network model: A comparison between multilayer perceptron (MLP) and radial basic function (RBF) algorithms. Arabian Journal of Geosciences, 6(8), pp 2873-2888.

Zhao, Y. and Y. Zhang (2008). Comparison of decision tree methods for finding active objects. Advances in Space Research, 41(12), pp 1955-1959.

Journal of Geomatics Vol 10 No. 1 April 2016

Early estimation of crop sown area by integrating multi-source data

D. Ram Rajak[1,2], Rajesh K. Jain[2] and Shibendu S. Ray[3]
[1]Space Applications Centre, ISRO, Ahmedabad – 380015, India
[2]Institute of Management, NIRMA University, Ahmedabad-382481, India
[3]Mahalanobis National Crop Forecasting Centre, MOA, New Delhi-110049, India
Email: rajakdr@yahoo.com

(Received: Feb 01, 2016; in final form: Mar 30, 2016)

Abstract: Satellite based remote sensing (RS) data at different spatial and temporal scales can provide crop sown area estimates needed by decision makers. Due to conflict of spatial resolution versus temporal frequency of data collection, getting early and accurate crop sown area at large scale is very difficult. This paper presents a methodology of early estimation of crop sown area at large scale by making use of high temporal coarse spatial resolution data and low temporal fine spatial resolution data. It also uses previous years' data for extracting a-priori knowledge of crop sowing area. Early crop area estimate was made for Gujarat state (India) for 2011-12 rabi season. Multi-date MODIS (MODerate resolution Imaging Spectroradiometer) data and two-date Resourcesat-2 AWiFS (Advance Wide Field Sensor) data upto mid-December were used for crop sown area early estimates. Multi-date MODIS data for previous five years provided a-priori information on crop presence / absence over the previous five crop seasons. While ISODATA was used for classifying multi-date MODIS and AWiFS data; hierarchical decision tree approach was used for integrating multi-source information. Incorporating two date AWiFS data and a-priori information with multi-date MODIS data increased crop sown area early estimates accuracy significantly.

Keywords: Crop sown area, MODIS, AWiFS, ISODATA, Decision tree

1. Introduction

Traditionally, the crop sown area is estimated from the sample data collected by different government institutes/departments or survey agencies. These methods are time consuming and labour intensive. Human subjectivity and biases increase in-accuracy levels of these estimates. Satellite based remote sensing (RS) data is one of the few sources for deriving frequent and reliable estimates of the crop sown area at different spatial scales. A number of research studies and projects have demonstrated the usefulness of RS data in making crop inventory over different parts of the world (Mc-Donald and Hall, 1980; Sharman, 1993; De Roover et al., 1993; Navalgund et al., 1991; Oza et al., 1996; Dadhwal et al., 2002; Parihar and Oza, 2006; Xiangming et al., 2006; Wardlow et al., 2007; Nigam et al., 2009; Nigam et al., 2012; Vyas et al., 2013; Ray et al., 2014; Sharma et al., 2014; Parihar, 2016; Karam et al., 2016; Rajak and Jain, 2016). Large Area Crop Inventory Experiment (LACIE, 1974-1977), covering USA, USSR, Brazil, Argentina, India etc. was one such study (Mc-Donald and Hall, 1980). Europe-wide crop production estimation was carried out by European Union under Monitoring Agriculture with Remote Sensing (MARS) project (Sharman, 1993; De Roover et al., 1993). In India, Crop Acreage and Production Estimation (CAPE) project demonstrated the potential of remotely sensed data for crop inventory (Navalgund et al., 1991). Dadhwal et al. (2002) have reviewed Indian experience of crop inventory using RS data. A multiple crops acreage estimation and production forecasting program based on multiple inputs was developed under FASAL (Forecasting Agricultural output using Space, Agro-meteorological and Land based observations) in India. Parihar and Oza (2006) have described the concept and program details. While Xiangming et al. (2006) have used multi-date MODIS (MODerate resolution Imaging Spectroradiometer) data for mapping paddy rice in South and South-East Asia. Wardlow et al. (2007) have used MODIS NDVI time series data for crop classification in U. S. Central Great Plains.

Nigam et al. (2009, 2011) used atmospherically corrected surface reflectance values in Red and NIR bands of INSAT 3A CCD to compute NDVI at continental scale and these NDVI values were further validated with global product to judge its spatio-temporal profiles and its range over different natural targets. Vyas et al. (2013) demonstrated that the spatially distributed crop sowing dates derived using INSAT 3A CCD data at 1 km×1 km resolution could be captured at regional scale in India. Ray et al. (2014) have summarized an operational methodology of multiple forecasting of multiple crops in India. Sharma et al. (2014) concluded that multi-year multi-date MODIS data could be used for monitoring gross annual changes of major rabi crops at regional scale.

Sud et al. (2015) presented a critical review of the literature related to concepts in crop area estimation and crop yield assessment. In addition, country-experiences were also reported while bringing out several issues and problems with regard to crop area and crop yield estimation. Karam et al. (2016) proposed a management tool for annual inventory and monitoring of cultivated lands using RapidEye and Landsat ETM+ imagery over a test area in Bekaa Valley, Lebanon. The study concluded that satellite imagery was essential for the definition of the existing cropping patterns in the pilot area and it helped in better estimation of seasonal irrigation needs at the scheme level. Parihar (2016) detailed the sequential developments in the use of single and multi-date optical and microwave remote sensing data for crop production forecasting in India. A methodology was developed by Nigam et al. (2015) using high temporal vegetation index data at 1km spatial resolution available from Indian geostationary satellite (INSAT 3A) to monitor progress of rabi crop area at country scale. The rabi crop area estimates obtained at the end of crop season at country level showed mean deviation of −18.1% with respect to reported DAC statistics during rabi season 2011–2012. At national scale, the INSAT- estimated rabi crop area showed 16.36% deviation from AWiFS derived rabi area at 2 km × 2 km grid, but no attempt was made to estimate crop sown area at state level. Sharma et al. (2014) estimated rabi sown area for Gujarat state using full season multi-date MODIS data but no attempt was made to arrive at an early estimation of the crop sown area. Rajak and Jain (2016) have emphasized the importance of two-source data i.e. AWiFS (Advance Wide Field Sensor) and LISS-III (Linear Imaging Self-scanning Sensor - 3) to improve crop acreage estimation at district scale.

There is no doubt that multi-source data analysis will become increasingly widespread in the future, due to increasing ease and lower cost of data collection, storage and manipulation. Availability of multi-source data of the same object at different times provides information on time varying characteristics of the object, if proper tools are available to analyse the multi-source data. In case of satellite based multi-source data, there are a number of commercial image processing software that may be used for storage, archival, and visualization of multi-source data. Extraction of the required information from such a multi-source dataset has remained a challenging task for long. Integration of information available from the previous years' data with current year's multi-source RS data has not been explored adequately for early estimation of crop sown area.

In this study, a methodology developed for early estimation of crop sown area over Gujarat state (India) using current year's multi-sensor data along with the information extracted from previous 5 years' RS data is presented. The methodology uses multi-source information i.e. multi-date satellite data from MODIS, two date satellite data from AWiFS, and a-priori crop history derived from multi-year multi-date MODIS data.

2. Study area and data used

This study was conducted over Gujarat, a western state of India with geographic area of 19.6 Million ha. Gujarat is an agriculturally rich state with a large number of crops grown in mainly rabi and kharif crop seasons. The major crops sown in kharif season (crops associated with the monsoon, mostly sown in June-July and harvested by September-October) include paddy (rice), cotton, groundnut, castor, jowar, bajra, tobacco, arhar, maize, sugarcane etc. Cotton, castor, tobacco, and sugarcane are the crops which continue beyond kharif season and usually available in the field during November – December period. Wheat, rapeseed & mustard, cumin, potato etc. are the major crops grown during rabi season (crops sown during winter and harvested before summer) in the state.

The satellite data used in this study include multi-date MODIS reflectance data over Gujarat for 2006-2007 to 2011-2012 rabi seasons and multi-date AWiFS data of full 2011-12 season (full season data was used for obtaining the classified image that was used as reference classified image). MODIS is a sensor aboard the NASA's Terra and Aqua satellites. The sensor views the entire Earth's surface every 1 to 2 days, acquiring data in 36 spectral bands at different spatial resolutions. Terra MODIS surface reflectance 8-day L3 global 250m (MOD09Q1) data were downloaded from the website: https://lpdaac.usgs.gov. The data used in the present study were from Julian day 281 (9th October) to Julian day 89 (30th March) in subsequent year for six rabi seasons. Thus, for 2010-11 rabi season, the time series contained 23 NDVI composite images, prepared from surface reflectance data. Overall, 115 MODIS images (23 images x 5 seasons) were processed and analysed over 5 years (2006-07 to 2010-11) for getting multi-year crop a-priori information. MODIS derived 9-dates NDVI time series upto mid-December was used for 2011-12 crop sown area early estimation. Two sets of Resourcesat-2 AWiFS data (Path/Row 92/56) for 2011-12 season were prepared. Set 1 having AWiFS data limited to mid-December and Set 2 having full rabi season data from October to March were analysed separately. While Set 1 comprised of November 17 and December 11, 2011 data, there were 7 dates of cloud-free data in Set 2. The sensor characteristics of AWiFS are given in Table 1.

Table 1: Characteristics of AWiFS onboard Resourcesat-2

Sr No	Characteristic	Value
1	Spectral band: Green (B2)	0.52 – 0.59 µm
2	Spectral band: Red (B3)	0.62 – 0.68 µm
3	Spectral band: NIR (B4)	0.77 – 0.86 µm
4	Spectral band: SWIR (B5)	1.55 – 1.70 µm
5	Spatial Resolution	56 m
6	Swath	740 km
7	Revisit period	5 days
8	Quantisation	12 bit

(Source: Bhuvan, 2012)

Crop and other land use / land cover details collected in field during crop season 2011-12 were used for training signature generation and validation in image classification. A sample of major crop parameters collected during the field visit is shown in Table 2.

Table 2: A sample of major crop parameters collected during the field visit in 2011-12

Field ID	**20111213-02**	-	**20111212-07**	-	**20111213-05**
Date	13 Dec 2011	-	12 Dec 2011	-	13 Dec 2011
Lat. (N)	23.872	-	23.685	-	23.774
Long. (E)	71.990	-	72.238	-	71.989
Crop Type	Wheat	-	Mustard	-	Castor
Crop Stage	CRI	-	Flowering	-	Capsule Formation
Field Size (m)	100x100	-	100 x 100	-	200x200
Synthetic Field Size (m)	200x200	-	200 x 200	-	-
Crop Fraction (%)	50	-	50	-	70
Date of Sowing	November III	-	Oct III week	-	N/A (Kharif)
-	-	-	-	-	-

3. Methodology

This study has three major data analysis components, namely analysis of multi-date and multi-year MODIS data, analysis of multi-date AWiFS data and integration of multi-source parameters for early crop sown area estimation.

3.1 Processing of MODIS and AWiFS data

MODIS MOD09Q1 data were converted from HDF-EOS format to ERDAS raster image format for further image processing through ERDAS IMAGINE software. MODIS surface reflectance values at pixel level were obtained by multiplying 16-bit unsigned data values with a factor of 0.0001 (Vermote et al., 2011).

In case of AWiFS data the Digital Numbers (DN) stored in the original data were converted to spectral radiance by using saturation radiance value available in data header file.

Accurate co-registration: Spatial characteristics of any land use / land cover including crops derived from different sources need to have common geo-referencing so that they can be integrated. It requires very accurate geo-referencing of the multi-source data. In this study, the multi-date MODIS data at 250m spatial resolution, which are well co-registered among each other, were co-registered with Resourcesat-2 AWiFS data at 56m spatial resolution. Both the datasets were brought to a common projection system of Albers Conical Equal Area (ACEA) projection and WGS84 datum.

NDVI and scaled NDVI calculation: An index derived from spectral values in Near Infra-Red (NIR) and Red (R) bands of electromagnetic spectrum, called Normalized Difference Vegetation Index (NDVI) is extensively used for studying vegetation using RS data. It responds to changes in the amount of green biomass, chlorophyll content and canopy water stress. NDVI is defined as ratio of the difference of spectral values (NIR-R) to the sum of spectral values (NIR+R). Its theoretical value ranges from -1.0 to +1.0. To avoid working with real/float numbers and to store in integer formats, it is sometimes scaled by multiplying and adding some constant values. In this case, the real values were multiplied by 100 and then 100 was added to get the scaled NDVI values.

$$\text{Scaled NDVI} = 100 + 100 * (NIR-R) / (NIR+R).$$

So the theoretical range of scaled NDVI became 0 to 200, hence the values were stored in single byte format.

Screening & smoothening of MODIS time series data: An algorithm, named Harmonic ANalysis of Time Series (HANTS) was employed for detecting the cloud contaminated pixels in MODIS data and for temporally interpolating the remaining non-contaminated data to construct gapless images at a prescribed interval of 8 days. The HANTS algorithm was devised and developed at NLR (Nationaal Lucht-en Ruimtevaartlaboratorium), in collaboration with KNMI (Koninklijk Nederlands Meteorologisch Instituut) and Alterra (Menenti et al., 1993; Verhoef et al., 1996; Roerink et al., 2000) the Netherlands. Its applications have been successfully demonstrated for vegetation monitoring, land surface temperature studies and generating cloud-free weather images (Wen et al., 2004; Xu and Shen, 2013; Sharma et al., 2014). The HANTS software can be downloaded free from the Naval Research Laboratory (NRL) website http://www.nlr.org/space/earth-observation/ or http://gdsc.nlr.nl/gdsc/en/tools/hants.. It can be implemented through MATLAB also (Abouali, 2012).

The HANTS algorithm can provide a much better smoothing of time series than most other methods can offer. Further details on HANTS can be found elsewhere (see Roerink et al., 2000; Wen et al., 2004; Verhoef et al., 2005). The basic mechanism is to calculate a Fourier series to the data, identify and remove outliers and replace them with the value produced by the Fourier series. This process is controlled by five parameters, which have to be set at the beginning of each HANTS run. The HANTS control parameters used are shown in Table 3.

Examples of thin cloudy data normalisation and thick cloudy data interpolation using HANTS technique are shown in Fig. 1.

3.2 Extracting data specific crop patterns

Data specific pattern analysis is an important element of multisource data mining. The idea is to mine each data type separately to get data patterns using appropriate mining techniques instead of combining all the data into one huge dataset before mining. Then assemble the data specific attributes (information) derived from all the data types separately and perform integrated analysis on them. This approach promotes data specific knowledge discovery at each data source independently to maximize utility of data specific information. In this study, based on the field knowledge, rabi crop locations were identified on the images and crop specific temporal NDVI patterns were derived from multi-date MODIS (2006-07 to 2010-11) as well as multi-date AWiFS data (2011-12, reference dataset).

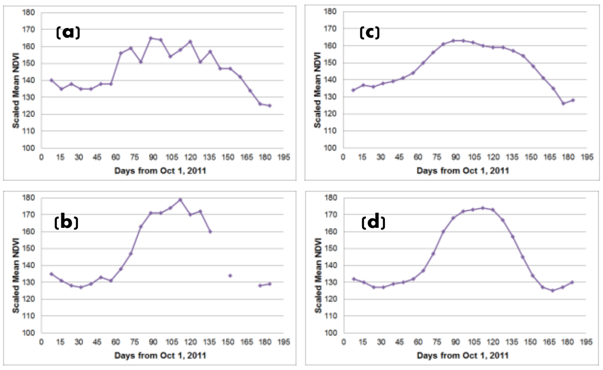

Figure 1: Examples of Harmonic ANalysis of Time Series (HANTS) applications: (a) scaled NDVI profile of a rabi crop with thin cloudy atmosphere, (b) scaled NDVI profile of another rabi crop with missing data due to thick cloudy atmosphere; (c) after applying HANTS over profiles in (a); and (d) after applying HANTS over profiles shown in (b)

3.3 ISODATA Classification

The Iterative Self-Organizing Data Analysis Technique (ISODATA) was used as an unsupervised classifier by recognizing multi-temporal patterns in the dataset (Ball and Hall, 1965). It is an iterative and heuristic procedure which assigns first an arbitrary initial cluster vector based on user's input. In the second step, it classifies each pixel of the data to the closest cluster in spectral domain. Merging and splitting of clusters is done, if conditions are met. Clusters are merged if either the number of pixels in a cluster is less than a certain threshold or if the centres of two clusters are closer than a certain threshold. Similarly, clusters are split into two different clusters if the cluster standard deviation exceeds a predefined/user defined value and the number of pixels is twice the threshold for the minimum number of pixels in a cluster. In the third step the new cluster mean vectors are calculated based on all the pixels in that cluster. The second and third steps are repeated until the "change" between two consecutive iterations is small. ISODATA has been found very effective at identifying spectral clusters in data. It is especially very useful while analysing a new data as we don't need to know much about the data beforehand. Care has to be taken that the data is structured well otherwise ISODATA may take long time if data is largely unstructured. Conceptual flow of the procedure followed in ISODATA clustering and spectral matching is shown in Fig. 2.

Before classifying 9-dates MODIS NDVI time-series data of 2011-12, temporal patterns of reference crops were obtained from 9-dates NDVI values at the crop locations collected during the in-season field surveys. Stacked 9-dates NDVI data was subjected to ISODATA and clusters were obtained for 2011-12 season. The temporal NDVI patterns of the ISODATA clusters were then matched with the reference patterns and classified into different classes based on their temporal profiles.

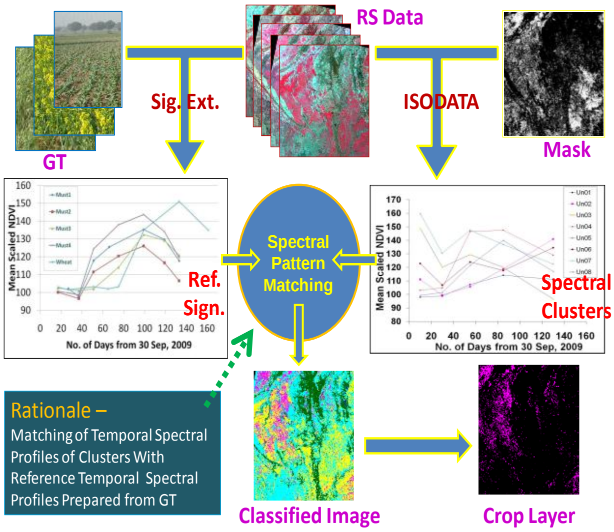

Figure 2: Conceptual flow of ISODATA clustering and spectral pattern matching showing major data analysis components

Multi-date full-season MODIS NDVI time series data from 2006-07 to 2010-11 were subjected to data screening and extrapolation before classification. The HANTS corrected data were then classified using ISODATA clustering. The temporal spectral profiles of ISODATA clusters were matched with the reference temporal spectral profiles and the clusters were labelled to rabi-crop and other than rabi classes. Thus classified images were obtained for 5 rabi seasons i.e. 2006-07 to 2010-11.

Two sets of multi-date AWiFS data, as described earlier, were processed to prepare classified images. Set 1 was classified by subjecting 7 dates of NDVI stack to ISODATA clustering and then labelling of clusters to rabi-crop and other classes. In case of Set 2, firstly December 11 AWiFS data was classified by ISODATA in vegetation (crops, forest, shrubs, plantations etc.) and other classes and ΔNDVI (i.e. $NDVI_{Dec11} - NDVI_{Nov11}$) image was used for classifying vegetation class in 4 sub-classes based on NDVI gradient.

3.4 Integration by decision tree approach

Decision tree approach is a commonly used method of information extraction in data mining. The objective is to create a model that estimates the value of a target variable based on several input variables available from single or multiple data sources. A decision tree is a flow-chart-like structure, where each internal (non-leaf) node denotes a test on an attribute, each branch represents the outcome of a test, and each leaf (or terminal) node holds a class label. The topmost node in a tree is the root node (Quinlan, 1993).

In this study three input images namely (i) a-priori crop history image from 5-years multi-date MODIS data, (ii) 9-dates MODIS derived classified image, (iii) 2-dates

AWiFS derived classified images were integrated to yield an output image.

The a-priori rabi crop history image was prepared by integrating 5 classified images of 2006-07 to 2010-11 seasons and the crop pixels were grouped in following 5 classes:

- Apr1: pixels with crop all the 5 years.
- Apr2: pixels with crop in 2010-11 and any 3 seasons.
- Apr3: pixels with crop in 2010-11 and any 2 seasons.
- Apr4: pixels with crop in 2010-11 and any 1 season.
- Apr5: pixels with crop in 2010-11 only.

Decreasing weightages were given to these classes, highest to Apr1 and lowest to Apr5, while this image was integrated for final classification of crop sown area for 2011-12 rabi season.

4. Results and Discussion

The MODIS / Terra MOD09Q1 and Resourcesat-2 AWiFS image sub-sets for Gujarat state were extracted from the original data from October to mid-December 2011. While MODIS two bands i.e. red (620 – 670 nm) and near infrared (841 – 871 nm) data were used, all the four bands data from AWiFS (Green: 0.52-0.59µm, Red: 0.62-0.68µm, NIR: 0.77-0.86µm, and SWIR:1.55-1.70µm) data were used in this study.

The MODIS reflectance images were used to derive scaled NDVI for all the nine 8-day interval dates (8, 16, 24 October, 1, 9, 17, 25 November, 3 and 11 December, 2011) of 2011-12 rabi season. Scaled NDVI images obtained from MODIS reflectance data are shown in Fig.3. The temporal variations of forest cover NDVI are clearly visible from October to December images. The spectral contrast between forest regions (for example Gir Forest and Dangs Forest) and their surroundings has continuously decreased from October to December. It is because of decrease in Forest NDVI and increase in crop NDVI during this time period.

In case of Resourcesat-2 AWiFS Set 1 data, cloud free images were available for 2 dates (November 17 and December 11) over the selected study period of October to mid-December. Colour Composite prepared from 2 dates data (Red: ΔNDVI, Green: red band of Dec 11, Blue: NIR band of Dec 11) is shown in Fig. 4. In case of AWiFS Set 2 data, similar methodology was followed and the NDVI time series was classified to rabi crop classified image using ISODATA clustering. As this dataset contained full rabi season data, the crop temporal spectral patterns of major crops were well discriminated from each other and this image was considered as reference classified image. Typical temporal NDVI patterns of three major rabi crops of Gujarat are shown in Fig. 5.

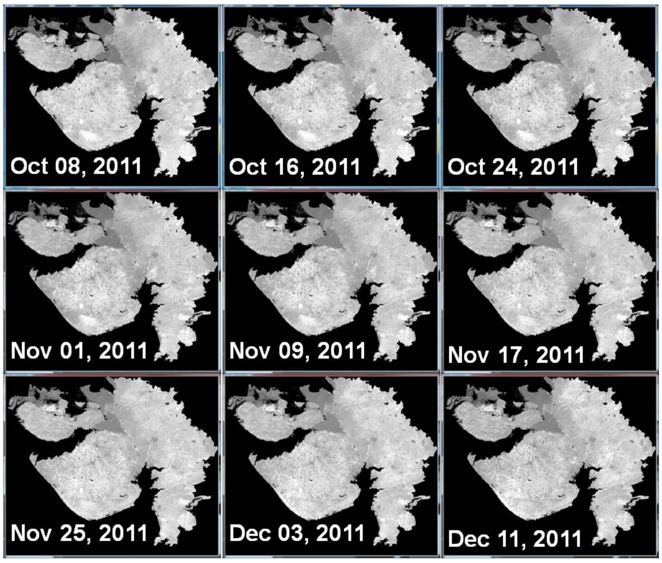

Figure 3: Scaled NDVI images obtained from MODIS reflectance data over Gujarat from October 8, 2011 to December 11, 2011 (2011-12 rabi season)

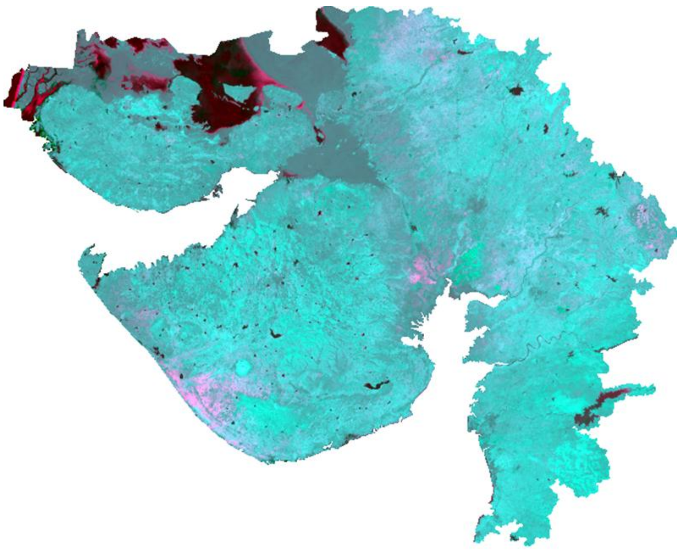

Figure 4: Colour Composite prepared from 2 dates AWiFS data (Red: ΔNDVI, Green: red band of Dec 11, Blue: NIR band of Dec 11). The regions with high ΔNDVI are red and pink in the image. The rabi crop area are visible in pink colour

A subset of the MODIS / Terra MOD09Q1 8-day reflectance data for Red and NIR bands was created for all the 5 seasons (2006-07 to 2010-11). Multi-date NDVI images were prepared from the reflectance images. The HANTS corrected NDVI stacked images were subjected to ISODATA clustering for each crop season. Based on the temporal spectral profiles shape matching with the reference profiles, unknown clusters were classified to different classes. Classes were merged to form rabi crop and other-than-rabi-crop theme images. The visual profile matching was carried out based on the overall NDVI pattern, peak value, time of peak, duration of peak value, growth gradient, decay gradient etc.

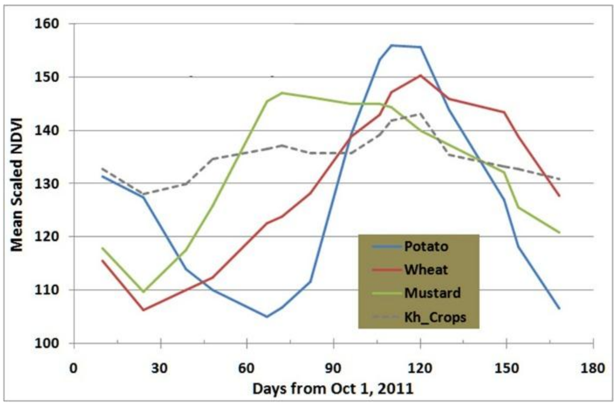

Figure 5: Typical temporal NDVI patterns of three major rabi crops and a kharif crop of Gujarat derived from multi-date AWiFS data

These five classified images for 2006-07 to 2010-11 seasons were used to create a-priori rabi crop history image for 2011-12 season. The a-priori rabi crop image is shown in Fig. 6.

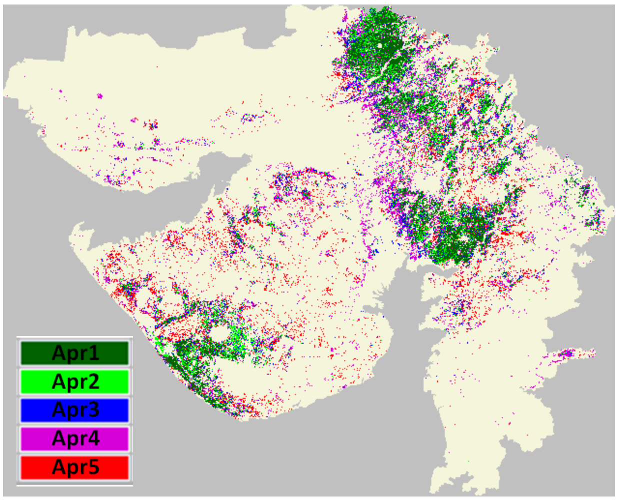

Figure 6: The a-priori rabi crop image prepared from 5-year multi-date MODIS data. While Apr1 represent the pixels with rabi crop for all the 5 years, Apr5 represents rabi crop during the previous season i.e. 2010-11

The crop sown area image for 2011-12 was obtained by integrating information extracted from 9-dates of MODIS images, 2-dates of AWiFS images and the a-priori rabi crop history image prepared from 5-years of multi-date MODIS images. The hierarchical decision rules were applied for obtaining this classified image and are given in Table 4. The pixels belonging to the fields where crop was grown during all the 5 rabi seasons were assigned a-priori category Apr1. Similarly, Apr2 to Apr5 categories were assigned as defined in Section 3.4. While forming decision rules for integration, Apr1 and Apr2 (crop at least 4 years) were given the highest weightage. The pixels belonging to Apr1 & Apr2 were classified to rabi crop class although ΔNDVI (AWiFS) was just greater than 0.0 with ΔNDVI (MODIS) was just greater than 0.05 (see Level 5, Table 4). However, Apr5 was given the least weightage as the pixels belonging to it were classified to rabi crop only with higher gradient values of both the ΔNDVIs (see Level 2, Table 4).

Table 4: The hierarchical decision rules applied for obtaining the classified image by integrating multisource data

Level	MODIS 9-Dates	AWiFS 2-Dates	A-priori (5-years)	Output, if YES
1	Non-rabi-crop class	Non vegetation class or ΔNDVI< 0	-	Non Rabi crop
2	Rabi crop with ΔNDVI>0.10	Veg. class with ΔNDVI> 0.05	Crop at least 1 year	Rabi crop 1
3	Rabi crop with ΔNDVI>0.10	Veg. class with ΔNDVI> 0	Crop at least 2 years	Rabi crop 2
4	Rabi crop with ΔNDVI>0.05	Veg. class with ΔNDVI> 0.05	Crop at least 3 years	Rabi crop 3
5	Rabi crop with ΔNDVI>0.05	Veg. class with ΔNDVI> 0	Crop at least 4 years	Rabi crop 4
6	Rabi crop	Vegetation class	-	Non Rabi crop

Note: In case of MODIS 9-Dates, ΔNDVI = (mean NDVI of 7,8,9 – mean NDVI of 4,5,6) and in case of AWiFS 2-Dates, ΔNDVI = (NDVI Dec 11 – NDVI Nov 17).

While the crop sown area estimated from 9-dates MODIS data was found to be 2.370 million hectares (0.913 Mha with NDVI>0.1 and 1.457 Mha with NDVI>0.05); the integrated dataset yielded rabi crop sown area of 1.125 million hectares. This shows that the classification based on only MODIS data overestimated the rabi sown area; as rabi crop area at the end of crop season was reported to be 2.045 million hectares (DES, 2016). The rabi crop sown area as on mid-December 2011 was reported to be 1.238 million hectares (DES, 2016), indicating that the area estimated by the proposed methodology is almost same as reported. However, it is not expected that the RS data upto mid-December should match the area estimated reported by mid-December. It is expected that the data upto mid-December may pick-up the crop sown at most upto November end. This indicates that the proposed methodology is slightly overestimating the crop sown area. The degree of over estimation could not be quantified as November-end crop sown area estimates are not available from any source. The classified image obtained through the proposed methodology was checked for its accuracy in classifying the rabi crops for 2011-12. It was compared with the reference crop sown area image obtained using full rabi season AWiFS data.

It was found that crop sown area images upto mid-December could pick up almost 57% of full season rabi crop area. Sharma et al. (2014) estimated the rabi sown crop area of 1.798 million hectare using full season MODIS data, but early estimation was not attempted.

Government of India (Department of Agriculture and Farmers' Welfare) estimated that almost 60% of full season rabi crop was sown as on December 16, 2011. The mapping accuracy of rabi sown area was found to be 88.6% with respect to the reference full season AWiFS image based rabi sown area. The full season crop sown area determined from the reference classified image was 1.972 million hectares. While the Government of India (DES, 2016) estimates were 1.238 and 2.045 million hectares as on December 16, 2011 and February 24, 2012, respectively.

5. Conclusion

A technique for early estimating crop sown area over a large region has been developed using multi-source remote sensing data. Crop sown area of Gujarat state (India) for 2011-12 rabi season was estimated by mid-December. The multi-source data used in this study included in-season MODIS 8-day composite, and two dates AWiFS data along with multi-year, multi-date MODIS derived a-priori crop image. Initial crop growth trends in terms of NDVI values were obtained from multi-date MODIS data from October to mid-December 2011. ISODATA clustering algorithm was used to cluster similar trends of temporal NDVI patterns. Spatial distribution of crop and non-crop fields/clusters was obtained from two dates AWiFS data (November 17 and December 11). Integration of the temporal patterns derived from MODIS data, spatial clusters derived from AWiFS data, and a-priori image derived from multi-year MODIS data was carried out using hierarchical decision tree approach. Reference crop sown area was obtained by using full crop season multi-date AWiFS data for 2011-12. It was found that the integration of in-season multi-source data provided the crop sown area estimates closer to the reference estimates.

Acknowledgements

This study was carried out as a part of the Ph. D. research activity undertaken by the first author. He thanks Director, Space Applications Centre, Ahmedabad for the motivation he provided. He expresses thanks to Project Director – FASAL for allowing him to access FASAL project RS data for this research. He also thanks Dr. J. S. Parihar for co-guiding his Ph.D. study. The constant encouragement and technical guidance provided by Dr. Markand Oza is highly appreciated and acknowledged. The MODIS data MOD09Q1 support from NASA EOSDIS LP DAAC (https://lpdaac.usgs.gov) is acknowledged.

References

Abouali, M. (2012). MATLAB Implementation of Harmonic ANalysis of Time Series (HANTS). http://www.mathworks.com/matlabcentral/fileexchange/38841-matlab-implementation-of-harmonic-analysis-of-time-series--hants-/.

Ball, G.H. and D.J. Hall (1965). ISODATA: A method of data analysis and pattern classification. Stanford Research Institute, Menlo Park, United States. Office of Naval Research.Information Sciences Branch.

Bhuvan (2012). Resourcesat-2 Handbook. http://bhuvan.nrsc.gov.in/bhuvan/PDF/ Resourcesat-2_Handbook.pdf. Accessed on Jan 28, 2016.

Dadhwal, V.K., R.P. Singh, S. Dutta and J.S. Parihar (2002). Remote sensing based crop inventory: A review of Indian experience. Tropical Ecology, 43(1): 107-122.

De Roover, B., S.C. De Mudker and R. Goossens (1993). The regional inventory (MARS) in Belgium. Proc. Int. Symp. "Operationalization of Remote Sensing", 19-23 April, ITC, Enschede, The Netherlands.

DES (2016). Personal communication. Crops and NFSM division, Department of agriculture, cooperation and farmers' welfare, Ministry of agriculture and farmers' welfare, Government of India.

Karam, Fadi, Nabil Amacha, Wassim Katerji, Weicheng Wu, Alfonso Domínguez and Safa Baydoun (2016). Using remote sensing to improve crop water allocation in a scarce water resources environment. International Journal of Science and Research, 5(1): 1481-1495. ISSN (Online): 2319-7064.

Mc-Donald, R.B. and F.G. Hall (1980). Global crop forecasting. Science, 280: 670-679.

Menenti, M., S. Azzali, A. de Vries, D. Fuller and S. Prince (1993). Vegetation monitoring in Southern Africa using temporal Fourier analysis of AVHRR/NDVI observations. Proc. Int. Symp. Rem. Sens. in Arid and Semi-Arid Regions, Lanzhou, China, 1993, 287-294.

Navalgund, R.R., J.S. Parihar, Ajai and P.P. Nageshwar Rao (1991). Crop inventory using remotely sensed data. Current Science, 61: 162–171.

Nigam, R., B.K. Bhattacharya, K.R. Gunjal, N. Padmanabhan and N.K. Patel (2009). A continental scale vegetation index from Indian geostationary satellite. ISPRS Archives XXXVIII-8/W3 Workshop Proceedings: Impact of Climate Change on Agriculture. http://www.isprs.org/proceedings/XXXVIII/8-W3/B5/3-22_F.pdf.

Nigam, R., B.K. Bhattacharya, K.R. Gunjal, N. Padmanabhan and N.K. Patel (2011). Continental scale vegetation index from Indian geostationary satellite: algorithm definition and validation. Current Science, 100(8):1184-1192.

Nigam, R., B.K. Bhattacharya, K.R. Gunjal, N. Padmanabhan, and N.K. Patel (2012). Formulation of time series vegetation index from Indian geostationary satellite and comparison with global product. Journal of the Indian Society of Remote Sensing, 40:1–9.

Nigam, R., S. Vyas, B.K. Bhattacharya, M.P. Oza, S.S. Srivastava, N. Bhagia, D. Dhar and K.R. Manjunath (2015): Modeling temporal growth profile of vegetation index from Indian geostationary satellite for assessing in-season progress of crop area, GIScience & Remote Sensing, DOI: 10.1080/15481603.2015.1073036. http://dx.doi.org/10.1080/15481603.2015.1073036

Oza, M.P., N. Bhagia, S. Dutta, J.H. Patel and V.K. Dadhwal (1996). National wheat acreage estimation for 1995-96 using multi-date IRS-1C WiFS data. J. Indian Soc. Remote Sensing, 24(4): 243-254.

Oza, M.P., N. Bhagia, D.R. Rajak and V.K. Dadhwal (2002). All India wheat inventory using multidate IRS WiFS and weather data. Proceedings of the ISPRS Comm. VII Symposium "Resource and Environmental Monitoring", Dec. 3-6 2002, Hyderabad, India, IAPRS and GIS, 34(7): 338-343.

Parihar, J.S., S. Panigrahy, N.K. Patel, D.R. Rajak, H.A. Patel and G.N. Patel (2010). Methodology for multiple pre-harvest rapeseed-mustard acreage estimation at state and national levels using multi-date AWiFS data. Scientific Report No. EOAM/SAC/FASAL-TD/SN/41/2010, Space Applications Centre (ISRO), Ahmedabad, India.

Parihar, J.S. and M.P. Oza (2006). FASAL: An integrated approach for crop assessment and production forecasting. Proc. SPIE 6411, Agriculture and Hydrology Applications of Remote Sensing, 641101; doi:10.1117/12.713157.

Parihar, J.S. (2016). FASAL concept in meeting the requirements of assessment and forecasting crop production affected by extreme weather events. Mausam, 67(1): 93-104.

Patnaik, C. and V.K. Dadhwal (1995). Study of crop discrimination by simulated LISS-III data. J. Indian Soc. Remote Sensing, 23(4): 195-199.

Potgieter, A.B., A. Apan, G. Hammer and P. Dunn (2005). "Spying" on the winter wheat crop – Generating objective planted area and crop production estimates using MODIS imagery. Proceedings of SSC 2005 Spatial Intelligence, Innovation and Praxis: The national biennial Conference of the Spatial Sciences Institute, September, 2005. Melbourne: Spatial Sciences Institute. ISBN 0-9581366-2-9.

Quinlan, J.R. (1986). Induction of decision trees. Machine Learning, 1:81–106.

Rajak, D.R., H.A. Patel, K.N. Chaudhari, N.K. Patel, S. Panigrahy and J.S. Parihar (2010). Spatial temporal sowing pattern of rapeseed-mustard crop in India using multi-date IRS AWiFS data. ISPRS Archives XXXVIII- 8/W20; Workshop Proceedings: Earth Observation for Terrestrial Ecosystems.http://www.int-arch-photogramm-remote-sens-spatial-inf-sci.net/XXXVIII-8-W20/56/2011/isprsarchives-XXXVIII-8-W20-56-2011.pdf.

Rajak, D.R. and Jain R.K. (2016). Toward improved crop acreage estimation using multi-source information. 19th Nirma International Conference on Management (NICOM-2016), Macro and Micro Dynamics for Empowering Trade, Industry and Society. Excel India Publishers, New Delhi. ISBN: 978-93-85777-07-3, Page: 82,92.

Ray, S.S., S. Neetu, Mamatha and S. Gupta (2014). Use of remote sensing in crop forecasting and assessment of impact of natural disasters: operational approaches in India.http://www.fao.org/fileadmin/templates/rap/files/Project/Expert_Meeting_17Feb2014_/P2-3_Remote_Sensing_for_Crop_Monitoring.pdf.

Roerink, G.J., M. Menenti and W. Verhoef (2000). Reconstructing cloudfree NDVI composites using Fourier analysis of time series, Int. J. Remote Sensing, 21(9): 1911–1917.

Sharman, M.J. (1993). The agriculture project of the Joint Research Centre: Operational use of Remote Sensing for agricultural statistics. Proc. Int. Symp. "Operationalization of Remote Sensing", 19-23 April, ITC, Enschede, The Netherlands.

Sharma N., D.R. Rajak, R.K. Jain, S. Palria and J.S. Parihar (2014). Monitoring rabi crop area using multi-year MODIS data: A case study of Gujarat, India. Journal of Geomatics, 8 (2): 211-215. http://www.isgindia.org/JOG/abstracts/October-2014/JOG-VOL08nO2-Oct2014_pg86%20-90.pdf

Sud U.C., T. Ahmad, V.K. Gupta, H. Chandra, P.M. Sahoo, K. Aditya, M. Singh and A. Biswas (2015). Research on Improving Methods for Estimating Crop Area, Yield and Production under Mixed, Repeated and Continuous Cropping. http://gsars.org/wp-content/uploads/2016/01/WP_Synthesis-of-Literature-and-Framework_Improving-Methods-for-Estimation-of-Crop-Area-190116.pdf.

Verhoef, W., M. Menenti and S. Azzali (1996). A color composite of NOAA-AVHRR based on time series (1981–1992). International Journal of Remote Sensing, 17:231–235.

Verhoef, Wout, Albert van der Kamp and Koelemeijer Robert (2005). Climate indicators from time series of

NDVI images (CITISEN). Final report, National Aerospace Laboratory NLR, NLR-CR-2005-474.

Vermote, E.F., S.Y. Kotchenova and J.P. Ray (2011). MODIS surface reflectance user's guide (ver 1.3). MODIS land surface reflectance science computing facility. http://modis-sr.ltdri.org/guide/MOD09_UserGuide_v1_3.pdf (last accessed April 1, 2016).

Vyas, S., R. Nigam, N.K. Patel and S. Panigrahy (2013). Extracting regional pattern of wheat sowing dates using multispectral and high temporal observations from Indian geostationary satellite. J Indian Soc Remote Sens, 41(4):855–864, DOI 10.1007/s12524-013-0266-3.

Wardlow, B.D., S.L. Egbert and J.H. Kastens (2007). Analysis of time-series MODIS 250 m vegetation index data for crop classification in the U.S. Central Great plains. Remote Sensing of Environment, 108: 290–310.

Wen Jun, Su Zhongbo, and Ma Yaoming (2004). Reconstruction of a Cloud-free Vegetation Index Time Series for the Tibetan Plateau. Mountain Research and Development 24(4):348-353, doi: http://dx.doi.org/10.1659/0276-4741(2004).

Xiangming Xiao, S. Boles, S. Frolking, C. Li, J.Y. Babu, W. Salas and B. Moore III (2006). Mapping paddy rice agriculture in South and Southeast Asia using multi-temporal MODIS images. Remote Sensing of Environment, 100: 95 – 113.

Xu, Yongming and Yan, Shen (2013). Reconstruction of the land surface temperature time series using harmonic analysis. Computers & Geosciences 61:126–132.

Journal of Geomatics Vol 10 No. 1 April 2016

Formosat-2 with Landsat-8 temporal - multispectral data for wheat crop identification using Hypertangent Kernel based Possibilistic classifier

Rohit Nandan[1], Ankit Kamboj[2], Anil Kumar[3], A. Senthil Kumar[3] and K. Venkata Reddy[1]
[1] National Institute of Technology, Warangal
[2]Gurukul Kangri Vishwavidyalaya, Haridwar
[3]Indian Institute of Remote Sensing, Dehradun, India
Email: rohitnandan72@gmail.com, ankitkamboj1726@gmail.com, anil@iirs.gov.in, senthil@iirs.gov.in and kvreddy@nitw.ac.in

(Received: Feb 27, 2016; in final form: Apr 18, 2016)

Abstract: Agriculture plays major role in India's economy, and provides undoubtedly the largest livelihood with its allied sectors. Crop type identification serves in number of applications such as crop yield forecasting, collecting crop production statistics, facilitating crop rotation records, mapping soil productivity, identification of factors influencing crop stress, assessment of crop damage and monitoring farming activity. To identify particular crop type in a single date imagery is a challenging task. However, Classification facilitates the multi-temporal images by taking into account changes in reflectance as a function of plant phenology. This research work deals with Possibilistic c-means classifier with Hypertangent kernel for wheat (Triticumaestivum) identification in Haridwar, Uttarakhand, India. The vegetation index outputs of Formosat-2 and Landsat-8 (Operational Land Imager) sensors were arranged in chronological order of their date and prepared three temporal datasets which cover whole phenological cycle of wheat. It was evaluated that for 2.7, 2.5, and 2.5 values of weighted constant (m), images of 4 (Formosat-2: 04 Dec 2014, 30 Jan 2015, 21 Feb 2015; Landsat-8: 16 Mar 2015), 5 (Formosat-2: 04 Dec 2014, 30 Jan 2015, 21 Feb 2015; Landsat-8: 16 Mar 2015, 01 Apr 2015), and 6 (Formosat-2: 04 Dec 2014, 30 Jan 2015, 21 Feb 2015, 09 Apr 2015; Landsat-8: 16 Mar 2015, 01 Apr 2015) date combination respectively represent the nicely separated wheat crop from other vegetation and were easily differentiated between early harvested and late harvested wheat crops. This study demonstrates that 5 date combination was sufficient to discriminate late harvested wheat crops and 6 date combination was sufficient to discriminate early harvested wheat crops.

Keywords: Wheat identification, Phenology, Soft classification, Possibilistic c-means (PCM), Kernel, Weighted constant

1. Introduction

Maps of crop type are created by national and multinational agricultural agencies, insurance agencies, and regional agricultural boards to prepare an inventory of what was grown in certain areas and when? This serves in number of applications such as crop yield forecasting, collecting crop production statistics, facilitating crop rotation records, mapping soil productivity, identification of factors influencing crop stress, assessment of crop damage and monitoring farming activity.

Traditional methods of obtaining specific crop maps are through census and ground surveying. In order to standardize measurements, remote sensing offers an efficient and well-founded means to map crop type and acreage. Spectral reflectance of vegetation varies with respect to change in plant phenology, stage and crop health. In India, different crops are grown in the vicinity of each other, so spectral response of target class may overlap with other class(s). Therefore, crop mapping using single date imagery is a real challenge (Wardlow et al., 2007; Masialeti et al., 2010). The information about the varying pattern of growth cycle and the occurrence of varying crop phenology stages in the time domain can help in discriminating or identifying crops using remote sensing technique (Murty et al., 2003; Niel et al., 2004; Doriaswamy et al., 2006; Misra et al., 2012). Hence, multi-temporal approach is more beneficial to identify specific crop.

The atmospheric effect on satellite imagery is common which affects the usability of data. For temporal analysis, the data should be free of rain, haze and clouds while acquiring data covering the crop growth season. But this requirement is rarely met. This hampers the temporal analysis results and provides gaps in temporal data sampling (Steven et al., 2003). The use of multiple sensors for filling up these periods of long absence in temporal data may provide a solution to this problem (Shang et al., 2008).

For crop identification, classification facilitates the multi-temporal images by taking into account changes in reflectance as a function of plant phenology. Pixel based classification method has been traditionally used to identify specific crops. But, the technique is efficient only when the spatial resolution of sensors match the Land Use/ Land cover class on the ground and there should not exist any spectral mixing at the inter-class boundaries. The problem of occurrence of mixed pixels can be tackled by applying fuzzy based classification approach. The fuzzy set theory was proposed by Zadeh (1965) to handle the uncertainty in class assignment. Bezdek et al. (1981) improved a fuzzy based classification technique; Fuzzy *c*-means (FCM) which was put forward by Dunn, 1973. In FCM, the membership value is a measure of the "degree of sharing" of the pixel for the class. While in the case of Possibilistic *c*-means (PCM); the membership value represents "the degree of belongings or compatibility or typicality" (Chawla 2010). PCM was proposed by Krishnapuram and Keller (1993). PCM algorithm has the capability to extract single class and handle the problem of noises and outliers, which commonly exist in the remote sensing data.

FCM and PCM fail to give results with higher accuracy, when the classes are linearly non-separable (Wu, 2006). In such a situation, if kernels are included in the existing algorithms then it has the capability to handle mixed pixels with linearly non-separable classes. Kernels are tools which take data to a higher dimension, such that the classes are linearly separable by a hyper plane. Zhang and Chen (2002) presented a kernel based Fuzzy *c*-means (FCM) algorithm which was tested on spherical dataset and real iris data. Kumar et al. (2006) studied the effect of different kernels while generating density estimation using SVM with respect to overall sub-pixel classification accuracy of multi-spectral data.

A crop can be discriminated by exploiting the variations in spectral response of various crops in a multi-dimensional feature space produced by different spectral bands, or time domain or both (Dadhwal et al., 2002). Working with temporal data, the number of spectral bands also increases. Hence, to reduce the spectral dimensionality of the data, temporal indices are generated. The vegetation indices maximize the sensitivity of plant biophysical parameters and perform radiometric correction in the satellite imagery (Jensen, 2009).

Wheat has proven itself to be a highly adapted crop across the world. Wheat is main cereal crop in India and staple food of millions of Indians, particularly in the northern and north-western parts of the country. Hence, importance of monitoring crop cannot be unnoticed. Specific crop mapping has essential role for crop acreage and yield estimation.

The major objective of this research is to propose a soft classifier algorithm which has the capability to extract wheat crop with better accuracy dealing with non-linearity within the classes. Specific objectives include: (1) To implement Hypertangent kernel based Possibilistic classifier for specific crop identification in bi-sensor multi-spectral data, and (2) To evaluate number of temporal images and optimized value of weighted constant that may be best suited for wheat crop identification.

2. Temporal vegetation index and classification approach

The Normalized difference vegetation index (NDVI) layers of different date were prepared and stacked in chronological order and prepared three temporal datasets of vegetation index. The NDVI was proposed by Kriegler et al. (1969) and the mathematical expression is given by equation (1).

$$NDVI = \frac{\rho_{NIR} - \rho_{Red}}{\rho_{NIR} + \rho_{Red}} \tag{1}$$

where, ρ_{NIR} represents reflectance at Near Infrared band and ρ_{Red} represents reflectance at Red band.

Possibilistic c-means algorithm is the modified form of FCM which was proposed by Krishnapuram and Keller (1993). The objective function for PCM is given in equation (2):

$$J_m(U,V) = \sum_{i=1}^{N}\sum_{j=1}^{C}(\mu_{ij})^m \left\|X_i - V_j\right\|^2 A + \sum_{j=1}^{C}\eta_j \sum_{i=1}^{N}(1-\mu_{ij})^m \tag{2}$$

where, U is the matrix between the number of pixel and number of classes. The equation (2) is subject to constraints,

for all i	$\max_j \mu_{ij} > 0$
for all j	$\sum_{i=1}^{N}\mu_{ij} > 0$
for all i, j	$0 \leq \mu_{ij} \leq 1$

where, X_i is the vector denoting spectral response of a pixel i, V_j is a collection of vector of cluster centres, μ_{ij} is class membership values of a pixel, c and N are number of clusters and pixels respectively, m is a weighting component (1<m<∞), which controls the degree of fuzziness.

η_j is dependent on the shape and average size of cluster j and is computed as in Eq. (3):

$$\eta_j = K\frac{\sum_{i=1}^{N}\mu_{ij}^m d_{ij}^2}{\sum_{i=1}^{N}\mu_{ij}^m} \tag{3}$$

The class memberships, μ_{ij} are obtained from equation (4):

$$\mu_{ij} = \frac{1}{1+\left(\frac{d_{ij}^2}{\eta_j}\right)^{\frac{1}{m-1}}} \tag{4}$$

where, d_{ij} represents the distance between the pixels value i and mean of the class j.

PCM is robust to handle mixed pixels but it fails to correctly classify the pixels when the classes are linearly non-separable (Wu, 2006). Kernel methods provide a compatible and reliable framework for developing nonlinear technique of classification and have useful properties when dealing with low number of training data, presence of heterogeneous land cover and different noise sources in the data.

In this paper a robust supervised fuzzy classification technique, Kernel based Possibilistic c- Means algorithm (KPCM) has been presented. Its basic idea is to transform the low dimensional input data into a higher dimensional feature space via a kernel method. After the implementation of kernels, the classes become linearly separable and PCM is performed on the feature space.

The mathematical expression of Hypertangent kernel used in this study is given in equation (5) (Kaur et al., 2012):

$$K(x, x_i) = 1 - tanh\left(-\frac{\|x_i - x_j\|^2}{\sigma^2}\right), \sigma > 0 \qquad (5)$$

Hence, the objective function of Kernel based Possibilistic c-Means (Zhang and Chen, 2003) is given by equation (6):

$$J_m(U,V) = \sum_{i=1}^{N}\sum_{j=1}^{c} \mu_{ij}{}^{m} K(X_i, V_j) + \sum_{j=1}^{C} \eta_j \sum_{i=1}^{N} (1 - \mu_{ij})^m \qquad (6)$$

The updated membership value can be computed as given by equation (7):

$$\mu_{ij} = \frac{1}{1 + \left(\frac{K(X_i, V_j)}{\eta_j}\right)^{\frac{1}{m-1}}} \qquad (7)$$

where,

$$K(X_i, V_j) = \left|\left|\emptyset(X_i) - \emptyset(V_j)\right|\right|^2 \qquad (8)$$

where, $\emptyset$ represents the kernel function. And

$$\left|\left|\emptyset(X_i) - \emptyset(V_j)\right|\right|^2 = K(X_i, X_i) + K(V_j, V_j) - 2K(X_i, V_j) \qquad (9)$$

The Hypertangent Kernel equation (5) helps to evaluate the above kernel function.

3. Study area and data used

The study area under this research is East side of Haridwar, Uttarakhand, India towards National Highway 74 as shown in fig. 1. Uttarakhand is a state in the northern part of India. The Haridwar district shares its boundaries by Dehradun in the north, Pauri Garhwal district in the east while, west and south are bounded by districts of Uttar Pradesh state. The central latitude and longitude of the study area taken are 29°52'20.3124"N and 78°10'25.0998"E respectively. The land is fertile with river Ganga flowing through the district and tourism and agriculture remains the backbone of the district. The major crops grown in the study area are rice, wheat, lentil, groundnut, mustard and plantations like citrus fruits, mango, litchi etc. In this study, remotely sensed temporal images of Formosat-2 and Landsat-8 (Operational Land Imager) were used for wheat crop identification. The sensors specifications are shown in Table 1(a) and 1(b).

Wheat (Triticumaestivum) is the Rabi season crop in India. The sowing window of wheat is 2nd week of November to 4th week of December in Haridwar district. Then it passes through a series of developmental phases from sowing to harvest. The harvesting period for wheat crop is mid-March to first week of April.

The combination of Formosat-2 and Landsat-8 (OLI) images NDVI outputs have been combined and prepared three datasets which cover major five growth phases (Tillering, Stem extension, Heading, Flowering and Ripening) of wheat crop. The datasets for Formosat-2 and Landsat-8 are shown in Table 2(a) and 2(b) respectively.

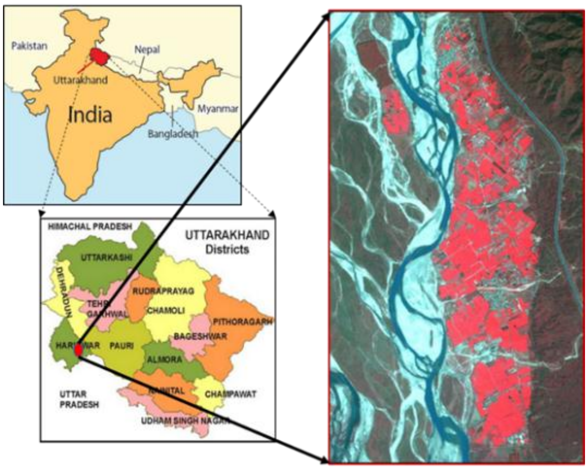

Figure 1: Study area: East Haridwar, Uttarakhand, India

Table 1(a): Formosat-2 Sensors Specifications (http://www.satimagingcorp.com/satellite-sensors/other-satellite-sensors/formosat-2/)

Band	Wavelength (in μm)	Spatial Resolution (in m)
Band 1 –Blue	0.45 – 0.52	8
Band 2 –Green	0.52 – 0.60	8
Band 3 –Red	0.63 – 0.69	8
Band 4 – Near Infrared (NIR)	0.76 – 0.90	8
P - Panchromatic	0.45 – 0.90	2

Table 1(b): Landsat-8 OLI Sensors Specifications (Landsat-8 Data User Handbook-June 2015)

Band	Wavelength (in μm)	Spatial Resolution (in m)
Band 1- Coastal/ Aerosol	0.433-0.453	30
Band 2- Blue	0.450-0.515	30
Band 3- Green	0.525-0.600	30
Band 4- Red	0.630-0.680	30
Band 5- Near Infrared (NIR)	0.845-0.885	30
Band 6-Short Wave Infrared	1.560-1.660	30
Band 7- Shot Wave Infrared	2.100-2.300	30
Band 8- Panchromatic	0.500-0.680	15
Band 9- Cirrus	1.360-1.390	30

Table 2(a): Formosat-2 temporal datasets

Formosat-2	
Date	Reference code
04 Dec 2014	F1
30 Jan 2015	F2
21 Feb 2015	F3
09 Apr 2015	F4

Table 2(b): Landsat-8 temporal datasets

Landsat-8 (OLI)	
Date	Reference code
16 Mar 2015	L1
01 Apr 2015	L2

Reference data for wheat was identified on the imagery from the GPS data collected during a field visit on 16 March 2015. During field survey the early sowing and late sowing wheat crop samples were collected based on the information provided by concern farmers. Further, this reference data was used as a training and testing data for classification and validation.

4. Methodology

Four temporal data of Formosat-2 from 04 Dec 2014 to 09 April 2015 and two temporal data of Landsat-8 (OLI) of 16 March 2015 and 01 April 2015, sensors have been used. These data were geometrically corrected for both sensors by using reference image as Formosat-2 21 Feb 2015 date. The Temporal Images were atmospherically corrected by ATCOR. The NDVI images were generated and linearly stretched in the scale of 0 to 255 by image enhancement technique, because of good visibility. The SMIC (Sub-Pixel Land Cover Mapping Image Classifier), a JAVA based image processing package (Kumar et al., 2006) supports 8 bit as well as 16 bit scale imagery has been used.

The vegetation index outputs of Formosat-2 and Landsat-8 (Operational Land Imager) sensors were arranged in chronological order of their dates and prepared three temporal datasets of 4 (Formosat-2: 04 Dec 2014, 30 Jan 2015, 21 Feb 2015; Landsat-8: 16 Mar 2015), 5 (Formosat-2: 04 Dec 2014, 30 Jan 2015, 21 Feb 2015; Landsat-8: 16 Mar 2015, 01 Apr 2015), and 6 (Formosat-2: 04 Dec 2014, 30 Jan 2015, 21 Feb 2015, 09 Apr 2015; Landsat-8: 16 Mar 2015, 01 Apr 2015) date combination, which cover whole phenological cycle of wheat.

Hypertangent kernel based PCM soft classifier has been applied on the all three date combination of temporal vegetation index datasets. By using testing data the optimized weighted constant and best temporal vegetation index datasets were evaluated by observing the difference in membership between the target class and other class(s). The maximum membership difference containing weighted constant value will be the optimized weighted constant. Best temporal vegetation index datasets to identify two classes of early harvested and late harvested wheat crops were evaluated by using the maximum membership difference between both classes among all three NDVI temporal datasets. The Flowchart of the methodology adopted is shown in Fig. 2:

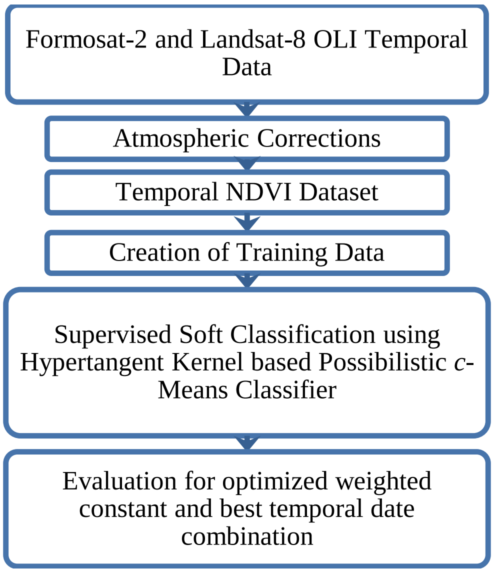

Figure 2: Methodology adopted

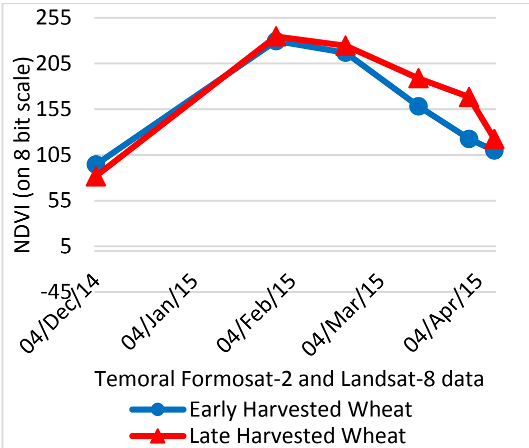

Figure 3: Spectral growth curve of wheat at training sites

5. Result and discussion

The spectral growth curve of early harvested and late harvested wheat crop has been shown in fig.3. The graph is showing the variation of NDVI between both classes with respect to time.

The weighted constant; m was optimized for 4, 5 and 6 date combination for two classes; early harvested wheat crop and late harvested wheat crop. The value of m was varied from 1.5 to 3.0 for each classification. However, the testing sites data were used to find the difference between membership values of both output fraction images. As the difference tends to be constant the corresponding value of m can be considered as its optimized value. The graphs shown in figure 4(a), 4(b) and 4(c) depict the difference between the membership values of classes as m was varied for 4, 5 and 6 date combination at unbiased sites. While in the case Hypertangent kernel based PCM optimized m was observed at 2.7, 2.5 and 2.5 respectively.

(a)

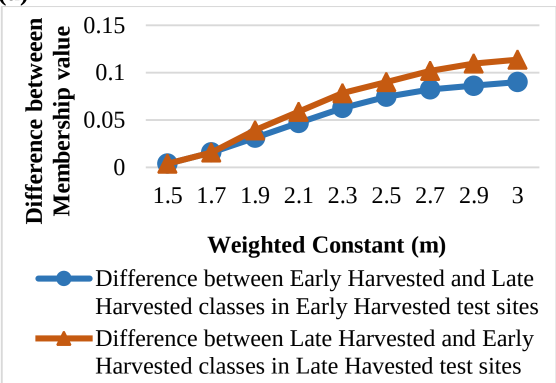

(b)

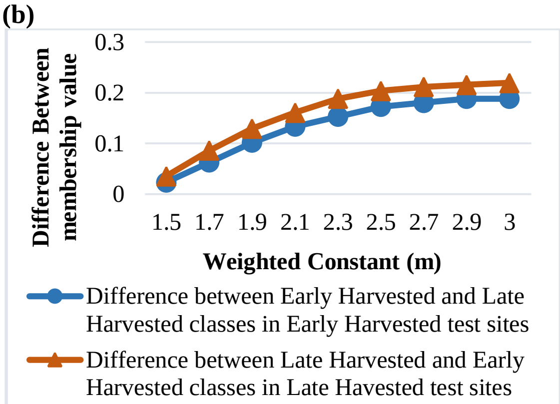

(c)

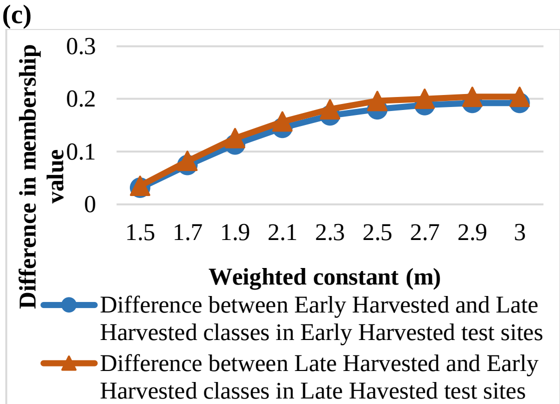

Figure 4: Weighted Constant (m) vs Difference between membership values for (a) 4 date combination datasets; (b) 5 date combination datasets; (c) 6 date combination datasets

The four dates classified results were not appropriate to discriminate both wheat classes. The Five dates and six dates classified results were represented the high difference between membership values of both classes at unbiased sites (The wheat crop area, which have not been used as training sites). However, five dates were found sufficient to discriminate late harvested wheat crops. The six dates classified results were also evaluated for good discrimination of early harvested wheat crop from other non-interest classes. Figure 5(a) and 5(b) represent nicely separated membership values in late harvested and early harvested wheat crop fields for 5 and 6 date combination temporal images. The classified images membership values have been stretched up in 8 bit scale for good visibility.

(a)

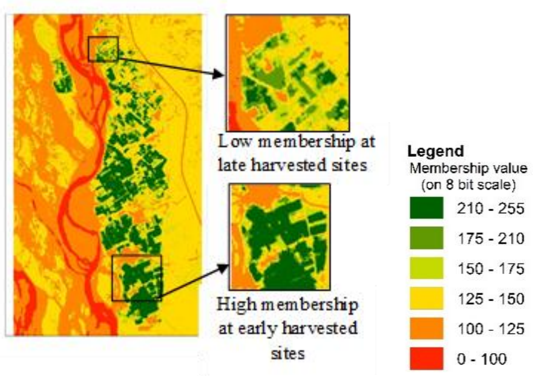

(b)

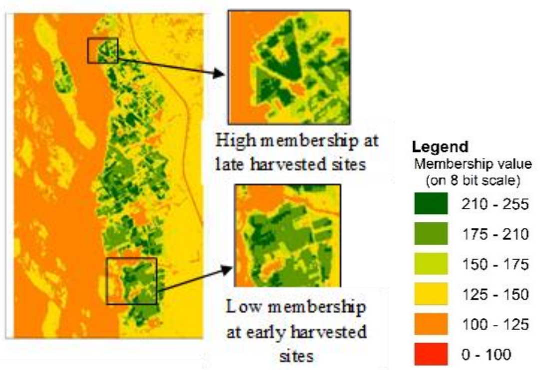

Figure 5: Classified images extracted by using Hyper Tangent Kernel based PCM classifier, (a) Class1- Early harvested wheat crop (Six date; optimized m= 2.5); (b) Class2- Late harvested wheat crop (Five date; optimized m= 2.5)

6. Conclusion

The study carried out in this research indicates the potential of bi-sensor approach in the temporal analysis studies. It has been observed that to identify wheat crop, the 5 growth phases covering images are enough. The Formosat-2 temporal data shows less spectral mixing than Landsat-8 because of the finer resolution of its sensor. Therefore, five and six date combination have more spectral mixing than four date combination because of coarser resolution Landsat-8 images contribution in datasets. The results indicate that 5 date combination was sufficient to discriminate late harvested wheat crops and 6 date combination was sufficient to discriminate early harvested wheat crops. Therefore, the study conclude that the Hypertangent kernel based Possibilistic c-means classification approach is robust to handle the mixed pixels to identify wheat crop. This selected best date can help in providing a temporal window for monitoring the wheat crop. This approach would help in generating accurate maps with the help of optimum number of strategically selected temporal remote sensing images covering the growing season of the crop, and help in saving resources spent in mapping too.

Acknowledgements

The authors would like to thank Sponsors the National Space Organization, National Applied Research Laboratories and jointly supported by the Chinese Taipei Society of Photogrammetry and Remote Sensing and the Center for Space and Remote Sensing Research, National Central University of Taiwan for providing Formosat-2 temporal images of Haridwar district, Uttrakhand, India. The first author is thankful to IIRS ISRO for allowing ten month M. Tech project on study of specific crop identification by using kernel based fuzzy classifier.

References

Aggarwal, R., A. Kumar, P.L.N. Raju and Y.K. Murthy (2014). Gaussian kernel based classification approach for wheat identification. ISPRS-International Archives of the Photogrammetry, Remote Sensing and Spatial Information Sciences, 1, pp. 671-676.

Bezdek, J.C., C. Coray, R. Gunderson and J. Watson (1981). Detection and characterization of cluster substructure I. Linear structure: fuzzy c-lines. SIAM Journal on Applied Mathematics, 40(2), pp. 339-357.

Chawla, S. (2010). Possibilistic c-means-spatial contextual information based sub-pixel classification approach for multi-spectral data. Unpublished Ph.D thesis, University of Twente (ITC), Enschede. pp. 14-15

Dadhwal, V.K., R.P. Singh, S. Dutta and J.S. Parihar (2002). Remote sensing based crop inventory: A review of Indian experience. Tropical Ecology, 43(1), pp. 107-122.

Department of the Interior U.S. Geological Survey (2015). Landsat-8 Data User Handbook, pp.9-10.

Doraiswamy, P.C., B. Akhmedov and A.J. Stern (2006). Improved techniques for crop classification using MODIS imagery. In Geoscience and Remote Sensing Symposium, 2006. IGARSS 2006. IEEE International Conference, pp. 2084-2087.
http://www.satimagingcorp.com/satellite-sensors/other-satellite-sensors/formosat-2/(Retrieved 30 May 2016)

Jensen, J.R. (2009). Remote sensing of the environment. 2nd Edition. Pearson Education, pp. 382-399.

Kaur, P., P. Gupta and P. Sharma (2012). Review and comparison of kernel based fuzzy image segmentation techniques. International Journal of Intelligent Systems and Applications (IJISA), 4(7), pp. 50.

Kriegler, F.J., W.A. Malila, R.F. Nalepka and W. Richardson (1969). Preprocessing transformations and their effects on multispectral recognition. In Remote Sensing of Environment, 4(1), pp. 97.

Krishnapuram, R. and J.M. Keller (1993). A possibilistic approach to clustering. Fuzzy Systems, IEEE Transactions on, 1(2), pp. 98-110.

Kumar, A., S.K. Ghosh and V.K. Dadhwal (2006). Sub-pixel land cover mapping: SMIC system. ISPRS International Symposium on Geospatial Databases for Sustainable Development, Goa, India.

Kumar, A., S.K. Ghosh, and V.K. Dadhwal (2006). Study of mixed kernel effect on classification accuracy using density estimation. In Proceedings of the ISPRS Commission VII Symposium (Vol. 36, No. Part 7).

Masialeti, I., S. Egbert and B.D. Wardlow (2010). A comparative analysis of phenological curves for major crops in Kansas. GIScience and Remote Sensing, 47(2), pp. 241-259.

Misra, G., A. Kumar, N.R. Patel, R. Zurita-Milla and A. Singh (2012). Mapping specific crop - A multi sensor temporal approach. In Geoscience and Remote Sensing Symposium (IGARSS), 2012 IEEE International conference, pp. 3034-3037.

Murthy, C.S., P.V. Raju and K.V.S. Badrinath (2003). Classification of wheat crop with multi-temporal images: Performance of maximum likelihood and artificial neural networks. International Journal of Remote Sensing, 24(23), pp. 4871-4890.

Shang, J., H. McNairn, C. Champagne and X. Jiao (2008). Contribution of multi-frequency, multi-sensor, and multi-temporal radar data to operational annual crop mapping. In Geoscience and Remote Sensing Symposium, 2008. IGARSS 2008. IEEE International (Vol. 3, pp. III-378). IEEE.

Steven, M.D., T.J. Malthus, F. Baret, H. Xu and M.J. Chopping (2003). Inter-calibration of vegetation indices from different sensor systems. Remote Sensing of Environment, 88(4), pp. 412-422.

Van Niel, T.G. and T.R. McVicar (2004). Determining temporal windows for crop discrimination with remote sensing: a case study in south-eastern Australia. Computers and Electronics in Agriculture, 45(1), pp. 91-108.

Wardlow, B.D., S.L. Egbert and J.H. Kastens (2007). Analysis of time-series MODIS 250 m vegetation index data for crop classification in the US Central Great Plains. Remote Sensing of Environment, 108(3), pp. 290-310.

Wu, X.H. (2006). A possibilistic c-means clustering algorithm based on kernel methods. In Communications, Circuits and Systems Proceedings, 2006 International Conference on (Vol. 3, pp. 2062-2066). IEEE.

Zadeh, L.A. (1965). Fuzzy sets. Information and control, 8(3), pp. 338-353.

Zhang, D. and S. Chen (2002). Fuzzy clustering using kernel method. In in The 2002 International Conference on Control and Automation, 2002. ICCA, 2002.

Zhang, D.Q. and S.C. Chen (2003). Kernel-based fuzzy and possibilistic c-means clustering. In Proceedings of the International Conference Artificial Neural Network, pp. 122-125.

India’s Journey Towards Excellence in Building Earth Observation Cameras

George Joseph Notion Press
ISBN: 9789352069989
Rs.450/; US$ 10.99

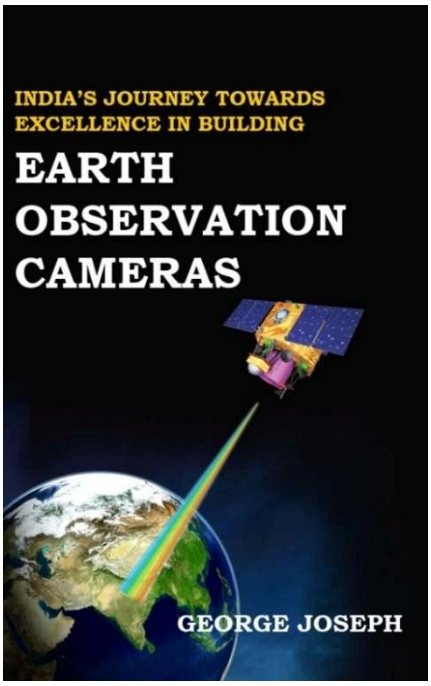

The book traces the evolution of earth observation cameras in Indian Space Research Organization (ISRO); how from a humble beginning of a two band framing camera ISRO went on to developing world class imaging system from space and the innovations carried out in the course of development of these sensors. The book also discusses the rational to choose various camera specifications based on the application needs.

The book starts with the beginning of the space program in India and systematically chronicles the journey of the development of advanced space based imaging system. The book also provides some basic technical insights into the building of space based remote sensing cameras, which have been presented in a way that can be understood by non-specialists too. In addition the book brings out the management aspects and the role played by leadership which make ISRO stand out as a successful high-tech organisation.

In addition to students and professionals in the field who will get a broad account of the functioning of space based camera systems and the nuances in the design, development and deployment of them, those in policy making and technical management in space agencies across the globe will also find the book useful to understand the path taken by India to achieve pre-eminence in this field.

> ***“I hope the book will interest a broad range of readers both within and outside the country. Those who were part of the journey will feel a sense of satisfaction and proud of what they could achieve and the younger readers will be inspired and encouraged to be part of this excitement. The book should interest all those who want to know how India has achieved preeminence in space based remote sensing.”***

A.S. Kiran Kumar
Chairman ISRO/Secretary DOS
(In the foreword to the book)

Author: Dr. George Joseph was director of the Space Applications Centre (ISRO), Ahmedabad. Under his overall guidance the development of electro-optical sensors started in ISRO.

Journal of Geomatics Vol 10 No. 1 April 2016

Crime mapping analysis of Ajmer city -A GIS approach

Ravi Sharma, Sarvesh Palria and Parul Bhalla
Department of Remote Sensing and Geo-informatics, M.D.S. University Ajmer – 305009
Email: ravisharma.rs08@gmail.com

(Received: Jan 23, 2015; in final form: Mar 18, 2016)

Abstract: Due to unemployment, the crime is increasing. Criminal acts like murder, rape, kidnapping, home breaking, theft, robbery are prohibited but exists all around the world. India is one major country where crime is increasing. The present study deals with the crime mapping of Ajmer city with GIS approach. The study is having objectives to generate crime maps to identify the crime pattern of Ajmer city. It is based on time series analysis to identify crime direction and hotspots of crimes. It also analyses type of hotspot, proximity of crimes to police stations, displacement of crime across time, crime rate of each ward and the socio-economic characteristics of city. This analysis provides insight to police with a view to decreasing crime rate.

Key Words: Crime rate, GIS, Hotspot, Land use/land cover, Crime map

1. Introduction

Crime is a human tendency, therefore, its distribution across the landscape is not geographically random. Place plays a vital role in understanding crime. To reduce crime, geography of crime needs to be understood as crime has an inherent geographical quality. When a crime occurs, it happens at a place with a geographical location (Chainey and Ratcliffe, 2005). For someone to commit a crime, one must come from a place (such as their home, work or school). This place could be the same location where the crime is committed or is often close to the place where crime occurred.

Jaishankar et al. (2004) showed that use of GIS provides a convenient tool for crime pattern analysis due to its geographic referencing capabilities. It provides valuable information concerning property of crimes including data on the social and physical characteristics of areas that contribute to localized criminal activity. Thangavelu et al. (2013) discussed about the importance of GIS, as it can be used as a tool to identify factors contributing to crime and thus allow police department to proactively respond to the situations before they become problematic. Crime analysis mapping is a valuable problem solving tool because it can lead to the identification of new problems facing law enforcement, lend a visual perspective to an analysis, assist in the development of an effective response, aid in the formation of partnerships by providing a common point of reference and assist evaluation procedures (Velasco and Boba, 2005).

A study of GIS based Decision Support System (DSS) for crime mapping in Ahmedabad city was conducted by Patel et al. (2014). They found that GIS based DSS is important as it uses geography and analysis as an interface for integrating and accessing massive amounts of location-based information. GIS based DSS allows police personnel to plan effectively for emergency response, determine mitigation priorities, analyze historical events and predict future events. GIS based DSS can also be used to get critical information in tactical planning and response. GIS helps to identify potential suspects of crime and thus leads to decrease the crime rate.

The present study focuses on the creation of the database of spatial and non-spatial attribute, calculation of crime rate and crime density in Ajmer city and identification of hotspots of different crime occurring in Ajmer city. Temporal crime pattern of Ajmer city is also analysed and illustrated using GIS tools.

2. Study area

Ajmer is the district of Rajasthan state. Ajmer city is the head quarter of the district. Ajmer city has a population of 542321. Ajmer city is a religious and tourist place. It is surrounded by NH-8, NH-14, NH-79 and NH-89. Ajmer city is surrounded by the Aravali hills. Ajmer city stretches from 26˚23' North to 26˚23' North and 74˚36' East to 74˚40' east. It has nine Police Stations (PS) and one Mahila PS. All nine PS boundaries of Ajmer city have been selected for study. Figure 1 shows the location map of study area.

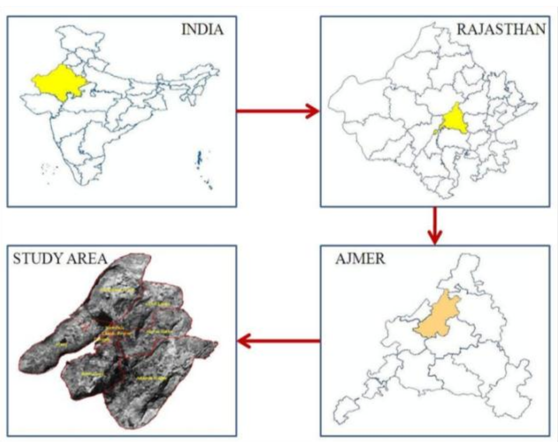

Figure 1: Location map of study area

3. Data used and methodology

The IPC crime incidents data is collected from the SP Office, Crime Branch & each PS of Ajmer city from 2009 to 2014 (Up to March 2014). Crime type data about murder, attempt to murder, rape, kidnapping, robbery, home breaking day and night, automobile theft and other theft are given in table 1. IPC crimes in different police stations of Ajmer city are given in table 2.

Table 1: Statistics of crime types in Ajmer city for various year

Crime Type	Year						Total
	2009	2010	2011	2012	2013	2014 (Upto March)	
Murder	11	60	16	14	12	0	60
Home breaking	82	436	55	58	134	32	436
Robbery	16	49	9	5	8	5	49
Kidnapping	27	155	17	22	64	7	155
Rape	10	103	20	13	35	14	103
Automobile theft	143	928	129	162	286	53	928
Other thefts	112	513	98	72	134	30	513
Attempt to murder	13	64	16	8	14	2	64
Total	414	2308	360	354	687	143	2308

Table 2: IPC crimes in different police stations of Ajmer city

S.No.	Police Station Name	Year						Total
		2009	2010	2011	2012	2013	2014(Upto March)	
1	Civil Lines	75	52	43	42	101	18	331
2	Clock Tower	56	21	29	25	49	11	191
3	Ganj	9	14	7	26	52	15	123
4	Dargah	31	19	31	26	25	5	137
5	Alwargate	29	36	46	39	78	13	241
6	Kotwali	71	67	77	64	81	13	373
7	Adarshnagar	26	27	22	33	82	16	206
8	Christianganj	73	83	80	62	157	33	488
9	Ramganj	44	31	25	37	62	19	218
	Total	414	350	360	354	687	143	2308

For spatial data analysis, Cartosat-I data and toposheets were used. Non-spatial attribute data were collected from all PS and crime branch office. GPS was used to collect geographic locations of crime incidence. Census data and ward map were collected from Statistical department and Nagar Nigam of Ajmer.

Thematic maps were generated on the yearly basis and year-wise maps were prepared for the period 2009- 2014 (upto March). Year-wise maps help to show the change detection of crime pattern and the direction of crime. Crime wise and crime type maps were prepared. These thematic maps were analyzed to find out the hotspot areas and then spatio-temporal crimes were identified. The methodology is given in figure 2.

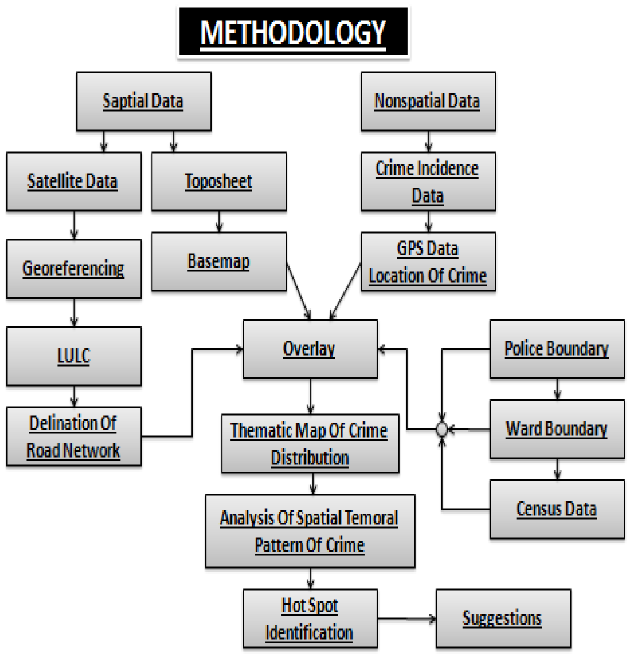

Figure 2: Flow chart of methodology

4. Result and discussion

Crime map of Ajmer city for the period 2009 – 2014 with PS boundary overlaid is given in figure 3. Location map of PS of Ajmer city according to municipal boundary is given in figure 4. Cartosat-I data was used for road network delineation and base map preparation from toposheet.

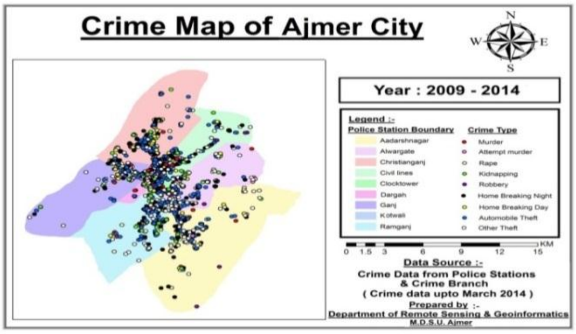

Figure 3: Crime map of Ajmer city (2009 – 2014) with police station (PS) boundary

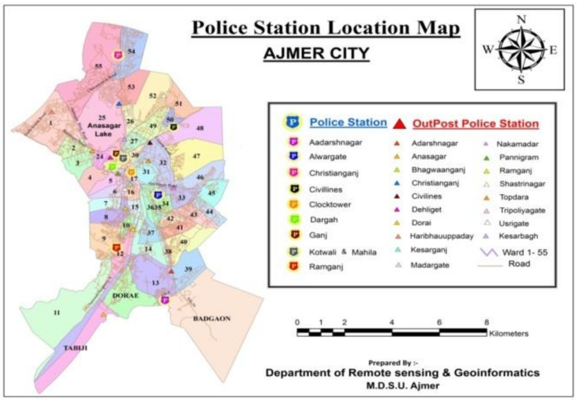

Figure 4: Location map of Police Stations (PS) of Ajmer city according to municipal boundary

By observing and analyzing the crime data of Ajmer city's nine PS, crime maps for various years as well as for various PS were prepared. Four illustrative such maps given in figure 5 (a – d). Composite crime map of Ajmer city (2009 - 2014) with municipal boundary of Ajmer city is given in figure 6. The PS-wise result and patterns are discussed below.

4.1 Aadarsh Nagar PS

After studying about 2009–2014 map of Aadarsh Nagar PS, it was observed that –murder and attempt to murder both were not found in the category of hotspot areas. Kidnapping had mainly occurred near Sethi colony. Home breaking and night crimes took place in Sethi colony and the 500 meter buffer zone of Aadarsh Nagar outpost police station. Robbery was mainly seen in Ricco industrial area, where mainly the official people visited.

Two wheelers and four wheelers were mainly stolen from the industrial area near Aadarsh Nagar and Pravatpura circle and Hatundi circle.

In the year 2009, permanent hotspot can be seen at Pratapura circle. In the year 2010, hotspot is shifted to Aadarsh Nagar colony, near Balupura road.

The Aadarsh Nagar colony development was at peak this year. Criminals are attracted at high density population area. In the year 2011, Pratappura circle (North and South) can be seen as major hotspot. Makupura circle can also be seen as the major Hotspot.

4.2 Civil Lines PS

After studying about 2009–2014 map of Civil Lines PS, it can be seen that –murder and attempt to murder both were not found in the category of hotspot area. Kidnapping mainly occurred near Lohakhan bus stand. Home breaking at Civil Lines area (Near Shastrinagar road). Two wheeler thefts happened at parking areas of Ajmer hospital, roadways bus stand, near Mission school, old RPSC, Civil Lines hospital, Collectorate parisar, and at Ajmer club park. Other theft area occurred at bus stand, Session court, Rajasthan Board, Lohakhan, Civil Lines and Ajmer club. Hotspots were found in 500meter buffer zone of Civil Lines PS and Out Post (OP) Civil Lines.

4.3 Clock tower PS

After studying about 2009–2014 map of Clock tower PS, it was found that murder and attempt to murder both are not found in the category of hotspot area. Kidnapping mainly occurred near Trambe station and Home breaking night at Janta market.

Two wheeler thefts occurred at Sant Francis hospital, Babu colony, Vimla market; Outside Jain namkin, GCA parking, Apna market. Four wheelers were mainly stolen from Sant Francis hospital and Babu colony. Other thefts occurred at Padav. Robbery occurred at Martin Bridge.

Hotspots were found in 100 meters buffer zone of Clock tower PS and OP Kesarganj were at high rate. No other hotspot was found in buffer zone of OP Usarigate.

4.4 Ganj PS

After studying about 2009–2014 map of Ganj P.S., it was found that murder and attempt to murder both were not found in the category of hotspot area. Kidnapping occurred at mainly 300 meter buffer zone of Ganj PS. Home breaking night, two wheeler theft and other theft crimes mainly occurred in 300 meter buffer zone of OP Anasagar and PS Ganj. Home breaking occurred mainly near Dehli gate and two wheeler theft mainly at Ramprashad ghat.

Proximity of crime with PS and outpost police station is very high and all hotspots were found 300 meter buffer zone to PS and OP.

4.5 Dargah PS

After studying about 2009–2014 map of Dargah PS, it was found that murder and attempt to murder both were not found in the category of hotspot area. Terrorist prefer a place where crowd is present because in such area one bomb blast may damage life of many people. Due to this reason an explosion occurred near courtyard outside the Dargah of Khawaja Moinuddin Chishti in Ajmer (11 Oct 2007). Dargah is sensitive area for terrorist attack so CCTV camera and metal detectors are essentially required in such area.

No robbery and four wheeler theft case was found in last 5 years in Dargah PS. area because of high crowd

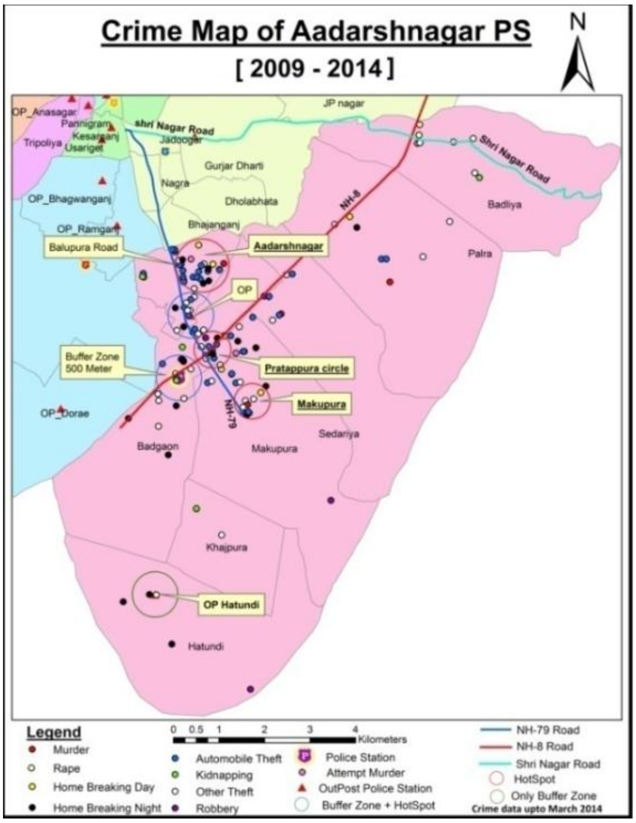

(a)

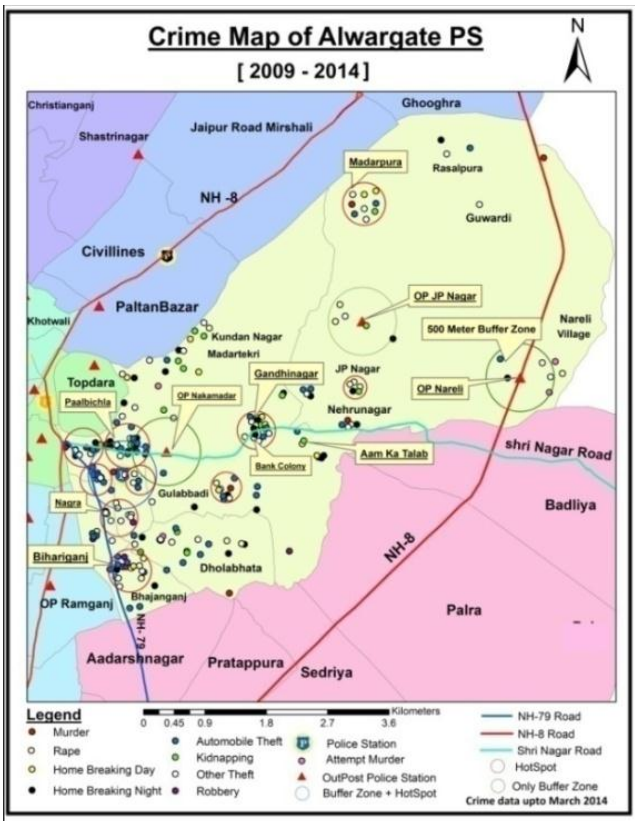

(b)

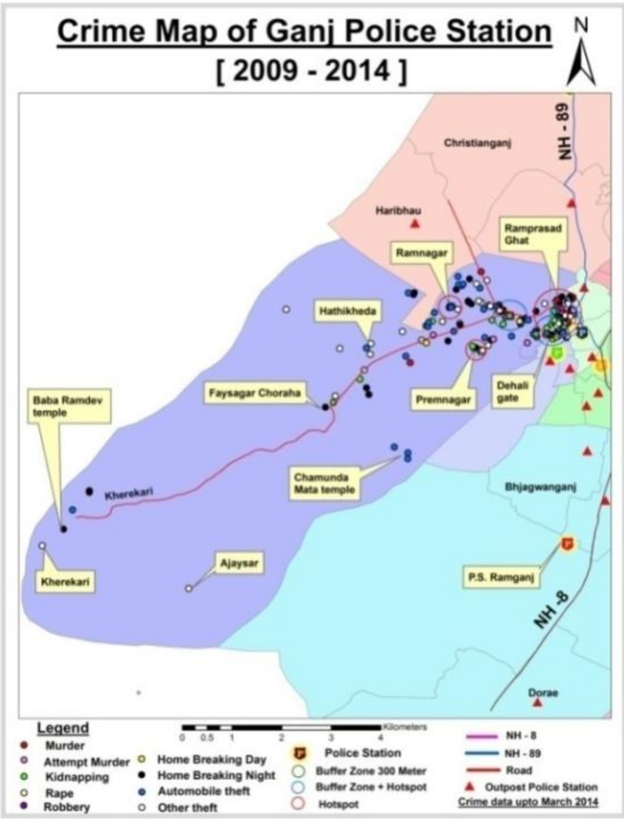

(c)

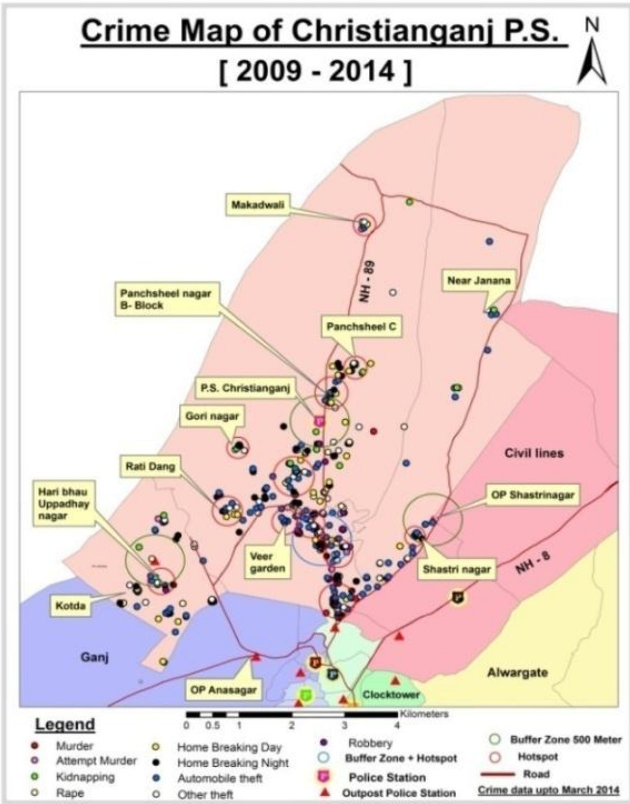

(d)

Figure 5: Crime map (2009 – 2014) of four Police Stations (PS) viz., (a) Aadarsh Nagar, (b) Alwar gate, (c) Ganj and (d) Christianganj

and place shorting for parking area. Other theft hotspot was found at Khwaja Mohinidin Chishti Dargah parisar because of high crowd. Home breaking occurred at night at Holidara. Two wheeler theft occurred at Nala market and Dhanmandi. Violence crime mainly occurred at Andarkot.

4.6 Kotwali PS

After studying about 2009–2014 map of Kotwali PS, it was found that murder and attempt to murder both were not found in the category of hotspot area. Home breaking at night mainly occurred near Information centre circle and Ajmer tower.

Two wheeler thefts mainly occurred at outside JLN hospital, K.C. complex, Swami complex, Bhesa complex, Ajmer tower, Amar plaza, Prabhat cinema, HDFC bank, Near G.P.O., near P.N.B. Kachhari road, P.R. marg, near Jagdamba bar and near Mango masala. Four wheeler thefts mainly occurred at J.L.N medical college and outside Swami complex. Other theft mainly occurred at JLN Hospital, PNB (Kachhari road) and 100 meter distance to PS at near P.R. marg.

Proximity of crime with Kotwali PS and OP Madar gate was very low because no hotspot area was found in 100 meter buffer zone. Hotspots are found in 100 meter buffer zone of OP Kesar bagh.

4.7 Alwargate PS

After studying about 2009–2014 map of Alwargate PS, it was found that murder and attempt to murder both were not found in the category of hotspot area. Kidnapping were mainly occurred near Kundannagar. Home breaking during day occurred at Gandhi nagar and night time crimes took place in main Alwar gate area near Srinagar road.

Robbery was mainly seen in the area of Martin bridge and Aamka talab. Two wheeler thefts occurred at main Alwargate area, Convent school, Shiv temple, LIC parking and 9 no. petrol pump. Four wheelers were mainly stolen from Heena garden and near Shrinagar road (main Alwargate area). Other theft area occurred at Martin bridge and near P.N.B.

Hotspots were found in 500 meters buffer zone of Alwargate PS and proximity of crime with outpost police station was low, crime occurred 500 meters away from the OP Nakamadar, OP J.P. nagar and OP Nareli. Some crime cases were found at Nagra, Bihariganj, Gokulnagar, Jadugar ,Vinaynagar and Madarpura.

4.8 Ramganj PS

After studying about 2009–2014 map of Ramganj PS, it was found that murder and attempt to murder both were not found in the category of hotspot area. Kidnapping mainly occurred near Pahadganj and Shubhas nagar. Rape and kidnapping at Shashibasti area. Home breaking during day occurred at Ajaynagar, Satguru colony and night time crimes took place in Chandverdai, Jhulelal colony and Ajaynagar.

Two wheeler thefts mainly occurred at Sabzi mandi, Railway hospital, Shiv temple (Ajay nagar), HMT parisar and Chungi naka. Other theft occurred at Rambag circle, near OP Ramganjand in Dorai at Hastivihar colony.

Hotspots were found in 500 meters buffer zone of OP Ramganj and OP Dorai and proximity of crime with PS Ramganj and OP Bhagwaanganj was found to be low.

4.9 Christian Ganj PS

After studying about 2009–2014 map of Alwar gate PS, it was found that murder and attempt to murder, kidnapping were not found in the category of hotspot area but criminal comes at Anasagar lake for hiding dead body so installation of CCTV camera is required at this place.

Home breaking during day occurred at Panchsheel nagar, UIT, main Christian ganj area and night time crimes took place in main Panchsheel A and B block, RPSC Colony, Aanandnagar and in 500 meters buffer zone area of Christian ganj OP. Two wheeler theft occurred at Anasagar chaupati, Reliance fresh, Miraj mall , Sagarvihar colony and Shastrinagar.

Proximity of crime with outpost police station was found to be high because Hotspot areas were found in 500meters buffer zone of OP Christian ganj, OP Shastrinagar and OP Haribhau Updhaynagar. No hotspot was found in buffer zone of Christian ganj PS.

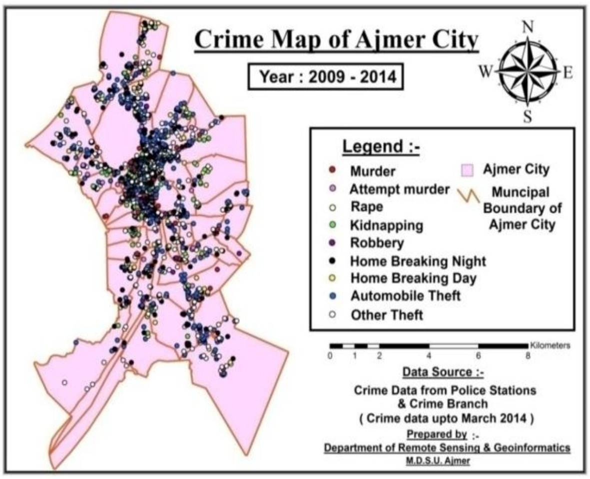

Figure 6: Crime map of Ajmer city (2009 - 2014) with municipal boundary of Ajmer city

Some examples of crime wise map

Different crimes maps of each PS were generated for identification of crime type of hotspot area and compared hotspots of different crimes.

Similarly, crime maps of other crime types such as murder, attempt to murder, rape, kidnapping, robbery, home breaking during day and night, two wheeler and four wheeler thefts and other theft for all nine PS of Ajmer city were generated. Crime data were classified into four time periods of the day viz. 06:00 to 12:00, 12:00 to-18:00, 18:00 to 22:00, and 22:00 to 06:00.

These types of maps were very useful in understanding the relationship between the geographical location, crime type and timing. The respective PS has started using this relationship knowledge against the criminals to reduce the crime. This knowledge has been obtained though GIS.

Crime rate per ten-thousand population, defined as

$$\text{crime rate} = \frac{\text{number of crime in area}}{\text{population of the area}} \text{X10000}$$

for Ajmer city was 37 per ten-thousand population.

Based on the analysis, some suggestions regarding crime were given to the police department in terms of where different types of crimes are occurring and whether these hotspot areas were covered by police force and CCTV camera. These suggestions will help to decrease crime rate.

5. Conclusion

In this study of crime mapping, year-wise and crime wise maps of the PS were generated. This was followed by in-depth analysis to identify hotspot of overall criminal activities and to understand relationship between geographical location, crime types and time of the crimes. Crime rate for Ajmer city was 37 per ten-thousand population.

After conducting the whole research, finally we conclude that police department should know which type of crimes are increasing and in which direction so as to reduce crime rate and to establish law and order in the city.

References

Chainey, S. and J. Ratcliffe (2005). GIS and crime mapping. A Journal of John Wiley and Sons, Ltd.

Cohen, L.E. and M. Felson (1979). Social change and crime rate Trends: A routine activities approach., American Sociological Review 44:588-608.

Fajemirokun, F., O. Adewale, T. Idowu, A. Oyewusiand and B. Maiyegun (2006). A GIS approach to crime mapping and management In Nigeria: A case study of was Victoria islandlagos, shaping the change. XXIII Congress Munich, Germany, October 8 – 13, 2006.

Gupta, R., K. Rajitha, S. Basu and S.K. Mittal (2012). Application of GIS in crime analysis: A gateway to safe city.7-9 February, 2012, India Geospatial Forum.

Jaishankar, K.S., Shanmugapriya and V. Balamurugan (2004). Crime mapping in India: A GIS implementation in Chennai city policing. Journal of Geographic Information Science, Volume 10, No. 1, 20-34.

Kumar, D.L.B., K. Selvavinayagam and S. Suresh Babu (2014). Assessment of crime and its mapping using remote sensing and 3D geo-spatial model for Chennai city. IJSETR Vol 9(8), 418-425.

Patel, K., P. Thakkar, L. Patel and P. Chandresh (2014). GIS based decision support system for crime mapping, analysis and identify hotspot in Ahmedabad city. International Journal of Modern Engineering Research Vol. 4 (1), 32 – 35.

Polvi., N., T. Looman, C. Humphries and K. Pease (1990). Repeat break and enter victimisation: Time course and crime prevention opportunity. Journal of Police Science and Administration 17:8-11.

Thangavelu, A., S.R. Sathyarai and S. Balasubramanian (2013). Assessment of spatial distribution of rural crime mapping in India: A GIS perspective International Journal of Advanced Remote Sensing and GIS, Volume 2, Issue 1, pp. 70-85.

Velasco, M. and R. Boba (2005). Manual of crime analysis map production. Journal of Community Oriented Policing Services, US Department of Justice, November.

Wilson, J.Q. and G.L. Kelling (1982). Broken windows: The police and neighborhood safety. The Atlantic Monthly 249(3): 29-38.

Journal of Geomatics

Vol 10 No. 1 April 2016

On the quality of orthometric correction determination

Raaed Mohamed Kamel Hassouna
Department of Civil Engineering, Faculty of Engineering in Shebin El-Kom, MenoufiaUniversity
Shebin El-Kom, Menoufia, Egypt
Email: rd3165@yahoo.com

(Received: Aug 23, 2015; in final form: Feb 21, 2016)

Abstract: In the present study, a comparison of accuracy and precision between two formulae for assessing Helmert's orthometric correction was carried out. Two test levelling lines were used for comparison. For the two lines, the actual levelling and gravity data were used as reference (real world) data, whereas respective UCPH2002 derived gravity values and SRTM30-interpolated elevation data were executed as erroneous input information. Practically, one formula proved to be less sensitive to the propagation of biases and random errors of the input data, thus yielding a remarkably accurate and precise orthometric correction. So, it is recommended to use this formula, especially when using interpolated end benchmarks elevations in the computation of the height correction. Furthermore, the determination of realistic uncertainties of the height corrections could help model them as observed parameters during the adjustment of levelling loops.

Keywords: Orthometric correction, Error analysis, Uncertainty, Accuracy

1. Introduction

Orthometric height (*OH*) is of a great importance for engineering and geophysical applications. Orthometric height differences are computed through the addition of the orthometric correction (*OC*) to the levelled height differences along the levelling lines. Such correction compensates for the error arising from the non-parallel geo-potential surfaces. So, via the application of *OC*, spirit levelling loop closures would theoretically vanish (Sanso and Vaniček, 2006). For this purpose, gravity information should be available at appropriate sections along the levelling route (Heiskanen and Moritz, 1967).

The impact of the accuracies of both gravity data and benchmarks' heights, on the computed *OC*, was previously studied by Filmer and Featherstone (2011). In this respect, besides Helmert *OC*, other two types of height corrections were considered. Also, the use of global geo-potential models derived gravity in Helmert *OC* assessment was investigated by Filmer et al. (2013) and Hassouna (2013). Regarding Helmert *OC* accuracy, such studies considered the common *OC* formula derived by Heiskanen and Moritz (1967). Also, no explicit investigation has been carried out on the *OC* precision, as expressed by its variance.

Hwang and Hsiao (2003) introduced a new formula for the computation of Helmert *OC*. However, the qualities of *OC*, as computed from the two formulae, have never been compared. Such comparison could flag the specific formula that is more accurate and/or more precise. Obviously, an accurate *OC* model would be more efficient if the input gravity and/or benchmark elevations exhibit some biases. A good example for gravity bias is the omission error of a geo-potential model, from which gravity data are derived. On the other hand, a more precise *OC* implies an optimal propagation of the input data random error through the *OC* model. While an accurately computed *OC* value is directly related to its nature as a correction for a systematic error, it could be claimed that the precision (or uncertainty) of *OC* is less stringent. However, such uncertainty expresses the spread of the computed *OC* about its computed value.

Motivated from the above, the objective of the current study is to compare the above two Helmert *OC* formulae, regarding the accuracy and precision of the resulting *OC*. Such investigation will comprise two levelling lines in Egypt with observed elevations and gravity data. The first line runs along the Nile valley, while the second is located in the Western desert. The two lines exhibit relatively moderate and mountainous terrain roughness, respectively. The qualities of geo-potential model derived gravity and digital terrain model (DTM) derived benchmark elevations are used for a practical comparison among the two formulae over the levelling lines. In this respect, the UCPH2002 geo-potential model (Howe and Tscherning, 2002) is used, up to degree and order 90. Also, the SRTM30 global elevation model (USGS, 2006) is utilized.

2. OC error analysis: comparative algorithms

The *OC* along a spirit levelling line, AB, is commonly expressed by (Heiskanen and Moritz, 1967)

$$OC = \sum_{i=1}^{k} \left(\frac{g_i}{\gamma_0} - 1 \right) \Delta n_i + \left(\frac{\bar{g}_A}{\gamma_0} - 1 \right) H_A - \left(\frac{\bar{g}_B}{\gamma_0} - 1 \right) H_A , \qquad (1)$$

where

Δn_i the geometric height increment relevant to the i[th] levelling section,

k the number of levelling sections,

g_i the observed gravity relevant to the i[th] section,

γ_0 the normal gravity at geodetic latitude 45° on the WGS-84 ellipsoid, which can be computed according to Moritz (1980),

H_A the elevation of the start benchmark A,

H_B the elevation of the end benchmark B,

$\bar{g}_A$ the mean gravity along the plumb line at A $\left(\bar{g}_A = g_A + 0.0424 H_A\right)$,

$\bar{g}_B$ the mean gravity relevant to B $\left(\bar{g}_B = g_B + 0.0424 H_B\right)$,

g_A & g_B the observed gravity at A and B, respectively.

Equivalently, but alternatively expressed, the *OC* could be formulated as follows (Hwang and Hsiao, 2003)

$$OC = \sum_{i=1}^{k} \left(\frac{g_i}{\bar{g}_B} - 1 \right) \Delta n_i + \left(\frac{\bar{g}_A}{\bar{g}_B} - 1 \right) H_A. \qquad (2)$$

Based on the different functional models in Eqs. (1) and (2), one could in general expect different error propagation characteristics. The following two sub-sections will explore both the systematic and random error analysis features for OC as estimated from Eqs. (1) and (2).

2.1 OC systematic error analysis

In the sense of Schofield and Breach (2007, Eq. 2.6 therein), it might be recognized that the resultant systematic error in *OC* could be assessed simply via the total differential. Thus, applying the total differential operator to Eq. (1), it follows that the resultant systematic error in *OC*, δOC, may be expressed as

$$\delta OC = \sum_{i=1}^{k} \frac{\partial OC}{\partial g_i} \delta g_i + \sum_{i=1}^{k} \frac{\partial OC}{\partial \Delta n_i} \delta \Delta n_i + \frac{\partial OC}{\partial \bar{g}_A} \delta \bar{g}_A + \frac{\partial OC}{\partial \bar{g}_B} \delta \bar{g}_B + \frac{\partial OC}{\partial H_A} \delta H_A + \frac{\partial OC}{\partial H_B} \delta H_B, \qquad (3)$$

where δg_i, $\delta \Delta n_i$, $\delta \bar{g}_A$, $\delta \bar{g}_B$, δH_A and δH_B denote the systematic errors in the respective input quantities. The partial derivatives and $\delta \bar{g}_A$, $\delta \bar{g}_B$ in Eq. (3) can be derived as follows (Filmer and Featherstone, 2011)

$$\frac{\partial OC}{\partial g_i} = \frac{\Delta n_i}{\gamma_0}, \qquad (4a)$$

$$\frac{\partial OC}{\partial \Delta n_i} = \frac{g_i}{\gamma_0} - 1, \qquad (4b)$$

$$\frac{\partial OC}{\partial \bar{g}_A} = \frac{H_A}{\gamma_0}, \qquad (4c)$$

$$\frac{\partial OC}{\partial \bar{g}_B} = -\frac{H_B}{\gamma_0}, \qquad (4d)$$

$$\frac{\partial OC}{\partial H_A} = \frac{\bar{g}_A}{\gamma_0} - 1, \qquad (4e)$$

$$\frac{\partial OC}{\partial H_B} = -\left(\frac{\bar{g}_B}{\gamma_0} - 1 \right), \qquad (4f)$$

$$\delta \bar{g}_A = \delta g_A + 0.0424 \delta H_A, \qquad (4g)$$

$$\delta \bar{g}_B = \delta g_B + 0.0424 \delta H_B. \qquad (4h)$$

So, Eq. (3) may be re-written as follows

$$\delta OC = \sum_{i=1}^{k} \frac{\Delta n_i}{\gamma_0} \delta g_i + \sum_{i=1}^{k} \left(\frac{g_i}{\gamma_0} - 1 \right) \delta \Delta n_i + \frac{H_A}{\gamma_0} \delta \bar{g}_A - \frac{H_B}{\gamma_0} \delta \bar{g}_B + \left(\frac{\bar{g}_A}{\gamma_0} - 1 \right) \delta H_A - \left(\frac{\bar{g}_B}{\gamma_0} - 1 \right) \delta H_B. \qquad (5)$$

On the other hand, the total differential of Eq. (2) can be expressed by

$$\delta OC = \sum_{i=1}^{k} \frac{\partial OC}{\partial g_i} \delta g_i + \sum_{i=1}^{k} \frac{\partial OC}{\partial \Delta n_i} \delta \Delta n_i + \frac{\partial OC}{\partial \bar{g}_A} \delta \bar{g}_A + \frac{\partial OC}{\partial \bar{g}_B} \delta \bar{g}_B + \frac{\partial OC}{\partial H_A} \delta H_A, \qquad (6)$$

with

$$\frac{\partial OC}{\partial g_i} = \frac{\Delta n_i}{\bar{g}_B}, \qquad (7a)$$

$$\frac{\partial OC}{\partial \Delta n_i} = \left(\frac{g_i}{\bar{g}_B} - 1 \right), \qquad (7b)$$

$$\frac{\partial OC}{\partial \bar{g}_A} = \frac{H_A}{\bar{g}_B}, \qquad (7c)$$

$$\frac{\partial OC}{\partial \bar{g}_B} = -\frac{1}{\bar{g}_B^{\,2}} \left[\sum_{i=1}^{k} g_i \Delta n_i + H_A \bar{g}_A \right], \qquad (7d)$$

$$\frac{\partial OC}{\partial H_A} = \left(\frac{\bar{g}_A}{\bar{g}_B} - 1 \right). \tag{7e}$$

Accordingly, Eq. (6) may be formulated as follows

$$\delta OC = \sum_{i=1}^{k} \frac{\Delta n_i}{\bar{g}_B} \delta g_i + \sum_{i=1}^{k} \left(\frac{g_i}{\bar{g}_B} - 1 \right) \delta \Delta n_i + \frac{H_A}{\bar{g}_B} \delta \bar{g}_A - \frac{1}{\bar{g}_B^{\,2}} \left[\sum_{i=1}^{k} g_i \Delta n_i + H_A \bar{g}_A \right] \delta \bar{g}_B + \left(\frac{\bar{g}_A}{\bar{g}_B} - 1 \right) \delta H_A . \tag{8}$$

2.2 OC random error analysis

The impact of random errors on *OC* follows from the application of the law of variance-covariance propagation to Eqs. (1) and (2). So, neglecting the error covariances and applying the error propagation principle to Eq. (1), the *OC* variance, σ^2_{OC} , is expressed by (e.g. Ghilani and Wolf, 2006)

$$\sigma^2_{OC} = \sum_{i=1}^{k} \left(\frac{\partial OC}{\partial g_i} \right)^2 \sigma^2_{g_i} + \sum_{i=1}^{k} \left(\frac{\partial OC}{\partial \Delta n_i} \right)^2 \sigma^2_{\Delta n_i} + \left(\frac{\partial OC}{\partial \bar{g}_A} \right)^2 \sigma^2_{\bar{g}_A} + \left(\frac{\partial OC}{\partial \bar{g}_B} \right)^2 \sigma^2_{\bar{g}_B} + \left(\frac{\partial OC}{\partial H_A} \right)^2 \sigma^2_{H_A} + \left(\frac{\partial OC}{\partial H_B} \right)^2 \sigma^2_{H_B} , \tag{9}$$

where σ_{g_i} , $\sigma_{\Delta n_i}$, $\sigma_{\bar{g}_A}$, $\sigma_{\bar{g}_B}$, σ_{H_A} and σ_{H_B} stand for the error standard deviations relevant to the input quantities, which reflects their precisions. The partial derivatives in Eq. (9) are the same derived in Eq. (4). So, Eq. (9) can be written as follows

$$\sigma^2_{OC} = \sum_{i=1}^{k} \left(\frac{\Delta n_i}{\gamma_0} \right)^2 \sigma^2_{g_i} + \sum_{i=1}^{k} \left(\frac{g_i}{\gamma_0} - 1 \right)^2 \sigma^2_{\Delta n_i} + \left(\frac{H_A}{\gamma_0} \right)^2 \sigma^2_{\bar{g}_A} + \left(\frac{H_B}{\gamma_0} \right)^2 \sigma^2_{\bar{g}_B} + \left(\frac{\bar{g}_A}{\gamma_0} - 1 \right)^2 \sigma^2_{H_A} + \left(\frac{\bar{g}_B}{\gamma_0} - 1 \right)^2 \sigma^2_{H_B} . \tag{10}$$

Similarly, applying the law of variance-covariance propagation to Eq. (2),

$$\sigma^2_{OC} = \sum_{i=1}^{k} \left(\frac{\partial OC}{\partial g_i} \right)^2 \sigma^2_{g_i} + \sum_{i=1}^{k} \left(\frac{\partial OC}{\partial \Delta n_i} \right)^2 \sigma^2_{\Delta n_i} + \left(\frac{\partial OC}{\partial \bar{g}_A} \right)^2 \sigma^2_{\bar{g}_A} + \left(\frac{\partial OC}{\partial \bar{g}_B} \right)^2 \sigma^2_{\bar{g}_B} + \left(\frac{\partial OC}{\partial H_A} \right)^2 \sigma^2_{H_A} , \tag{11}$$

which after using Eq. (7) gives

$$\sigma^2_{OC} = \sum_{i=1}^{k} \left(\frac{\Delta n_i}{\bar{g}_B} \right)^2 \sigma^2_{g_i} + \sum_{i=1}^{k} \left(\frac{g_i}{\bar{g}_B} - 1 \right)^2 \sigma^2_{\Delta n_i} + \left(\frac{H_A}{\bar{g}_B} \right)^2 \sigma^2_{\bar{g}_A} + \left[\frac{1}{\bar{g}_B^{\,2}} \left[\sum_{i=1}^{k} g_i \Delta n_i + H_A \bar{g}_A \right] \right]^2 \sigma^2_{\bar{g}_B} + \left(\frac{\bar{g}_A}{\bar{g}_B} - 1 \right)^2 \sigma^2_{H_A} . \tag{12}$$

Also, using the law of error propagation, it follows that

$$\sigma^2_{\bar{g}_A} = \sigma^2_{g_A} + (0.0424)^2 \sigma^2_{H_A} , \tag{13a}$$

$$\sigma^2_{\bar{g}_B} = \sigma^2_{g_B} + (0.0424)^2 \sigma^2_{H_B} . \tag{13b}$$

3. Input data and input errors for the test levelling lines

The current study considers two levelling lines in Egypt with observed elevations and gravity data. The first line (Line I) runs along the Nile valley, while the second (Line II) is located in the Western desert. Line I and line II exhibit relatively moderate and mountainous terrain roughness, respectively. Figure 1 depicts two post maps for the gravity points along both lines. While the available terrestrial gravity and elevation data are used as real world reference values in the current investigation, the input "erroneous" gravity and height information (input into the error analysis algorithms) are derived from the UCPH2002 geo-potential model and the SRTM30 terrain model, respectively. First, geo-potential model derived surface gravity was derived as the sum of the UCPH2002-synthesized surface gravity disturbances relative to WGS-84 and the respective normal gravity values (Forsberg and Tscherning, 2008; Filmer and Featherstone, 2011; Filmer et al., 2013; Hassouna, 2013). On the other hand, the SRTM30 grid was used to interpolate respective elevation data at the points of lines I and II, via the B-spline interpolation algorithm (Cimmery, 2010).

Table 1 lists the different features of the two levelling lines under consideration. Table 2 shows the statistics of the differences among the derived "erroneous" gravity and benchmark elevation values; and the respective reference values over the investigated lines.

4. Numerical error analyses comparison

Regarding *OC* accuracy, as given by Eqs. (5) and (8), the section-wise varying δg_i in Table 2 were used to represent the respective gravity biases, while δg_A and δg_B were supposed to be the gravity biases at the start and end benchmark, respectively. While such gravity biases represent the geo-potential model omission error, it could be comparable to gravity biases that could arise from the interpolation of the respective gravity values from a specific gravity data base. In the same manner, δH_A and δH_B (in Table 2) were used as the elevation biases relevant to the start and end benchmarks. Such biases might seem realistic for the actual lines I and II, provided that the typical surveyor, although could perform a precise spirit levelling, might not have access to the official elevations for all benchmarks in a levelling network. Accordingly, a way out is to use interpolated elevations for the assessment of *OC* (Filmer and Featherstone, 2011).

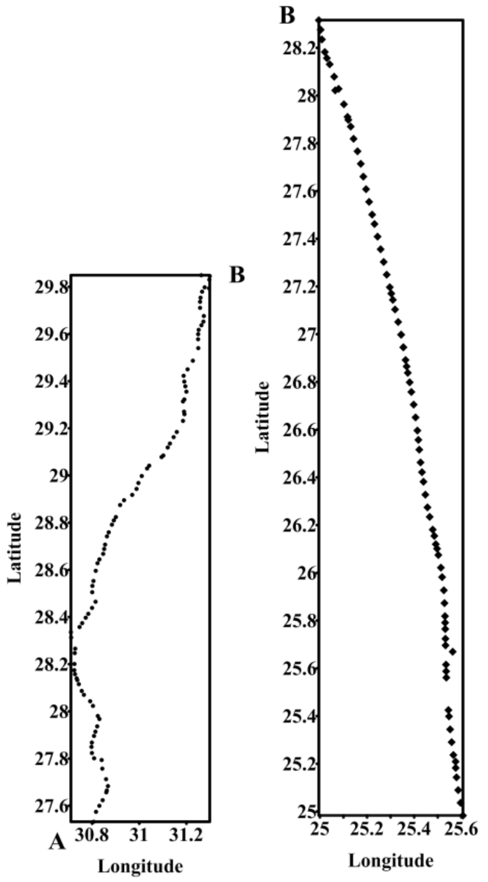

Figure 1: Post maps for Lines (I) and (II)

Table 1: Different features of the two levelling profiles

Line	No. of gravity sections	ΔH (m)	Mean elevation (m)	Length (km)
I	93	-24.68	34.85	280.4
II	78	-391.82	268.18	369.2

The observational noises of the observed (reference) gravity data for the test lines are in the order of 1 mgal. Also, the error budget for the reference elevations of the start and end benchmarks could be as worse as a few centimeters. However, such small uncertainties might not represent those of any eventual interpolated gravity or elevation values, which are greatly affected by the local gravity and terrain signal roughness. So, it was decided to use the spatial standard deviations of the gravity discrepancies, $\sigma_{\delta g_i}$, as representing σ_{g_i} over each levelling line, as given in Table 2.

Similarly, the spatial precision of the elevations discrepancies in Table 2, $\sigma_{\delta H_i}$, was used to represent both σ_{H_A} and σ_{H_B} for each levelling line. Such values were used to evaluate the *OC* precision, σ_{OC} , using Eqs. (10) and (12) for the two lines. Also, as far as the aim of the current work is to compare the accuracy and precision of two formulae in furnishing the *OC*, the very pessimistic biases and standard deviations in Table 2 could help test the sensitivity of the two formulae to systematic and random error propagation. In particular, interpolated benchmark elevations and synthesized or interpolated gravity data could exhibit such bad qualities. It should be emphasized that spirit levelling is characterized by high quality height increments. So, the height increments, Δn_i , were considered errorless over the whole computations.

During the assessment of the *OC* quality features, using Eqs. (5), (8), (10) and (12), the reference gravity, elevations and height increment values were used as the evaluation points of the respective partial derivatives. Also, it should be kept in mind that the input biases and uncertainties of gravity and benchmark elevations were marginally treated. In other words, as will be depicted by Tables 3 and 4, if the gravity accuracy or precision is emphasized, the benchmark elevations are assumed errorless and vice versa. Such separation in error analysis could enable individual investigations of the effect of gravity and benchmark elevations' qualities on that of the *OC*.

It is worth mentioning that $\left(\delta\bar{g}_A \,\&\, \delta\bar{g}_B\right)$ and $\left(\sigma\bar{g}_A \,\&\, \sigma\bar{g}_B\right)$ were appropriately computed from Eqs. (4g & 4h) and (13), respectively, taking into account whether or not the gravity or benchmark elevations are kept errorless.

In the above sense, Tables 3a and 3b summarize the accuracies of *OC*, as computed from Eq. (5) and Eq. (8). Also, Tables 4a and 4b show the respective items, but regarding the precisions of *OC* determination obtained via Eqs. (10) and (12).

5. Discussion and concluding remarks

Tables 3a and 3b show that in general, the accuracies of *OC* determination by the two formulae deteriorate as the terrain roughness increases. Table 3a implies that Eqs. (1) and (2) yield equally accurate *OC* values, if one deals with highly accurate (i.e. nearly errorless) benchmark elevations. Table 3a shows also that in such case, geo-potential models derived gravity could safely be used to assess quite accurate *OC* values in case of moderate terrain roughness, as that represented by line I. This is easy to conclude from the respective two zero values for δOC . Numerically, this can be attributed to the insignificance of the non-vanishing terms in Eqs. (5) and (8) for line I. On the other hand, Table 3b shows a dramatic deterioration of *OC* accuracy, if computed via Eq. (1), compared to that assessed by Eq. (2). Regarding line I, such deterioration is less pronounced. So, in general, Eq. (2) yield more accurate *OC* magnitudes, if interpolated benchmark heights are to be used along with highly accurate gravity data.

Table 2: Statistics of the discrepancies among the erroneous and reference quantities for the two lines

Line	Item	Unit	$Mean\ \delta g_i$	$\sigma_{\delta g_i}$	$Min.\ \delta g_i$	$Max.\ \delta g_i$	δg_A	δg_B
I	$(g_{UCPH\,2002} - g_{observed})$	$(mgal)$	4.65	8.33	-17.46	22.70	11.50	20.78
II			23.79	13.17	3.00	50.43	10.35	17.95
Line	**Item**	**Unit**	$Mean\ \delta H_i$	$\sigma_{\delta H_i}$	$Min.\ \delta H_i$	$Max.\ \delta H_i$	δH_A	δH_B
I	$(H_{SRTM\,30} - H_{observed})$	(m)	-2.26	1.51	-5.71	1.83	-3.34	-2.37
II			-2.66	32.90	-133.39	200.11	14.94	-8.50

Table 3a: Comparison among the *OC* accuracies (gravity accuracy emphasized)

Line	δg_i $(mgal)$	δg_A $(mgal)$	δg_B $(mgal)$	δOC (mm) **(Eq. 5)**	δOC (mm) **(Eq. 8)**
I	Section-wise varying	11.50	20.78	0.0	0.0
II		10.35	17.95	-4.6	-4.6

Table 3b: Comparison among the *OC* accuracies (elevation accuracy emphasized)

Line	δH_A (m)	δH_B (m)	δOC (mm) **(Eq. 5)**	δOC (mm) **(Eq. 8)**
I	-3.34	-2.37	2.0	0.6
II	14.94	-8.50	-40.2	-4.7

Table 4a: Comparison among the *OC* precisions (gravity precision emphasized)

Line	σ_{g_i} $(mgal)$	σ_{g_A} $(mgal)$	σ_{g_B} $(mgal)$	σ_{OC} (mm) **(Eq. 10)**	σ_{OC} (mm) **(Eq. 12)**
I	8.33			0.5	0.5
II	13.17			8.3	8.3

Table 4b: Comparison among the *OC* precisions (elevation precision emphasized)

Line	σ_{H_A} and σ_{H_B} (m)	σ_{OC} (mm) **(Eq.10)**	σ_{OC} (mm) **(Eq. 12)**
I	1.51	3.1	0.3
II	32.90	78.7	11.3

Regarding *OC* uncertainty, almost all the above comments relevant to Tables 3a and 3b still apply for Tables 4a and 4b. So, Eq. (2) is more precise than Eq. (1), when interpolated benchmark elevations are used. So, generally, for a high quality *OC* determination, it is recommended to use Eq. (2). Such results should be understood to hold to the investigated interpolated benchmark elevations and synthesized gravity values along levelling lines. Besides being more economic, such levelling data sources may be the only available tool for assessing *OC*. The use of the SRTM30 and the UCPH2002 low resolution models in the current study was for the sake of handling an instance worst case. A future work may test other high resolution DTMs and geo-potential models for representing erroneous data.

A further related criterion could be the assessment of the values and qualities of *OCs* for height differences along profiles, which are extracted from DEMs. Such terrain models may be derived from satellite imagery or photogrammetry. In this respect, the published uncertainty of elevations would often be of the order of that discussed in the current study. Accordingly, Eq. (2) is expected to show better error propagation characteristics.

Finally, it could seem rational and innovative to model the *OCs* as biases over levelling circuits in vertical networks. In this sense, *OCs* over levelling lines might be treated as observed weighted parameters during the adjustment of levelling nets (e.g. Ghilani and Wolf, 2006). Of course, the weights of such parameters should lean on the respective error standard deviations, and hence, the importance of *OC* precision may arise. This in turn could optimally help pick out the random loop closures parts during the adjustment.

Acknowledgment

Three unknown reviewers are acknowledged for their critical review of the manuscript.

References

Cimmery, V. (2010). User guide for SAGA (version 2.0.5). Volumes 1 and 2, August, 2010, SAGA System for Automated Geoscientific Analyses. Available: http:// www. saga-gis.org.

Filmer, M.S. and W.E. Featherstone (2011). Error propagation for three common height-system corrections to differential levelling. Journal of Spatial Science 56(1), pp. 39-58.

Filmer, M.S., C. Hirt and W.E. Featherstone (2013). Error sources and data limitations for the prediction of surface gravity: a case study using benchmarks. Stud. Geophys. Geod., 57(1), pp. 47-66.

Forsberg, R. and C.C Tscherning (2008). An overview manual for the GRAVSOFT geodetic gravity field modelling programs. 2nd ed., National Space Institute (DTU-Space), Denmark, August.

Ghilani, C. and P. Wolf (2006). Adjustment computations: Spatial data analysis. 4th ed., John Wiley & Sons, Hoboken, New Jersey.

Hassouna, R. (2013). Geo-potential models as a tool of densifying gravity for orthometric correction computation. Engineering Research Journal, Faculty of Engineering in Shebin El-Kom, Menoufia University, Egypt,36(4), pp. 475-479.

Heiskanen, W.A. and H. Moritz (1967). Physical Geodesy. W.H. Freeman and Company.

Howe, E. and C.C. Tscherning (2002). Analysis of one month of CHAMP state vector and accelerometer data for the recovery of the gravity potential. Poster presented at the XXVII General Assembly of the European Geophysical Society, Nice, France, April 21-26.

Hwang, C. and Y.S. Hsiao (2003). Orthometric corrections from levelling, gravity, density and elevation data: a case study in Taiwan. Journal of Geodesy, 77(5-6), pp. 279-291.

Moritz, H. (1980). Geodetic reference system 1980. Bulletin Géodésique, 54(3), pp. 395-405.

Sanso, F. and P. Vaniček (2006). The orthometric height and the holonomity problem. Journal of Geodesy, 80(5), pp. 225-232.

Schofield, W. and M. Breach (2007). Engineering surveying (6th ed.). Elsevier.

USGS (2006). SRTM30. Available: http://dds.cr.usgs. gov/srtm/.

Guidelines for "National Geomatics Award for Excellence”

This award has been instituted to recognize outstanding and conspicuously important contribution in promoting geomatics technology and applications at the country level. The contributions should have made major impact on the use of this technology for national development.

Areas of contribution considered for the award are:

1. Geographical Information System
2. Global Positioning System
3. Photogrammetry
4. Digital Cartography

The award shall consist of Rs. 50,000/- in cash, a medal and citation.

Eligibility

Any citizen of India, engaged in activities related to geomatics technology and its applications is eligible for this award. The prize is awarded on the basis of work primarily done in India.

The age limit for awardees is 45 years or above as on June 30 of the year of award.

Selection

A duly constituted Award Committee will evaluate all nominations received. The committee shall consist of eminent experts in the field of geo-spatial technology, to be identified by the Executive Council, ISG. The committee shall forward selected name/s to ISG – EC for approval and announcement. Apart from those persons, whose nominations have been received, the Committee may consider any person or persons who, in their opinion, have made outstanding contributions to development of geo-spatial technology and applications.

The award can be withheld in any year if, in the opinion of the committee, no candidate is found suitable in that particular year.

Presentation of the Award

The award shall be presented during the Annual Convention of ISG. Local Hospitality shall be taken care by ISG & Air fare (low cost) may be reimbursed if awardees request for it.

How to make Nomination

The nominations can be proposed by Head of a major research institute/ centre; Vice-Chancellor of a university; Secretary of Government Scientific Departments; President of a National Academy, President, Indian Society of Geomatics / Indian Society of Remote Sensing / Indian National Cartographic Association / ISG fellow or two life members of the society with more than 10 year old membership.

A candidate once nominated would be considered for a total period of two years. Nomination should be sent in the prescribed format to Secretary, ISG.

The last date for receiving nominations shall be September, 31 or otherwise extended.

Nomination Format for "National Geomatics Award for Excellence”

1. Name of the Nominee
2. Postal Address
3. Academic Background (Bachelor degree onwards)
4. Field of Specialisation
5. Important positions held (in chronological order)
6. Professional Experience including foreign assignments.
7. Important Awards / Honours
8. Important Publications/Patents: (A set of ten most important publications to be enclosed with this form)
9. Contributions of Nominee based on which the nomination is sent (in 1000 words, also provide a statement in 50 words which may be used for citation.):
10. Other Relevant Information:

Proposer:

Signature
Name
Address
Phone/ Fax
E-mail
Life Membership No. (in case of ISG Member):

Place & Date

Endorsed by (in case nomination is by 2 ISG Life members)

Signature
Name
Address
Phone/ Fax
E-mail
Life Membership No. (in case of ISG Member):

Place & Date
(The proposer should give a brief citation of the nominee's work)

National Geomatics Award

National Geomatics Award to be given each year: a) for original and significant contribution, b) for innovative applications in the field of Geomatics. Each award comprises a medal, a citation and a sum of Rs 25,000/- The guidelines for these awards are available on ISG website.

ISG Chapter Award for Best Performance

The best chapter award will be given to an active chapter of Indian Society of Geomatics, which has made significant contribution to further the mandate and goal of the society. The award consists of a citation and medal

President's Appreciation Medal for Contribution to the ISG

This award will be given to a member of the society, who has made noteworthy contribution to the growth of the ISG (its main body or any chapter). The Award consists of a Medal and a Citation.

Prof. Kakani Nageswara Rao Endowment Young Achiever Award

Indian Society of Geomatics instituted a new award from year 2013 named "Prof. Kakani Nageswara Rao Endowment Young Achiever Award", to encourage young researchers/scientists/academicians pursuing research in the field of geospatial technology/applications. The award carries a cash prize of Rs.10,000/- along with a citation.

NATIONAL GEOMATICS AWARDS 2016

Indian Society of Geomatics has instituted two National Geomatics Awards to be given each year for a Original and significant contribution, b Innovative application(s) in the field of Geomatics. Each award comprises a medal, a citation and a sum of Rs. 25,000/-.

The guidelines for the award are as under

Areas of contribution considered for the award

1. Geographical Information System
2. Global Positioning System
3. Photogrammetry
4. Digital Cartography

Eligibility

Any citizen of India engaged in scientific work in any of the above-mentioned areas of research is eligible for the award.

The awards are to be given for the work largely carried out in India.

- First award will be given for original contribution in the field of Geomatics supported by publications in a refereed journal of repute.
- Second award will be given for carrying out innovative application(s).
- The contribution for the first award should have been accepted by peers through citation of the work.
- Work based on the applications of existing technologies will not be considered for the first award.
- The work should have made impact on the overall development of Geomatics.

How to Send Nomination

Nominations should be sent in the prescribed format, completed in all aspects to the Secretary, Indian Society of Geomatics, Space Applications Centre Campus, Ahmedabad 380 015 by August 31, 2016.

Selection Process

An expert committee, consisting of at least three members, constituted by the Executive Council of the Indian Society of Geomatics, will scrutinize the nominations and recommend the awardees' names to the Executive Council. The Council will decide on the award based on the recommendations.

FORMAT FOR AWARD NOMINATION

1. Name of the Candidate:
2. Present Position:
3. Positions held earlier (chronological order):
4. Academic qualifications (Bachelor's degree onwards):
5. Names of at least three Indian Scientists/Technologist in the area as possible referees *:
6. Brief write up on the work (500 words) for which award is claimed:
7. Publication(s) on the above work (reprint(s) to be enclosed):
8. List of other publications of the candidate:
9. Citation of the work for which award is claimed:
10. Impact of the work (for which award is claimed) on the development in the field of Geomatics (500 words):
11. Whether the work has already won any award? If so, give details:

The Applications in the above format (five copies) should be submitted (by Registered Post or Speed Post) to

The Secretary, Indian Society of Geomatics,
Space Applications Centre Campus,
Ahmedabad-380015

so as to reach by August 31, 2016.

*ISG is, however, not bound to accept these names and can refer the nomination to other experts/peers

Journal of Geomatics Vol 10 No. 1 April 2016

INDIAN SOCIETY OF GEOMATICS FELLOWS

Shri Pramod P. Kale, Pune
Dr George Joseph, Ahmedabad
Dr A.K.S. Gopalan, Hyderabad
Dr Prithvish Nag, Varanasi
Dr Baldev Sahai, Ahmedabad
Shri A.R. Dasgupta, Ahmedabad
Dr R.R. Navalgund, Bangaluru
Shri Rajesh Mathur, New Delhi
Dr Ajai, Ahmedabad
Prof P. Venkatachalam, Mumbai

ISG - PATRON MEMBERS

P-1 Director, Space Applications Centre (ISRO), Jodhpur Tekra Satellite Road, Ahmedabad - 380 015
P-2 Settlement Commissioner, The Settlement Commissioner & Director of Land Records-Gujarat, Block No. 13, Floor 2, Old Sachivalay, Sector-10, Gandhinagar – 382 010
P-3 Commissioner, Mumbai Metropolitan Region Development Authority, Bandra-Kurla Complex, Bandra East, Mumbai - 400 051
P-4 Commissioner, land Records & Settlements Office, MP, Gwalior - 474 007
P-5 Director General, Centre for Development of Advanced Computing (C-DAC), Pune University Campus, Ganesh Khind, Pune - 411 007
P-6 Chairman, Indian Space Research Organization (ISRO), ISRO H.Q., Antariksha Bhavan, New BEL Road, Bengaluru 560 231
P-7 Director General, Forest Survey of India, Kaulagarh Road, P.O. I.P.E., Dehra Dun – 248 195
P-8 Commissioner, Vadodara Municipal Corporation, M.S. University, Vadodara - 390 002
P-9 Director, Centre for Environmental Planning and Technology (CEPT), Navarangpura, Ahmedabad - 380 009
P-10 Managing Director, ESRI INDIA, NIIT GIS Ltd., 8, Balaji Estate, Sudarshan Munjal Marg, Kalkaji, New Delhi - 110 019
P-11 Director, Gujarat Water Supply and Sewerage Board (GWSSB), Jalseva Bhavan, Sector – 10A, Gandhinagar - 382 010
P-12 Director, National Atlas & Thematic Mapping Organization (NATMO), Salt Lake, Kolkata - 700 064
P-13 Director of Operations, GIS Services, Genesys International Corporation Ltd., 73-A, SDF-III, SEEPZ, Andheri (E), Mumbai - 400 096
P-14 Managing Director, Speck Systems Limited, B-49, Electronics Complex, Kushiaguda, Hyderabad - 500 062
P-15 Director, Institute of Remote Sensing (IRS), Anna University, Sardar Patel Road, Chennai - 600 025
P-16 Managing Director, Tri-Geo Image Systems Ltd., 813 Nagarjuna Hills, PunjaGutta, Hyderabad - 500 082
P-17 Managing Director, Scanpoint Graphics Ltd., B/h Town Hall, Ashram Road, Ahmedabad - 380 006
P-18 Secretary General, Institute for Sustainable Development Research Studies (ISDRS), 7, Manav Ashram Colony, Goplapura Mod, Tonk Road, Jaipur - 302 018
P-19 Commandant, Defense institute for GeoSpatial Information & Training (DIGIT), Nr. Army HQs Camp, Rao Tula Ram Marg, Cantt., New Delhi - 110 010
P-20 Vice President, New Rolta India Ltd., Rolta Bhavan, 22nd Street, MIDC-Marol, Andheri East, Mumbai - 400 093
P-21 Director, National Remote Sensing Centre (NRSC), Deptt. of Space, Govt. of India, Balanagar, Hyderabad - 500 037
P-22 Managing Director, ERDAS India Ltd., Plot No. 7, Type-I, IE Kukatpalli, Hyderabad - 500 072
P-23 Senior Manager, Larsen & Toubro Limited, Library and Documentation Centre ECC Constr. Gp., P.B. No. 979, Mount Poonamallee Road, Manapakkam, Chennai - 600 089.
P-24 Director, North Eastern Space Applications Centre (NE-SAC), Department of Space, Umiam, Meghalaya 793 103
P-25 Progamme Coordinator, GSDG, Centre for Development of Advanced Computing (C-DAC), Pune University Campus, Pune – 411 007
P-26 Chief Executive, Jishnu Ocean Technologies, PL-6A, Bldg. No. 6/15, Sector – 1, Khanda Colony, New Panvel (W), Navi Mumbai – 410 206
P-27 Director General, A.P. State Remote Sensing Applications Centre (APSRAC), 8th Floor, "B" Block, Swarnajayanthi Complex, Ameerpet, Hyderabad- 500 038
P-28 Director, Advanced Data Processing Res. Institute (ADRIN), 203, Akbar Road, Tarbund, Manovikas Nagar P.O., Secunderabad – 500 009
P-29 Managing Director, LEICA Geosystems Geospatial Imaging Pvt. (I) Ltd., 3, Enkay Square, 448a Udyog Vihar, Phase-5, Gurgoan- 122 016
P-30 Director, Defense Terrain Research Limited (DTRL), Ministry of Defense, Govt. of India, Defense Research & Development Organisation, Metacafe House, New Delhi – 110 054
P-31 Chairman, OGC India Forum, E/701, Gokul Residency, Thakur Village, Kandivali (E), Mumbai – 400 101
P-32 Managing Director, ML Infomap Pvt. Ltd., 124-A, Katwaria Sarai, New Delhi – 110 016
P-33 Director, Rolta India Limited, Rolta Tower, "A", Rolta Technology Park, MIDC, Andheri (E), Mumbai – 400 093
P-34 Director, State Remote Sensing Applications Centre, Aizawl – 796 012, Mizoram

Instructions for Authors

The journal covers all aspects of Geomatics – geodata acquisition, pre-processing, processing, analysis and publishing. Broadly this implies inclusion of areas like GIS, GPS, Photogrammetry, Cartography, Remote Sensing, Surveying, Spatial Data Infrastructure and Technology including hardware, software, algorithms and model. It endeavours to provide an international forum for rapid publication of developments in the field – both in technology and applications.

To begin with the frequency of publication will be six- monthly. However, depending on the response and interest, frequency of publication may be reviewed.

A manuscript for publication must be based on original research work done by the author(s). It should not have been published in part or full in any type of publication nor should it be under consideration for publication in any periodical. Unsolicited review papers will not be published.

The Editorial Board or the Indian Society of Geomatics is not responsible for the opinions expressed by the authors.

Language

The language of the Journal will be English (Indian). However, manuscripts in English (US) and English (British) are also acceptable from authors from countries located outside India.

Manuscript Format

Each paper should have a title, name(s) of author(s), and affiliation of each of the authors with complete mailing address, e-mail address, an abstract, four to six keywords, and the text. The text should include introduction/background, research method, results, discussion, followed by acknowledgements and references. The main text should be divided in sections. Section headings should be concise and numbered in sequence, using a decimal system for subsections. Figures, images and their captions should be inserted at appropriate points of the text. Figures, images and tables should fit in two column format of the journal. If absolutely necessary, figures, images and tables can spread across the two columns. Figures and images, however, should not exceed half a page in height. A title should be provided for each Table, Image and Figure. All figures and images should be in 600 dpi resolution and sized as per column/margin width. Authors must ensure that diagrams/figures should not lose easy readability upon reduction to column size. The SI (metric) units and international quantities should be used throughout the paper. In case measurements are given in any other system, equivalent measurements in SI (metric) units should be indicated in brackets.

Use MS Word with English (UK/US) or English (Indian) dictionary. The page size should be A4 paper, with 2 cm margin on all sides. Title, authors and affiliation should be centred. Abstract should be justified across margins. The manuscript text should be in two columns of 8.2 cm each with a gutter of 6mm between them. Use only Times New Roman fonts. Title should be 12 points bold. Authors and affiliation should be 9 points. All other text including headings should be 10 points. Heading numbering scheme should be decimal e.g. 1, 1.1, 1.2.3, etc. Headings should be in bold.

Normally length of a published paper should be about 6-10 pages in A4 size including figures. Use of illustrations in colour should be restricted and resorted to only where it is absolutely necessary and not for enhancing the look of the paper. If the number of colour illustrations exceeds five, authors' institution may be asked to reimburse the extra cost involved, which at current rates is about Rs. 2500 per coloured figure/diagram/plate/illustration.

Submission of Manuscript

Submissions should be in electronic form via email. The manuscript may be sent by email to drajai1953@gmail.com. In exceptional cases hard copy submission in camera ready form may be allowed with the prior permission of the Chief Editor. Submission in any other form will be returned to the author. To speed up the review process, authors are advised to provide a list of three probable reviewers with their institutional address and e-mail IDs.

Guidelines for Citing References

Names of all cited publications should be given in full. No abbreviations should be used. Following procedure is to be adopted.

Journal Publications

Bahuguna, I.M. and A.V. Kulkarni (2005). Application of digital elevation model and orthoimages derived from IRS-1C Pan stereo data in monitoring variations in glacial dimensions, Journal of the Indian Society of Remote Sensing, 33(1), 107- 112. (to be referred to in the text as Bahuguna and Kulkarni (2005) or if more than two sets of authors are to be referred to, as (Bahuguna and Kulkarni, 2005; Jain et al., 1994)) When more than two authors are to be referred to, use Jain et al. (1994). However, in References, all authors are to be mentioned.

Publication in a Book

Misra, V.N. (1984). Climate, a factor in the rise and fall of the Indus Civilization – Evidence from Rajasthan and Beyond in Frontiers of the Indus Civilization (B.B. Lal and S.P. Gupta: Chief Editors) Books and Books, New Delhi, pp. 461-489

Papers Published in Seminar/ Symposium Proceedings

Jain, A., A.R. Shirish, M. Das, K. Das, M.C. Porwal, and P.S. Roy (1994). Remote Sensing and Geographic Information System – An approach for the assessment of biotic interference in the forest ecosystem. Proceedings. 15th Asian Conference on Remote Sensing,Bangaluru, November 17-23, 1994, pp. 65-72.

Books

Possehl, Gregory L. (1999). Indus Age: The beginnings. Oxford and IBH Publishing Corporation, New Delhi.

Reviewing

Each paper will be reviewed by three peers. Papers forwarded by members of the Editorial or Advisory Boards along with their comments would get processed faster and may be reviewed by two referees only.

Sample format for Authors is available in downloadable form at ISG website: www.isgindia.org/JOG/Sample_format.doc

Copyright

The copyright of the paper selected for publication will rest with the Indian Society of Geomatics. Corresponding author shall be required to sign a copyright assignment form, on behalf of all authors, once the paper is selected for publication. Authors are, however, at liberty to use this material elsewhere after obtaining permission from the Indian Society of Geomatics.

If the authors have used any copyright material in their manuscript, it is understood that they have obtained permission from the owner of the copyright material and they should convey the same along with the manuscript to the Chief Editor.

Certificate of Original Work

The authors will also provide a certificate that the paper is an original work, not published or being considered for publication elsewhere.

In the event the certificate turns out to be false, the Journal shall ban the author(s) from publishing in the Journal for a period of five years and inform the same to all other related publications.

Reprints

Authors will be provided soft copy (PDF) of their paper, no hard copy reprints will be provided.

Indian Society of Geomatics (ISG)

(www.isgindia.org)

Membership Application Form

To

The Secretary
Indian Society of Geomatics
39, Basant Bahar - II
Bopal, Ahmedabad – 380058

Sir,

I want to become a Member/ Life Member/ Sustaining Member/ Patron Member/ Foreign Member/ Student Member of the Indian Society of Geomatics, Ahmedabad for the year ______. Membership fee of Rs. ______/- is being sent to you by Cash/DD/Multicity Cheque. (In case of DD/ Cheque No. _________, drawn on Bank ______________________________.

I agree to abide by the Constitution of the Society.

Date:

Place:

Signature

1. Name:____
2. Address:____

____ PIN: __________

Phone:______________ Fax: ______________ Email: ______________________________

3. Date of Birth: ____
4. Qualifications ____
5. Specialisation: ____
6. Designation & Organisation.: ____
7. Membership in other Societies: ____

____

8. Mailing Address: ____

____ PIN: __________

Proposed by:
(Member's Name and No)

Signature of Proposer

For Office Use

ISG Membership No:

ISG Receipt No. : Date:

MEMBERSHIP SUBSCRIPTION

Sr. No.	Membership Category	Admission Fee		Annual Subscription Rs. (Indian)
		Rs. (Indian)	**US$ (Foreign)**	300.00
1.	Annual Member	10.00	-	
2.	Life Member a) Admitted before 45 years of age b) Admitted after 45 years of age	 2500.00 2000.00	 250.00 200.00	
3.	Sustaining Member	-		2000.00
4.	Patron Member	5000.00	3000.00	
5.	Student Member	10.00	-	100.00

MEMBERSHIP GUIDELINES

1. Subscription for Life Membership is also accepted in two equal installments payable within a duration of three months, if so desired by the applicant. In such a case, please specify that payment will be in installments and also the probable date for the second installment (within three months of the first installment).
2. A Member of the Society should countersign application of membership as proposer.
3. Subscription in DD or Multicity Cheque should be made out in the name of 'INDIAN SOCIETY OF GEOMATICS' and payable at Ahmedabad.
4. Financial year of the Society is from April 1 to March 31.
5. For further details, contact Secretary, Indian Society of Geomatics at the address given above.
6. ISG has chapters already established at the following places. Ahmedabad, Ajmer, Bhagalpur, Bhopal, Chennai, Dehradun, Delhi, Hyderabad, Mangalore, Mumbai, Mysore, New Delhi, Pune, Srinagar, Tiruchirappalli, Vadodara and Visakhapatnam. Applicants for membership have the option to contact Secretary/Chairman of the local chapter for enrolment. Details can be found at the website of the Society: www.isgindia.org
7. Journal of the Society will be sent only to Patron Members, Sustaining Members and Life Members.

www.bhuvan.nrsc.gov.in

Features

- Pocket Bhuvan
- Multi-Lingual Bhuvan
- Time Series Visualisation
- Robust NOEDA (NRSC Open EO Data Archive)
- Societal applications
- Online shapefile creation

QR Code

इसरो ISRO

View Globe through bhuvan

Gateway to Indian Earth Observation

Improved Products From Resourcesat-2

Part of Aleppo, Syria (5m Color)

- Geo Orthokit
- Ortho Rectified
- Bundle
- Merged

70 km Multi Spectral Data of 5.8m

Better Radiometric Resolution